Fluid-Rock Interaction Studies on an Enhanced Geothermal System in the Cooper Basin, South Australia

THE UNIVERSITY of ADELAIDE

Gideon Bani Kuncoro

School of Chemical Engineering

The University of Adelaide

A thesis submitted for examination for the degree of

Doctor of Philosophy in Chemical Engineering

October 2014

Declaration

This work contains no material which has been accepted for the award of any other degree or diploma in any university or other tertiary institution and, to the best of my knowledge and belief, contains no material previously published or written by another person, except where due reference has been made in the text.

I give consent to this copy of my thesis when deposited in the University Library, being made available for loan and photocopying, subject to the provisions of the Copyright Act 1968.

Signature: ……. Date: …….

(Gideon Bani Kuncoro)

Summary

Engineered Geothermal System (EGS) has great potential to supply electricity by harnessing stored thermal energy from high temperature granitic rocks. Since reserves of coal, oil, and natural gas are being depleted at an increasing rate, this route provides opportunities to generate electrical power without producing greenhouse gas emissions or long lasting nuclear wastes, at a cost that is competitive to those generated from fossil fuels. Australia has a vast amount of thermal area, though the heat exchange occurs at a significantly greater depth (5 km) to conventional geothermal system. Clearly, the study of fluid-rock interaction is crucial and remains largely poorly addressed and known. A compounding factor is the fact that fundamental processes associated with mineral dissolution and precipitation, and the developed pressure temperature gradient remain poorly understood. Furthermore, a number of issues relating to geothermal geochemistry are required to be considered and explored to ensure safe, economic energy production from the "hot rocks". Low pH and saline waters at temperatures exceeding 200^{o}C are highly corrosive. Thus, it is vital to prevent the generation of scaling as the brines cool during transport to the surface.

The objectives of this study were to investigate the geochemistry, the fluid-rock interaction, and model the precipitation rate of silica. Experimental work was carried out to observe the fluid-rock interaction, including analysis on the rock to monitor the dissolved elements in the circulating fluid, and the water chemistry after the interaction. The granite samples were analysed using x-ray diffraction and results showed that the rock consist of mainly quartz, albite and K-feldspar.

This study concentrated on the dissolution rate of granite by observing the silica concentration in the liquid phase with the aid of previous dissolution rate studies of pure quartz, albite and K-feldspars (Rimstidt and Barnes, 1980; Hellmann, 1994; Worley, 1994; Brantley, 2008; Brown, 2011b). In order to investigate the fluid-rock interaction in the Cooper Basin geothermal

system (i.e. Habanero 3 well), three experimental methods at a laboratory scale were developed. To simplify the process, the gas phases were not introduced to the system. The first method allows the interaction of fluid and rock samples in a closed system where no fluid is required to be replaced (fluid mass is constant) during the experimental period. The experiment is conducted in Teflon lined autoclaves for different interaction periods and the maximum temperature chosen was 220^{o}C due to the limitation of the Teflon liners used. This method was used firstly to obtain the equilibrium silica concentration at various temperatures. The experimental results showed good agreement with the literature values. The equilibrium silica concentrations obtained from dissolution at 120^{o}C, 140^{o}C, 160^{o}C, 170^{o}C, 200^{o}C and 220^{o}C for 56 days were 56 ± 3 ppm, 94 ± 6 ppm, 137 ± 6 ppm, 175 ± 7 ppm, 282 ± 11 ppm, and 350 ± 28 ppm, respectively. The second observation was the dissolution kinetics in pure water. The SigmaPlot software was used to fit the experimental data and obtain the equilibrium silica concentration and silica dissolution rate constant based on a first order global rate equation by Worley (1994). The results were compared with a compiled quartz dissolution literature values and showed good agreement, however values differ slightly due to the different materials and experimental conditions. The obtained dissolution rate constants were then regressed using the Arrhenius equation describing a kinetic rate constant with an activation energy of 64.53 kJ/mol.

A number of factors affecting the dissolution rate of granite were observed. One factor was the effect of particle size on the dissolution rate of granite. The experimental results agree with literature, which demonstrated that the dissolution rates increased with decreasing granite particle size (increasing the surface area). Another observation undertaken was the effect of electrolyte (250 ppm NaCl solution) on the granite dissolution rate. The results concluded that the dissolution rate in 250 ppm NaCl solution yielded a two-fold increase compared to that in pure water. One other observation was on the effect of pH in granite dissolution rate. The experimental results agree with the literature confirming that the increase of dissolution rates at lower pH was due to the presence of organic acid (acetic acid) in the pH buffer used. At pH above 8 the dissolved silica species that is significant is not solely $SiO_{2(aq)}$ (H_4SiO_4). The hydrogen atoms from H_4SiO_4 can dissociate and release $H_3SiO_4^-$ ion which is very soluble in

water. As the pH increase, further hydrogen dissociation is possible to form $H_2SiO_4^{2-}$ which is also soluble in water and thus increasing the silica concentration, leading to an increased dissolution rate.

The second method used a closed loop batch flow-through cell that was designed to mimic the circulation of the fluid-rock interaction hence enabling the observation of the changes in the chemical properties of the host rock and circulating fluid that may occur. This method involved two different experimental systems. The first system allows the continuous interaction of the fluid (pure water and 250 ppm NaCl solution) and rock samples at 250^{o}C (close to the actual geothermal reservoir temperature) to study the dissolution kinetics of silica from the granite for different interaction periods. This system was also used to study the effect of fluid/rock ratio. The experimental results agree with the literature which illustrate a decrease in solid/liquid ratio (increase in fluid/solid ratio) would increase the reaction rate. The second system allows the interaction of fluid and rock samples also in a closed loop batch flow-through cell, using pure water and 250 ppm NaCl solution for 7 days and 28 days, and the fluid is consistently replaced every 24 hours for the specified interaction periods. This system was designed to accelerate the mineral dissolution to observe which minerals were more soluble. SEM results revealed that severe pitting exists on the surface of the granite, as a consequence of rapid dissolution, and it was observed that fine particles were present between and on the surface of the granite which increased the particles surface area, enhancing the dissolution rate. The SEM back-scatter images revealed albite as the more soluble phase, since more cavities were observed through the albite phases compared to the K-feldspar phases in the granite samples.

The third method involved a high pressure open loop flow through system, where fresh water is continuously injected to the system. This system was configured to observe the influence of pressure in rock water interaction. Three pressure conditions at 250^{o}C were chosen (at vapour pressure, 100 bars, and 200 bars). The experimental results showed that the silica concentration increased with pressure, agreeing with the published literatures.

In order to validate the experimental results, the React program from the Geochemist Workbench software was used to simulate the granite dissolution reaction path and generate silica dissolution and silica precipitation rates. The simulation in React is based on the transition state theory model (Rimstidt and Barnes, 1980; Bethke, 1996). The results of the modelling showed consistent plots with the experimental results however generated different values of rate constants and equilibrium silica concentrations. React was also used to calculate the amount or rate of silica precipitation with the assumption that the aperture of the fracture was 10 cm and the surface roughness was 2. For granite dissolution in pure water, the amount of silica that may precipitate was approximately 298 mg/28 days, and in 250 ppm NaCl solution is 309 mg/28 days. From the available information, the sealing rate from granite dissolution in water was 2.30 cm/1000 years, and that in NaCl solution was 2.41 cm/1000 years.

Since this was a simplified model and only the major components of the granite were included, it may have influenced the reaction path calculated by React, affecting the silica concentration output and reaction rate. Another contributing factor may be that the active surface area of the granite in the experiment differs with the BET surface area obtained in this study. In addition, the published reaction rate constant may have different experimental conditions (e.g. different composition of minerals, particle size, duration of experiments, different reactors). As well, the input of the reaction rate constant was allowed for single minerals, and the model may not simulate the exact laboratory experimental conditions. Moreover, this study measured the dissolution of granite solely from the release of silica to the solution. Since the literature published reaction rate constant from pure minerals (e.g. albite), this reaction rate constant may not be the appropriate value to specify the albite component in the granite. In other words, the reaction path of dissolving three pure minerals in water may not be identical to the dissolution mechanism of granite with the same mineral composition. Since the model output resulted in some differences compared to the experimental results, this suggests that modelling and experiments should work together to predict more accurate outputs.

Acknowledgements

Firstly, I would like to thank God for the strength and wisdom to complete my doctorate program. I would like to express my appreciation to those who have greatly contributed and assisted me to complete this research. In particular I would like to acknowledge:

A/Prof. Yung Ngothai, School of Chemical Engineering, The University of Adelaide, my principal supervisor, for the encouragement and support, guidance, discussions, ideas and the opportunity to carry out research in this field. Thank you for the friendly atmosphere while conducting this research.

NOTE:
These images are included on page vii of the print copy of the thesis held in the University of Adelaide Library.

A/Prof. Brian O'Neill, School of Chemical Engineering, The University of Adelaide, my co-supervisor, for the guidance and assistance in the calculations and design of the flow-through hydrothermal cell, experimental, as well as dissolution kinetics and thermodynamics.

Prof. Allan Pring, School of Chemistry and Physics, The University of Adelaide, and The South Australian Museum, my co-supervisor, for the expertise in the area of mineralogy and geochemistry, as well as access to XRD equipment and laboratories in the SA museum.

A/Prof. Joel Brugger, School of Earth and Environmental Sciences, The University of Adelaide and South Australian Museum, my co-supervisor, for the guidance and discussions in geochemistry, modelling and Geochemist Workbench simulations. As well to Dr. Barbara Etschmann for the valuable input in experimental and modelling.

Mr. Jason Peak, Mr Michael Jung and Mr. Jeffrey Hiorns, the Chemical engineering workshop team, for assistance in putting together the experimental apparatus, maintenance and making sure the apparatus were working well.

Dr. Benjamin Wade and Aoife McFadden, from the Adelaide Microscopy Centre, for their assistance and training in using the XL30 scanning electron microscope, ICP-MS, and the MicroMeritics Gemini VII with nitrogen adsorption for BET surface area determination.

Mr. John Stanley from the School of Earth and Environmental Sciences for the XRF analyses on the granite samples.

Gujie Qian, Fang Xia, Kevin Li and Jing Zhao for their support in experimental and expertise in software and laboratory equipment.

The research described in this paper has been funded by the Department of Primary Industries and Resources of South Australia (PIRSA) and Geodynamics.

This research would not have been possible without the support of all the people mentioned above.

I would like to dedicate this thesis to my beloved parents, Dr. Tjahjono Koentjoro, MPH, PhD and Dr. Lina Koerniawati, MPH, and my sister Yael Esthi Nurfitri Kuncoro, SpKK. I thank them for all the love and support in the whole process of completing this study. And of course to my lovely wife, Elita Santosaputri, B.Med.Sc., BMBS, for her love, support, patience, and understanding, also in accompanying my late night laboratory works. I would also like to dedicate this thesis to my parents-in-law, Drs. Andreas Santoso, MBA and Yusnita Santoso for their support and encouragement. Finally, to my baby boy, Evan Amadeo Kuncoro, my pride and joy, for his presence, smile and laughter.

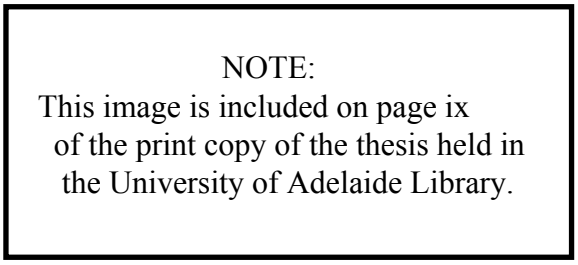

I hope that the results of my thesis would satisfy the expectations of the people associated and provide a significant contribution to the society.

List of Publication

Kuncoro, G., Ngothai, Y., O'Neill, B., Pring, A. and Brugger, J., 2011. Preliminary Kinetic Study on Rock-Fluid Interaction of the Enhanced Geothermal Systems in Cooper Basin, South Australia. *Proceedings: 33rd New Zealand Geothermal Workshop, Auckland*, 21-23 November 2011.

Kuncoro, G., Ngothai, Y., O'Neill, B., Pring, A. and Brugger, J. 2010. A Preliminary Study on Na-Cl-H_2O-Rock Interactions of the Hot Fractured Rock Geothermal System in Cooper Basin, South Australia. *Proceedings of the Third Australian Geothermal Energy Conference 2010*, Adelaide, 16-19 November 2010.

Kuncoro, G., Ngothai, Y., O'Neill, B., Pring, A. and Brugger, J. 2010. A Case Study of Rock-Fluid Interaction in the Enhanced Geothermal System in Cooper Basin, South Australia. *Proceedings of Chemeca 2010*, Adelaide, 26-29 November 2010.

Kuncoro, G. B., Ngothai, Y., O'Neill, B., Pring, A., Brugger, J. and Yanagisawa, N., 2009. Laboratory-scale Study of Fluid-Rock Interactions of the EGS in Cooper Basin, South Australia. *Geothermal Resource Council Transactions*, **34**, pp. 697-701.

Kuncoro, G., Ngothai, Y., O'Neill, B., Pring, A., Brugger, J. 2009. A Preliminary Study on Fluid-Rock Interactions of the Hot Fractured Rock Geothermal System in Cooper Basin, South Australia. *Proceedings of the second Australian Geothermal Energy Conference 2009*, Brisbane, 11-13 November 2009.

Table of Contents

List of Figures

List of Tables

Chapter 1 Introduction and Motivation

Whilst the energy demand in Australia is increasing, reserves of coal, oil and natural gas are depleting at an ever increasing rate. Along with many renewable energy technologies that are currently being developed, geothermal energy has significant potential to supply electricity by harnessing stored thermal energy from the earth without producing greenhouse gas emissions or long-lasting nuclear wastes, at a cost which will be competitive to those generated from fossil fuels.

Geothermal energy provides an established electricity source in many countries, including The United States, New Zealand, Iceland, Japan, Philippines and many more. Geothermal energy is presently a proven provider to supply the energy demands in many countries. Furthermore, a vast area of relatively high temperature (250^{o}C) hot rock has been discovered in Cooper Basin, South Australia, potentially providing the best hot rock reserves in the world (Geodynamics, 2009b). The proposed area for geothermal operation in Cooper Basin, South Australia, is not a "conventional" geothermal system, but an engineered geothermal system (EGS) that occurs at significantly greater depth (up to five kilometres), where the energy source is hot granitic basement rock that is heated by radioactive decay rather than by volcanism (Geodynamics, 2009b). The thermal area in Cooper Basin is one of the deepest reservoirs for energy extraction, hence very little information regarding the geochemistry of the rocks and chemistry of the trapped groundwater is available at these extreme conditions, particularly 250^{o}C and high pressure in the reservoir producing 6000 psi (423 bar) at well head. Despite these challenging conditions, this vast thermal area may, in future years, be a useful source to provide energy and produce baseline electricity. Before this technology can be developed, there are significant challenges that need to be understood and overcome in enhanced geothermal systems. The injection of fresh water to the reservoir is likely to alter the equilibrium with the surrounding groundwater. As well, the composition of the groundwater may differ significantly from the fresh water injected through the granite to extract energy. The flow of large volumes

of injected water may cause partial chemical dissolution or alteration of granites, which could potentially increase the dissolved solids such as silica, and other metals in the circulating fluid. Also, the saturation of metals in fluids is volume-dependent, very small volumes of fluid require significant under-cooling before they will precipitate their metals. The complexity of the system in part stems from the high temperatures (>>200^{o}C), high pressures and possible high salinity of the fluid (>1 % wt.).

Unfortunately, the fundamental processes associated with mineral dissolution and precipitation, and the pressure-temperature gradient remain poorly understood (Marks et al., 2010). To date, literature demonstrates that different geothermal reservoirs generate wide variations in the geochemical composition of the circulating water. Furthermore, it is impossible to generalize the actual field experience of mineral deposition in geothermal systems into one consistent theory due to the vast chemical and operational variation between field sites (Robinson, 1982). Despite the fact that there have been a number of studies on fluid-rock interactions for different geothermal sites (Rimstidt and Barnes, 1980; Robinson, 1982; Posey-Dowty et al., 1986; Savage et al., 1987; Grigsby et al., 1989; Savage et al., 1992; Azaroual and Fouillac, 1997; Tarcan, 2005; Yanagisawa et al., 2005; Castro et al., 2006; Marks et al., 2010), and studies on rock-chloride solutions (Ellis, 1968; Dove and Crerar, 1990; Icenhower and Dove, 2000), it is highly probable that their results will not be directly applicable to the hot granite-based geothermal systems in the Cooper Basin. Clearly, a detailed study of fluid-rock interaction for this geographical area is crucial.

A number of issues relating to geothermal geochemistry are required to be considered and explored to ensure safe, economic energy production from the “hot rocks”. Low pH and saline waters at temperatures exceeding 200^{o}C are highly corrosive. At such, it is vital to prevent the generation of scales as the brines cool during their transport to the surface. This project aims to predict mineral dissolution and scaling. One elemental shortcoming in this project is the limitation of technology to obtain core samples that contain fractures at these extreme depths and conditions. In EGS, hydraulic stimulation results in the re-opening of existing fractures that

are optimally oriented and critically stressed for shear failure. Therefore, the minerals that will be available for dissolution are the secondary minerals that have been deposited over time on the walls of those existing fractures. These altered-mineral assemblages are different from those found in bulk rock. The available rock samples are from drill cuttings from bulk rock at 4000 m, thus do not represent the secondary minerals present in the existing fractures. As a necessary step, this project will investigate primarily on silica dissolution from granite in the bulk rock and silica scaling, as many silica scaling issues arise in geothermal systems. Clearly, there is a need to understand and quantify the potential scaling rates due to silica deposition in energy recovery pipes due to differences in silica solubility as a function of the temperature changes occurring within the system. A second and equally important fouling issue is the maintenance of open pores within the hot rocks to maximize the contact surface area and lifetime of the reservoir. Furthermore, clogging of the fracture network that allows the brines to exchange thermal energy with the host rock in the reservoir will result in costly shutdowns. Clogging may occur both by precipitation of minerals or by hydration of pre-existing minerals with associated volume increase. These phenomena must be understood, quantified and modelled to optimize recovery and reservoir life. Therefore, this study focused on the investigation of fluid-rock interaction and observed the dissolution of the minerals. A literature review on previous mineral dissolution studies has been performed to provide a foundation for this study and aid in the dissolution modelling. Three main methods for the experimental work were developed to investigate the silica dissolution kinetic and changes in the chemical properties of the fluid and host rock. The experimental results were then used to model the silica dissolution rate. Simulations on granite dissolution were also performed to fit the experimental results and obtain the dissolution rate constant. The obtained dissolution rate constant was then used to calculate the fracture sealing rate/precipitation rate.

Chapter 2 Literature Review

The Habanero geothermal system in Cooper Basin, South Australia is the first man-made geothermal system or enhanced geothermal system (EGS) or hot fractured rock (HFR) in Australia. Since this geothermal operation is a breakthrough technology, understanding the system and identifying the key fouling issues are crucial to ensure a safe and economic energy production. Consequently, the prime objective of this research will be the determination of key understandings of the fluid-rock interaction that occur within the reservoir of the Habanero geothermal site in the Cooper Basin. This chapter reviews the need of green energy and the potential options that are available. It covers key aspects of geothermal energy production and the history of geothermal energy in Australia. As well, past studies of mineral dissolution and precipitation kinetics in rock water interactions are summarized here.

2.1 Electricity Demand in Australia

Energy exists in plethora of forms. A highly attractive form of energy is electricity given the relative simplicity of its transport and control. Electricity can be used in many ways and can be efficiently converted to a wide variety of energy outputs, such as light and heat. Electric power generation is normally extracted from various energy sources ranging from oil, coal, natural gas, nuclear and many others. The principal feedstock for electricity generation in Australia is in the form of black and brown coal (Switkowski et al., 2006), as illustrated in Figure 2.1. A typical coal-fired power plant is shown in Figure 2.2 (CO2CRC, 2012).

However, the reserves of coal are depleting at an increasing rate while the energy demand is rising rapidly. Figure 2.3 (Switkowski et al., 2006) shows the forecast of Australia's electricity demand to year 2050. Unfortunately, coal fired power plants emit the highest level of greenhouse gases (Aye, 2005), as illustrated in the left side of Figure 2.3. Figure 2.4 (Switkowski

et al., 2006) shows the sources of Australia's greenhouse gas emissions in year 2004. Electricity generation from coal contribute roughly one third of Australia's greenhouse gas load.

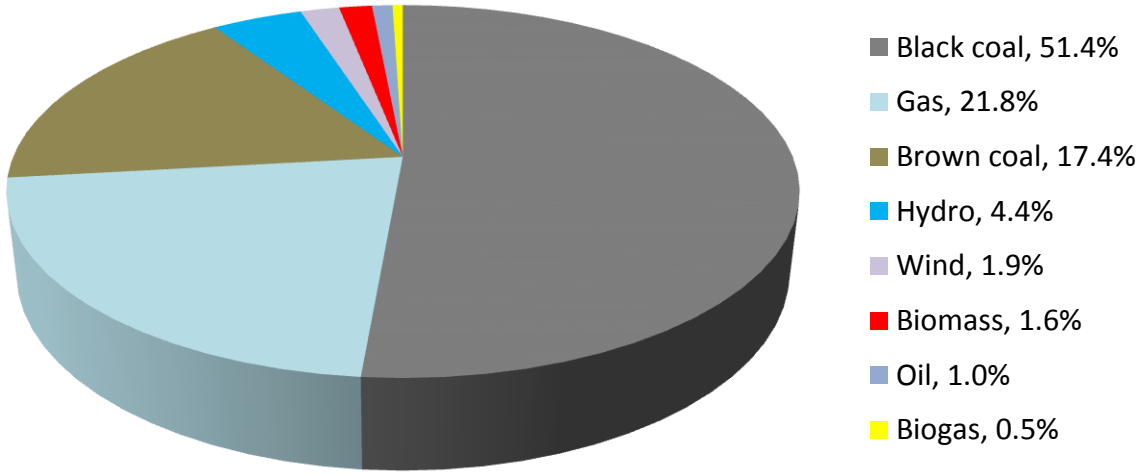

Figure 2.1 Australia's sources for power generation

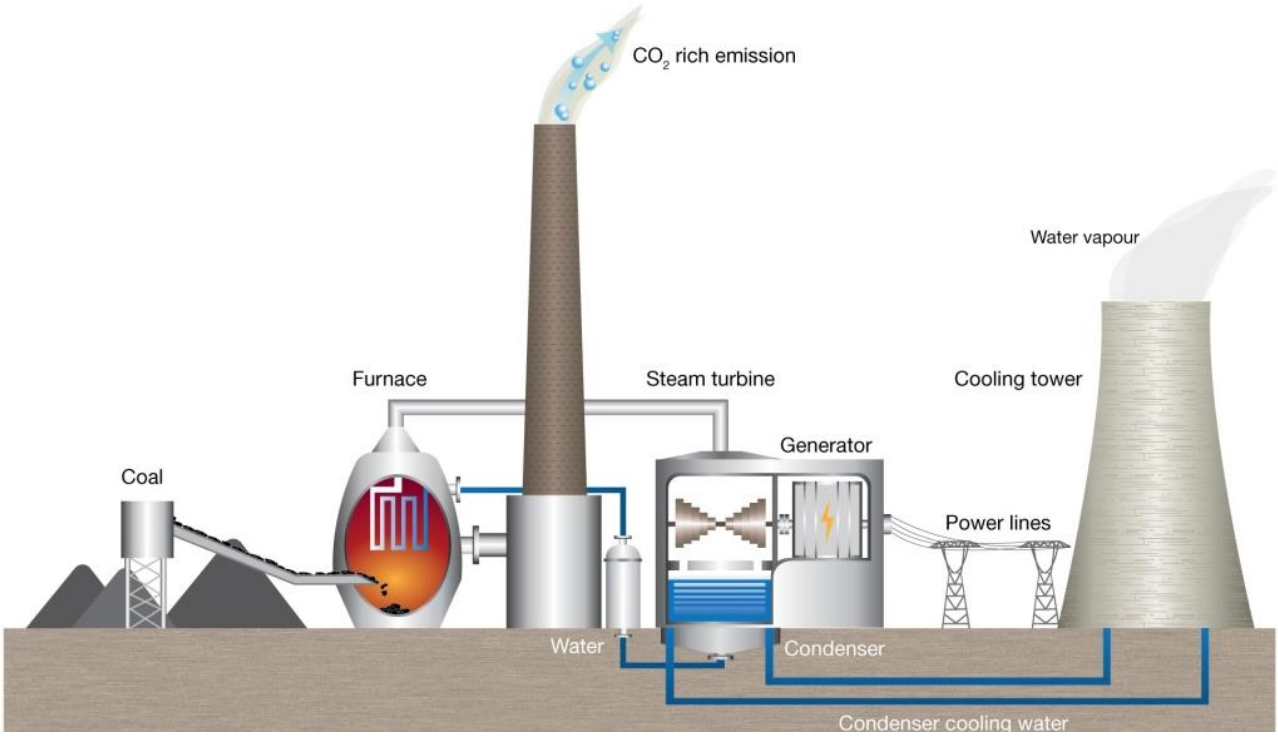

Figure 2.2 A coal fired power plant

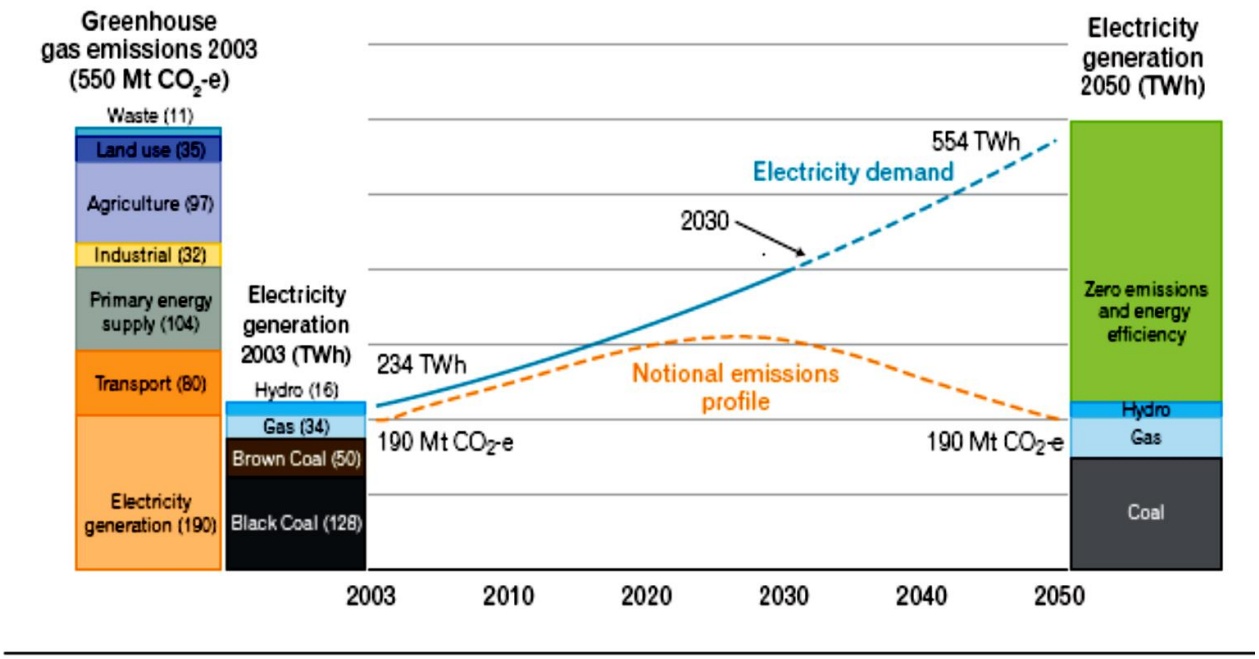

Figure 2.3 Forecast of Australia's electricity demand

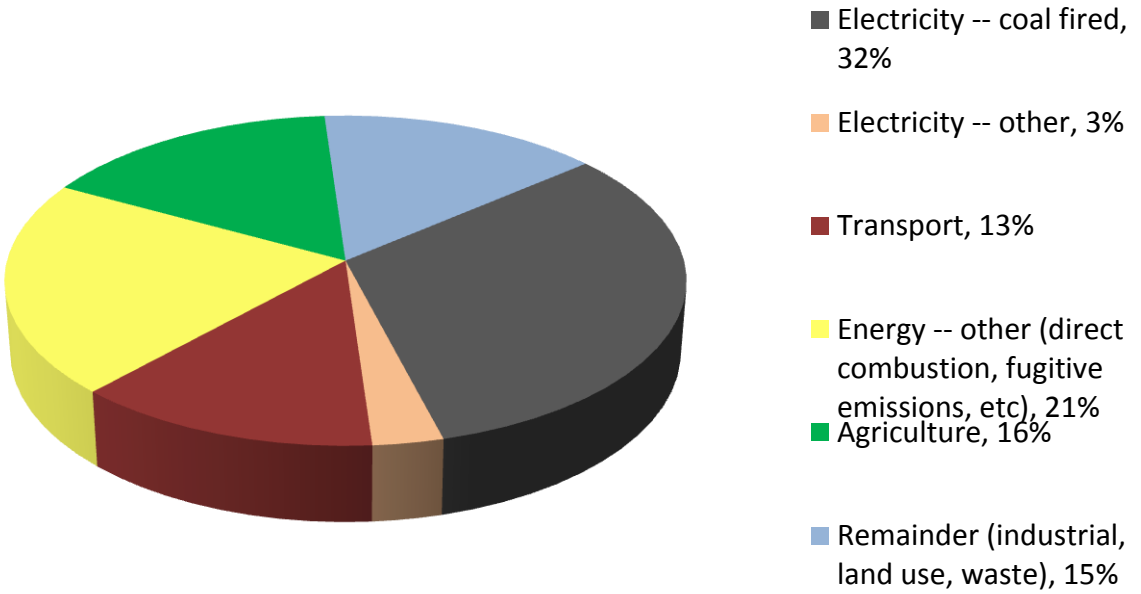

Figure 2.4 Australia's greenhouse gas emissions in 2004

The Australian government launched its carbon pollution reduction scheme to reduce greenhouse emissions in 2011 (IHT, 2007), and the development of cleaner alternatives and renewable source for electricity are crucial. In addition, the Mandatory Renewable Electricity Target (MRET) introduced in April 2001 requires that by 2010 an extra annual 9,500 GWh of Australia's energy must be delivered from renewable energy technology compared to the 1997 baseline (Chopra, 2005). Clearly, in order to achieve the Australian Government's emission target and to continue to supply the energy demand, it is crucial to develop more environmentally sustainable processes.

There are a wide variety of potential renewable energy resources that are currently being developed or have been commercialized into the Australia market. Examples include solar hot water systems, solar thermal installations, cogeneration, photovoltaic, stand-alone power systems, small and micro hydro-schemes, small wind turbines and biomass technology (Aye, 2005). Despite the development of various renewable energy resources, there appears to be no sustainable alternative for baseline production of electrical energy (sadly, nuclear energy has significant drawbacks including strong political opposition, serious long term environmental problems and intractable weapons proliferations issues), it is imperative to continue to search for and to develop new sustainable resources for power supply generation. A potentially attractive source for sustainable baseline power is the utilisation of hot fractured rock (HFR) or engineered geothermal system (EGS), and this technology is the principal focus of this study. Prior to discussing engineered geothermal system, a brief overview of "conventional" geothermal system will be reviewed in Section 2.2.

2.2 Geothermal Energy

The thermal energy emitted from the core of the earth (the magma) is the major source of geothermal energy. It is derived from the hot molten core of the earth and the decay of natural radioisotopes (Mink, 2004). There are four known types of geothermal resources; these are

hydrothermal, geo-pressured, hot dry rock or engineered geothermal system (EGS), and magma (Mink, 2004). In this chapter only hydrothermal and EGS will be discussed.

2.2.1 Hydrothermal/volcanic system

Hydrothermal systems utilize heat that is relatively close to the surface of the earth (Mink, 2004). This energy from the earth is transferred to the surface by the circulation of ground water and molten magma. In some areas, groundwater is naturally transported to the earth's surface in the form of hot steam or hot water such as geysers and hot springs. This thermal energy near the earth's surface may be utilized as an energy source when a sufficient amount of fluid and requisite permeability of the rock are present to enable heat transfer to the surface (Mink, 2004).

Table 2.1 Major geothermal producers

Country	Total geothermal production (%)
United States	28.1
Philippines	17.0
Mexico	11.1
Italy and San Marino	8.8
New Zealand	8.0
Iceland	7.5
Indonesia	5.8
Japan	4.8
El Salvador	2.5
Kenya	2.1
Costa Rica	2.0

Thermal energy obtained from hydrothermal sources is proven and continues to play a major role in electricity generation in a number of countries (e.g. New Zealand, Iceland, Japan, etc.). As well, it has also been used for space heating (in the United States) where the reservoirs containing the hot fluids exist at a shallower depth, exhibit high temperatures and appropriate rock permeability (Tenma et al., 2008). The major producers of geothermal energy (UNSD, 2009) are listed in Table 2.1.

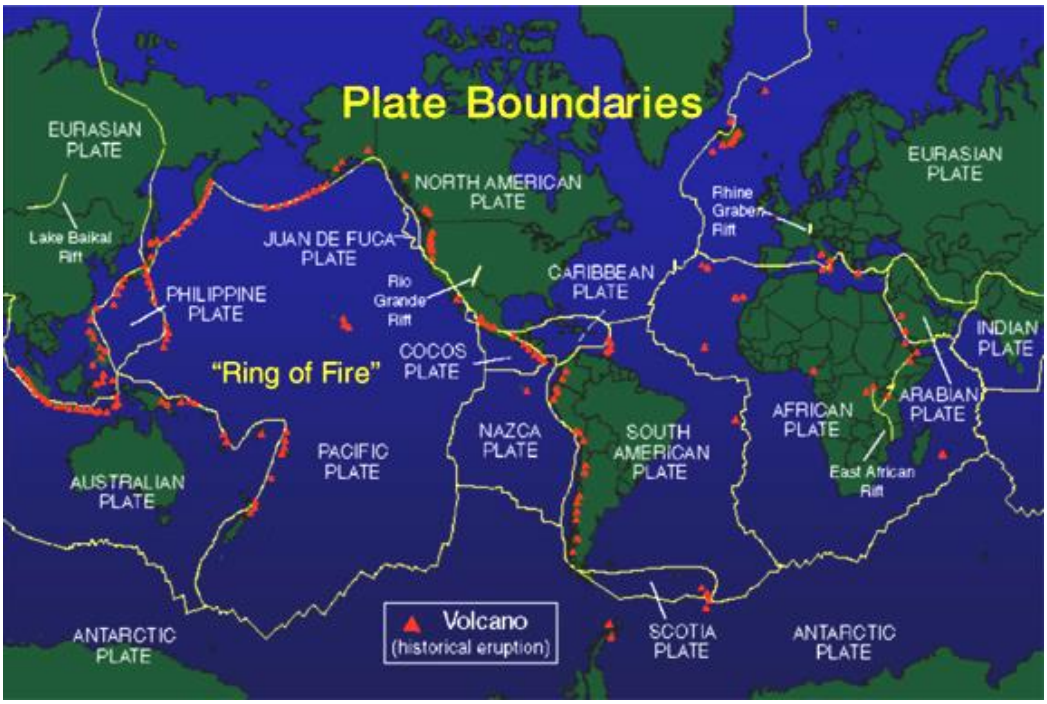

Figure 2.5 Plate boundary map

Figure 2.5 illustrates the plate boundaries across the world and the locations of historical eruption of volcanoes (GEO, 2012a). Figure 2.6 (GEO, 2012b) identifies the locations of geothermal plants across the globe. It is readily observed that countries located near volcanoes or plate boundaries are the major geothermal power producers. Many locations along the plate boundaries are available for potential geothermal power production.

A projection of geothermal energy production for different regions is provided in Figure 2.7 (Westenhaus, 2011). This schematic shows that interest is growing to utilize the geothermal

resources for power generation with low carbon emissions and significant geothermal resources are still available to be utilized for electricity generation. The new technology exploiting geothermal system for electricity generation with low to zero carbon emission is referred to as an engineered geothermal system (EGS).

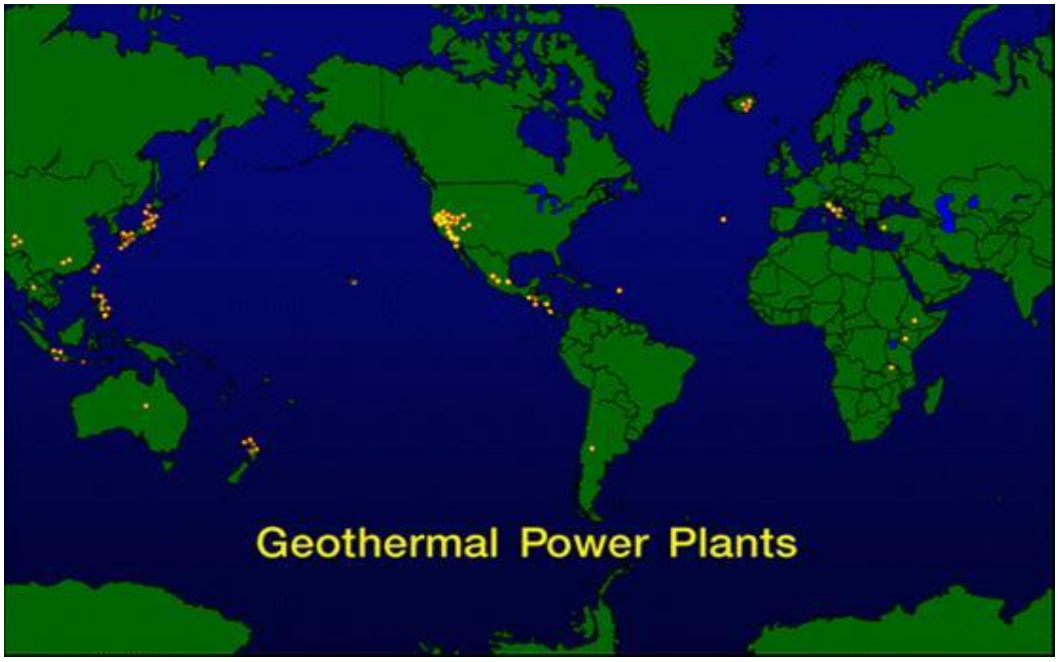

Figure 2.6 Location of geothermal power plants in the world

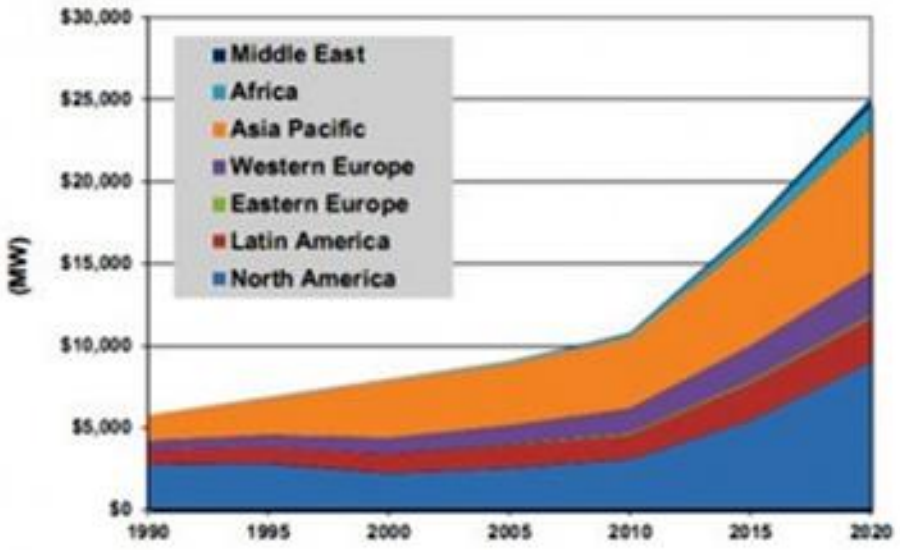

Figure 2.7 Geothermal growth projection

2.2.2 Engineered geothermal system

An engineered geothermal system (EGS) is defined as mining heat from hot rocks. EGS sites exist in many parts of the world, including Germany, America, Japan, United Kingdom, and France. A study by Durst and Vuataz (2000) compiled a selection of physical data and fluid composition from six EGS reservoirs. The physical data is provided in Table 2.2 and Table 2.3, and the fluid composition is provided in Table 2.4. From the compiled data above, it is shown that each EGS has its own characteristics.

Table 2.2 Physical data from six EGS reservoirs

HDR site	Bad Urach	Fenton Hill	Hijiori	Ogachi	Rosemanowes	Soultz-sous-Forets
Country	Germany	America	Japan	Japan	United Kingdom	France
Rock type	Metatexite occasionally altered along joins and veins	Biotite granodiorite	Granodiorite widely altered	Granodiorite altered along the cracks	Granite occasionally altered along joins and veins	Granite altered along the veins
Reservoir depth (m)	3300	3500	2200	711~719 and 990~1027	2400	3200~3600
Well	Urach 3	EE-2	HDR-3	Production well	RH15	GPK-2
Well depth (m)	3325	4010	2303	1100	2780	3876
Sampling date	1978	27-Jul-92	Nov-91	1993	15-Aug-88	16-Nov-97

Table 2.3 Physical data from six EGS reservoirs (cont.)

HDR site	Bad Urach	Fenton Hill	Hijiori	Ogachi	Rosemanowes	Soultz-sous-Forets
Country	Germany	America	Japan	Japan	United Kingdom	France
Production test	none	3.5 months	3 months	22 days	5.5 months	4 months
Type of sample	Downhole	Wellhead	Wellhead	Wellhead	Downhole	Wellhead
Injected fluid	none	Fresh water closed loop	Fresh water	Fresh water	Fresh water (TDS < 0.1 g/kg)	Formation fluid
Rock temperature (^oC)	143	327	250-270	170-230	99.8	165
Fluid temperature (^oC)	143	182	167	108	99.8	142
pH	4.2	na	na	na	8.8 (25^oC)	4.8
Redox potential (mV)	na	na	na	na	Na	~ -250
TDS (g/kg)	na	3.434	1.4	1.25	0.419	101

TDS: total dissolved solids

na: data not analysed or not available

Table 2.4 Fluid composition from six EGS reservoirs

HDR site	Bad Urach	Fenton Hill	Hijiori	Ogachi	Rosemanowes	Soultz-sous-Forets
Country	Germany	America	Japan	Japan	United Kingdom	France
Fluid composition	(mg/kg)					
Na	558.65	898.90	298.87	298.87	100.70	24461.12
K	159.91	89.14	12.90	17.59	3.41	3385.91
Ca	150.29	18.00	36.07	4.01	13.79	6893.42
Mg	0.45	0.10	na	na	0.08	141.21
Cl	large amount	953.69	187.90	49.63	73.03	55448.80
SO_4	present	377.53	49.95	153.70	74.45	225.75
HCO_3	na	588.20	109.83	561.36	73.83	147.66
F	na	17.00	na	6.65	11.38	3.99
SiO_2	156.82	424.20	240.34	162.23	65.49	140.00
Fe	110.57	0.80	na	na	0.02	29.99
Al	0.58	1.19	na	na	0.20	<0.40

na: data not analysed or not available

The basic technique for extracting energy from EGS was established in the early 1970s at the Los Alamos National Laboratory, New Mexico (Wyborn et al., 2005). An illustration of an EGS thermal extraction process is provided in Figure 2.8.

The initial step in the extraction process is the construction of a well with the sufficient depth to reach into the high temperature basement. Wells drilled for enhanced geothermal system (EGS) projects are similar to those for hydrothermal/volcanic sites apart from the depth which is significantly greater for EGS applications. After the first well has been completed, a segment of the bottom portion is isolated using a packer, which provides pressure and flow isolation.

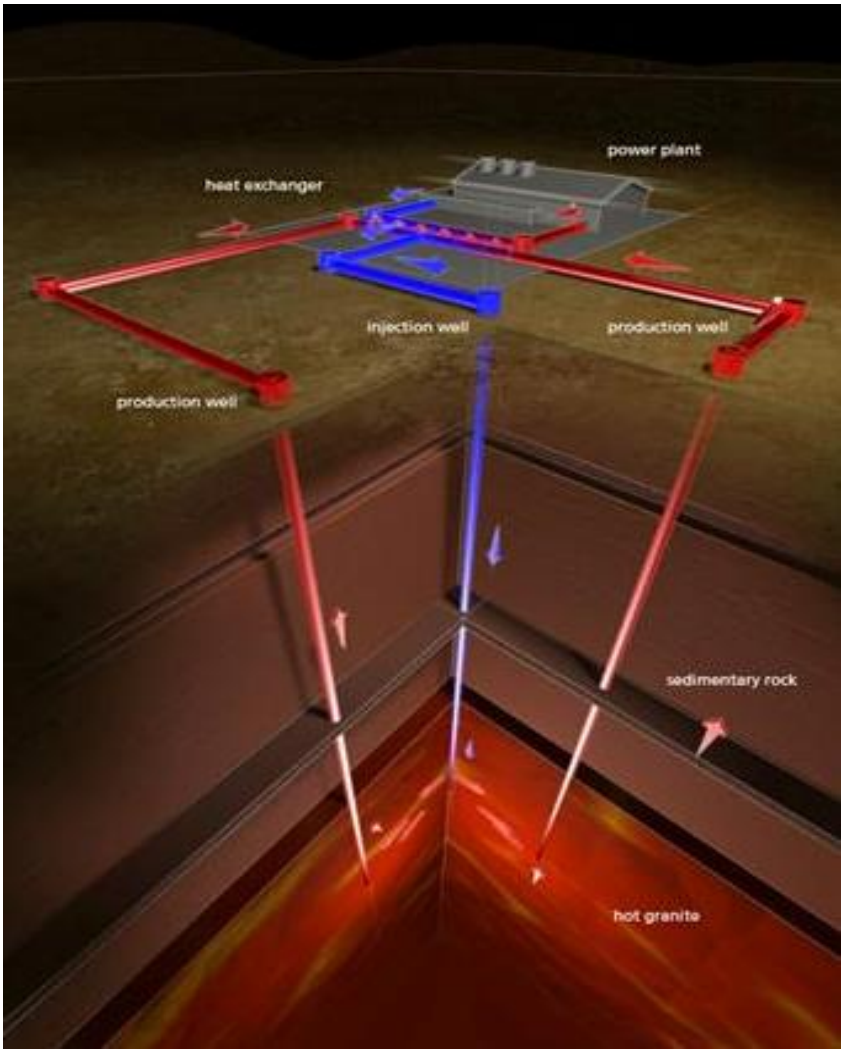

Figure 2.8 Enhanced Geothermal System (EGS) thermal extraction process

Hydraulic fracturing fluids are then pumped at high pressure through the packer and forced in the surrounding rock body to form a permeable reservoir consisting of interconnecting fractures (so-called fracking). The shape and orientation of the permeable zone created by hydraulic fracturing is a function of the natural stress features existing within the host rock (Mink, 2004). To complete the subsurface system, a second well is required to be drilled into the permeable zone sufficiently separated from the first well. Water is then pumped through the injection well, then after extracting thermal energy as it flows through the permeable fractures on a tortuous path, it returns to the surface at a higher temperature through the

production well. On the surface, thermal energy is extracted from the outlet geothermal fluid (water) using binary cycle, as shown in Figure 2.9.

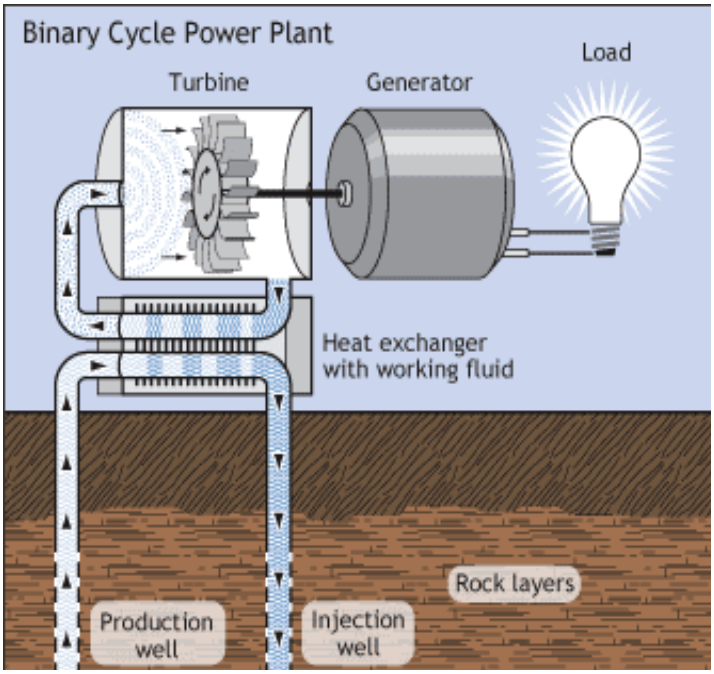

Figure 2.9 Binary cycle power plant

After the thermal energy has been extracted, the fluid is then recycled back into the permeable reservoir through the injection well. The thermal energy is extracted from the geothermal fluid using the secondary fluid with a significantly lower boiling point (EERE, 2009). The word binary appears due to the exploitation of this secondary fluid. Heat from the geothermal fluid causes the secondary fluid to flash to its vapour phase, driving the turbine, which then drives the generator producing electricity. This cycle enables the thermal energy recovery whilst avoiding any evaporation (phase change) of the geothermal fluid (Mink, 2004)

2.2.3 Geothermal energy in Australia

Although Australia is located outside the "Ring of Fire", a commercially operated power generator using geothermal energy has been constructed in Birdsville, in the south west of Queensland. This power plant uses artesian water from the Great Artesian Basin that has a

temperature of 98^{o}C to produce 150 kW from a binary cycle plant. The population of Birdsville is normally around one hundred people and their requirement for electric power follows a seasonal pattern, with the highest demand in the summer time, when air conditioning is used extensively (250 kW), and lowest demand in winter (120 kW). However, once every year the population increases to roughly 5000 during the horse race's weekend, a major tourist event in the outback. Hence, in order to manage this annual variation of the electric power demand, an integrated mix of generation systems are used (Chopra, 2005): one geothermal power station with a nominal power rating of 150 kW, one liquefied petroleum gas (LPG) generator set with a nominal power rating 300 kW, and two 150 kW diesel generator sets.

Previously, a geothermal power station was installed on the bore in 1989 (Burns et al., 2000) and it commenced the operation in 1992. Unfortunately, this system experienced serious technical problems primarily due to the choice of R114 (a chlorofluorohydrocarbon) as the working fluid. This system was subsequently upgraded in 1999 as follows (Chopra, 2005): by conversion from the R114 chlorofluorohydrocarbon working fluid to iso-pentane, installation of a new plate heat exchanger, multi stage liquid pump and the installation of larger diameter pipes and fittings to handle the volume increase of the new working fluid. The upgraded Birdsville geothermal plant currently provides a net power output of 120 kW. A schematic diagram of the upgraded Birdsville Geothermal Power Station (Chopra, 2005) is provided in Figure 2.10. With an online availability exceeding 95%, the geothermal plant currently provides the town's total electricity requirements at night and during the cooler seasons (EPA, 2005).

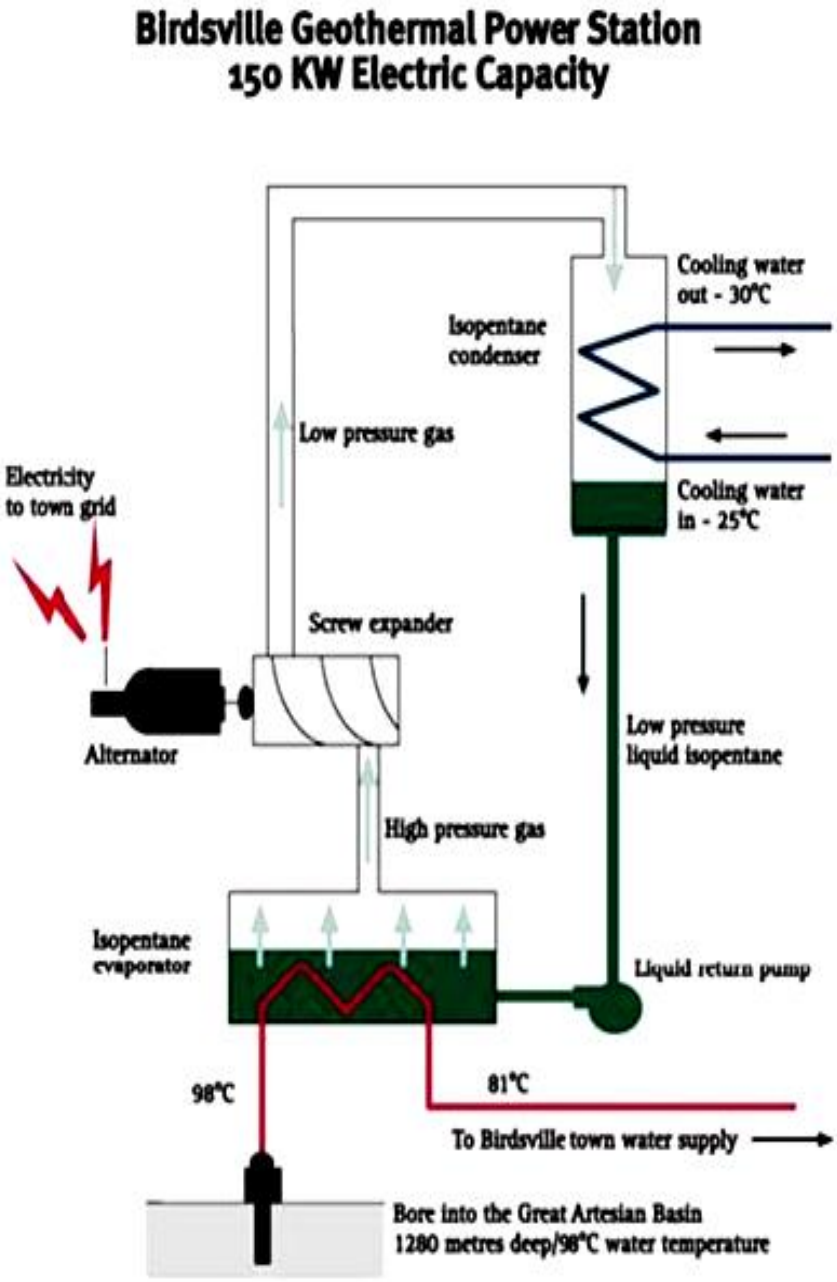

Figure 2.10 Schematic diagram of the Birdsville Geothermal Power Station (Queensland Environmental Protection Agency)

Another geothermal system currently being developed is an engineered geothermal system (EGS), where the heat exchange occurs at a significantly greater depth compared to conventional geothermal system and the heat source is hot granitic basement rock that are heated from radioactive decay rather than by volcanism. This is due to the vast amount and

high temperature (250^{o}C) thermal area discovered in the northern part of South Australia. The temperature profile of earth's crust in Australia at 5 km deep is presented in Figure 2.11 (Somerville et al., 1994) cited in (Chopra and Holgate, 2005). Hence, EGS geothermal energy (heat mining) is perceived by the government as a potentially promising alternative energy resource, which is largely being developed in Australia. In addition, electricity generated from EGS is likely to be cost competitive with those generated from other resources as provided in Figure 2.12 (Geodynamics, 2009a) which compares the cost of electricity in Australian dollars per MWh generated from various sources. As well, hot dry rock systems or EGS are a proven technology, which has been shown to provide significant contributions in supplying energy in many countries, such as Germany, America, Japan, United Kingdom, and France (Durst and Vuataz, 2000; Mink, 2004).

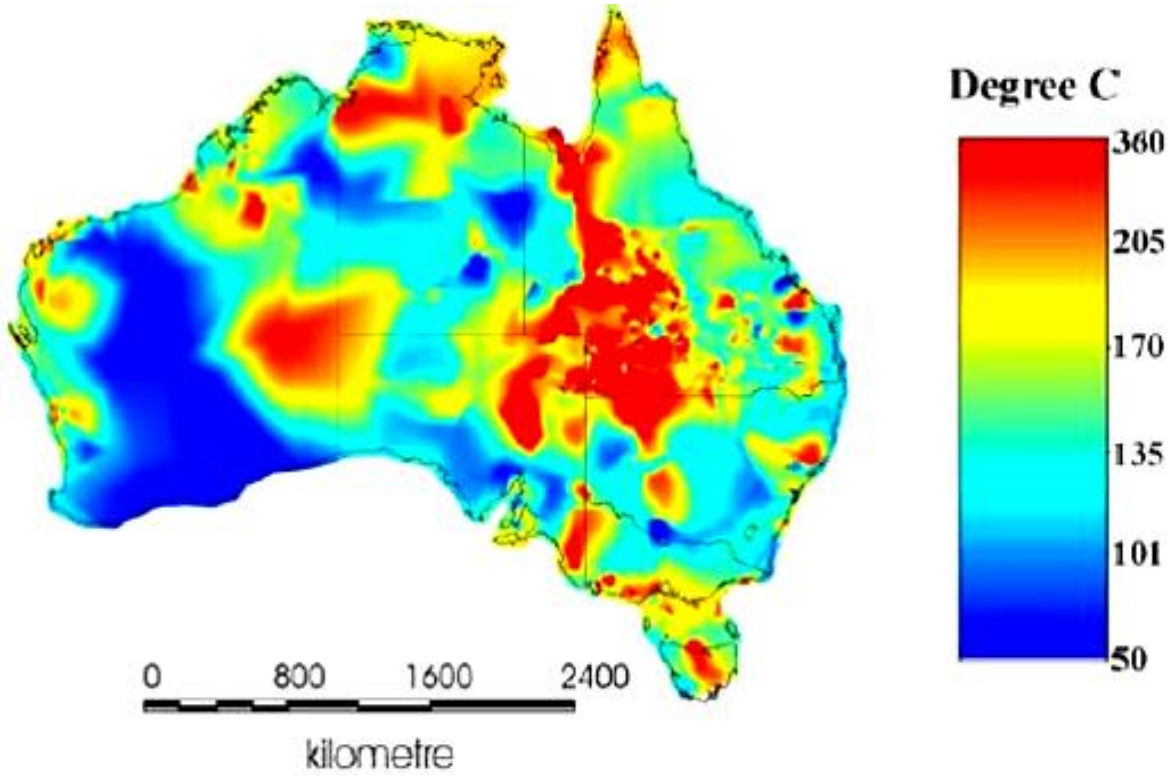

Figure 2.11 Australia's geological temperature at 5 km depth

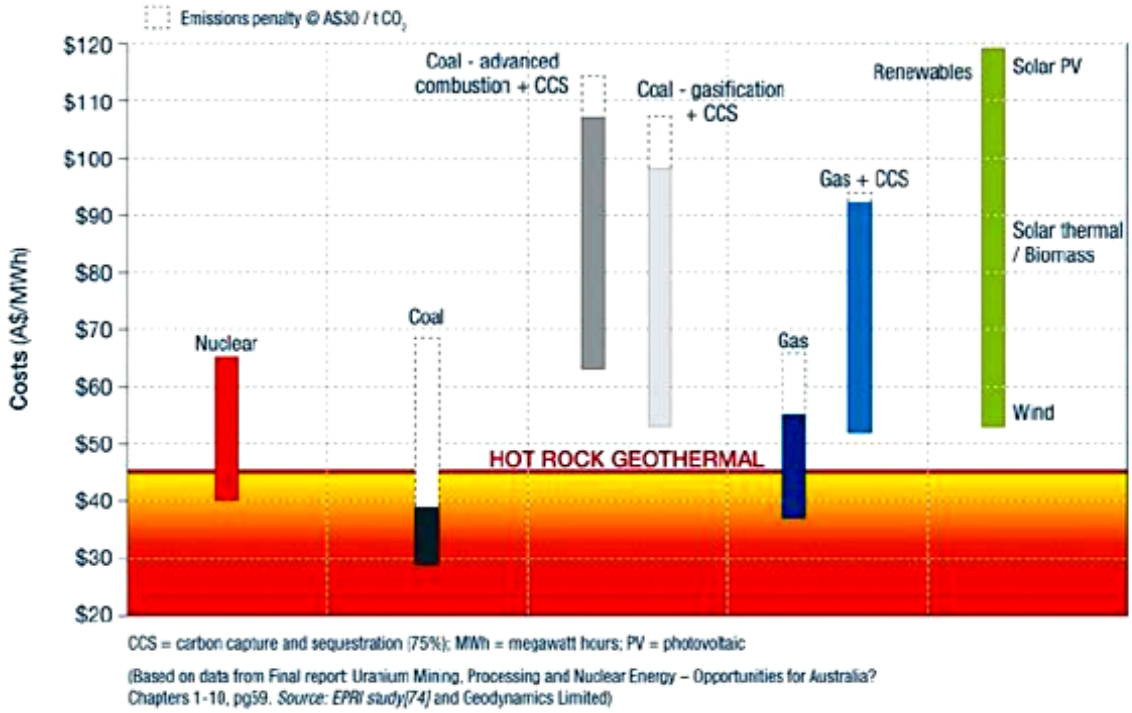

Figure 2.12 Comparison of electricity cost produced from hot dry rock versus other resources

Since 2001 when the first geothermal exploration license was granted, there have been 48 companies with 384 geothermal exploration license applications awarded covering an area of 358,906 km^2 Australia wide (PIRSA, 2011). This area is illustrated in Figure 2.13, which shows the regions where geothermal exploration licenses have been applied around Australia as of February 2009 (PIRSA, 2011). Figure 2.14 (PIRSA, 2012) presents an inset view of the geothermal exploration licenses in the South Australian region. This region is where the subject of this study is located, namely, the Habanero wells in the Copper Basin geothermal system and this is the first enhanced geothermal system in Australia.

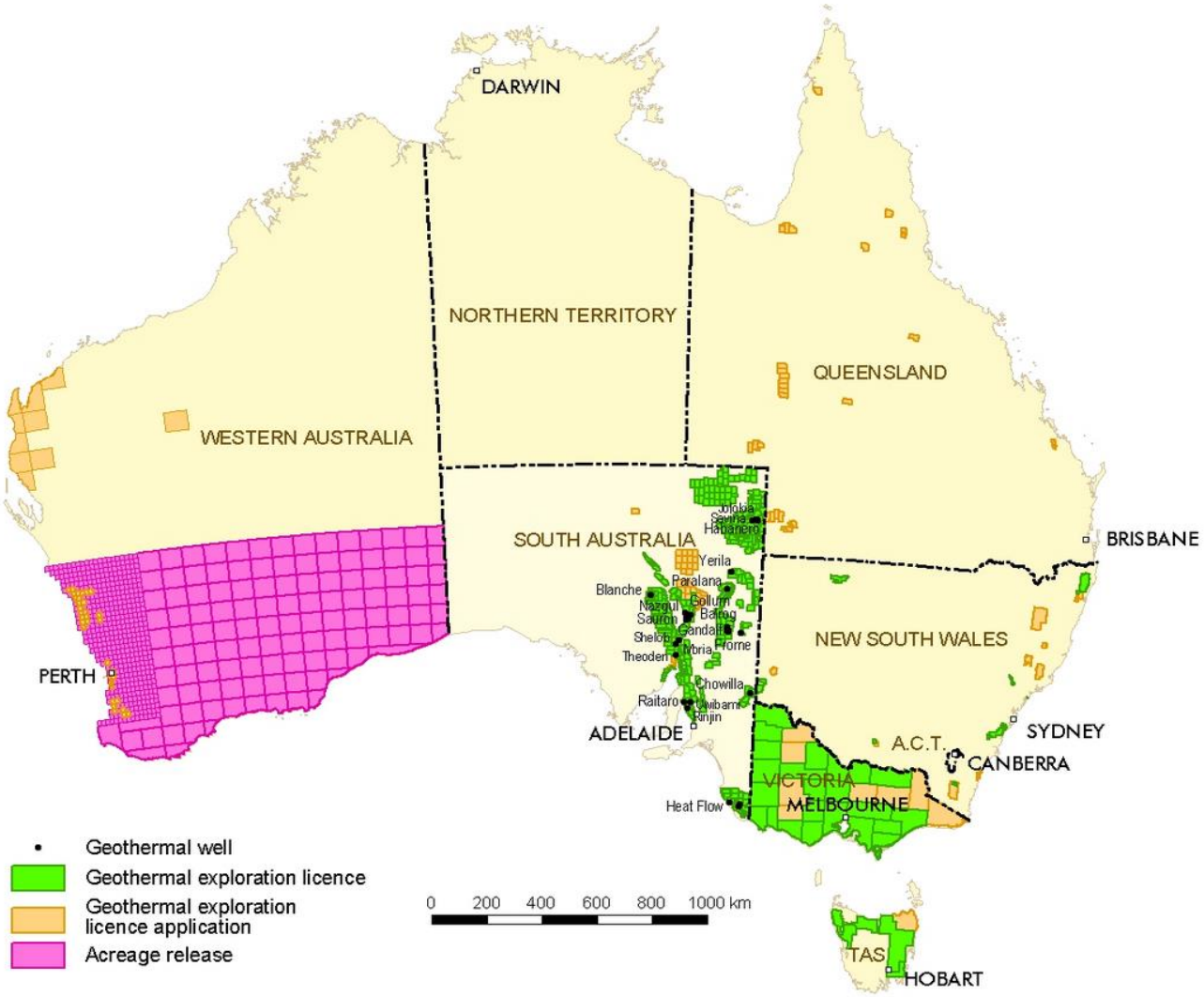

Figure 2.13 Australian map showing geothermal exploration licenses, applications, and gazettal areas

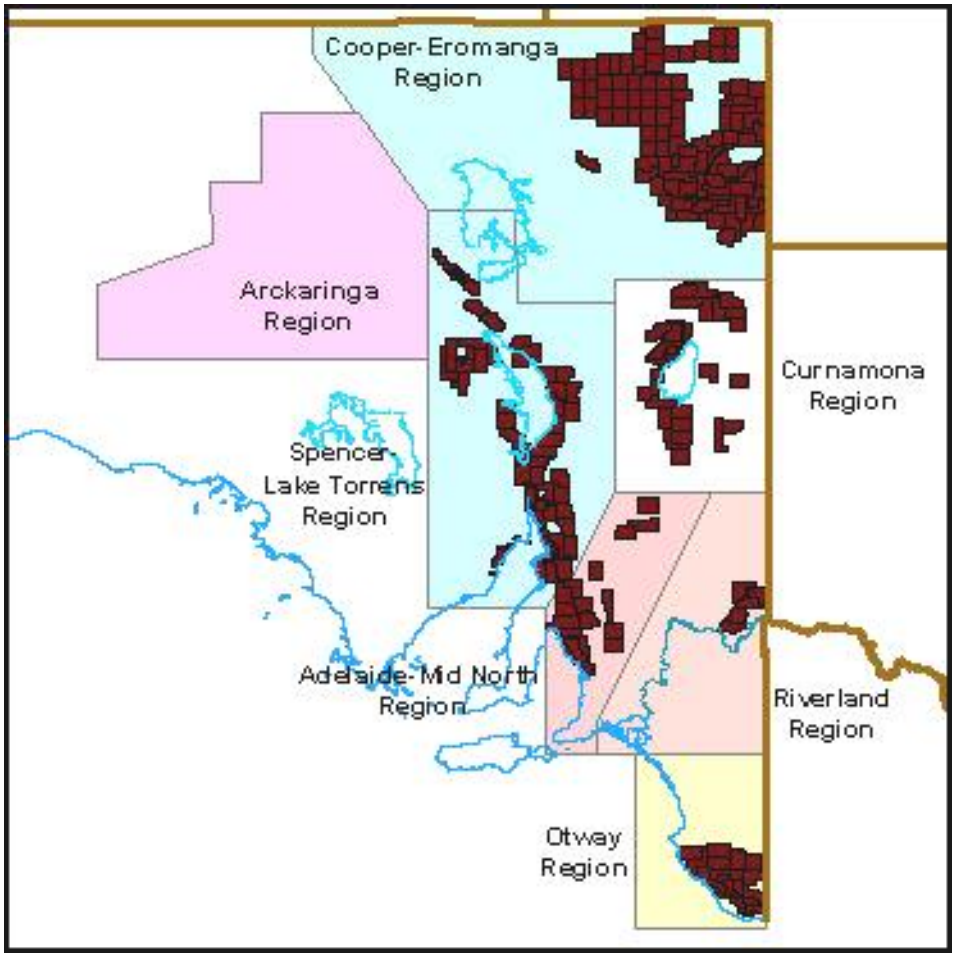

Figure 2.14 Geothermal exploration licenses in the South Australian region

The Cooper Basin geothermal system developed by Geodynamics Pty Ltd is located in Innamincka, in the northern region of South Australia. The Cooper Basin tenement currently consists of three Habanero wells (Habanero 1, 2 and 3), Jolokia 1 well, and Savina 1 well and currently additional well development is still progressing. The tenement map is provided in Figure 2.15 (Gurgency, 2010). These wells in Cooper Basin are deep wells reaching to a depth greater than 5 km. To date, Geodynamics has successfully accomplished their proof of concept and a working 1 MW pilot plant is being developed. External sources from surface water (Darby's Bore and Cooper's Creek) will provide make up water for the recirculating water system (Wyborn, 2010). The composition of the groundwater may differ significantly from the fresh water injected through the granite to extract the thermal energy. Due to the injection of fresh water to the reservoir, the equilibrium with the surrounding groundwater is highly likely

to be altered. The flow of large volumes of injected water will most probably cause partial chemical dissolution or alteration of granites, which could potentially increase the dissolved solids such as silica and other metals in the circulating fluid. This phenomenon will be strongly geologically dependent as each site will have its own rock composition.

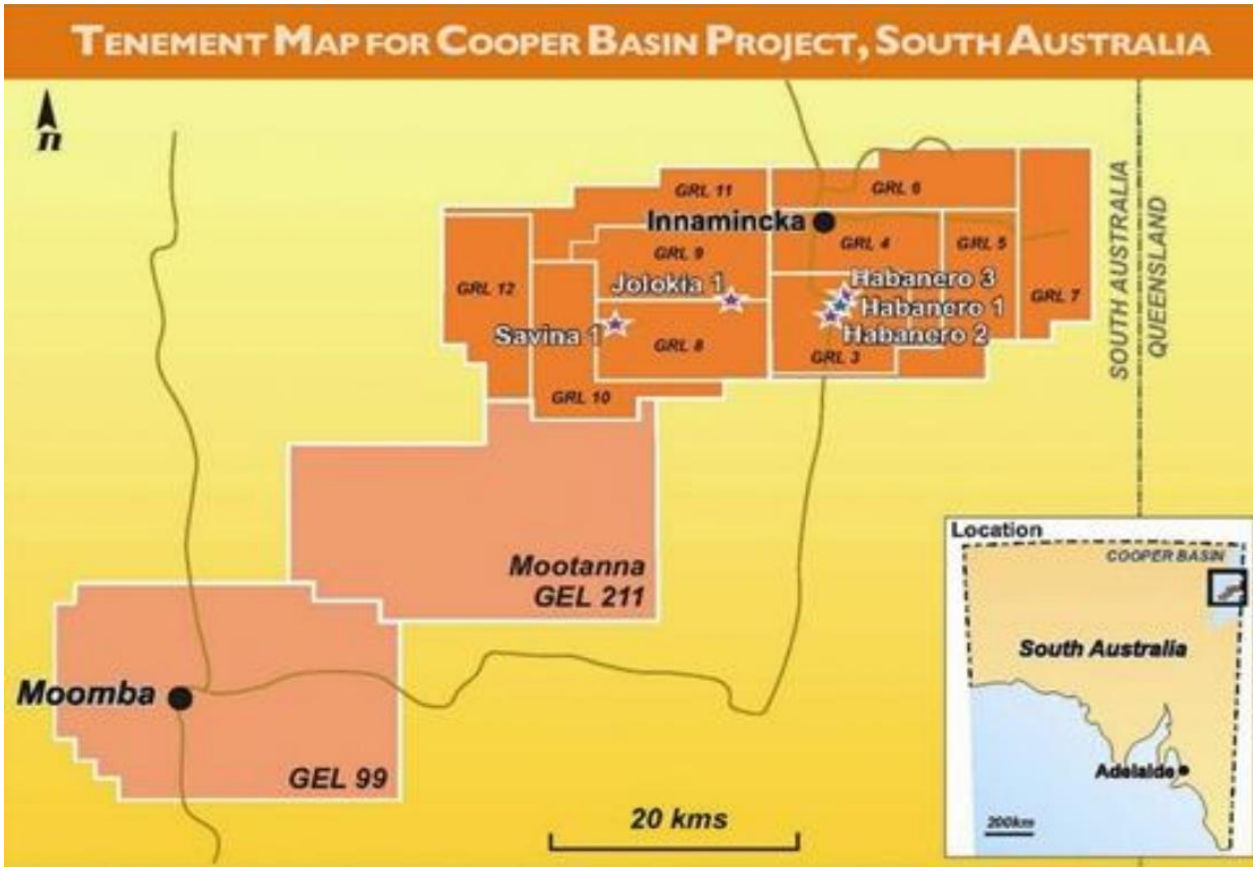

Figure 2.15 Tenement map of the Cooper Basin geothermal system

Clearly, the study of fluid rock interaction is crucial and remains largely poor addressed and known. A compounding factor is the fact that fundamental processes associated with mineral dissolution and precipitation, and the developed pressure-temperature gradient remain poorly understood (Marks et al., 2010). To date, literature confirms that different geothermal reservoirs are characterised by wide variations in the geochemical composition of the circulating water. Furthermore, it is impossible to generalize the actual field experience of mineral deposition in geothermal systems into a single consistent theory due to the vast

chemical and operational variation between field sites (Robinson, 1982). Despite the fact that a number of studies on fluid-rock interactions for different geothermal sites have been undertaken (Rimstidt and Barnes, 1980; Robinson, 1982; Posey-Dowty et al., 1986; Savage et al., 1987; Grigsby et al., 1989; Savage et al., 1992; Azaroual and Fouillac, 1997; Tarcan, 2005; Yanagisawa et al., 2005; Castro et al., 2006; Marks et al., 2010), and studies on rock-chloride solutions (Ellis, 1968; Dove and Crerar, 1990; Icenhower and Dove, 2000), it is probable that the results of these workers efforts will unlikely be directly applicable to the hot granite based geothermal systems in Cooper Basin. As a consequence, the work presented in this study is likely to be unique.

As the Cooper Basin geothermal system is the first enhanced geothermal system to be developed in Australia, it would be potentially valuable to review previous work on rock water interaction and mineral dissolution. This subject will be discussed in detailed in Sections 2.5. However, prior to reviewing the previous work on fluid-rock interaction, it is important to initially understand the supporting theory behind fluid-rock interaction. The kinetics and thermodynamics of likely geochemical reactions will be reviewed in the next section.

2.3 Geochemical Reactions

The fluid phase in a natural geothermal system has an exceptionally long residence time (thousands of years) at a relatively high temperature (> $150^{o}C$ – $300^{o}C$) and these high temperature suggest significant fluid-rock interaction (Grigsby et al., 1989). Given the system's long residence time, it is normally assumed that the fluid phase has attained a state of chemical equilibrium (Grigsby et al., 1989). Clearly, when fresh water is introduced to the system to extract the thermal energy, the system will be perturbed and it will no longer remain in equilibrium. Such a change will undoubtedly lead to precipitation and dissolution for different paths in the mineral assemblage. Precipitation is a major problem in geothermal energy extractions. Minerals may precipitate depending on the elements present in the granite and the injected brine. Silica scaling is a well-known problem in geothermal systems which occurs

when the fluid reaches super-saturation with respect to amorphous silica, during heat extraction or partial flashing (Robinson, 1982). The formation of silica scales in pipelines, heat exchangers and reinjection wells is common where geothermal fluids are supersaturated with silica (Brown and Dunstall, 2000).

2.3.1 Thermodynamics

According to Prigogine (1967) cited in Brantley and Conrad (2008), "Irreversible thermodynamics treats systems that are removed from equilibrium by modelling how the entropy changes with time as equilibrium is approached." The change of entropy of a system dS is the sum of the entropy supplied to the system by its surroundings, d_eS and the entropy produced in the system, d_iS (Prigogine, 1961):

$$dS = d_eS + d_iS \quad \textbf{(2.1)}$$

where: d_iS is never negative. If $d_iS = 0$, it is a reversible process, while when $d_iS > 0$, it is an irreversible process.

For a closed system at constant pressure and temperature, the relationship between the change of entropy with the change in Gibbs free energy (Brantley and Conrad, 2008):

$$Td_iS = -dG_{sys} \quad \textbf{(2.2)}$$

For a spontaneous one reaction at constant pressure and temperature, the expression using the extent of reaction is:

$$T\frac{d_iS}{dt} = A\frac{d\xi}{dt} \quad \textbf{(2.3)}$$

If $\frac{d_iS}{dt} > 0$ is the entropy of production, $A = -\Delta G_{reaction}$ is the chemical affinity of the reaction (the driving force of the reaction). The value of $A > 0$ ($\Delta G_{reaction} < 0$) when a reaction occurs spontaneously, and at equilibrium the value of $A = 0$.

For any reaction, a correlation between $\Delta G_{reaction}$, equilibrium constant, K_{eq} and reaction activity quotient, Q is:

$$\Delta G_{reaction} = -A = RTln\left(\frac{Q}{K_{eq}}\right) \quad \textbf{(2.4)}$$

where: R is the gas constant and T is the absolute temperature.

The dissolution of solid silica phases (SiO_2) in water has been extensively studied (Mackenzie and Gees, 1971; Fournier and Rowe, 1977; Robinson, 1982; Grigsby, 1989; Worley, 1994). The solubility data for various silica phases (Rimstidt, 1979) cited in (Robinson, 1982) is provided in Figure 2.16. Quartz is thermodynamically the most stable phase of silica (Robinson, 1982), thus its solubility at any given temperature is lower to the other silica phases.

In saturated solutions with pH less than 9, dissolved silica is nominally in the form of silicic acid (Goto, 1956). It is widely accepted that silica-water reaction is a simple surface reaction to form silicic acid monomer:

$$SiO_{2(s)} + 2H_2O_{(l)} \rightleftharpoons H_4SiO_{4(aq)} \text{or } \mathrm{SiO_{2(aq)}} \quad \textbf{(2.5)}$$

The solubility constant for the reaction is (Verma, 2000a):

$$K_{SiO_2} = exp\left(\frac{-\Delta G_F^{T,P}}{RT}\right) = \frac{[H_4SiO_4]}{[SiO_2][H_2O]^2} = [H_4SiO_4] \quad \textbf{(2.6)}$$

where: $\Delta G_F^{T,P}$ = the Gibbs' free energy of formation for the reaction

T = temperature

P = pressure

R = gas constant

Solid brackets indicate molar concentration (mol/L) of the species

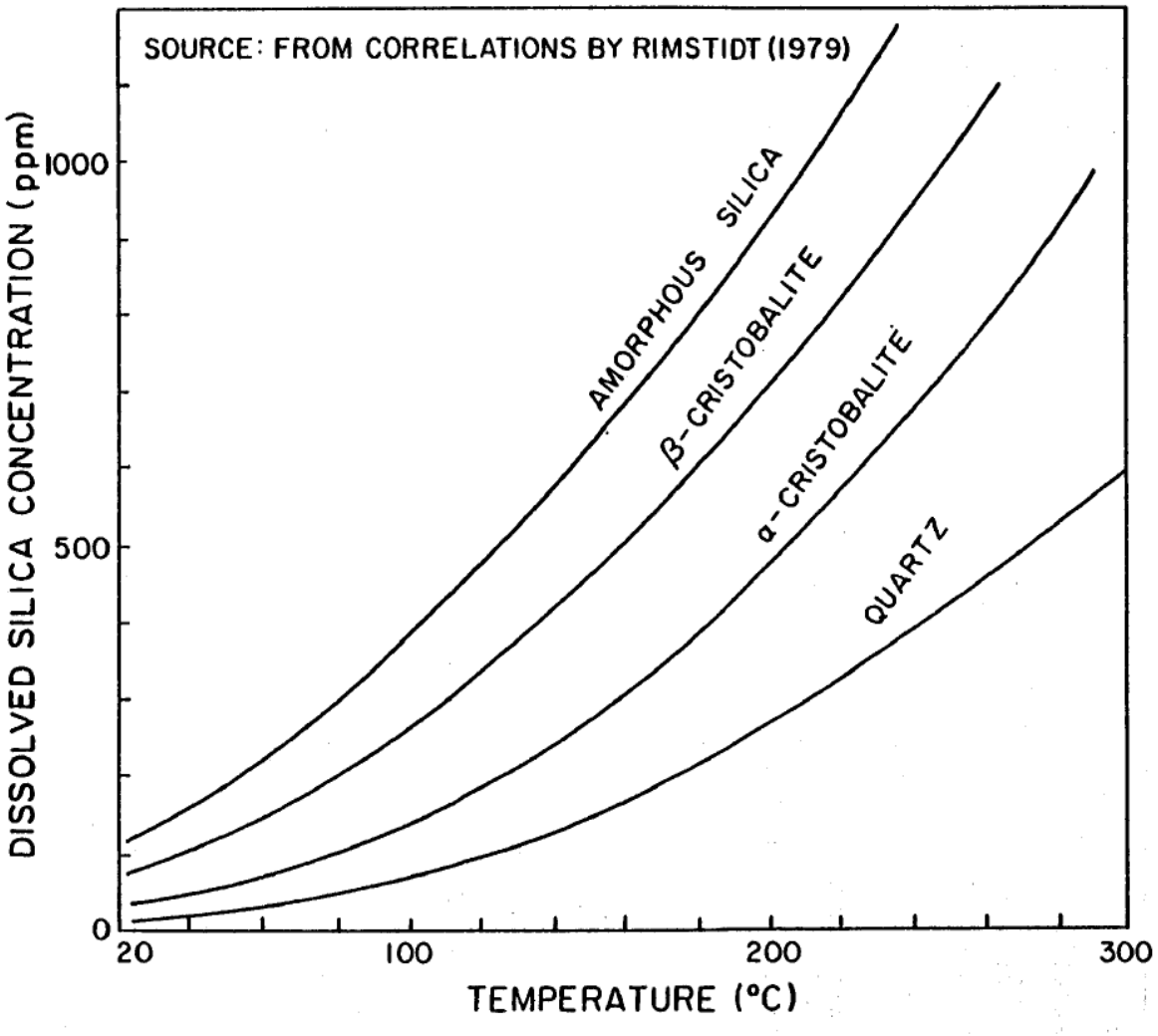

Figure 2.16 Equilibrium solubilities of silica phases

2.3.2 Kinetics of silica dissolution

Chemical kinetics or reaction kinetics is the study of chemical reaction rates and reaction mechanisms (Fogler, 2006). To understand how a reaction progresses, one may undertake kinetic experiments to measure the rates of change of the reactants and the products. In order to quantify the progress of the reaction, one must define the extent of reaction. It is important to understand the foundation of a reaction. A more in-depth review of reaction kinetics is provided by Laidler (1965), Brantley et al. (2008) and Zhang (2008).

Many studies have been performed to understand the kinetics of quartz dissolution (Kitahara, 1960b; Van Lier et al., 1960; Weill and Fyfe, 1964; Rimstidt and Barnes, 1980; Robinson, 1982; Grigsby, 1989; Dove and Crerar, 1990; Berger et al., 1994; Tester et al., 1994; Worley, 1994; Gautier et al., 2001), and feldspar dissolution (Lagache, 1976; Anbeek, 1992; Hellmann, 1994; Arnórsson and Stefánsson, 1999; Stefánsson and Arnórsson, 2000; Hellmann and Tisserand, 2006). However, only a very small number of studies have observed the dissolution of granite (Robinson, 1982; Worley, 1994; Ganor et al., 2005)

It is widely known that the dissolution of quartz to silicic acid follows the reversible reaction presented in Equation (2.5). The dissolution of albite in water follows the reaction (Arnórsson and Stefánsson, 1999):

$$NaAlSi_3O_8 + 4H_3O^+ \rightleftharpoons Na^+ + Al^{3+} + 3H_4SiO_{4(aq)} \quad \textbf{(2.7)}$$

Complex geochemical reaction can occur in many elementary steps. As an example, to dissolve one formula unit of albite would occur in a number of elementary reaction steps: ion exchange of H^+ for Na^+, followed by hydrolysis of 3 Al-O-Si and 6 Si-O-Si linkages.

The dissolution of K-feldspar (microcline) in water follows the reaction (Arnórsson and Stefánsson, 1999):

$$KAlSi_3O_8 + 4H_3O^+ \rightleftharpoons K^+ + Al^{3+} + 3H_4SiO_{4(aq)} \quad \textbf{(2.8)}$$

The solubility constants (K) for albite and microcline as a function of temperature $(T\ in\ Kelvin)$ (Stefánsson and Arnórsson, 2000) are presented by Equations (2.9) and (2.11), respectively:

$$logK = -96.267 + \frac{305542}{T^2} - \frac{3985.50}{T} - 28.588 \times 10^{-6} \times T^2 + 35.790 \times \log(T) \quad \textbf{(2.9)}$$

$$logK = -78.594 + \frac{311970}{T^2} - \frac{6094.13}{T} - 27.776 \times 10^{-6} \times T^2 + 30.308 \times \log(T) \quad \textbf{(2.10)}$$

As complex geochemical reaction steps can occur in feldspar dissolution, it is expected for highly complex geochemical reactions to occur in granite dissolution. It may be observed from Equations (2.5), (2.7) and (2.8) that the dissolution reactions result in the appearance of H_4SiO_4 in solution (dissolved silica). Therefore, in order to simplify the reaction kinetics, we would determine the dissolution rate of Habanero 3 granite through the rate of appearance of silica in the water. Since quartz is the dominating phase in the Habanero 3 granite (see Section 3.2.2), the dissolution of granite is then assumed to follow the dissolution kinetics of quartz.

According to Worley (1994), the forward reaction rate (r_f) for quartz dissolution is proportional to the active surface area divided by the mass of water in the system:

$$r_f = k_f \frac{A_s}{M_w} \tag{2.11}$$

and based on the principle of collision theory, the reverse reaction rate (r_r) is linearly proportional to the product concentration (H_4SiO_4 in molal) and the ratio of surface area (A_s) to mass of water (M_w):

$$r_r = k_r \frac{A_s}{M_w} m_{H_4SiO_4} \tag{2.12}$$

The net rate (r_{net}) of change of $m_{H_4SiO_4}$ can be obtained by subtracting Equation (2.12) from Equation (2.11):

$$r_{net} = \frac{dm_{H_4SiO_4}}{dt} = r_f - r_r = \frac{A_s}{M_w}\left(k_f - k_r m_{H_4SiO_4}\right) \tag{2.13}$$

At equilibrium:

$$r_{net}^{eq} = r_f - r_r = 0 = k_f - k_r m_{H_4SiO_4}^{sat} \tag{2.14}$$

Solving for k_r:

$$k_r = \frac{k_f}{m_{H_4SiO_4}^{sat}} \tag{2.15}$$

According to Lasaga (1984):

$$K_{eq} = \frac{k_f}{k_r} \tag{2.16}$$

Substituting Equation (2.15) to Equation (2.13) yields:

$$r_{net} = \frac{dm_{H_4SiO_4}}{dt} = k_f \frac{A_s}{M_w}\left(1 - \frac{m_{H_4SiO_4}}{m^{sat}_{H_4SiO_4}}\right) \tag{2.17}$$

where: $m_{H_4SiO_4}$ = concentration of dissolved silica (molal)

$m^{sat}_{H_4SiO_4}$ = equilibrium concentration of dissolved silica (molal). It is important to note that $m^{sat}_{H_4SiO_4}$ and $m_{H_4SiO_4}$ represent the concentration of silica (SiO_2) in water.

t = time (s)

k_f = kinetic rate constant for dissolution (mol/m^2.s)

k_r = kinetic rate constant for precipitation (mol/m^2.s)

A_s = active surface area (m^2)

M_w = mass of water (kg)

The term $\left(1 - \frac{m_{H_4SiO_4}}{m^{sat}_{H_4SiO_4}}\right)$ can be defined as the degree of under-saturation. Rewriting the equation in a different form gives:

$$\frac{dm_{H_4SiO_4}}{dt} = k_f \frac{A_s}{M_w}\left(\frac{m^{sat}_{H_4SiO_4} - m_{H_4SiO_4}}{m^{sat}_{H_4SiO_4}}\right) \tag{2.18}$$

Rearranging Equation (2.18) becomes:

$$\frac{dm_{H_4SiO_4}}{dt} = \frac{k_f}{m^{sat}_{H_4SiO_4}} \frac{A_s}{M_w}\left(m^{sat}_{H_4SiO_4} - m_{H_4SiO_4}\right) \tag{2.19}$$

The integration form is:

$$\int_{0}^{m_{H_4SiO_4}} \frac{dm_{H_4SiO_4}}{\left(m_{H_4SiO_4}^{sat} - m_{H_4SiO_4}\right)} = \frac{k_f}{m_{H_4SiO_4}^{sat}} \frac{A_s}{M_w} \int_{0}^{t} dt \quad \textbf{(2.20)}$$

For a constant temperature and volume, the integration of Equation (2.20) and applying boundary conditions of $m_{H_4SiO_4} = 0$ at t = 0 and $m_{H_4SiO_4} = m_{H_4SiO_4}$ at t = t becomes a linear form:

$$ln\left(\frac{m_{H_4SiO_4}^{sat} - m_{H_4SiO_4}}{m_{H_4SiO_4}^{sat}}\right) = -k_f \frac{A_s}{m_{H_4SiO_4}^{sat} M_w} t \quad \textbf{(2.21)}$$

To simplify:

$$\left(\frac{m_{H_4SiO_4}^{sat} - m_{H_4SiO_4}}{m_{H_4SiO_4}^{sat}}\right) = \theta \quad \textbf{(2.22)}$$

Substituting Equation (2.15) to Equation (2.17) gives the r_{net} using the reverse rate constant:

$$r_{net} = \frac{dm_{H_4SiO_4}}{dt} = k_r \frac{A_s}{M_w} \left(m_{H_4SiO_4}^{sat} - m_{H_4SiO_4}\right) \quad \textbf{(2.23)}$$

Integration of Equation (2.23) yields:

$$ln\theta = ln\left(\frac{m_{H_4SiO_4}^{sat} - m_{H_4SiO_4}}{m_{H_4SiO_4}^{sat}}\right) = -k_r \frac{A_s}{M_w} t \quad \textbf{(2.24)}$$

A study by Robinson (1982) has used a similar kinetic rate to Equation (2.23). This kinetic rate equation was used to obtain the concentration of the dissolved silica (silicic acid) in the outlet fluid in order to evaluate the likelihood of silica scaling. In a closed vessel, the rate of quartz dissolution (Robinson, 1982):

$$\frac{dC}{dt} = ka^*(C^\infty - C) \quad \textbf{(2.25)}$$

The integration of Equation (2.25) assuming that $C_0 = 0$, yields:

$$ln\left(\frac{C^{\infty} - C}{C^{\infty}}\right) = -ka^{*}t \quad \textbf{(2.26)}$$

where: C_0 = initial concentration of silicic acid (ppm)

C = concentration of silicic acid (ppm) at time t

t = time (s)

k = kinetic rate constant for dissolution (m/s)

a^{*} = $^{S}/_{V}$ = ratio of quartz surface area to fluid volume (m^{-1})

C^{∞} = equilibrium concentration of dissolved silica (ppm)

Robinson (1982) mentioned that this rate law is empirical, however, the assumption of a first order dependence of rate on surface area and the degree of under-saturation of the fluid is reasonable.

2.3.3 Kinetics of silica scaling

The rate of silica scaling is controlled by two distinct processes: liquid-phase polymerization followed by heterogeneous nucleation and deposition in solution competes with direct heterogeneous deposition of monomeric dissolved silica for the available silicic acid molecules (Gudmundsson and Bott, 1979).

Factors that control the rate of polymerization of dissolved silica are pH, salinity, the degree of supersaturation, the presence of solid substances, and temperature. The steps involved in the polymerization of monomeric silica species to the precipitation or aggregation (Iler, 1955) is presented in Figure 2.17.

$$Si(OH)_4 \xrightarrow{Polymerization} Colloidal\ (sol)$$

$$particles \xrightarrow{Aggregation} Network\ of\ particles\ (gel)$$

$$Dilute\ sol \xrightarrow{Aggregation} Weak\ gel\ or\ precipitate$$

$$Concentrated\ sol \xrightarrow{Aggregation} Strong\ firm\ gel$$

$$Wet\ gel \xrightarrow{Drying} Shrunken\ gel; Surface\ of particles\ in\ gel\ covered\ by\ Si\ OH\ groups$$

Figure 2.17 Steps involved in silica polymerization

The polymerization rate of dissolved silica (Goto, 1956) follows nth order kinetics:

$$-\frac{dC}{dt} = k(C - C_e)^n \quad \textbf{(2.27)}$$

where: C = concentration of monomeric silica

C_e = equilibrium concentration of monomeric silica at a particular temperature

k = rate constant

n = order of reaction

Kitahara (1960a) cited in Owen (1975) reported that the order of reaction, n = 2 in acidic solutions and n = 3 in alkaline solutions. The results showed that polymerization rates increase with increasing temperatures.

According to Icopini et al. (2005) cited in Brantley and Conrad (2008), the rate of disappearance of aqueous silica from a supersaturated amorphous silica solution followed a fourth order rate law given as:

$$r = -\frac{d[H_4SiO_4]}{dt} = k_4\left[H_4SiO_{4(aq)}\right]^4 \quad \textbf{(2.28)}$$

The high order of reaction was suggested to be a complex reaction mechanism which they derived as polymerization of monomeric to tetrameric silica via monomer additions:

$$H_4SiO_{4(aq)} + H_4SiO_{4(aq)} \rightarrow H_6Si_2O_{7(aq)} + H_2O \quad \textbf{(2.29)}$$

$$H_6Si_2O_{7(aq)} + H_4SiO_{4(aq)} \rightarrow H_8Si_3O_{10(aq)} + H_2O \quad \textbf{(2.30)}$$

$$H_6Si_3O_{10(aq)} + H_4SiO_{4(aq)} \rightarrow H_8Si_4O_{12(aq)} + 2H_2O \quad \textbf{(2.31)}$$

The overall reaction is:

$$4H_4SiO_{4(aq)} \rightarrow H_8Si_4O_{12(aq)} + 2H_2O \quad \textbf{(2.32)}$$

Assuming that the reaction proposed in Equation (2.29) has a rate constant k_1 and Equation (2.30) has a rate constant k_2 occur faster than Equation (2.31) with rate constant k_3, the two faster reaction could achieve equilibrium (with their equilibrium constants K_1 and K_2, respectively. Thus Equation (2.31) could control the overall rate expressed as:

$$k_4 = k_3 f(y) \frac{K_1 K_2}{a_{H_2O}^2} \quad \textbf{(2.33)}$$

where: $f(y)$ represents a term incorporating activity coefficients for the silica phases and a_{H_2O} is the activity of water

A study of thermodynamic and kinetics of silica scaling by Brown (2011b) summarises the mechanism of amorphous silica deposition by formation of silica colloids, and direct monomeric silica deposition to surfaces. Brown (2011b) pointed out two important parameters, the silica saturation temperature and the silica saturation index (SSI).

The silica saturation temperature is the temperature at which the separated water reaches amorphous silica saturation, and if a geothermal fluid is separated above this temperature then silica scaling cannot occur. The SSI is the ratio of silica concentration in the brine and the equilibrium amorphous silica solubility at that particular condition. Silica scaling is possible when SSI > 1.0.

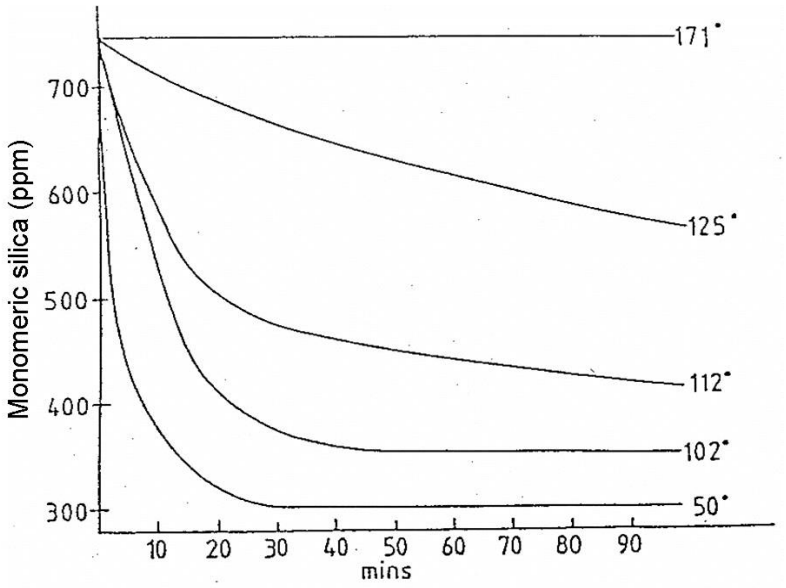

Figure 2.18 Rate of monomeric silica disappearance as a function of time at various temperatures (Brown, 2011b)

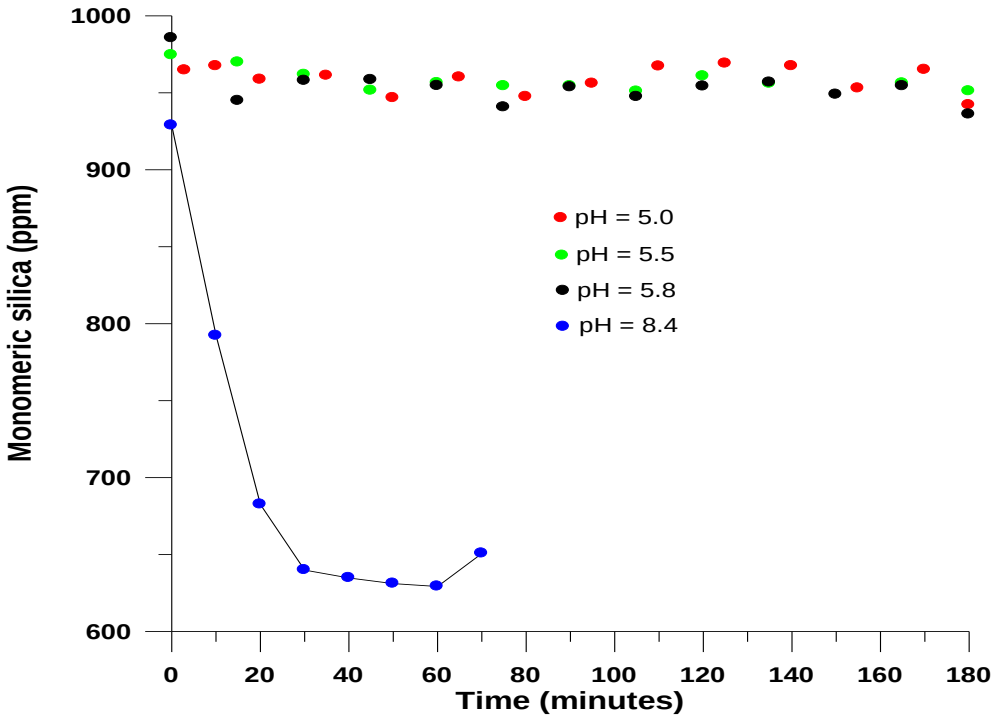

Figure 2.19 Silica polymerisation as a function of pH (Brown, 2011b)

An example of silica polymerization being influenced by temperature is presented in Figure 2.18, where at 171^{o}C no polymerisation has occurred since the fluid is above silica saturation

temperature. As the temperature decreases, the SSI and the polymerisation rate increased. The polymerisation rate may also be measured as a function of pH as can be seen in Figure 2.19.

The solubility of amorphous silica (Volosov et al., 1972 cited in Gudmundsson and Bott, 1979) for temperature ranging from 25^{o}C to 305^{o}C is:

$$c = 15.1 \times 10^{3} exp\left(\frac{-1354}{T}\right) \quad \textbf{(2.34)}$$

where: c = the concentration of silica (mg/kg)

T = temperature (K).

Another study on the solubility of amorphous silica was performed by Fournier and Rowe (1977). The solubility of amorphous silica at a given temperature is:

$$\log C = -\frac{731}{T} + 4.52 \quad \textbf{(2.35)}$$

where: C = the concentration of silica (mg/kg)

T = temperature (K).

2.4 Geochemical Modelling

Using the experimental data, the modelling of granite dissolution and silica precipitation was performed using The Geochemist Workbench software. The modelling includes observing mineral solubility, mineral dissolution, tracing reaction path, observing the precipitation of the minerals, and quantifying mineral precipitation.

According to Bethke (1996), the study of dissolution and precipitation involves five generalized steps:

1. Diffusion of reactants from the bulk fluid to the mineral surface
2. Adsorption of the reactants onto reactive sites

3. A chemical reaction involving the breaking and creation of bonds
4. Desorption of the reaction products
5. Diffusion of the products from the mineral surface to the bulk fluid

Bethke (1996) states that reaction for common minerals is surface controlled or transport controlled, in which many cases tend to be surface controlled. The rate law used in the modeling is derived from transition state theory (Rimstidt and Barnes, 1980; Aagaard and Helgeson, 1982; Bethke, 1996; Kubicki, 2008).

2.4.1 Transition-state theory applied to silica dissolution

The Transition-state Theory (Evan and Polanyi, 1935; Eyring, 1935) has been used to determine reaction rate. Kubicki (2008) has recently utilized the Transition-state theory in rates and reaction mechanism in geochemical kinetics.

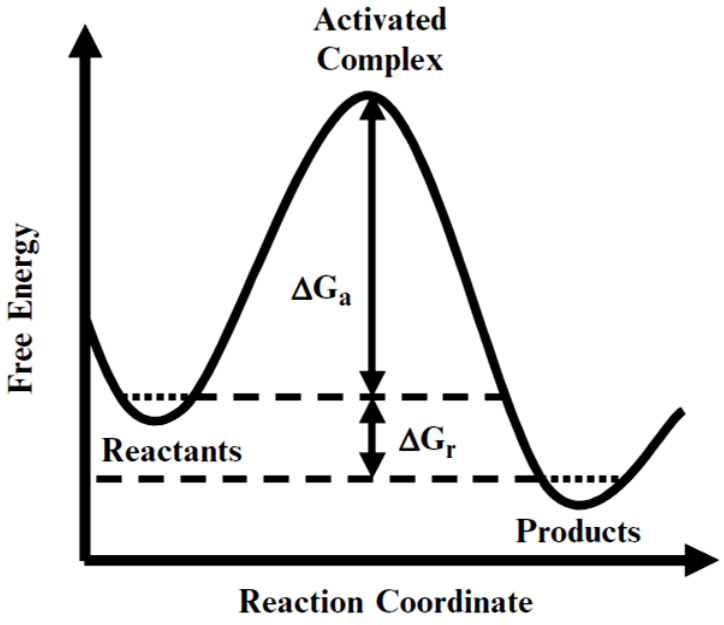

Figure 2.20 Schematic of free energy maximum through which reactants must pass to become products

Transition state theory affirms that an activated complex (transition state) exists along the minimum energy path from reactants to products (Worley, 1994). An illustration of a transition state complex is shown in Figure 2.20 (Kubicki, 2008).

In particular Rimstidt and Barnes (1980) has applied the transition state theory to silica dissolution in water. Consider the reaction:

$$SiO_2(s) + 2H_2O(l) \rightleftharpoons H_4SiO_4(aq) \quad \textbf{(2.36)}$$

This reaction consists of two opposing reaction:

$$SiO_2 + 2H_2O \rightleftharpoons (SiO_2 \cdot 2H_2O)^* \quad \textbf{(2.37)}$$

$$(SiO_2 \cdot 2H_2O)^* \rightarrow H_4SiO_4 \quad \textbf{(2.38)}$$

$$H_4SiO_4 \rightleftharpoons (SiO_2 \cdot 2H_2O)^* \quad \textbf{(2.39)}$$

$$(SiO_2 \cdot 2H_2O)^* \rightarrow SiO_2 + 2H_2O \quad \textbf{(2.40)}$$

Rismstidt and Barnes (1980) used this form of the activated complex to simplify their calculations. They determined a kinetic rate law for quartz dissolution and precipitation (for the derivation of the kinetic rate law, see Rimstidt and Barnes (1980)):

$$r_{H_4SiO_4} = k'_+ \left(1 - \frac{Q}{K}\right) \quad \textbf{(2.41)}$$

where: $r_{H_4SiO_4}$ = the reaction rate (mol/s; positive for precipitation)

k'_+ = apparent dissolution rate constant = $(A/M)\gamma_{H_4SiO_4} a_{SiO_2} a^2_{H_2O} k_+$

A = the relative surface area compared to a standard system with 1 m^2 surface area,

M = the relative mass of water compared to a standard system with 1 kg of water

$\gamma_{H_4SiO_4}$ = activity coefficient of H_4SiO_4

a_{SiO_2} = activity of SiO_2

a_{H_2O} = activity of water

k_+ = the dissolution rate constant (mol/cm^2.s),

Q = activity product and

K = the equilibrium constant for dissolution reaction.

Brantley (2008) have reviewed extensively the kinetics of mineral dissolution. She stated that for a complex mechanism that is rate limited by a single elementary reaction, the transition state theory may be applied to the overall reaction. As transition state theory suggest, the forward rate minus the reverse rate is linear with respect to ΔG near equilibrium following the equation:

$$r_{net} = -k_+ \prod a_j^{m_j} \left(1 - exp\left(\frac{n_i \Delta G}{RT}\right)\right) \quad \textbf{(2.42)}$$

where: r_{net} = the forward reaction rate – reverse reaction rate

a_j = activity of species j in the rate-determining reaction

k_+ = rate constant for the forward rate

m_j and n_i = constant

R = gas constant

T = absolute temperature

ΔG = $RTln\left(\frac{Q}{K_{eq}}\right)$ = driving force for reaction

Q = activity quotient

K_{eq} = equilibrium constant

Bethke (1996) compiled the rate constants of quartz and amorphous silica dissolution as determined by Rimstidt and Barnes (1980) listed in Table 2.5.

Table 2.5 Rate constants k_+ (mol/cm^2.s) for dissolution of silica minerals in water at various temperatures

T (^{o}C)	Quartz	α-Cristobalite	Amorphous silica
25	4.20×10^{-18}	1.71×10^{-17}	7.32×10^{-17}
70	2.30×10^{-16}	6.47×10^{-16}	2.19×10^{-15}
100	1.88×10^{-15}	4.48×10^{-15}	1.33×10^{-14}
150	3.09×10^{-14}	6.12×10^{-14}	1.49×10^{-13}
200	2.67×10^{-13}	4.81×10^{-13}	9.81×10^{-13}
250	$1.46 \times 10^{--12}$	2.55×10^{-12}	4.43×10^{-12}
300	5.71×10^{-12}	1.01×10^{-11}	1.51×10^{-11}

Knauss and Wolery (1986) studied the dissolution of albite and they found that the reaction follows a different rate law which is pH dependent. The rate law for albite (for pH < 1.5):

$$r_{albite} = A_s k_+ a_{H^+} \left(\frac{Q}{K} - 1\right) \quad \textbf{(2.43)}$$

For pH range of about 1.5 to 8:

$$r_{albite} = A_s k_+ \left(\frac{Q}{K} - 1\right) \quad \textbf{(2.44)}$$

For higher pH ranges:

$$r_{albite} = A_s k_+ a_{H^+}^{-1/2} \left(\frac{Q}{K} - 1\right) \quad \textbf{(2.45)}$$

where: r_{albite} = the reaction rate (mol/s; positive for precipitation)

a_{H^+} = activity of H^+

A_S = the mineral's surface area,

k_+ = are the mineral's rate constant (mol/cm^2.s),

Q = activity product and

K = the equilibrium constant for dissolution reaction.

A study on transition state theory was also applied to alkali feldspar dissolution. This study was undertaken by Aagaard and Helgeson (1982). The general rate equation for silicate hydrolysis:

$$\frac{d\xi}{dt} = ks\left(\prod_i a_i^{-\hat{n}_{i,j}}\right)\left(1 - exp\left(-\frac{A}{\sigma RT}\right)\right) \quad \textbf{(2.46)}$$

where: ξ = overall progress variable for the process

k = rate constant

s = effective surface area in contact with the aqueous solution

a_i = activity of the i^{th} species in the system

$\hat{n}_{i,j}$ = stoichiometric reaction coefficient of the i^{th} reactant species in the j^{th} reaction corresponding to reversible formation of the critical activated complex

σ = rate of decomposition of the activated complex relative to that of the overall reaction

A = chemical affinity of the overall reaction

R = gas constant

T = absolute temperature

t = time

Aagaard and Helgeson (1982) suggested that the formation of an activated complex on the surface of an alkaline feldspar lead to the breakout of the activated complex to the acid aqueous phase. The schematic of the process is provided in Figure 2.21, and the change in Gibbs free energy is shown in Figure 2.22.

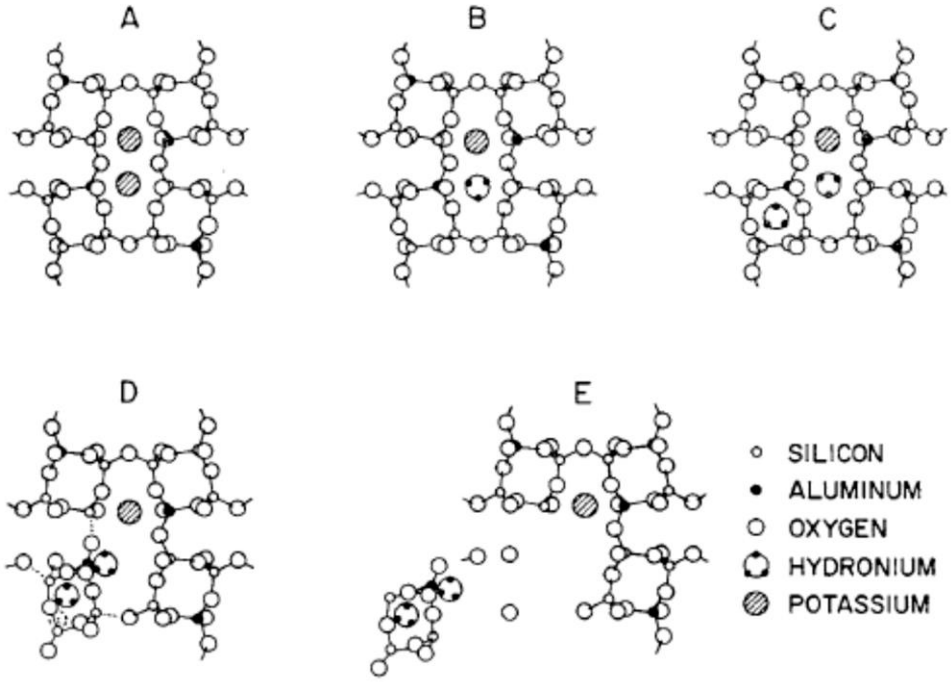

Figure 2.21 Schematic of the formation of an activated complex on a surface of K-feldspar grain reacting with an acid aqueous solution

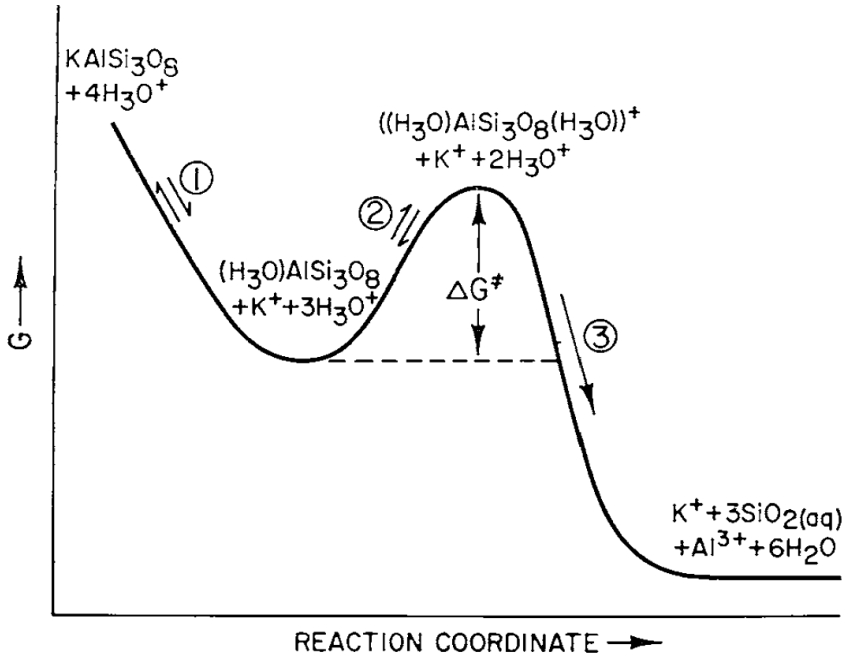

Figure 2.22 Schematic representation of the Gibbs free energy change associated with the hydrolysis of K-feldspar in an acid aqueous solution

2.4.2 Non-linear regression and curve fitting

Brantley and Conrad (2008) discussed that first order reaction kinetics are suitable to describe many geochemical systems. Worley (1994) used a first order global rate equation in his dissolution studies and fits his experimental data well. Worley's equation (Equation (2.47)) is essentially equivalent to the absolute rate theory or transition state theory derived for quartz dissolution by Rimstidt and Barnes (1980) (Equation (2.41)), however a small difference occur where Worley's equation is based on concentration instead of activities. The rate equation generated by Worley (1994) will be used in this study to obtain the dissolution rate constant and will be compared to the results generated by Geochemist Workbench software which uses the rate equation generated by Rimstidt and Barnes (1980). Worley's equation and the non-linear regression solution will be discussed here.

2.4.2.1 Non-linear rate equation

The first order global rate equation used by Worley (1994) is given below (recall Equation (2.17)):

$$r_{net} = \frac{dm_{H_4SiO_4}}{dt} = k_f \frac{A_s}{M_w}\left(1 - \frac{m_{H_4SiO_4}}{m^{sat}_{H_4SiO_4}}\right) \quad \textbf{(2.47)}$$

where: $m_{H_4SiO_4}$ = concentration of silicic acid (molal)

$m^{sat}_{H_4SiO_4}$ = equilibrium concentration of dissolved silica (molal)

t = time (s)

k_f = kinetic rate constant for dissolution (mol/m^2.s)

A_s = active surface area (m^2)

M_w = mass of water (kg)

Rewriting the equation in a different form gives (recall Equation (2.19)):

$$\frac{dm_{H_4SiO_4}}{dt} = k_f \frac{A_s}{m^{sat}_{H_4SiO_4} M_w}\left(m^{sat}_{H_4SiO_4} - m_{H_4SiO_4}\right) \quad \textbf{(2.48)}$$

and the results after integration (recall Equation (2.21)):

$$ln\left(\frac{m_{H_4SiO_4}^{sat} - m_{H_4SiO_4}}{m_{H_4SiO_4}^{sat}}\right) = -k_f \frac{A_s}{m_{H_4SiO_4}^{sat} M_w} t \quad \textbf{(2.49)}$$

Rearranging Equation (2.49):

$$ln\left(1 - \frac{m_{H_4SiO_4}}{m_{H_4SiO_4}^{sat}}\right) = -k^{\#} t \quad \textbf{(2.50)}$$

where:

$$k^{\#} = \frac{k_f}{m_{H_4SiO_4}^{sat}} \frac{A_s}{M_w} \quad \textbf{(2.51)}$$

It can be seen from Equation (2.50) that the units of $k^{\#}$ is s^{-1}. Equation (2.50) in exponential form:

$$\left(1 - \frac{m_{H_4SiO_4}}{m_{H_4SiO_4}^{sat}}\right) = e^{-k^{\#} t} \quad \textbf{(2.52)}$$

Rearranging Equation (2.52):

$$\frac{m_{H_4SiO_4}}{m_{H_4SiO_4}^{sat}} = 1 - e^{-k^{\#} t} \quad \textbf{(2.53)}$$

Further rearrangement yields:

$$m_{H_4SiO_4} = m_{H_4SiO_4}^{sat}\left(1 - e^{-k^{\#} t}\right) \quad \textbf{(2.54)}$$

The above equation form can be used in SigmaPlot (known as exponential rise to maximum model) to fit the experimental data.

2.4.2.2 Solving non-linear regression using SigmaPlot

The form of the rate equation provided in Equation (2.54) has the same form of the SigmaPlot non-linear model (exponential rise to maximum model):

$$f(x) = a_0(1 - e^{-a_1 x}) + e \quad \textbf{(2.55)}$$

The correlations between Equations (2.54) and (2.55) are:

- $f(x)$ represents $m_{H_4SiO_4}$
- x represents t
- a_0 represents $m^{sat}_{H_4SiO_4}$
- a_1 represents $k^{\#}$

By plotting the value of $m_{H_4SiO_4}$ versus time, the parameters a_0 and a_1 can be solved using the Gauss-Newton method (Chapra and Canale, 2002). The Gauss-Newton method provides solution based on determining the values of the parameters that minimize the sum of the residuals between the data and the non-linear equations (Chapra and Canale, 2002). This method requires iteration to obtain the solution. The summary of the iteration path is summarised in Appendix A.

2.5 Previous Fluid-Rock Interaction Studies

Characterization of the fluid's geochemistry is important in the evaluation of the performance of the natural geothermal systems (Grigsby et al., 1989). The importance of understanding the chemical interactions due to the injection of fluid into hot granite is crucial for problems concerning clogging caused by precipitation and heat loss caused by dissolution (Azaroual and Fouillac, 1997). Furthermore, given the large thermal gradients associated with heat extraction, considerable potential for the redistribution mass (particularly silica) may occur. Therefore the need for physical-chemical models to predict the changes and anticipate problems prior to the occurrence (Savage et al., 1992) is paramount. In addition, there are a great number of operating problems that can occur due to the chemical properties of the working brines, such as corrosion and scaling in the pipes and precipitation of minerals in the fractures (Weare and Weare, 2002). However, relatively little information is available regarding the rates and chemical mechanisms of mineral reactions in hydrothermal solutions (Posey-Dowty et al.,

1986). Furthermore, it is impossible to generalize the actual field experience of mineral deposition in geothermal systems into one consistent theory due to the vast chemical and operational differences among cases (Robinson, 1982). Consequently, many studies regarding fluid-rock interactions have been undertaken (Robinson, 1982; Savage, 1986; Savage et al., 1987; Richards et al., 1992; Savage et al., 1992; Azaroual and Fouillac, 1997; Gianelli and Grassi, 2001; Yanagisawa et al., 2005; Nishimoto and Yoshida, 2010).

In addition, many studies, particularly on the subject of quartz and feldspars dissolutions kinetics have been performed (Kitahara, 1960b; Ellis, 1968; Rimstidt and Barnes, 1980; Robinson, 1982; Lasaga, 1984; Posey-Dowty et al., 1986; Savage, 1986; Grigsby, 1989; Dove and Crerar, 1990; Tester et al., 1994; Worley, 1994; Azaroual and Fouillac, 1997; Durst and Vuataz, 2000; Icenhower and Dove, 2000; Verma, 2000a; Verma, 2000b; Gianelli and Grassi, 2001; Burton et al., 2004; Tarcan, 2005; Yanagisawa et al., 2005; Castro et al., 2006; Pfingsten et al., 2006; Nami et al., 2008; Marks et al., 2010; Brown, 2011b). Investigators determined the mineral dissolution rate data by measuring solution concentration versus time, also by weight loss method to determine the amount of mineral dissolved during the experiment (Worley, 1994). From previous investigations, key factors that affect the dissolution kinetics include temperature, pH, ionic strength, and pressure on the dissolution rate. These factors are discussed here, as well as batch and flowthrough reactor designs.

2.5.1 Temperature effects

The temperature effects on quartz dissolution have been studied extensively by many researchers (Weill and Fyfe, 1964; Fournier, 1977; Fournier and Potter II, 1982a; Tester et al., 1994; Worley, 1994; Rimstidt, 1997; Verma, 2000a; Verma, 2000b; Brown, 2011b). Many have proposed an equation to show the relationship between temperature and equilibrium silica concentration from quartz dissolution. The relationship between the silica content and temperature may be used to predict a geothermal reservoir temperature (geothermometry). Many researchers have proposed equations relating the solubility of quartz for different

temperature ranges. Fournier (1977) proposed an equation relating the solubility of quartz for temperatures between 0 – 250°C:

$$t\,^{o}_{C} = \frac{1309}{5.19 - \log C} - 273.15 \qquad \textbf{(2.56)}$$

And also for quartz (after steam loss):

$$t\,^{o}_{C} = \frac{1522}{5.75 - \log C} - 273.15 \qquad \textbf{(2.57)}$$

where: C is the silica concentration in water (mg SiO_2/kg water), and t is the temperature (°C)

Fournier and Potter II (1982b) cited in diPippo (1985) updated the previous equation and is valid for temperatures between 20°C and 340°C:

$$t = -42.196 + 0.28831 \times C - 3.6685 \times 10^{-4} \times C^2 + 3.1665 \times 10^{-7} \times C^3 + 77.034 \times \log C \qquad \textbf{(2.58)}$$

where: C is the silica concentration in mg/kg and t is the temperature (°C).

Fournier and Potter II (1982a) proposed an equation correlating the solubility of quartz in water for temperatures ranging from 25°C to 900°C at pressures up to 10,000 bars:

$$\log m = A + B(\log V) + C(\log V)^2 \qquad \textbf{(2.59)}$$

the coefficients A, B, and C are:

$A = -4.66206 + 0.0034063T + 2179.7T^{-1} - 1.1292 \times 10^{6}T^{-2} + 1.3543 \times 10^{8}T^{-3}$

$B = -0.0014180T - 806.97T^{-1}$

$C = 3.9465 \times 10^{-4}T$

where: m is the saturated silica concentration (mol/kg H_2O), V is the specific volume of pure water, and T is the absolute temperature (K).

Rimstidt (1997) proposed the following equation correlating the solubility of quartz in pure water for a temperature range between 0 – 300°C:

$$\log m = -\frac{1107.12\ (\pm 10.77)}{T} - 0.0254(\pm 0.0247) \quad \textbf{(2.60)}$$

where: m is the molal solubility of quartz and T is the absolute temperature

Verma (2000b) developed an expression along the water-vapour saturation curve for temperatures between 0 – 374°C:

$$\log SiO_2 = -\frac{1175.7(\pm 31.7)}{T} + 4.88(\pm 0.08) \quad \textbf{(2.61)}$$

where: SiO_2 represents the equilibrium silica concentration (ppm) and T is the absolute temperature (K)

Brown (2011b) suggest a correlation that is valid for temperatures between 0 – 250°C, a different form to Equation (2.56):

$$\log C = -\frac{1309}{T} + 5.19$$

where: C is the equilibrium silica concentration (mg/kg), and T is the absolute temperature (K).

In addition to the relationship between temperature and the solubility of silica, another important variable is the rate constant. According to Worley (1994), the global rate constants can be correlated with an Arrhenius-like expression. The Arrhenius equation is provided in Equation (2.62):

$$k_+ = Ae^{-Ea/RT_K} \quad \textbf{(2.62)}$$

where: k_+ = dissolution rate constant

A = frequency factor

E_a = activation energy

R = gas constant

T_K = absolute temperature

A compilation of global activation energy for quartz dissolution reported by some investigators and the data is given in Table 2.6.

Table 2.6 Compiled global activation energy

Investigator	Global activation energy (kJ/mol)	Temperature range (^oC)
Siebert et al (1963)*	79	205 – 345
Rimstidt and Barnes (1980)	67.4 – 76.6	100 – 300
Robinson (1982)	78.3 ± 18.5	150 – 250
Dove and Crerar (1990)	71 ± 9	100 – 300
Bennett (1991)	73	25 – 70
Worley (1994)	89 ± 5	25 – 625

*cited in (Worley, 1994)

Blum and Stillings (1995) cited in Chen and Brantley (1997) have reviewed the published literature for albite dissolution and concluded, that the activation energy for albite dissolution is 14.3 kcal/mol (59.8 kJ/mol). Palandri and Kharaka (2004) also compiled values of activation energies for many minerals including quartz, albite, and k-feldspars.

In addition to the quartz geothermometer, the Na-K geothermometer has been used extensively in geothermal investigations (Stefánsson and Arnórsson, 2000). The Na-K geothermometer is based on the cation exchange reaction between albite and K-feldspar (adularia) which is temperature-dependent, where the ratio of Na/K decreases with increasing fluid temperature (Karingithi, 2009).

According to Browne (1978) cited in Stefánsson and Arnórsson (2000), albite and K-feldspars often occur as secondary minerals, predominantly at temperatures exceeding 200^{o}C. Additionally, according to Giggenbach (1981) cited in Stefánsson and Arnórsson (2000), the Na^{+}/K^{+} activity ratio has been suggested to be controlled by equilibrium between the solution, low-albite and microcline.

2.5.2 pH effects

It is known that dissolution rate of quartz and feldspars are influenced by pH. The effects of pH in dissolution rate of quartz and feldspars have been studied by many researchers (Kamiya et al., 1974; Knauss and Wolery, 1988; Grigsby, 1989; Hellmann, 1994; Worley, 1994; Chen and Brantley, 1997; Bickmore et al., 2006; Hellmann et al., 2010). Many researchers have found that solution pH have a great effect on the dissolution rate, where the dissolution rate of feldspar is lowest at near neutral pH, and increases in both acid and basic regions (Chen and Brantley, 1997), which was also observed in the dissolution of quartz (Worley, 1994). The pH effect as well as temperature effect on quartz dissolution rate is displayed in Figure 2.23 (Worley, 1994) and the albite dissolution rate in Figure 2.24 (Palandri and Kharaka, 2004). The data presented in Figure 2.23 suggest that the dissolution rate increases by raising the solution pH above 5 and lowering the pH below 2, while similarly the data presented in Figure 2.24 suggest that the dissolution rate increases by raising the solution pH above 8 and lowering the pH above 4. A simple general equation expressing the influence of pH in a dissolution reaction (Chen and Brantley, 1997) is:

$$r = k\{H^{+}\}^{n} \qquad \textbf{(2.63)}$$

where: k is the rate constant (mol cm^{-2} s^{-1})

$\{H^{+}\}$: is the activity of H+ in solution

n = an empirical constant

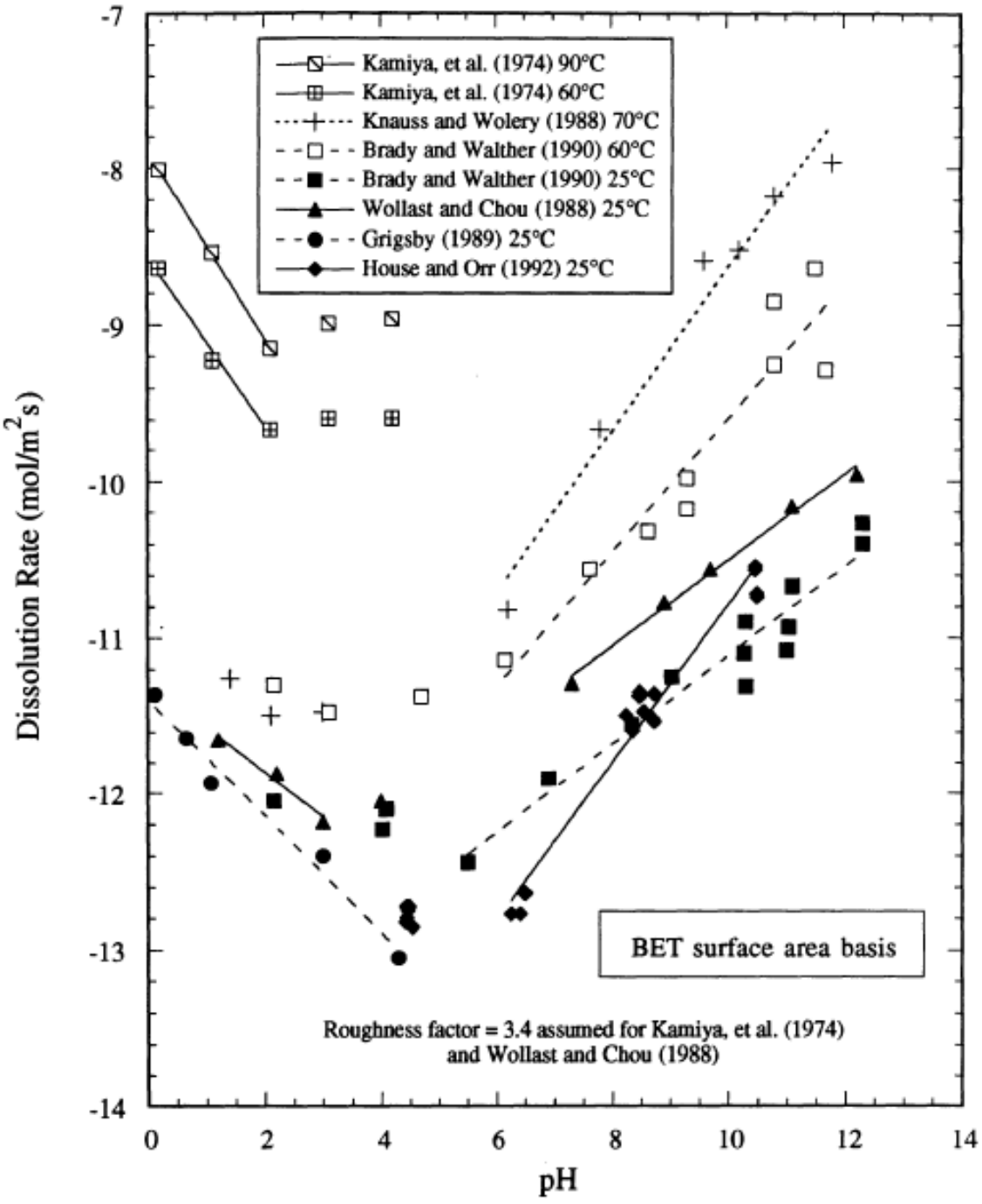

Figure 2.23 The effect of pH on the dissolution rate of quartz

Investigators carried out experiments to determine the value of the empirical constant, n. Hellman (1994) found that the absolute value of n increased from 0.2 to 0.6 as the temperature increased from 100 – 300^{o}C.

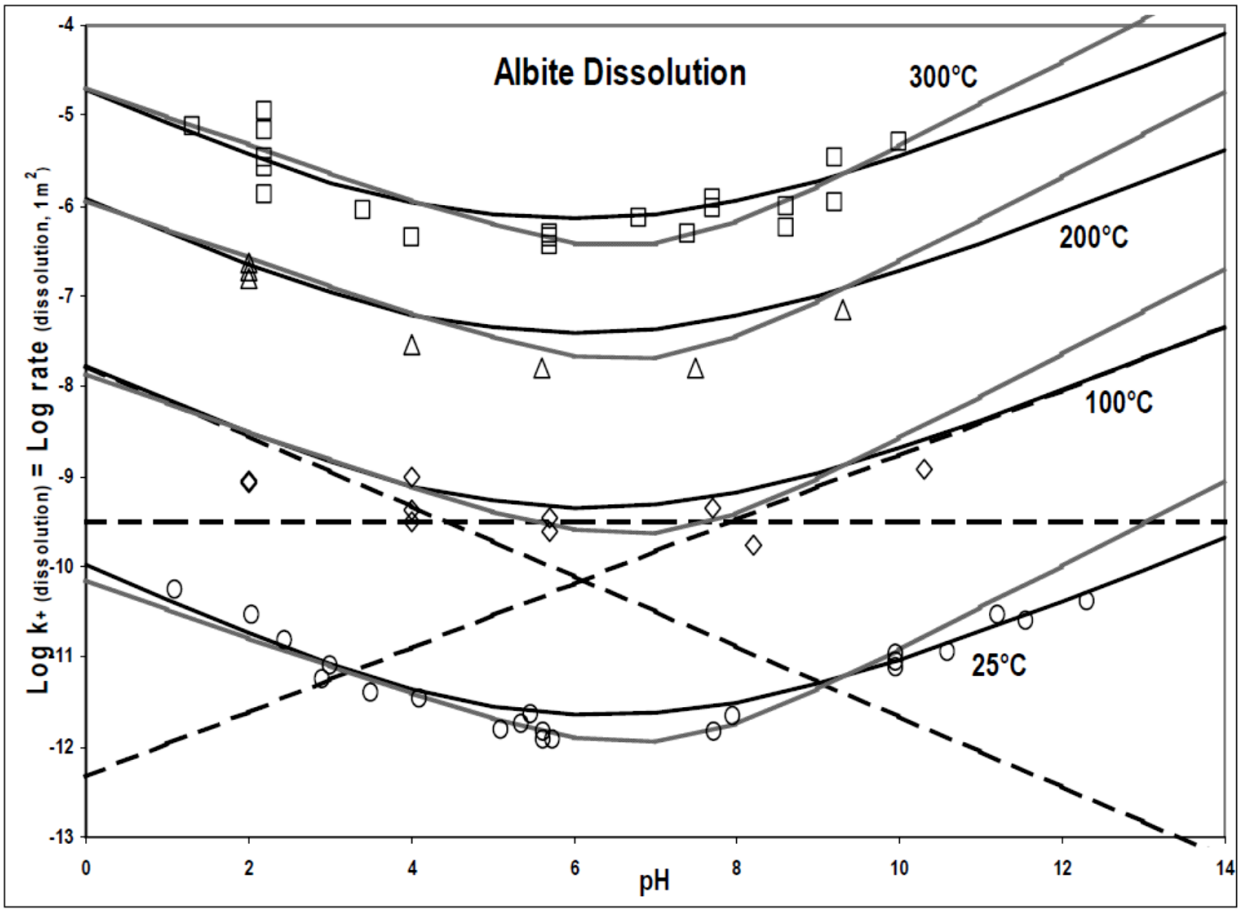

Figure 2.24 The effect of pH on the dissolution rate of albite

Knauss and Wolery (1986) suggest that the absolute value for albite dissolution at 70°C is n = 1 at pH values between 1 and 3, and n = 0 at pH values between 3 and 8. Chow and Wollast (1984) showed that the value of n = 0.5 for albite dissolution at 25°C at pH below 5.

Brady and Walther (1992) cited in Chen and Brantley (1997) suggested that the dissolution rates of minerals will become more pH dependent as the temperature increases. Chen and Brantley (1997) also summarised from the H^+ and OH^- adsorption experiments (Machesky, 1990; Brady and Walther, 1992) that increased temperature leads to increased cation adsorption and decreased anion adsorption at constant pH.

Chen and Brantley (1997) suggest that there are at least two different dissolution mechanisms for feldspar dissolution, a proton-promoted reaction in the acid region and a hydroxyl-promoted reaction in the basic section.

2.5.3 Ionic strength effects

A key factor to know where the dissolution of quartz or granite occurs to determine the dissolution rate is the composition of the surrounding aqueous solution (Worley, 1994), thus the importance of the effect of ionic strength in mineral dissolutions. Many investigators have previously studied the effect of ionic strength effects on the rate of mineral dissolutions (Ellis, 1968; Dove and Crerar, 1990; Worley, 1994; Dove, 1999; Icenhower and Dove, 2000; Davis et al., 2011).

Dove and Crerar (1990) studied the effect of NaCl, KCl, LiCl, and $MgCl_2$ (0 – 0.15 molal for a temperature range 100 – 300^{o}C) in quartz dissolution rate and found that the presence of these electrolytes increased the dissolution rate compared to using pure water. Their results showed that NaCl and KCl have the greatest impact, where the quartz dissolution rates increased by 1.5 orders of magnitude.

Brantley (2008) found that the presence of alkali or alkaline earth cations in solution at low concentration increase the dissolution rate of quartz and amorphous silica by factors up to 100 times at low and high temperatures. In addition, she also concluded that the presence of aqueous Al^{3+} inhibits the dissolution of albite (Chen and Brantley, 1997; Chen, 2000) and quartz (Dove, 1995).

Dove (1999) studied the dissolution kinetics of quartz dissolution in mixed cation solutions (dilute mixtures of magnesium, calcium, barium and sodium chloride salts) in near neutral pH at temperatures ranging from 175 to 295^{o}C. She found that in single salt solutions the dissolution rate increased in the order: $Mg^{2+} < Ca^{2+} \approx Na^{+} < Ba^{2+}$. For mixtures of two salts, the dissolution rate was slowed when magnesium is introduced to solutions containing sodium, calcium or

barium ions. A competitive adsorption-rate model was used to quantify the behaviour in salt mixtures. Dove et al. (2005) cited in Brantley (2008) continued her study and proposed a model to explain why salt solution increases the quartz dissolution rate but inhibit feldspar dissolution.

2.5.4 Pressure

Pressure is another factor that influences the dissolution of silica in water. Morey et al. (1962) produced a graph showing the solubility of quartz (ppm) at temperatures ranging from 25 – 300^{o}C at saturated vapour pressure and 1000 bar. Worley (1994) compiled quartz solubility data from various studies and generated a similar plot provided in Figure 2.25.

Fournier and Potter II (1982a) proposed an equation correlating the concentration of silica in water at various temperatures and pressures. The correlation is provided in Equation (2.59). This correlation was used to illustrate the change of dissolved silica concentration at different pressure. It may be observed from Figure 2.26 that the concentration of silica dissolved in water increases with increasing pressure. The values of quartz solubilities generated from this correlation were close to the values reported by Vala Ragnarsdóttir and Walther (1983) who performed a reversed quartz solubility experiment. The solubility of quartz (in terms of log molality) at 250^{o}C and at 250, 500 and 1000 bars were -2.126, -2.087 and -2.038, respectively. From their experimental results, Vala Ragnarsdóttir and Walther (1983) combined other reported quartz solubility measurements and generated a pressure sensitive silica geothermometer equation applicable to solutions in equilibrium with quartz at temperatures between 180^{o}C to 340^{o}C that has undergone adiabatic steam loss.

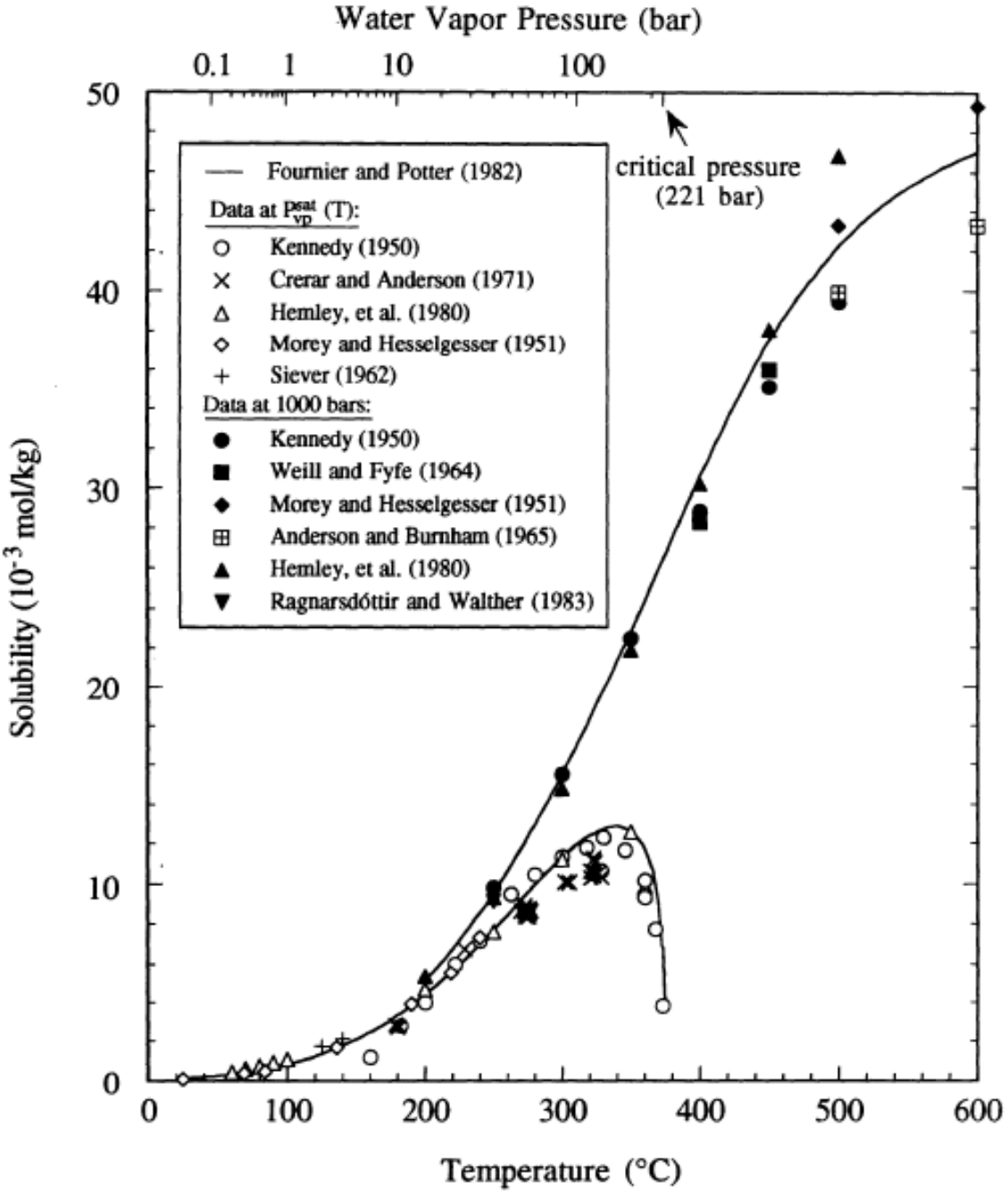

Figure 2.25 Compilation of quartz solubility data at saturated vapour pressure and at 1000 bars (Worley, 1994)

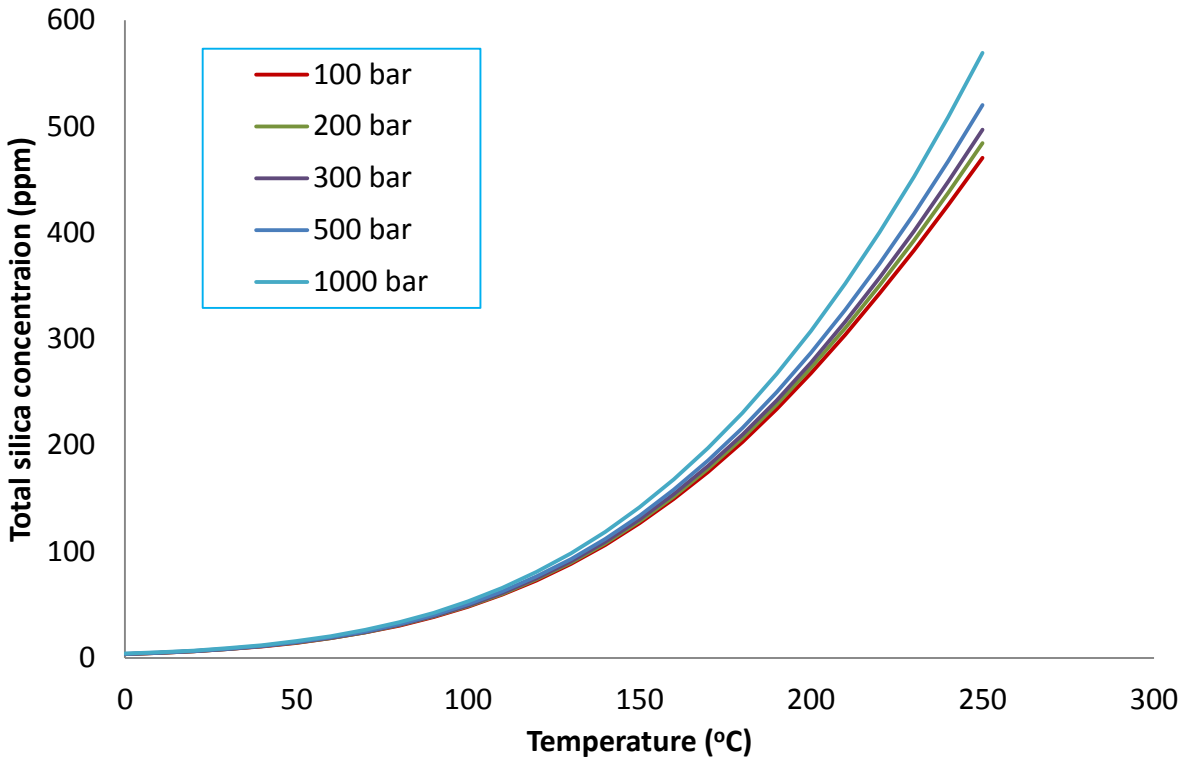

Figure 2.26 Pressure effect in quartz dissolution using the correlation by Fournier and Potter II (1982a)

2.5.5 Reactor design

Many researchers have conducted fluid-rock interactions to investigate the dissolution rate of mainly quartz and feldspars. These investigations have been performed in both batch reactors and continuous flow reactors. Prior to 1984, fluid-rock interaction studies were performed in batch reactors (Kitahara, 1960b; Siebert et al., 1963; Weill and Fyfe, 1964; Rimstidt and Barnes, 1980; Robinson, 1982). The basic equation to obtain the dissolution rate (r_{net}) in a batch reactor is:

$$\int_0^t r_{net}\,dt = m_{H_4SiO_4}(t) - m_{H_4SiO_4}(0) \qquad \textbf{(2.64)}$$

where: $m_{H_4SiO_4}(0)$ = initial concentration (mol/kg)

$m_{H_4SiO_4}(t)$ = final concentration (mol/kg) after time t (s)

A better approach to achieve a more accurate dissolution rate is to fit the experimental data (dissolved silica concentration) to a rate law. As an example, Robinson (1982) used a batch stirred autoclave for quartz dissolution experiments and developed a global rate law. The schematic diagram of his batch stirred autoclave is provided in Figure 2.27. The general relationship for dissolution rate in a closed vessel is provided in Equation (2.25). According to Robinson (1982), the description of the autoclave reactor is: the reactor vessel is a Pressure Products Industries 316SS Magnetic Drive Reactor for agitation with rotation speed from 200 – 900 rpm with a working volume of 1 L. The electrical resistance heating jacket is controlled using an Athena temperature controller which receives temperature signal from a thermocouple placed in the thermocouple well. The reactor has a sampling valve connected to a tube immersed in cold water bath to allow cooling of the liquid sample below boiling point.

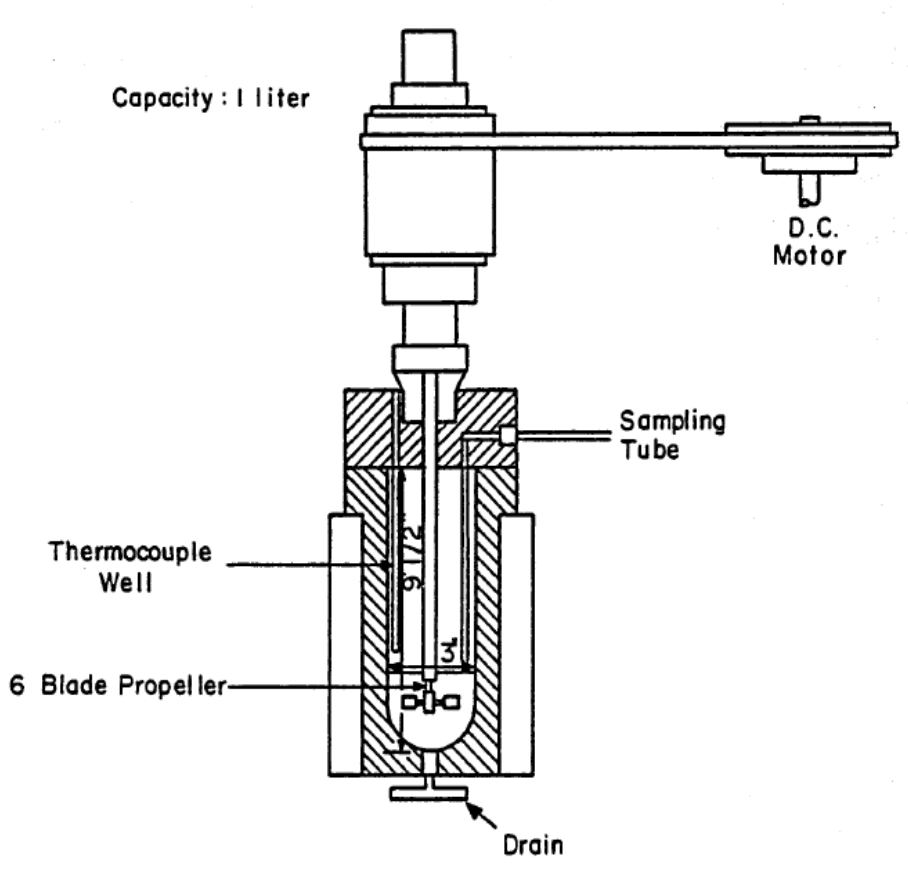

Figure 2.27 Stirred autoclave reactor used by Robinson (1982)

Batch reactors are relatively easier to operate and more precise when determining slower reaction kinetics, however, some disadvantages include the need to undertake complex data analysis coupled with a requirement for more data, thereby the increasing the data collection time (Worley, 1994).

Since 1984, continuous flow reactors have been used for fluid-rock interaction studies (Chou and Wollast, 1984; Knauss and Wolery, 1988; Grigsby, 1989; Dove and Crerar, 1990; Worley, 1994; Azaroual and Fouillac, 1997). Generally, the continuous flow reactors that have been used were assumed to behave as ideal continuous-flow stirred tank reactors (CSTR) where perfect mixing exists and therefore the outlet composition equals to the composition at any location in the reactor (Worley, 1994). When density and flow are assumed constant, the general mass balance is:

$$r_{net} = \frac{\left(m^{out}_{H_4SiO_4} - m^{in}_{H_4SiO_4}\right)}{\tau} \qquad \textbf{(2.65)}$$

where: r_{net} = the bulk rate reaction (mol/kg.s)

$m^{in}_{H_4SiO_4}$ = concentration of the inlet stream (mol/kg)

$m^{out}_{H_4SiO_4}$ = concentration of the outlet stream (mol/kg)

τ = residence time of the reactor (s)

= liquid mass in the reactor/mass flow rate through the reactor

Worley (1994) used a titanium continuous-flow stirred tank reactor to study the kinetics of quartz dissolution and granite dissolution, whilst expanding the temperatures and pressure ranges (200^{o}C and 600 psig). A schematic of the upgraded titanium continuous flow stirred tank reactor is provided in Figure 2.28. The description of the upgraded experimental apparatus used by Worley (1994): The reactor was constructed from titanium with a 2.4 L working volume and was wrapped in heating tape and insulated to maintain isothermal conditions. It has a titanium basket with a 0.45 L working volume made from 50 mesh rigid wire screen to hold the samples, with baffles on the inside surface. This basket may be used in two modes of

operation, stationary and spinning. A modified Autoclave Engineers magnetic drive unit was used to rotate the titanium basket. A 60 L propylene feed tank was used to hold and supply deionized water and a metering pump by Fluid Metering Inc. was used to continuously feed to the reactor. An electrically heated preheater tube was installed for the feed stream, and a water-cooled heat exchanger for the product stream.

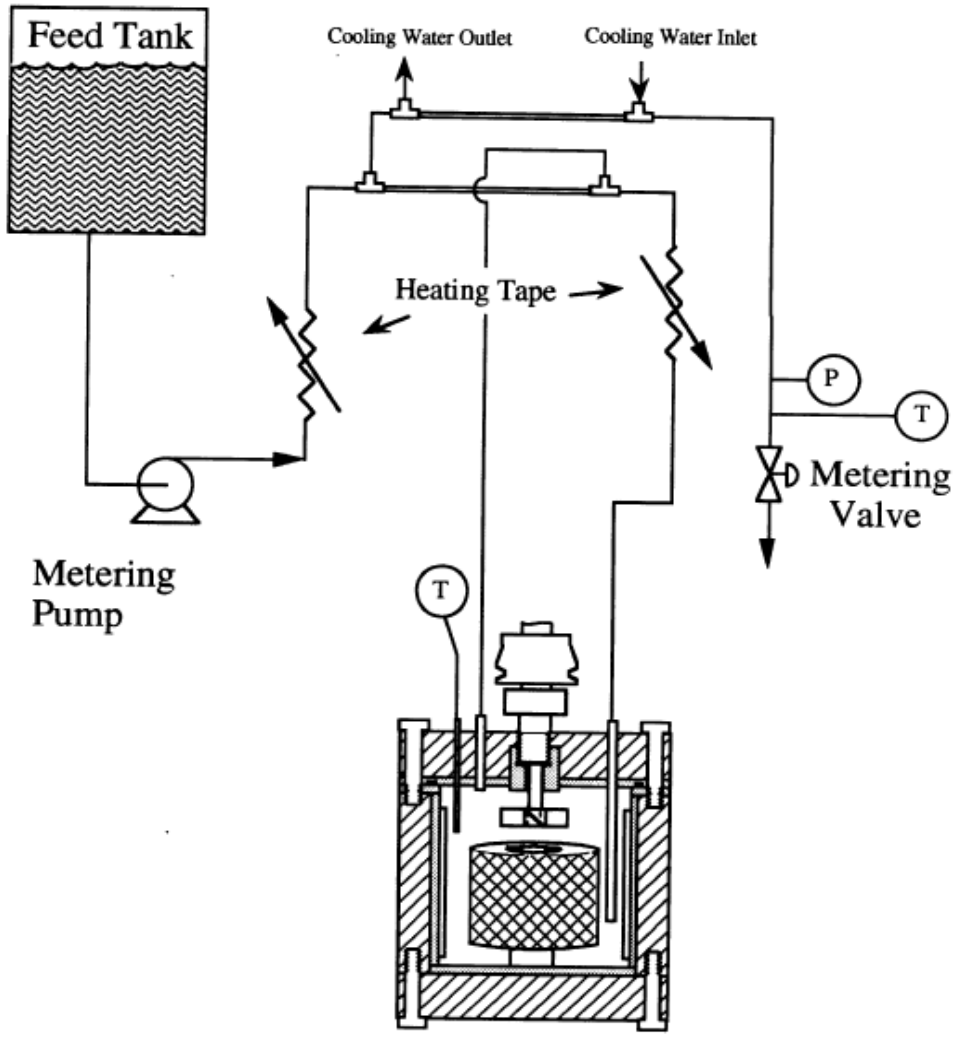

Figure 2.28 Titanium continuous-flow stirred tank reactor used by Worley (1994)

A fluid-rock interaction study of the Soultz-sous-Forets geothermal site in France was performed by Azaroual & Fouillac (1997). Their flow through reactor set up is provided in Figure 2.29.

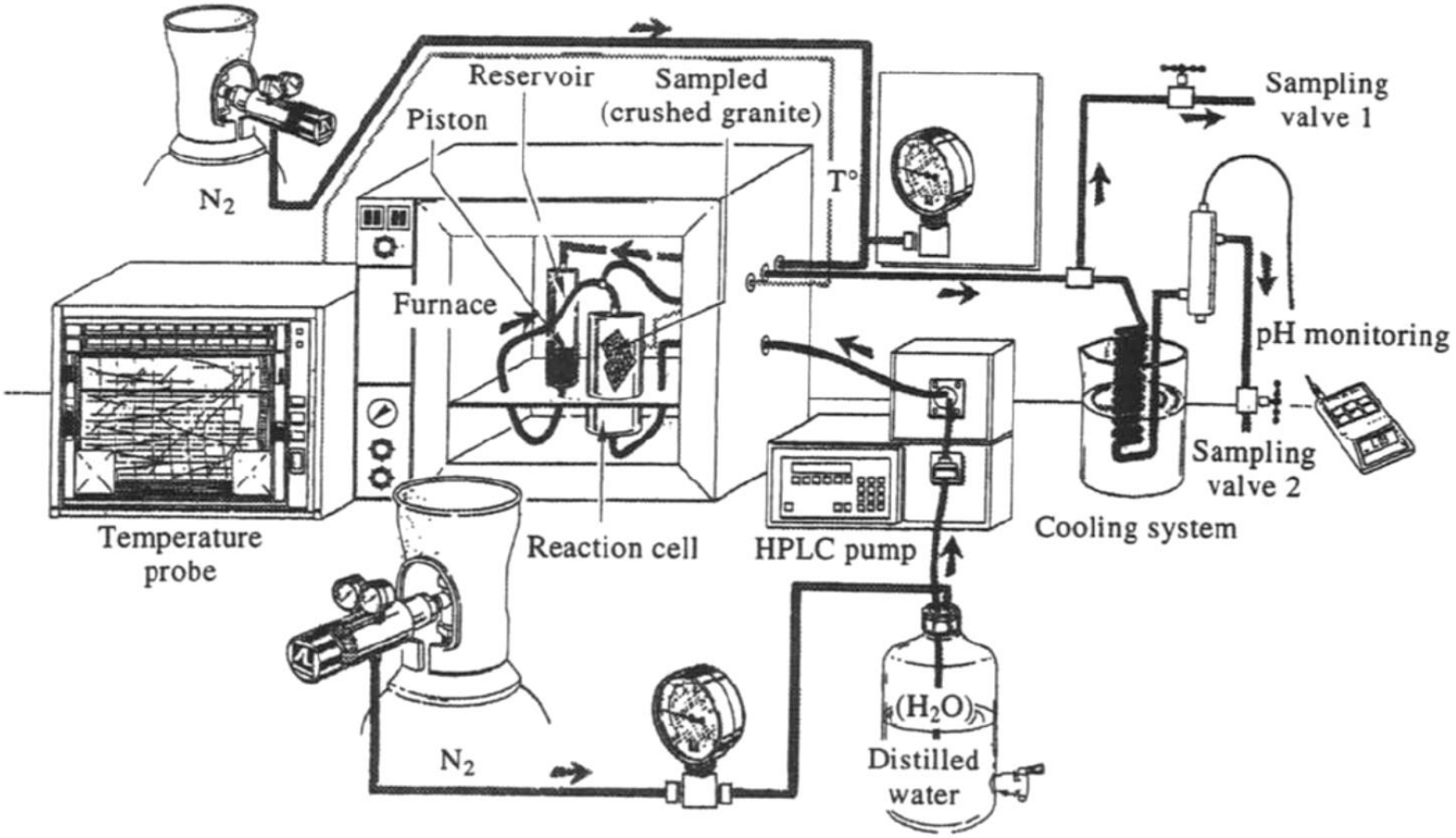

Figure 2.29 Experimental apparatus used by Azaroual & Fouillac (1997)

These fluid flow systems have been preferred to batch systems as fluid sampling does not affect the fluid-rock ratio and fluid chemistry can be monitored throughout the duration of the experiment without affecting the operating conditions. The description of the experimental system used by Azaroual and Fouillac (1997): All components of the system used inert materials PEEK (Poly-Ether-Ether Ketone). High performance liquid chromatography (HPLC) pump was used to circulate the reacting solution, which the flow rate can be adjusted to 10 mL/min. A titanium reaction cell containing the rock sample was placed in a furnace having a reservoir to temporary store the fluid after flowing through the reaction cell and before sampling. Posey-Dowty et al. (1986) pointed out that this system behaves as a plug flow system.

Chapter 3 Field Sampling at Habanero 3 Well, Cooper Basin

A visit to the Habanero geothermal site was initially undertaken as part of the project. This opportunity was used to obtain samples of the host rocks, and fluids from the Habanero 3 well head in the Cooper Basin. The results of this investigation provided valuable information for the experimental design of future fluid-rock interaction studies. This chapter summarises the method of analysis and results of the host rock and fluids from the Habanero 3 well.

3.1 Materials and methods

The key material derived for these experimental studies was the nature of the hot rocks. The hot rocks samples were provided by Geodynamics Ltd. from the Habanero No. 3 well. These samples were drill cuttings obtained from the spinner cage from a depth of 4000 m (Wyborn, 2008). The rock samples were analysed under a petrographic microscope and studies were also undertaken with a scanning electron microscope (SEM) to observe the mineralogical compositions. Finally, X-ray diffraction (XRD) studies were also performed to determine the composition of the rock sample.

A water sample was taken from Habanero 3 well head. This well produces water at a temperature of 200^{o}C and pressure 4000 - 6000 psi (275 – 415 bar). The water sample was acquired by extracting the high pressure high temperature fluid from the well head using ¼ inch diameter stainless steel sampler connected to a cooling coil, flashing the fluid to atmospheric pressure and venting the liquid to ample bottles (St. Clair, 2008). The water samples were sent to AWQC (Australian Water Quality Centre) for analysis. The analyses include alkalinity test conducted by automated acidimetric titration, chloride and reactive silica concentrations were

determined by Automated Flow Colorimetry, and the concentration of metals were determined by ICP (Inductively Coupled Plasma) Spectrometry.

A gas sample obtained from the field was a high pressure fluid sample taken from the same sampling point of the water sample. The gas was captured using a high pressure sampling vessel (Swagelok) connected directly to the ¼ inch stainless steel sample point without using the cooling coil. The resulting sample consisted of two phases, vapour and liquid. Initial analysis was performed only on the gas phase. This analysis was carried out by Amdel Pty. Ltd. (a NATA registered laboratory). The gas analysis method (Fordham, 2008) was based on ASTM D1945-96 and relied on the conventional practice in gas chromatography (GC) applications. The analysis was conducted at atmospheric pressure and 15^{o}C. The procedure of the analysis followed the guideline proposed by Fordham (2008). A brief summary of the procedure follows: the gas was collected in an evacuated gas bag and run on a gas chromatograph containing a packed column, thermal conductivity detector (TCD) and flame ionization detector (FID). The sample and a standard gas were analysed using the same procedures and reported on a molar basis. Two different columns were used; a Poropak column for determination of the hydrocarbons and carbon dioxide, while a molecular sieve column was used to measure the nitrogen and oxygen, hydrogen and helium concentrations. Argon was calculated by running the oxygen sample on gas chromatography using both helium and argon as carrier gases, and calculating the difference. The results are shown in Section 3.2.

3.2 Preliminary results and discussions

From the analysis results, elements that dissolved in the circulating water and the nature of salinity or corrosiveness of the circulating water were determined. This work allowed us to develop potential preventative measure to reduce the effect of the fluid-rock interaction (e.g. scale build up or corrosion).

3.2.1 Habanero well outlet fluid chemistry

This section presents the outlet fluid chemistry obtained from Geodynamics Habanero well geothermal site. Table 3.1 to Table 3.6 was taken from an Environmental Impact Report by Iliescu (2004).

Table 3.1 Habanero 1 water analysis

Date collected	MUD May	13/5/03	13/5/03	15/5/03	15/5/03	15/5/03
Hydroxide as OH	<1	<1	<1	<1	<1	<1
Carbonate as CO_3	<1	<1	<1	<1	<1	<1
Bicarbonate as HCO_3	10300	2099	2099	2279	2219	2279
Total Alkalinity (Calc as $CaCO_3$)	8500	1720	1720	1868	1819	1868
Chloride as Cl	11000	11188	11448	11233	11177	10959
Nitrate as NO_3	<1	<1	<1	<1	<1	<1
Sulfate as SO_4	3500	292	260	222	223	219
Total Anions		13579	13807	13734	13619	13457
Total Anions meq/L		355.64	362.30	358.40	355.86	350.62
Total silicon as SiO_2	60	214	193	148	133	124
Potassium as K	2900	1190	1170	1145	1040	1130
Sodium as Na	11500	6890	6820	6950	6550	6850
Barium as Ba	100	1	<1	2	1	<1
Calcium as Ca	210	63	69	75	69	74
Iron as Fe	120	157	105	318	275	360
Magnesium as Mg	50	14	23	14	14	18
Strontium as Sr	7	<1	4	5	5	6
Aluminum as Al	2	2	2	<1	<1	<1
Total Cations		8315	8191	8509	7954	8438
Total Cations meq/L		342.87	337.64	353.71	331.00	351.50
Calculated TDS		20928	20608	20608	20416	20352
Conductivity at 25^{o}C (µS/cm)		32700	32200	32200	31900	31800
Resistivity at 25^{o}C (MOhm)		0.31	0.31	0.31	0.31	0.31
pH	7.3	7.4	7.5	6.5	6.5	6.5

Table 3.2 Habanero 1 water analysis (cont.)

Date collected	26/7/03	MUD July	26/7/2003 (Mixed with mud filtrate)	3/8/2003 8260 strokes	3/8/2003 8340 strokes
Hydroxide as OH	<1	<1	<1		
Carbonate as CO_3	<1	<1	<1		
Bicarbonate as HCO_3	2183	4000	3094		
Total Alkalinity (Calc as $CaCO_3$)	1789	3300	2536	1700	1700
Chloride as Cl	10715	5000	7062	9400	9200
Nitrate as NO_3	2	<1	<1		
Sulfate as SO_4	33	450	280	150	110
Total Anions	12933		10436		
Total Anions meq/L	338.34		255.49		
Total silicon as SiO_2	n.d.		n.d.	74	86
Potassium as K	786	300	430	820	830
Sodium as Na	5910	4500	4680	6300	6100
Barium as Ba	2	3	10	0.39	0.43
Calcium as Ca	207	200	170	76	79
Iron as Fe	94	5	47	4	15
Magnesium as Mg	29	30	25	17	17
Strontium as Sr	13	4	5		
Aluminum as Al	<1	<1	<1		
Total Cations	7041		5367		
Total Cations meq/L	295.26		227.89		
Calculated TDS	19840		15168		
Conductivity at 25^{o}C (µS/cm)	31000		23700		
Resistivity at 25^{o}C (MOhm)	0.32		0.42		
pH	6.5	8.5	7.6	7.5	7.6

Table 3.3 Habanero 1 gas analysis

Gas (% vol.)	15/5/03	15/5/03
N	4.18	1.86
He	0.95	0.40
CO_2	83.09	89.45
CH_4	11.70	8.27
Ar	<0.01	0.01
O	0.07	<0.01
CO_2/CH_4	7.1	10.8

Table 3.4 Habanero 3 production well head condition

Conditions	1	2	3
Well-Head temperature (^oC)	198	205	205
Separator Pressure (bar gauge)	1.24	1.33	1.33

Table 3.5 Habanero 3 gas analysis

Gas (% vol.)	1	2	3
CO_2 (total)	82.68	80.78	81.77
H_2S	0.47	0.60	0.51
Ar	0.04	0.04	0.04
He	0.89	0.95	0.90
H_2	0.04	0.03	0.03
CH_4	12.11	13.58	12.96
N_2	3.78	4.03	3.80

Table 3.6 Habanero 3 water analysis

HABANERO 3 Well	1	2	3	4	5
Reservoir pH at 250^{o}C	5.92	5.94	5.96	n.a	n.a
Elements (units in mg/L)					
Total NH_3	1.96	2	2	n.a	n.a
Sb	3.1	2.6	2.6	n.a	n.a
As	2.6	2.7	2.7	n.a	n.a
Ba	n.a	n.a	n.a	n.a	n.a
B	196	204	204	208	199
Ca	23.9	22.7	22.7	30	32
Cs	41.8	43.7	43.7		
Cl	7346	7554	7554	7336	7654
F	15.6	16.1	16.1		
Li	187	189	189	191	202
Mg	0.23	0.24	0.24		
K	569	558	558	627	638
Rb	14.6	15.3	15.3		
Si (as SiO_2)	457	449	449	474	462
Na	3759	3835	3835	3898	4044
SO_4	36.7	31.9	31.9	n.a	n.a
U	< 0.00036	< 0.00036	< 0.00036	n.a	n.a

Fluid analyses were conducted to obtain a more recent data. The fluid was sampled from the hot dry rock geothermal site in Cooper Basin, Habanero 3. The gas analysis was performed by Amdel and the water analysis was undertaken by the Australian Water Quality Centre (AWQC). The fluid analyses results are shown in Table 3.7 and Table 3.8, respectively.

Table 3.7 Habanero 3 gas analysis by AMDEL

Gas	% vol.
CO_2 (total)	27.99
H_2S	n/a
Ar	0.23
He	2.99
H_2	0.09
CH_4	39.68
N_2	26.38

Table 3.8 Habanero 3 water analysis by AWQC

HABANERO 3	1	2	Average
Elements (units in mg/L)			
total NH_3	0.288	0.269	0.2785
Sb	1.77	1.97	1.87
As	0.005	0.003	0.004
Ba	13.6	18.4	16
B	223	222	222.5
Ca	26.6	24.3	25.45
Cl	8110	8360	8235
F	17	17	17
Li	246	251	248.5
Mg	0.5	0.4	0.45
K	637	650	643.5
Si (as SiO_2) reactive	**150**	**156**	**153**
Na	3790	3830	3810
SO_4	37.2	34.8	36
U	< 0.005	< 0.005	<0.005

Comparison was made between the Habanero 3gasr analysis from the Environmental Impact Report and Amdel. The gas analysis results from Amdel showed a lower CO_2 concentration and a higher N_2 concentration compared to the values reported in the Environmental Impact Report. This indicates that the CO_2 may have leaked out from the high pressure sampling cylinder and air has contaminated the sample.

Comparison was also made between the Habanero 3 water analysis from the Environmental Impact Report and AWQC. It is seen that most of the elements were in the same range; however the Si concentration from the AWQC result was quite low, since only the reactive silica was measured.

3.2.2 Habanero rock analysis

A petrographic analysis of the Habanero 3 rock samples were carried out using an SEM (scanning electron microscope) at Adelaide Microscopy Centre. Figure 3.1 shows SEM images of the rock sample from various points. Three polished thin sections were prepared and a petrographic description was prepared with the assistance of Mr. Wally Fander of the South Australian Museum. The initial assessment concluded that the rock sample from Habanero 3 appears to be a feldspar syenite composed chiefly of albite, near end member composition and microcline which has a mottled texture with little to no quartz. The feldspars are variably (incipiently to extensively) veined and replaced by patches of fine grained cloud carbonate with a manganese rock composition. Microcline appears more susceptible to replacement than the albite. The rock also contains euhedral crystals of pyrite, small patches of sphalerite, fluorapatite and a number of other accessory minerals. Later analysis revealed that the rock is actually a quartz-rich granite and the fragments examined by Mr. Fander must have been from a feldspar-rich vein.

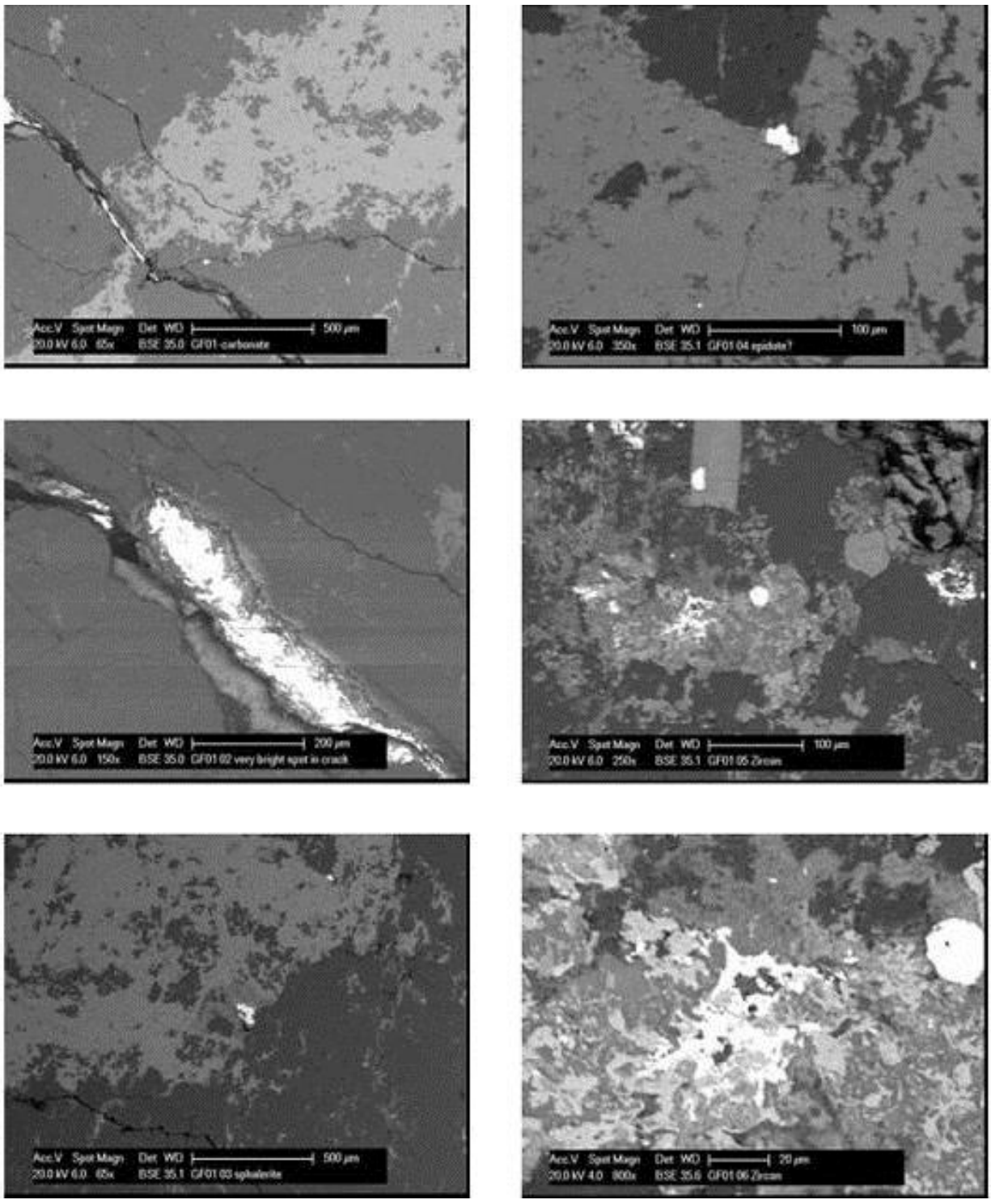

Figure 3.1 Back-scattered SEM image of Habanero 3 well rock sample from various points

Mineralogical studies were carried out to observe the components of the rock sample. X-ray diffraction (XRD) was carried out by The Commonwealth Scientific and Industrial Research Organization (CSIRO) and using TOPAS software for quantification. The XRD results are provided in Table 3.9. X-ray Fluorescence (XRF) studies were also carried out to observe the mineralogy of the sample and used for comparison with the XRD analysis. The XRD results are provided in Table 3.10. It can be seen that the XRF results complemented the XRD analysis. The major components in the XRD results are quartz (SiO_2), albite ($NaAlSi_3O_8$) and K-feldspar ($KAlSi_3O_8$), where this can be confirmed with the XRF result showing high concentrations of SiO_2, Al_2O_3, Na_2O and K_2O.

After the field sampling, dissolution and rock-fluid interaction experiments were conducted in the laboratory. The experimental techniques are explained in Chapter 4 and experimental result in Chapter 5.

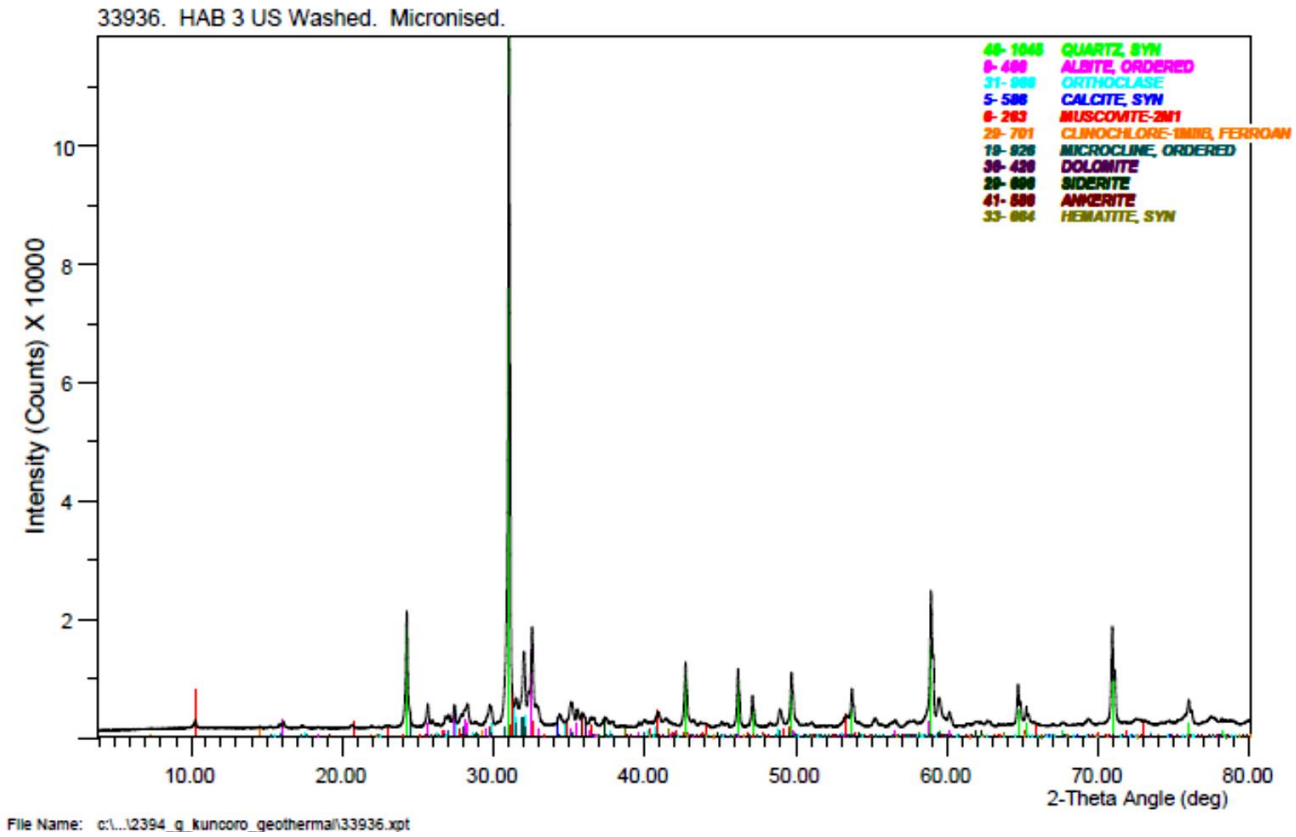

Figure 3.2 XRD pattern of Habanero 3 rock sample after ultrasonically cleaned

Table 3.9 Quantitative XRD analysis using TOPAS

Element	(wt. %)
Quartz (SiO_2)	50
Albite ($NaAlSi_3O_8$)	23
Orthoclase ($KAlSi_3O_8$)	2
Microcline ($KAlSi_3O_8$)	19
Calcite ($CaCO_3$)	1
Muscovite ($KAl_2(AlSi_3O_{10})(OH)_2$)	3
Dolomite/Ankerite ($Ca(Mg\ Fe)(CO_3)_2$)	1
Siderite ($FeCO_3$)	1
Total	100

Table 3.10 XRF analysis

Elements	XRF Major (1)	XRF Major (2)	XRF Major (3)	Average
SiO_2 %	77.27	76.68	77.24	77.06
Al_2O_3 %	10.62	10.44	10.44	10.50
Fe_2O_3 %	1.46	1.23	1.31	1.33
MnO %	0.08	0.05	0.07	0.06
MgO %	0.09	0.00	0.02	0.04
CaO %	0.60	0.44	0.47	0.50
Na_2O %	2.54	2.37	2.44	2.45
K_2O %	4.45	4.23	4.27	4.32
TiO_2 %	0.07	0.02	0.06	0.05
P_2O_5 %	0.01	0.00	0.01	0.01
SO_3 %	0.15	0.12	0.09	0.12
LOI %	2.10	3.11	3.14	2.78
Total %	99.44	98.69	99.54	99.22

XRF carried out at University of Adelaide, School of Earth and Environmental Sciences (by John Stanley)

Chapter 4 Experimental Techniques

The results from the Habanero 3 field sampling (provided in Chapter 3) showed that the reservoir of the Habanero geothermal system lies in the granitic body of the Earth's crust, which has quartz and feldspars as the major components. Quartz and feldspars have been studied extensively by many researchers and their findings complement this study. This study focuses on granite dissolution, involving multiple mineral components. Within this chapter, the material selection, material preparation and general methods employed in this study are discussed.

4.1 Materials

The two main components for this study are the rock samples and the circulating fluid. It is essential to use rock samples that represent the reservoir at Habanero 3 well in Cooper Basin geothermal site. Unfortunately, it is impossible to have samples with a constant composition due to the vast size of the geothermal site and the depth of the hot rocks. Consequently, representative samples were chosen and these were assumed sufficient to adequately describe the nature of the reservoir and minimize any sample variance. The samples were drawn from 10 kg of drill cutting sampled from Habanero 3 site. These drill cuttings were provided by Geodynamics Ltd from an approximate depth of 4000 m. The samples were washed with purified (Milli-Q) water. Milli-Q water was used because it possessed an extremely low mineral content, thereby minimizing any contaminants. The purified water was obtained by feeding RO (reverse osmosis) treated water to a Milli-Q apparatus (brand: Milli-Q Academic by Millipore), having 18.2 MΩ electrical resistivity. Nitric acid (4% vol.) was used for liquid sample preservation.

4.2 Sample Preparation

The mineral preparation steps include: crushing into smaller particle size to increase the surface area followed by separation to different size fraction, with subsequent cleaning to remove fine particles and surface contaminations. Previous researchers have used different methods to remove the very fine particles from the sample. According to Holdren and Berner (1979), the fine particles could be removed by ultrasonically cleaning of the sample with acetone and then etched with 5% HF/0.09 N H_2SO_4. A study by Azaroual and Fouillac (1997) suggested that in order to remove ultrafine particles, the solid should be washed with a solution of HF (5%) and H_2SO_4 (0.1 N) for 20 minutes. Another study (Chou and Wollast, 1984) verified with scanning electron microscopy (SEM) that the fine particles were removed by several ultrasonic washing with acetone. However, a study by Lin and Clemency (1981) revealed that washing with HF or organic solvents removes cations such as Na and K, thereby disturbing the surface chemical composition.

For this study, the sample preparations protocol was as follows: the drill cutting samples received from Geodynamics Ltd were tumbled mixed and a random portion of the rock sample was selected. This portion was then ground using a ceramic mortar and pestle, and subsequently it was sieved to obtain a size distribution 100 – 200 µm. The rock samples were ultrasonically cleaned with pure water to remove very fine particles. Cleaning with acid or other solvents may have an undesired impact on the rock sample hence this practice was avoided (Lin and Clemency, 1981). Approximately 5 g of rock sample and 200 mL of purified water (Milli-Q) were prepared in a 250 mL flask and placed in an ultrasound bath (brand: Soniclean) for 15 minutes at high ultrasonic power setting. After the treatment, the Milli-Q water was decanted and replaced with fresh 200 mL Milli-Q water. This was repeated for three sets. After three sets have been completed, the rock sample was then dried in an oven at 120^{o}C for 48 hours and cooled and kept in a dessicator. The resulting cleaned samples were then mixed and stored in a dessicator. Other sample size distributions, 40 – 60 µm and 200 – 400 µm, were also prepared and cleaned according to the aforementioned protocol. An image of

100 – 200 µm sample size granite after ultrasonically cleaned is provided in Figure 4.1. It is seen that no ultrafine particles adhere to the surface of the granite.

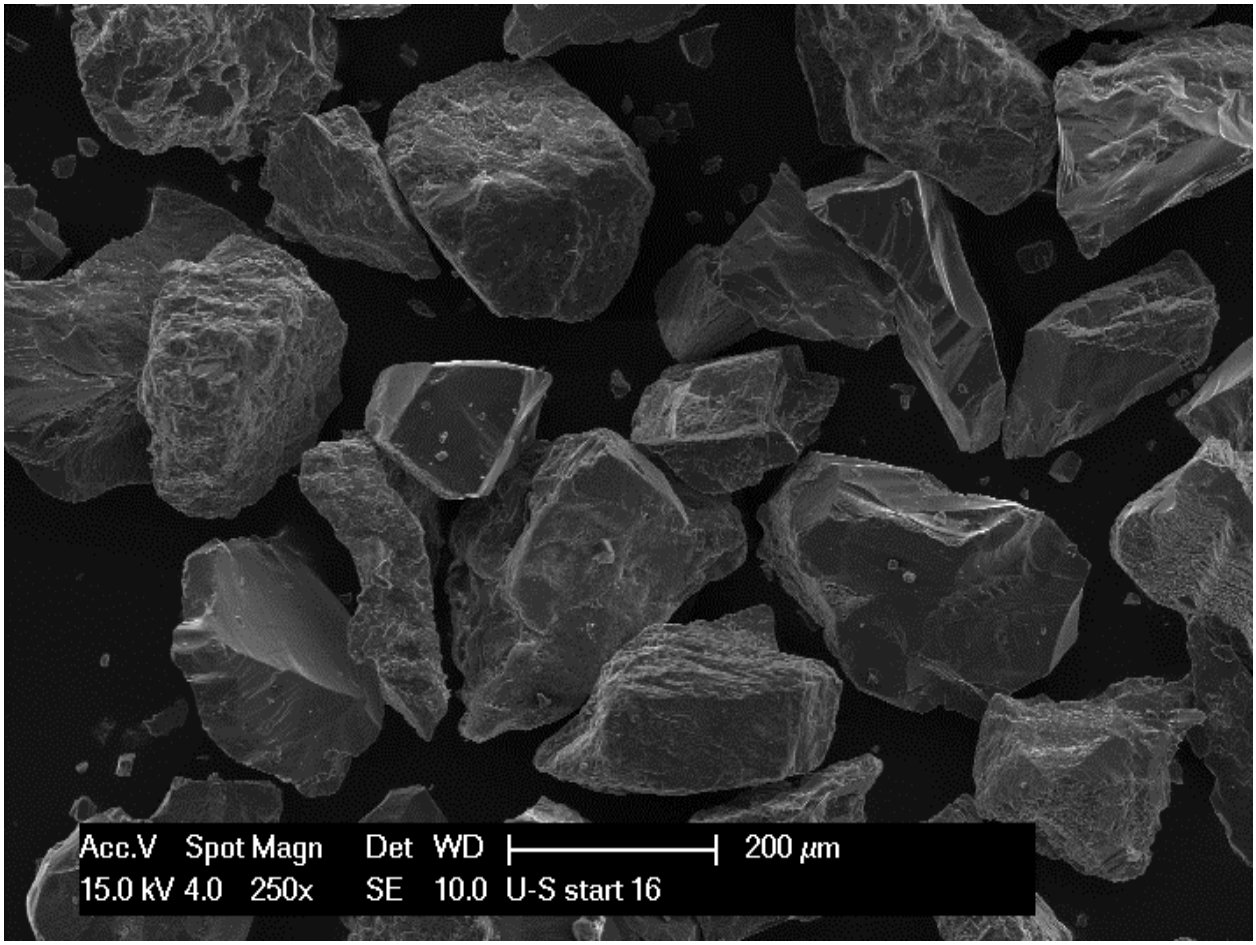

Figure 4.1 Surface of granite particles after ultrasonically cleaned (100-200 µm)

4.3 Mineral Characterisation and Surface Area Basis

Mineral characterisation is an important phase in determining fluid-rock interaction. Several different methods have been proposed by previous researchers to characterise bulk mineral compositions. As an example, Lauglin and Eddy (1977) used a standard polarizing microscope and manual point counter to obtain their modal analyses (mineral phases/composition). Knauss and Wolery (1986) used electron microprobe to determine the bulk composition of albite and muscovite. Ganor et al., (2005) also used electron microprobe to determine the mineral

composition of Elat granite. Mineral identification in a sample is of fundamental importance in mineral characterisation studies. X-ray diffraction (XRD) and x-ray fluorescence (XRF) have been used for mineral identification in sedimentary rocks (Till and Spears, 1969). XRD is used to identify and also quantify the mineral components, and XRF provides the elemental compositions in terms of metal oxides.

The mineral composition of the ultrasound cleaned sample in this study was identified using XRD patterns recorded at the Science Centre of the South Australian Museum and at Commonwealth Scientific and Industrial Research Organisation (CSIRO), and quantified using TOPAS software by Mark Raven at CSIRO. XRF analyses were also undertaken to obtain the elemental composition in terms of metal oxides for comparison. XRF analyses were carried out by John Stanley at the School of Earth and Environmental Sciences of The University of Adelaide.

Surface morphology is also an important parameter in mineral characterisation. The observation of the surface morphology may provide qualitative information of the samples. Worley (1994) used scanning electron microscope (SEM) to observe the surface morphology of quartz and granodiorite. Relating closely to surface morphology is the mineral surface area. Determining the active surface area is crucial for mineral dissolution studies. Many researchers have characterised mineral surface area using the Brunauer-Emmet-Teller (BET) adsorption method as well as geometric surface area (assuming particles are smooth spheres). Helgeson et al. (1984) stated that using BET method may provide an overestimation of the active surface area. In addition, Gautier et al., (2001) have discussed the proposition that the geometric surface area may provide a more accurate parameter for dissolution rate estimations. Hodson (2006) summarised in his study of anorthite and biotite dissolution that the BET surface area is the most appropriate term for laboratory based dissolution rate normalization, whilst geometric and geometric-edge surface area should be measured for field dissolution studies. Therefore, both measures of surface area basis (e.g. geometric and BET) are important and have been considered in this study.

This study used Philips XL30 FEGSEM with EDAX EDS located in the Adelaide Microscopy Centre at University of Adelaide to observe the surface morphology of the granites. The XL30 was used to observe the surface of the samples comparing unwashed samples, ultrasonically cleaned samples and samples after batch and flow-through experiments under secondary electron (SE) detector. Additionally, XL30 is used to observe the mineral phases in the granite under backscatter electron (BSE) detector and also EDAX analyses to identify and semi quantify the composition of the samples. The Phillips XL30 settings used were 15kV acceleration voltage with 4x spot size and a working distance of 10mm.

The specific surface areas of the granite used in this study were obtained by both BET – N_2 and also geometric studies. The BET values were measured using MicroMeritics Gemini VII with nitrogen adsorption by Aoife McFadden at the Adelaide Microscopy Centre, and also at RMIT University by Frank Antolasic. In order to validate the BET results, Figure 4.2 which shows a plot of BET surface area multiplied by the density of the sample versus the reciprocal of particle size was generated. Figure 4.2 shows a linear relationship between BET surface area and particle size, which agrees with the finding from the study by Dubois et al (2010).

The specific geometric surface areas (A_s^*) were calculated using Equation (4.1) (Worley, 1994). This equation is used with the assumption that the particles are spheres and masses based on an effective spherical diameter (d_e) and the mixed density of the mineral (ρ_{mix}).

$$A_s^* = \frac{\pi (d_e)^2}{\frac{\pi}{6}(d_e)^3 \rho} = \frac{6}{d_e \times \rho_{mix}} \quad \textbf{(4.1)}$$

To obtain the average diameter of the particles, a particle size distribution analysis was carried out in a Malvern Mastersizer 2000. Three measurements were carried out for each particle size range. The results are provided in Table 4.1. The d_{50} average diameter is used as the equivalent spherical diameter to calculate the specific surface area.

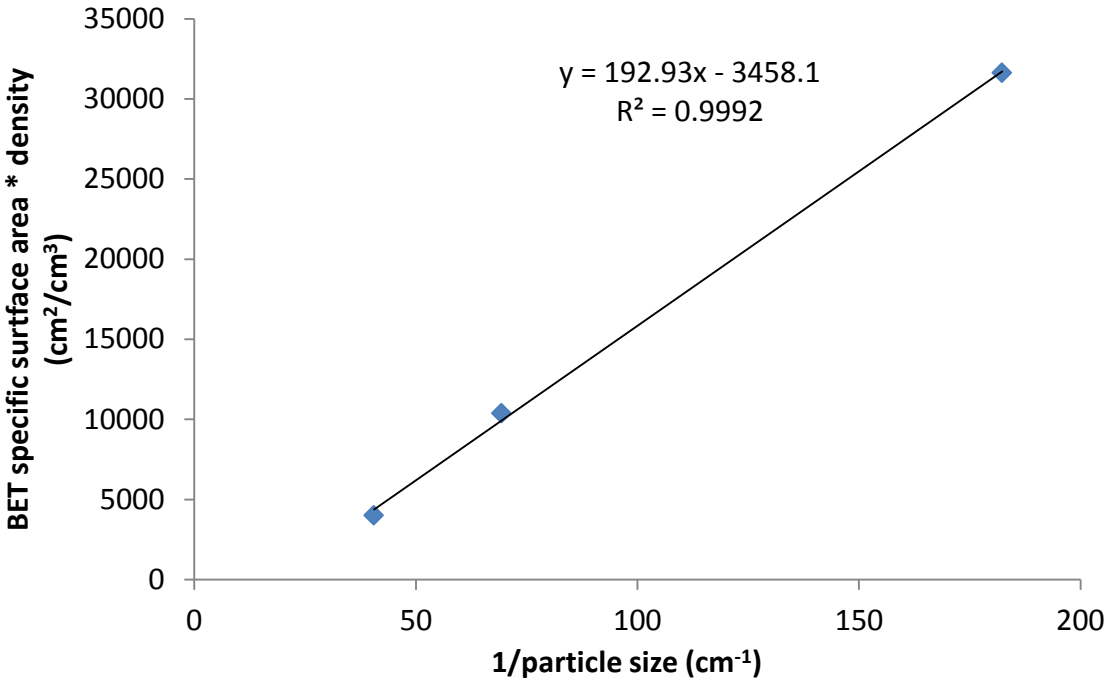

Figure 4.2 Relationship between BET surface area and particle size

The densities of the mineral contents in the sample are provided in Table 4.2, and the mixed density is calculated based on the weight percent (see Table 6.6). Using see Table 6.6 and Table 4.2, the mix density for the Habanero 3 granite is 2.63 x 10^3 kg/m^3. The summary of the specific surface area based on BET-N_2 and geometric is given in Table 4.3.

Table 4.1 Particle size distribution

Particle size range (μm)	d(50) 1 (μm)	d(50) 2 (μm)	d(50) 3 (μm)	d(50) average (μm)
40 - 60	45.928	45.867	45.890	45.895
100 - 200	176.75	176.80	176.30	176.61
200 - 400	310.48	310.53	310.17	310.39

Table 4.2 Densities of minerals

Mineral	Density (kg/m^3)	Reference
Quartz	2.66 x 10^3	(mindat.org, 2010c)
Albite	2.615 x 10^3	(mindat.org, 2010a)
K-Feldspar	2.56 x 10^3	(mindat.org, 2010b)

Table 4.3 Specific surface area of Habanero 3 granite (A_s^*)

Particle size (μm)	d_e (m)	BET (m^2/g)	Geometric (m^2/g)
40 – 60	4.59x10^{-5}	1.2033*	0.0497
100 – 200	1.77x10^{-4}	0.3947**	0.0129
200 – 400	3.10x10^{-4}	0.1522*	0.0074

*) carried out at Adelaide Microscopy Centre (by Aoife McFadden)

**) average result between Adelaide Microscopy Centre (by Aoife McFadden) and RMIT University (by Frank Antolasic)

4.4 Liquid Phase Analyses

An analytical technique that has been widely used by many researchers to determine the concentration of dissolved substances in water is spectrometry. Well known examples include Atomic Absorption Spectroscopy (AAS), Inductively Coupled Plasma Mass Spectrometry (ICP-MS), Inductively Coupled Plasma Optical Emission Spectroscopy (ICP-OES), Inductively Coupled Plasma Atomic Emission Spectroscopy (ICP-AES) and UV-Spectrophotometer.

In this study, the outlet liquid samples from fluid-rock experiments were analysed using different equipment depending on the analytes. Jenway 3510 pH meter was used to measure the pH solution at room temperature. Dilutions were performed whenever required to adjust the sample concentration to the equipment range. To determine the dissolved silica concentration, a HACH portable UV-spectrophotometer DR2000 was used. The HACH spectrophotometer procedure was based on the silicomolybdate method (HACH, 2000). The

concentration of dissolved cations was determined using solution ICP-MS by Benjamin Wade and Aoife McFadden at the Adelaide Microscopy Centre. Some samples were also sent to the South Australian Research Development Institute (SARDI) to be analysed using ICP-OES. This work was carried out by Barbara Rone-Clarke and Maria Segade at the South Australian Research Development Institute (SARDI) for comparison of the dissolved silica results from the HACH portable UV spectrophotometer and the major cation concentration results from ICP-MS. The anion concentration for some water samples were analysed using a nutrient analyser Aquakem v. 7.2.AQ2VA3 at SARDI. Since all equipment provides results in ppm concentrations, conversion to molality will be carried out accordingly.

Chapter 5 Fluid - Rock Interaction Experiments

Fluid-rock interaction experiments are important to understand a geothermal system, and this point is reinforced by the large volume of published work on mineral dissolutions, although most studies have focused on pure quartz and feldspars. As this study focuses on the dissolution rate of silica in granite, and published rate studies of pure quartz and feldspars should provide an important point of comparison for our results.

In order to simplify this study, the gas phase was not introduced to the system. It can be seen from the Habanero 1 and Habanero 3 gas analyses provided in Table 3.3 and Table 3.5, respectively, that it consist mostly of $CO_{2(g)}$. According to Brantley (2008), the silicate dissolution rate exhibit only a weak or negligible dependence on P_{CO_2} under alkaline conditions, at constant pH. Therefore, the absence of the gas phase should have only a small or negligible effect on the silicate dissolution in this fluid-rock interaction study. To investigate the interaction of fluid and rock in the Cooper Basin geothermal system (i.e. Habanero 3 well), three experimental methods at a laboratory scale were developed. The first method involves the interaction of fluid and rock samples in a closed system where no fluid is replaced (fluid mass is constant) during the experimental period. This method was used to obtain the equilibrium silica concentration at various temperatures, to observe the dissolution kinetics in pure water and dilute NaCl solution, and to determine the effect of pH and particle size on silica dissolution rate. However, the maximum temperature chosen was 200^{o}C, due to the limitation of the Teflon lined reactors used.

The second method uses a closed loop batch flow-through cell that was designed to mimic the circulation of the fluid-rock interaction thereby enabling the observation of the changes in the chemical properties of the host rock and circulating fluid that may occur. This method involved

two different experimental systems. The first system allows the interaction of the fluid and rock samples at 250^{o}C (close to the actual geothermal reservoir temperature) to study the dissolution kinetics of silica from the granite where fluid is constantly flowing through the rock samples for different interaction periods. This system was also used to study the effect of fluid/rock ratio. This second system allows the interaction of fluid and rock samples also in a closed loop batch flow-through cell, however the fluid is constantly replaced every 24 hours for the specified experimental period. This method was designed to accelerate the mineral dissolution to observe which minerals were more soluble.

The third method involved a high pressure open-loop fluid rock interaction system, where fresh water is continuously injected to the system. This system was configured to observe the influence of pressure in rock water interaction.

5.1 Static System

The static system in this study refers to a state where the fluid is circulated purely by convection in the fluid in a reactor or reservoir while interacting with the rock sample (solid). This system is used to measure the equilibrium concentration of dissolved elements and to study the dissolution kinetics of the granite. Figure 5.1(a) illustrates the dismantled stainless steel autoclave (Li, 2012). Figure 5.1(b) depicts the assembled stainless steel autoclave which consists of: (1) stainless steel autoclave cap with springs, (2) a teflon cap, (3) a teflon tube, (4) a stainless steel autoclave body, (5) the liquid phase and (6) the solid phase.

Figure 5.2 presents the experimental set up. Several sets of stainless steel autoclave were placed in an oven at the desired temperature. Due to temperature constraint introduced by the thermal stability of teflon, it was decided that the maximum temperature for this set up would be 220^{o}C. Unfortunately, due to the experimental arrangements and available equipment, no mixing was introduced in the system.

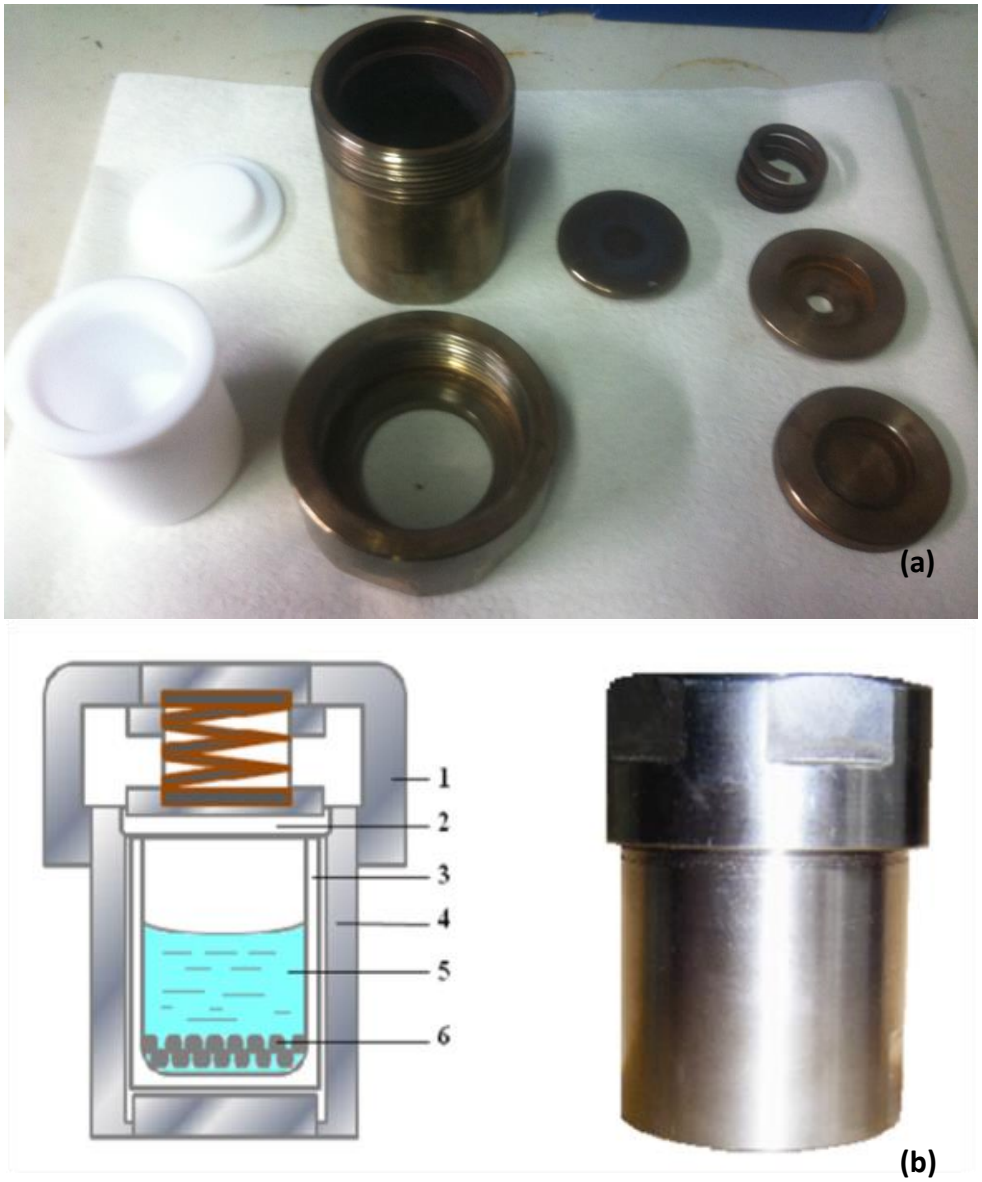

Figure 5.1 Stainless steel autoclave with Teflon liners

This static system was used to determine the equilibrium silica concentration, silica dissolution kinetics, influence of particle size on silica dissolution kinetics, effect of sodium chloride on silica dissolution kinetics, and influence of pH on silica dissolution kinetics. These experiments are detailed in Sections 5.1.1 to 5.1.5.

Figure 5.2 Photograph of static Teflon experimental set up

5.1.1 Equilibrium silica concentration in water at various temperature

The equilibrium silica concentration is an important parameter for the silica dissolution rate constant determination. An experiment was conducted to determine the equilibrium silica concentration in water at various temperatures. The results were fitted with exponential model using Sigmaplot software to obtain the approximate equilibrium silica concentration and dissolution rate constant. In addition, other dissolved elements primarily Na, K and Al were also observed.

5.1.1.1 Materials

The main components required for this experiment were the prepared rock samples with particle size distribution of 100 – 200 µm and purified water (Milli-Q water), where the sample preparations have been described in Section 4.2. A dilute nitric acid solution (4% vol.) was also prepared for the liquid sample preservation.

5.1.1.2 Start-up procedures

Approximately 0.5 g of rock samples and 14 mL of pure water (Milli-Q water) were prepared in each Teflon tube. The total volume of a teflon tubes is 18 mL and a free space of 4 mL was left for water volume expansion. The teflon tubes were then placed into the stainless steel autoclave. Anti-seize (silver goop) was used on the threads to prevent the seizure of the caps locking to the autoclave following prolonged exposure to high temperature in the oven. After application of the anti-seize, the autoclave was capped, placed on to a bench vice and tightened using a wrench.

5.1.1.3 Experimental procedures and sampling

The fluid-rock interaction experiments were performed at six different temperatures (120^{o}C, 140^{o}C, 160^{o}C, 170^{o}C, 200^{o}C, and 220^{o}C) for 56 days in an oven at saturated vapour pressure. At the conclusion of the experiment, the autoclaves were quenched with cold water for 15 minutes, and the solution pH was measured immediately and recorded. The liquid phase was decanted to a polypropylene container and a 5 mL sample was taken and diluted to 1:10 ratio then preserved with 4% nitric acid to maintain the dissolved elements in solution and minimize polymerization that may occur (Brown, 2011a). The reactive silica (H_4SiO_4) concentration was measured following the HACH silicomolybdate method using a HACH portable spectrophotometer DR2000. The Si concentration (converted to SiO_2) was also measured using an Inductively Coupled Plasma Optical Emission Spectrometry (ICP-OES) at the South Australian Research and Development Institute (SARDI. The concentration of the major cations: Na, K, and Al was measured using an Inductively Coupled Plasma Mass Spectrometry (ICP-MS) at the Adelaide Microscopy Centre. The solid phase (rock samples) was left in the teflon tubes and dried in an oven at 120^{o}C for 48 hours.

5.1.1.4 Results and discussion

The experimental results confirm that the equilibrium reactive silica concentration increases with temperature. The initial pH of the water was nearly neutral (approximately pH 5.5) and the solution pH increased to approximately 8.5 after 56 days of interaction. In order to validate

the experimental results, it is appropriate to compare the test results with a known published correlation. Four correlations were considered. The first correlation (Equation (2.59)) was proposed by Fournier and Potter II (1982b) and was valid for temperatures ranging from 25°C to 900°C at pressures up to 10,000 bar. The second correlation was proposed by Rimstidt (1997) and valid for a temperature range from 0°C to 300°C which is summarised in Equation (2.60). The third (Equation (2.61)) was developed by Verma (2000b) and was valid for temperatures between 0 – 374°C, and the fourth was a study by Brown (2011b), which discussed the relationship equilibrium quartz concentration at various temperatures as given according to Equation (2.56).

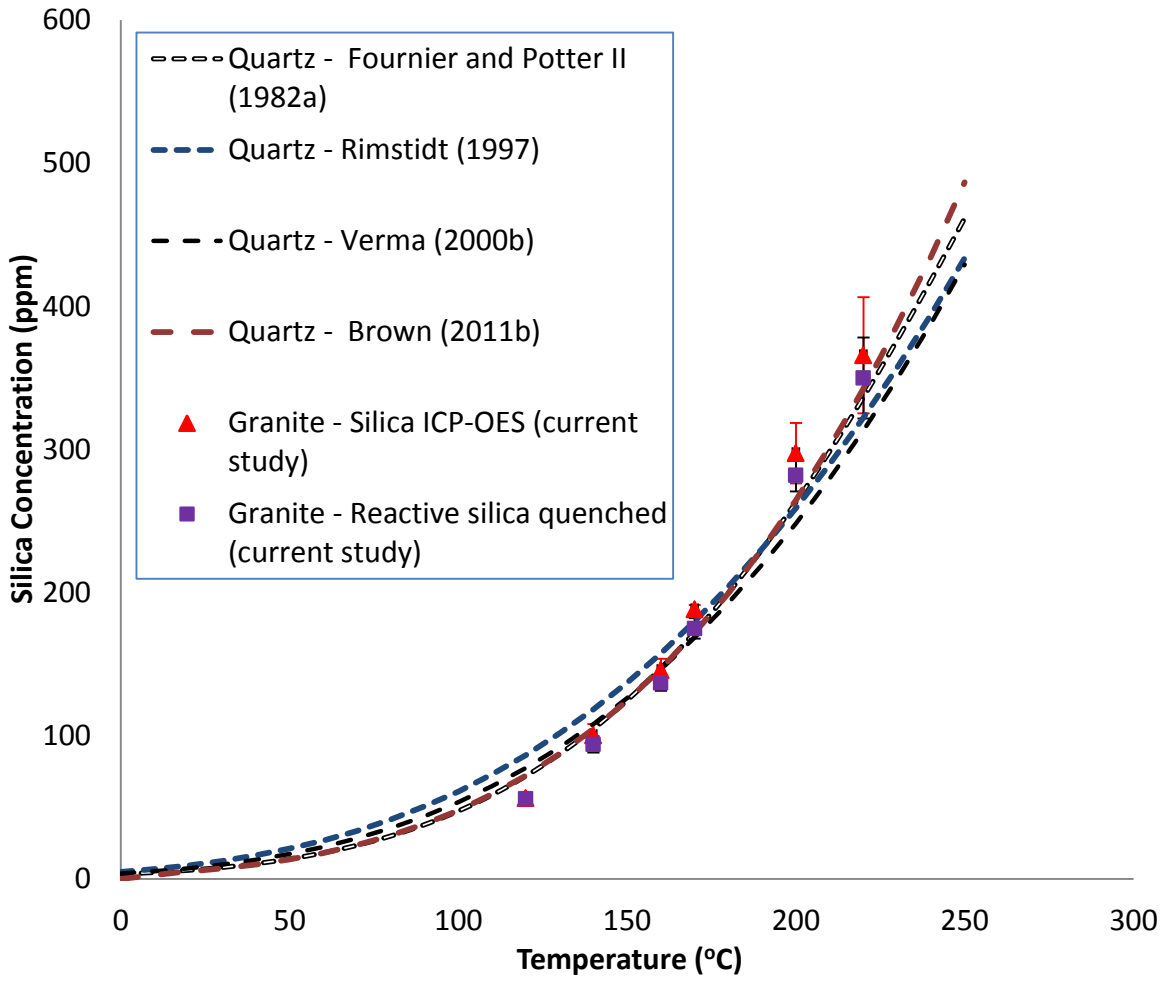

Figure 5.3 Experimental results showing silica concentration at temperatures 120°C, 140°C, 160°C, 170°C, 200°C, and 220°C

The experimental results revealed that the dissolved silica concentration increased exponentially with temperature and provided a reasonable fit for the plots from the correlations used. The experimental results were then plotted in terms of log C versus 1/T (K) to obtain a linear fit and an equation was developed to correlate the silica dissolution for the rock sample from Habanero 3 well at various temperatures. The silica concentration obtained from silicomolybdate method and ICP-OES were compared. The plot is provided in Figure 5.4. It is seen from the plot that the slope differs slightly. A study by Worley (1994) showed that the concentration of silica measure in ICP is slightly higher when compared against the molybdite method. In order to observe how the equilibrium silica concentration changes with temperature, the generated correlation was then plotted against temperatures ranging from 0 – 250^{o}C.

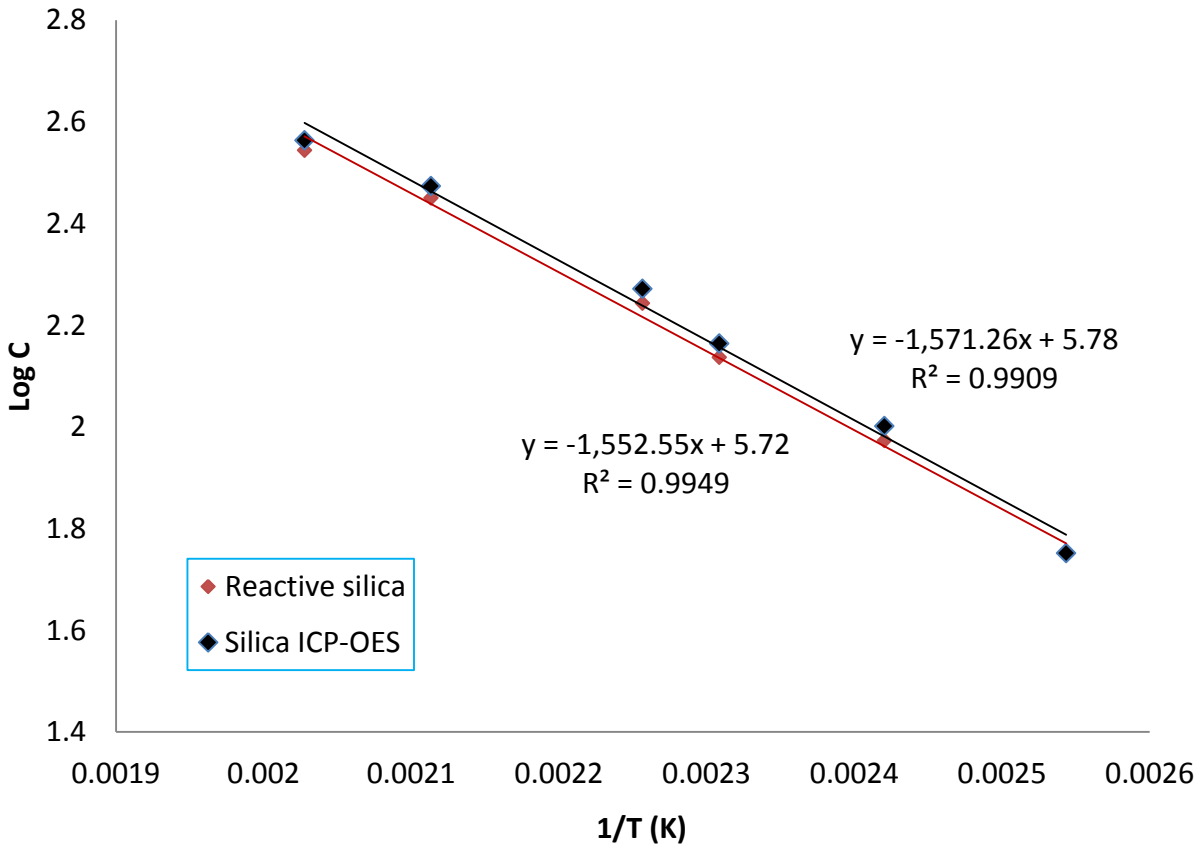

Figure 5.4 Linearization of equilibrium silica concentration from experimental data

The resulting equation for reactive silica is given by:

$$Log\ C = -\frac{1552.55\ (\pm 154.06)}{T} + 5.72\ (\pm 0.35) \quad \textbf{(5.1)}$$

The equation obtained for silica concentration from ICP-OES is:

$$Log\ C = -\frac{1571.26\ (\pm 208.92)}{T} + 5.78(\pm 0.48) \quad \textbf{(5.2)}$$

The results were then compared together with some of the published correlation and the resulting plot is provided in Figure 5.5.

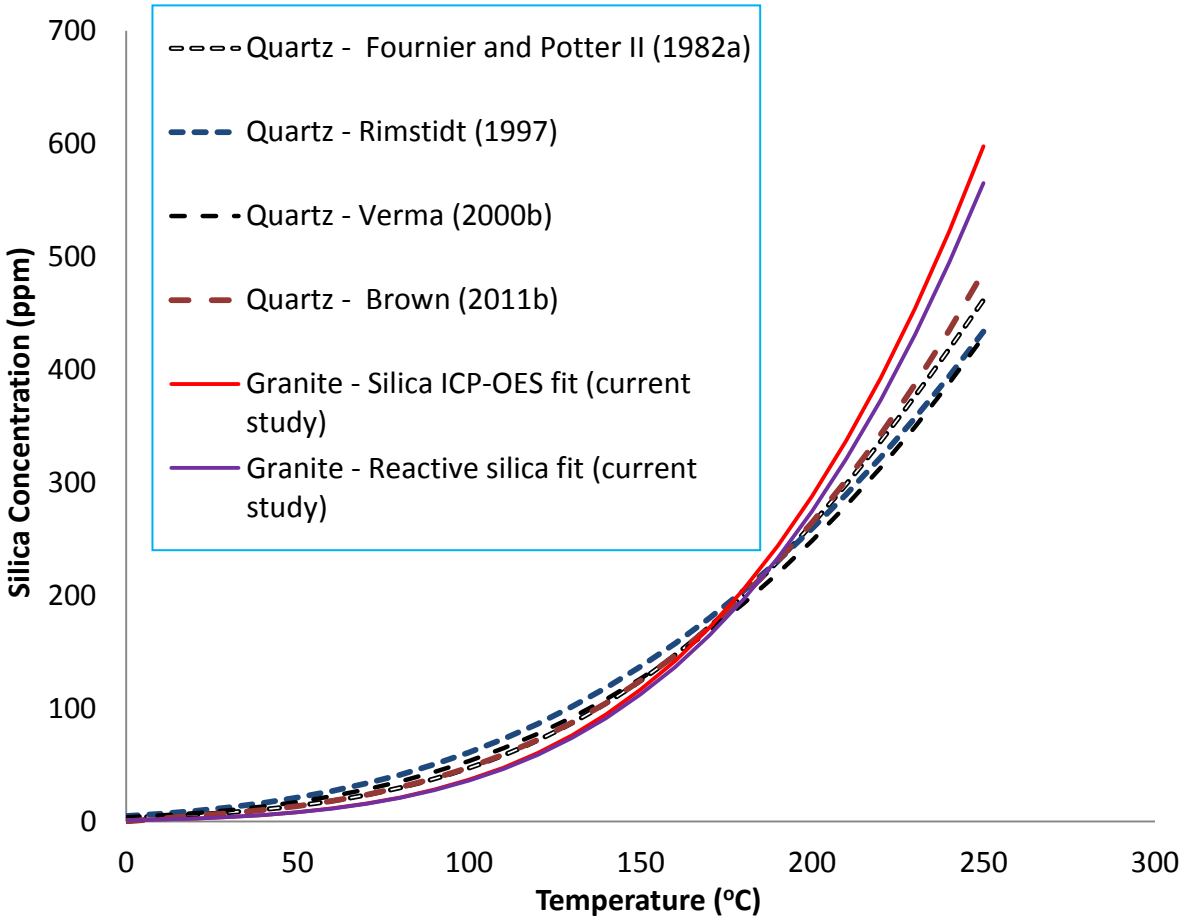

Figure 5.5 Equilibrium silica concentration at various temperatures compared with literature

The experimental results showed a similar trend line and fit reasonably well with the literature although at temperatures greater than 200°C the deviation increased. This deviation may be caused by the comparison of granite dissolution (present study) to previous pure quartz dissolution studies (Rimstidt and Barnes, 1980; Fournier and Potter II, 1982b; Robinson, 1982; Worley, 1994; Rimstidt, 1997; Verma, 2000b). Since the granite used in this study is primarily composed of sodium feldspars (albite), potassium feldspars (microcline) and about 50% quartz, it is possible that the solubility of the granite is greater to pure quartz.

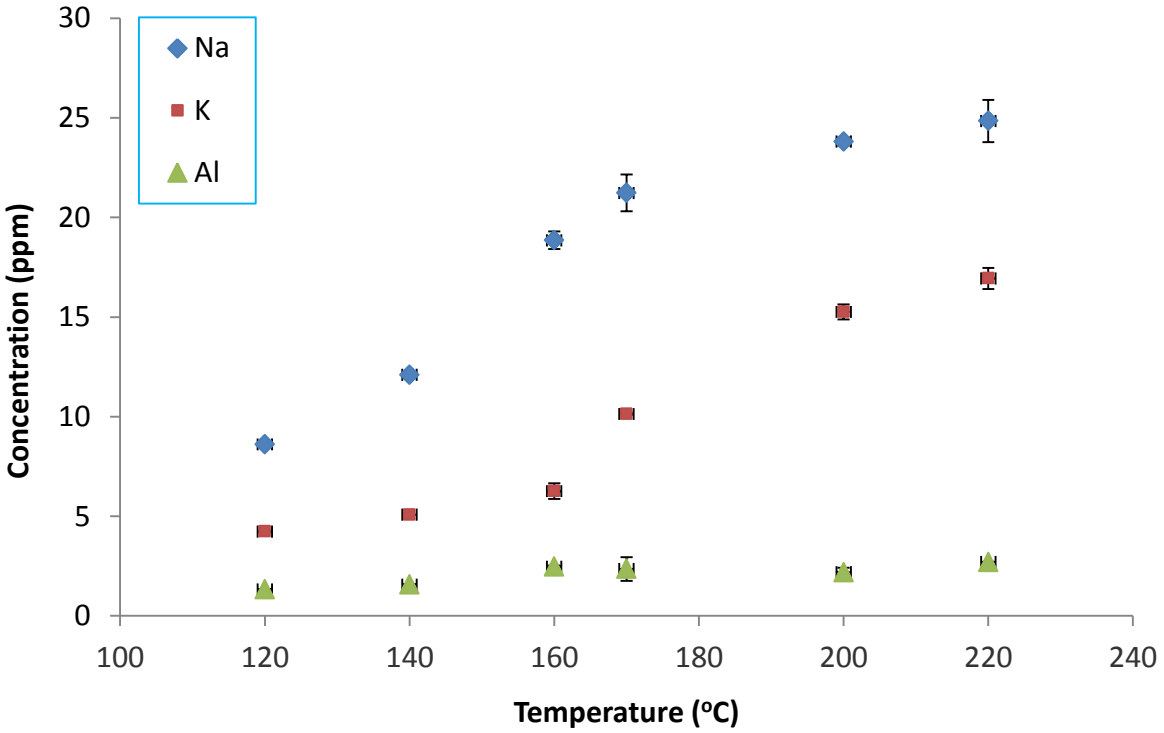

Figure 5.6 Equilibrium concentrations of dissolved Na, K, and Al at various temperatures

The dissolved concentrations of Na, K and Al from granite dissolution at various temperatures are presented in Figure 5.6. The presence of Na, K and Al in the solution suggests that the albite and K-feldspars from the granite dissolved to the liquid phase. As expected, the concentration of Na, K and Al increased with temperature. The complete set of data is provided in Appendix B.1.

5.1.2 Granite dissolution kinetics in water

This kinetic study was conducted to generate the dissolution profile of the granite from Habanero 3 well in water at four different temperatures (160^{o}C, 170^{o}C, 200^{o}C and 220^{o}C) and determine the activation energy. Due to the limitations of teflon, the experiments were carried out at temperatures not exceeding 220^{o}C. The results of this experiment would be used to verify and compare the silica profile from the flow-through cell experiments at 250^{o}C.

5.1.2.1 Materials and experimental

The materials used in this granite dissolution experiment were the rock samples with particle size distribution of 100 – 200 µm, Milli-Q water, and 4% vol. nitric acid solution for liquid sample preservation. The start-up procedures were carried out as specified in Section 5.1.1.2. Static fluid-rock interaction experiments for silica dissolution kinetics were performed at 160^{o}C, 170^{o}C, 200^{o}C and 220^{o}C for 1, 3, 7, 14, 21 and 56 days in an oven at saturated vapour pressure. The procedures undertaken at the conclusion of the experimental period is specified in Section 5.1.1.3. This liquid sample were then analysed using an Inductively Coupled Plasma Mass Spectrometry (ICP-MS) at the Adelaide Microscopy Centre to obtain the concentration of cations, mainly sodium (Na), potassium (K), aluminum (Al). The reactive silica or silicic acid (H_4SiO_4) concentration was measured following the HACH silicomolybdate method using a HACH portable spectrophotometer DR2000. Since silicic acid (H_4SiO_4) is the dominant specie in the aqueous phase from silica dissolution (Verma, 2000a), it will be the main point of interest in this experiment. The solid phase (rock samples) was left in the teflon tubes and dried in an oven at 120^{o}C for 48 hours. The rock samples were then weighed and recorded. The rock samples were then analysed using the scanning electron microscope (SEM) to observe the surface morphology of the particles and to qualitatively determine the mineralogy. The remaining rock samples were then stored in a dessicator.

5.1.2.2 Results and discussion

Results shows that the reactive silica concentration increases with time, and the equilibrium reactive silica concentration increases with temperature. In addition, the time to achieve

equilibrium decreases with temperature. It is important to validate the experimental results (the equilibrium concentration at different temperatures and the dissolution rate constant) against published literature. SigmaPlot was used to fit the experimental results according to the model from Equation (2.55) to obtain the equilibrium silica concentration and dissolution rate constant. The plot is provided in Figure 5.7.

The curve fitting applied to the experimental results followed the first-order exponential model according to Equation (2.55):

$$f(x) = a_0(1 - e^{-a_1 x}) + e \quad \textbf{(5.3)}$$

where: the unit for a_0 is ppm and for a_1 is per day.

Rewriting in terms of reaction kinetics (recall Equation (2.54):

$$m_{H_4SiO_4} = m^{sat}_{H_4SiO_4}\left(1 - e^{-k^{\#}t}\right) \quad \textbf{(5.4)}$$

where: $m_{H_4SiO_4}$ is the concentration of silica (defined as $SiO_{2(aq)}$, therefore using the molecular weight of SiO_2 instead of H_4SiO_4) at time t, $m^{sat}_{H_4SiO_4}$ is the equilibrium concentration (molal) and $k^{\#}$ is the pseudo rate constant (s^{-1}).

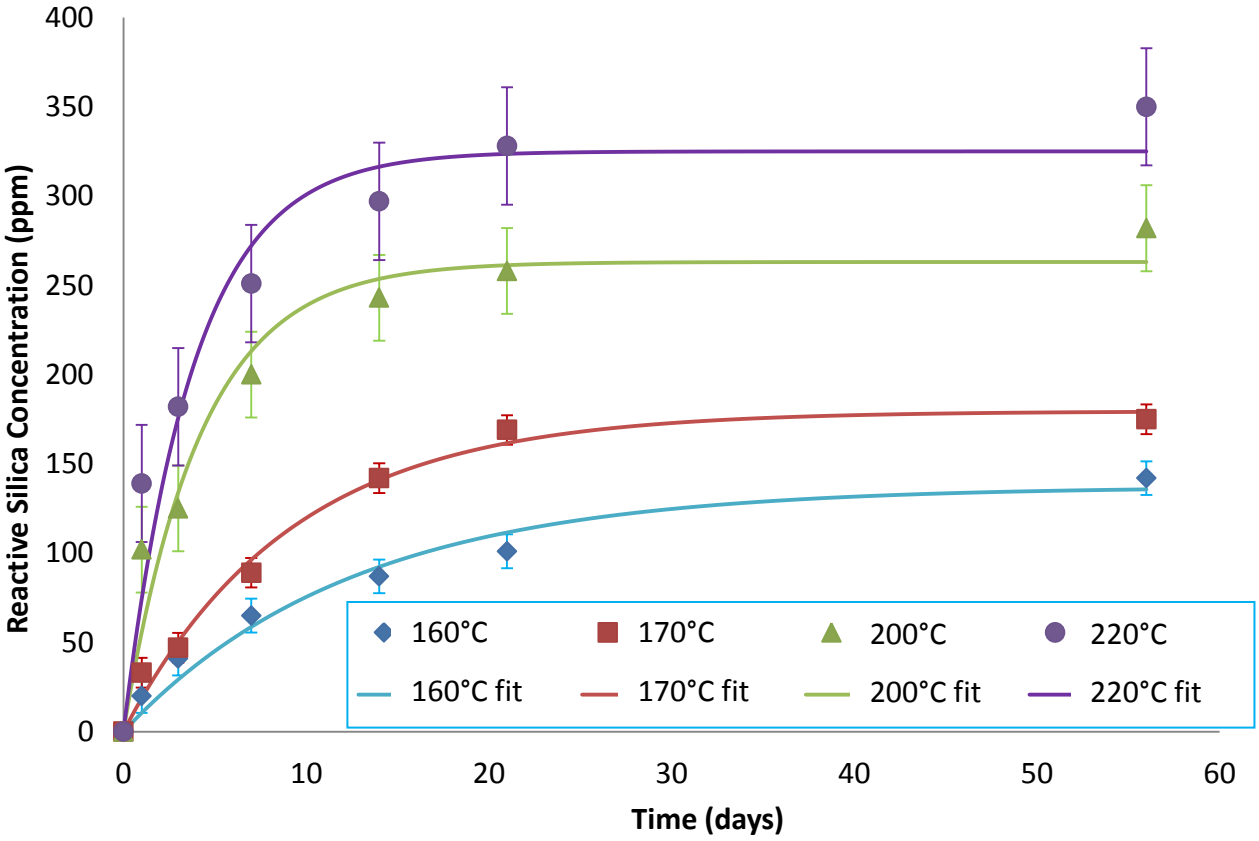

Figure 5.7 Reactive silica concentration profile for four different temperatures (160°C, 170°C, 200°C, 220°C)

It should be noted that this rate law is empirical. The derivation of the model is given in Section 2.4.2. From the curve fitting results, it can be seen that the Equation (5.4) proves to provide a reasonably good fit. The results from the curve fitting using SigmaPlot is given in Table 5.1.

Table 5.1 Constants from curve fitting model using SigmaPlot for 100 – 200 µm sample size

T (°C)	a_0 (ppm)	a_1 (d^{-1})	*Standard error of estimate (ppm)*
160	137.30	0.0797	9.4631
170	179.50	0.1098	8.2770
200	263.07	0.2375	24.037
220	320.72	0.3022	32.845

Since the experimental results are expressed in the units of mg of dissolved silica per kg of water (ppm) for a time period in days, a conversion of the concentration to molality (mol dissolved silica per kg of water) and time to seconds are essential for Equation (2.21) to be applicable. Recall the correlations between Equations (2.54) and (2.55):

- a_0 represents $m_{H_4SiO_4}^{sat}$
- a_1 represents $k^{\#}$

Therefore the constants obtained using SigmaPlot with the appropriate units in molal and $k^{\#}$ (s^{-1}) are provided in Table 5.2.

Table 5.2 Constants from SigmaPlot in terms of (molal) and $k^{\#}$ (s^{-1}) for 100 – 200 µm sample size

T (°C)	$m_{H_4SiO_4}^{sat}$ *(molal)*	$k^{\#}$ *(s^{-1})*
160	0.0023	9.22×10^{-7}
170	0.0030	1.27×10^{-6}
200	0.0044	2.75×10^{-6}
220	0.0053	3.50×10^{-6}

Thus, solving the forward (dissolution) reaction rate k_f using Equation (2.51):

$$k_f = \frac{k^{\#} m_{H_4SiO_4}^{sat} M_w}{A_s} \quad \textbf{(5.5)}$$

Another approach to obtain the dissolution rate constant is by linearization of the model according to Robinson (1982). Recalling Equation (2.21), the plot of $ln\left(\frac{m_{H_4SiO_4}^{sat} - m_{H_4SiO_4}}{m_{H_4SiO_4}^{sat}}\right)$ vs t will result in a straight line giving a slope $k^{\#}$, and the equilibrium silica concentration is approximated by taking the value of the peak where the curve starts to plateau (dashed lines in Figure 5.8). However, since it is difficult to approximate the equilibrium silica concentration, this method was therefore abandoned.

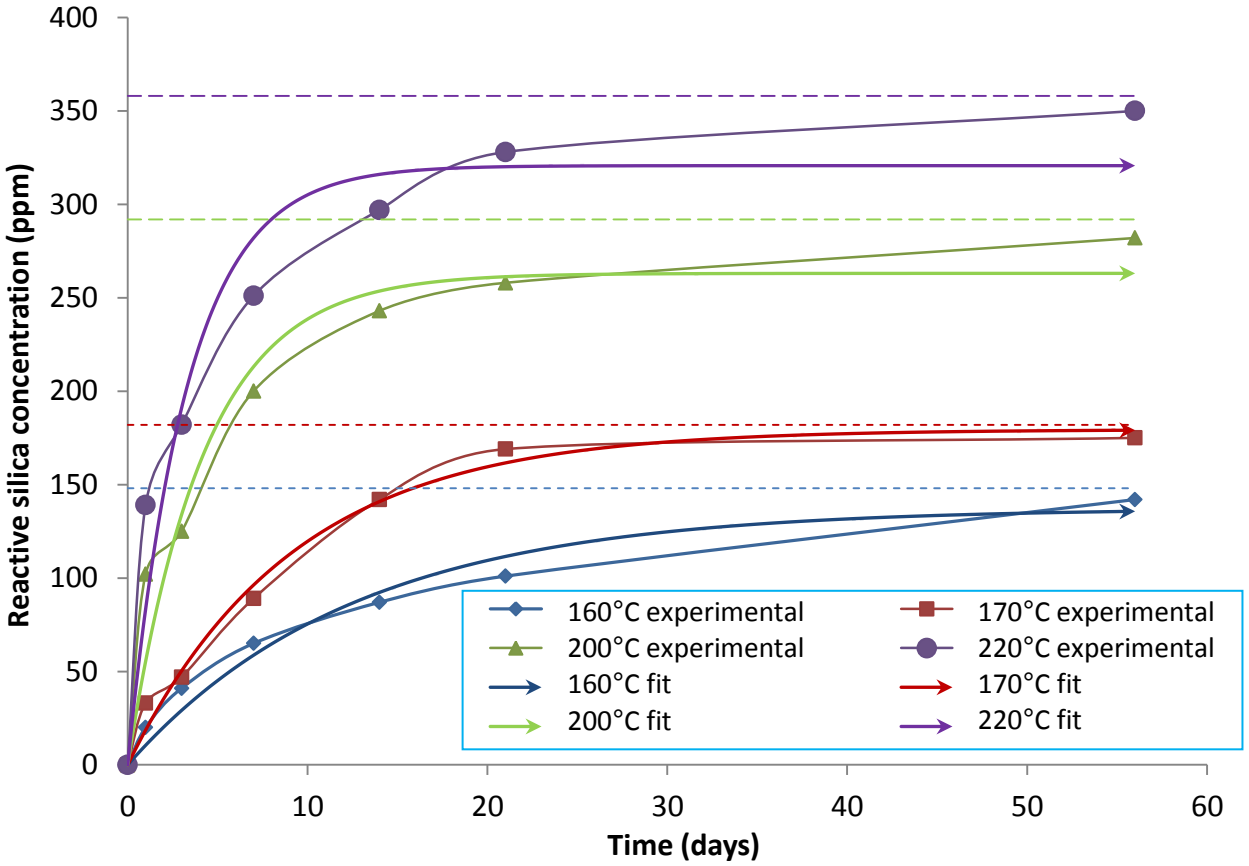

Figure 5.8 Approximation of equilibrium silica concentration (showed by the dashed lines)

The sample particle size used in this experiment was 100 – 200 µm and sample size was approximately 0.5 g with liquid volume 14 mL (1.40×10^{-5} m^3). Calculating the mass of water, while knowing density of water (ρ) at conditions 25°C and 1 atm is $997.045\ \mathrm{kg}/m^3$ (Perry and Green, 1997):

$$M = \rho \times V = 997.045 \times 1.4 \times 10^{-5} = 1.42 \times 10^{-2}\ \mathrm{kg}$$

With the above information, the active surface area (A_s) may be calculated from the specific surface area:

$$A_s = A_s^* \times mass\ of\ sample \qquad \textbf{(5.6)}$$

For obtaining the rate constant (k_f) using the specific geometric surface area, the shape of the samples are assumed to be spheres. The particles size diameter was obtained from a particle

size distribution analysis carried out in a Malvern Mastersizer 2000. Three measurements were carried out to obtain an average particle size diameter. The results are provided in Table 4.1. This average particle size diameter (d_{50}) is used as the equivalent spherical diameter to calculate the specific surface area. The effective spherical diameter for the sample size between $100 - 200\ \mu m$ $(100 - 200 \times 10^{-6}\ m)$ is $176.61\ \mu m$ $(1.77 \times 10^{-4}\ m)$.

Knowing the mixed density of the granite is $2.63 \times 10^{6}\ g/m^3$ $(2.63 \times 10^{3}\ kg/m^3)$, calculating the specific geometric surface area using Equation (4.1):

$$A_S^* = \frac{6}{1.77 \times 10^{-4}\ m \times 2.63 \times 10^{6}\ g/m^3} = 1.29 \times 10^{-2}\ m^2/g$$

Knowing the mass of the sample, calculating the active surface area:

$$A_s = 1.29 \times 10^{-2}\frac{m^2}{g} \times 0.5g = 6.46\ \times 10^{-3}\ m^2$$

Knowing that for 160°C the $k^{\#} = 9.22 \times 10^{-7}/s$, the rate constant can be calculated using Equation (5.5). Therefore the forward rate constant (dissolution) based on geometric specific surface area for 160°C is:

$$k_f = \frac{(9.22 \times 10^{-7})(0.0023)(1.42 \times 10^{-2})}{6.46\ \times 10^{-3}} = 4.55 \times 10^{-9}\ {}^{mol}/_{m^2 s}$$

To calculate the active surface area based on BET-N_2 specific surface area:

$$BET\ A_s = 0.3947\frac{m^2}{g} \times 0.5g = 0.2720 m^2$$

Again, knowing for 160°C the $k^{\#} = {}^{9.22 \times 10^{-7}}/_{s}$, the rate forward rate constant (dissolution) calculated using Equation (5.5) is:

$$k_f = \frac{(9.22 \times 10^{-7})(0.0023)(1.42 \times 10^{-2})}{0.2720} = 1.49 \times 10^{-10}\ {}^{mol}/_{m^2 s}$$

Using the same method, values of k for different temperatures were calculated. The results are shown in Table 5.3 and Table 5.4.

Table 5.3 Dissolution rate constants for four different temperatures based on geometric surface area

T (^{o}C)	T (K)	1/T (K)	Geometric k_f $(mol/m^2 \cdot s)$	$ln(k_f)$	$log(k_f)$
160	433.15	2.31 x 10^{-3}	4.55 x 10^{-9}	-19.208	-8.3419
170	443.15	2.26 x 10^{-3}	8.20 x 10^{-9}	-18.617	-8.0852
200	473.15	2.11 x 10^{-3}	2.60 x 10^{-8}	-17.465	-7.5849
220	493.15	2.03 x 10^{-3}	4.03 x 10^{-8}	-17.026	-7.3941

Table 5.4 Dissolution rate constants for four different temperatures based on BET surface area

T (^{o}C)	T (K)	1/T (K)	BET k_f $(mol/m^2 \cdot s)$	$ln(k_f)$	$log(k_f)$
160	433.15	2.31 x 10^{-3}	1.49 x 10^{-10}	-22.627	-9.8267
170	443.15	2.26 x 10^{-3}	2.69 x 10^{-10}	-22.036	-9.5700
200	473.15	2.11 x 10^{-3}	8.54 x 10^{-10}	-20.881	-9.0697
220	493.15	2.03 x 10^{-3}	1.33 x 10^{-9}	-20.440	-8.8784

Felipe et al. (2005) cited in Kubicki (2008) recommended to calculate the rate constant as a function of temperature and obtain the activation energy. This activation energy is calculated from the slope of a line produced from a plot of natural log of the rate constant $ln(k_f)$ versus $1/T$ based on geometric and BET surface area. An Arrhenius plot using the data from Table 5.3 and Table 5.4 is shown in Figure 5.9. It can be seen that the surface area basis does not influence the slope.

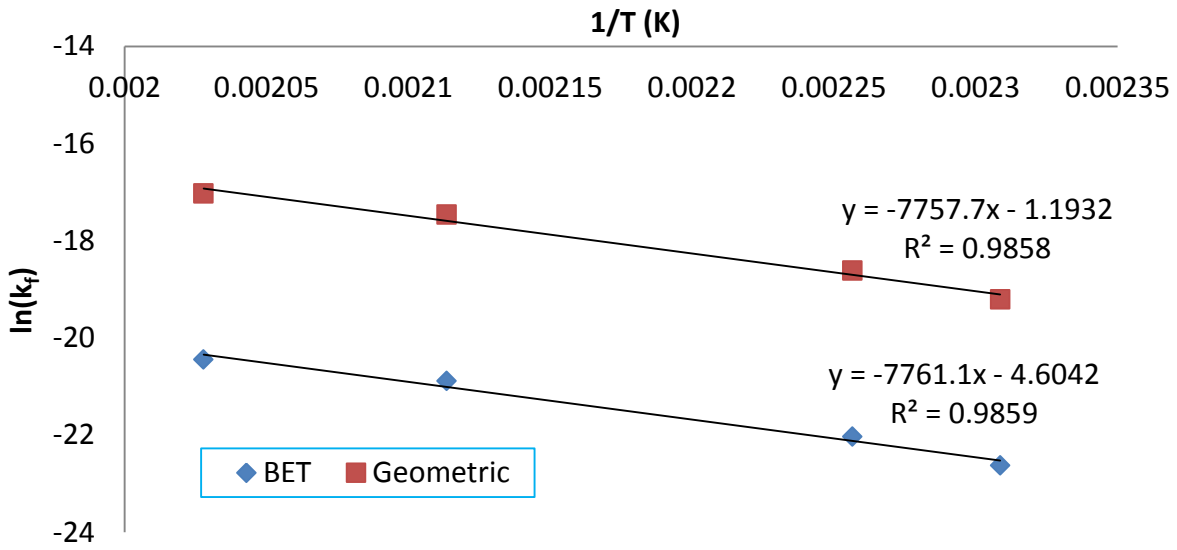

Figure 5.9 Arrhenius plot for 160°C, 170°C, 200°C and 220°C

The slopes generated in Figure 5.9 can be used to calculate the activation energy and the pre-exponential factor or frequency factor using the linear form of the Arrhenius equation (Fogler, 2006):

$$k_f = A\, e^{\frac{-E_a}{RT_K}} \tag{5.7}$$

where: k_f = the rate constant $(J/m^2 \cdot s)$

A = the pre-exponential factor or frequency factor

E_a = the activation energy (J/mol)

R = the gas constant = $8.314\ J/mol \cdot K$

T_K = the absolute temperature in Kelvin

The linear form of Equation (5.7) is:

$$\ln k = \ln A - \left(\frac{E_a}{R} \times \frac{1}{T}\right) \tag{5.8}$$

The equation generated for geometric specific surface area basis from Figure 5.9 is:

$$y = -7757.7x - 1.1932 \tag{5.9}$$

where: $\ln A = -1.1932$

$A = 0.3042$

Calculating the activation energy using Equation (5.8) with the obtained slope from Figure 5.9:

$$-\left(\frac{E_a}{8.314}\right) = -7757.7$$

$$E_a = 7757.7 \times 8.314 = 64602.3\,{}^{J}/_{mol}\left(64.4975\,{}^{kJ}/_{mol}\right)$$

The equation generated for BET specific surface area basis from Figure 5.9 is:

$$y = -7761.1x - 4.6042 \quad \textbf{(5.10)}$$

where: $\ln A = -4.6042$

$A = 0.0100$

Again, calculating the activation energy using Equation (5.8) with the obtained slope from Figure 5.9:

$$-\left(\frac{E_a}{8.314}\right) = -7761.1$$

$$E_a = 7761.1 \times 8.314 = 64525.8\ J/mol\ (64.5258\ kJ/mol)$$

The value of the obtained activation energy is lower compared to the published activation energy for quartz provided in Table 2.6. A lower value of activation energy is consistent with the granite being more reactive. Although the composition of the granite used in this study consist of mostly quartz (50%), the presence of albite, which has an activation energy value of 59.8 kJ/mol, appears to strongly increase the solubility of the granite. In addition, the estimation of the activation energy in this study is based on the release of monomeric silica to the solution. A suggestion for further studies are to perform granite dissolution experiments at other temperatures, therefore, by having more data points, the determination of activation energy for granite may be more accurate.

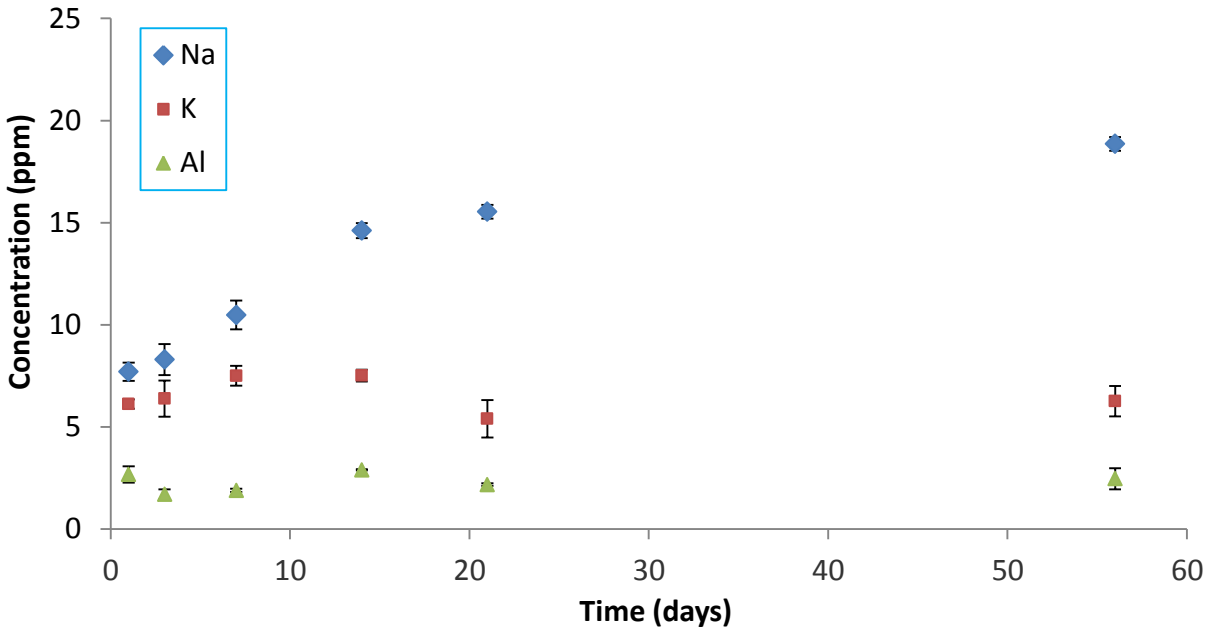

Figure 5.10 Concentration of dissolved Na, K, and Al from granite dissolution in water at 160°C

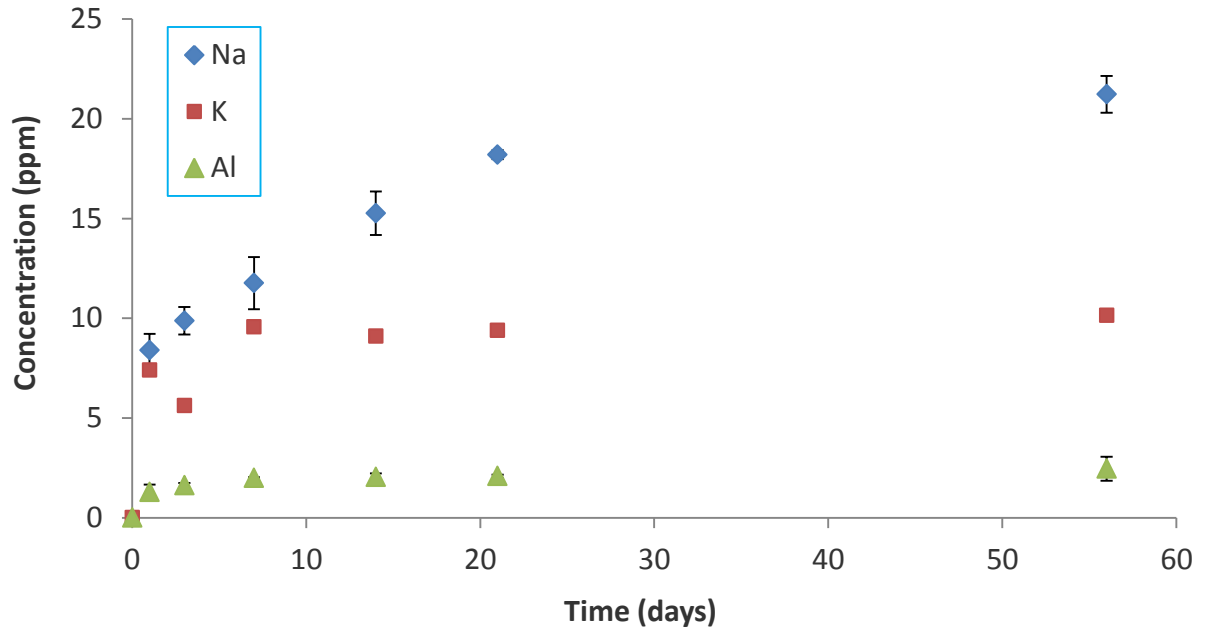

Figure 5.11 Concentration of dissolved Na, K, and Al from granite dissolution in water at 170°C

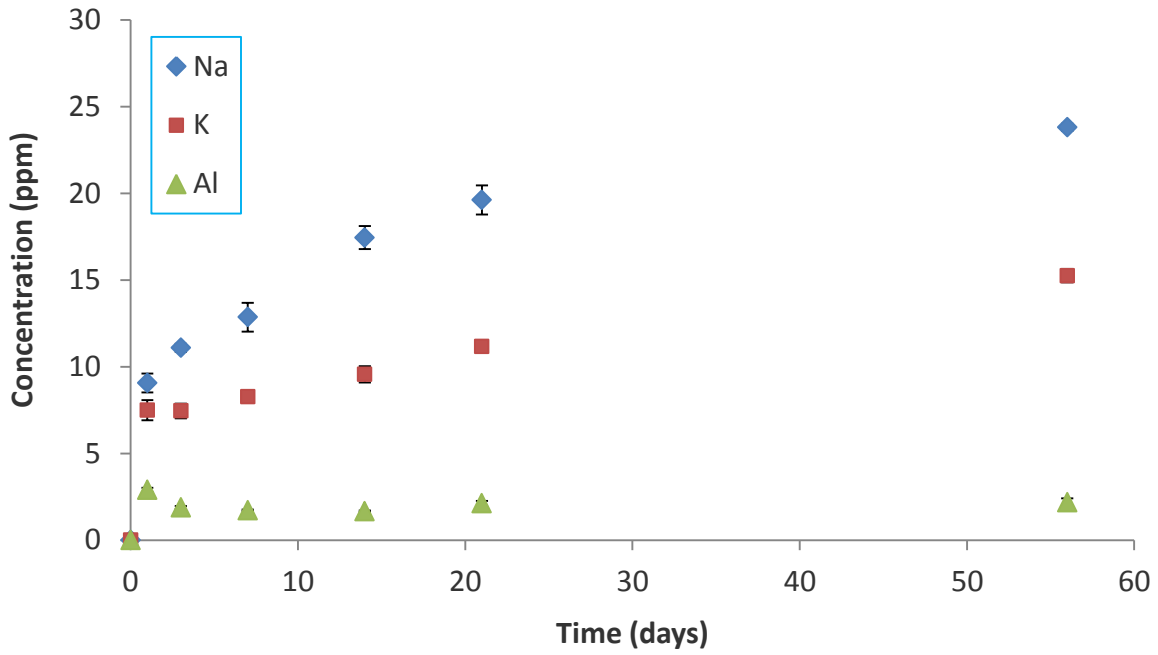

Figure 5.12 Concentration of dissolved Na, K, and Al from granite dissolution in water at 200°C

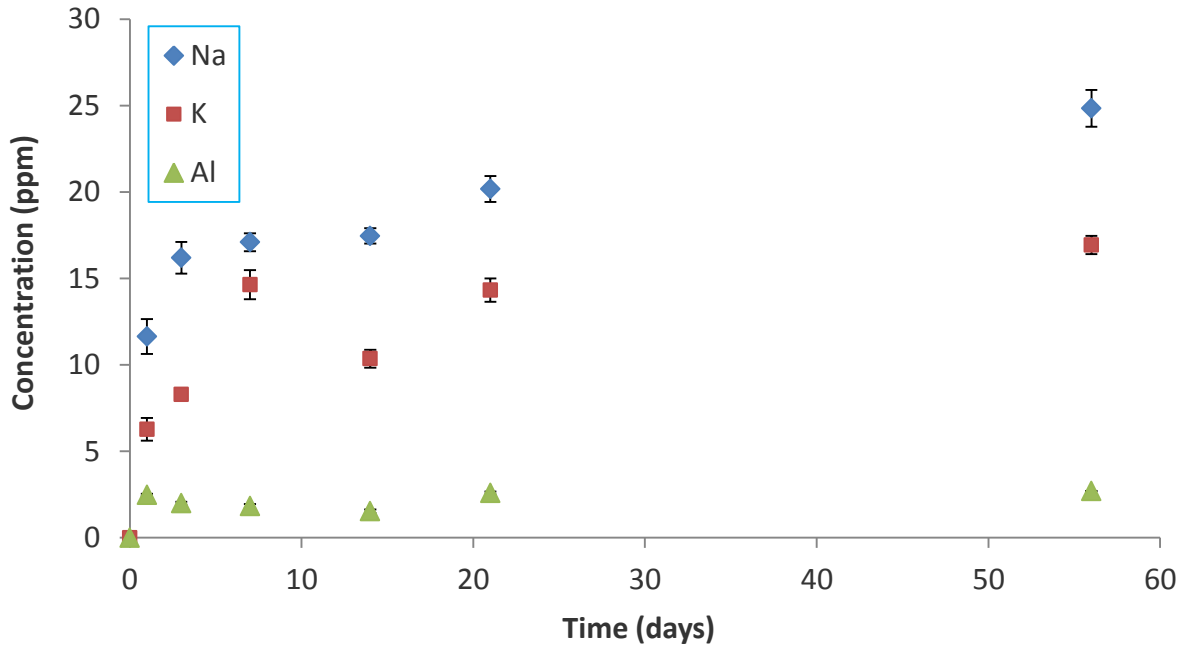

Figure 5.13 Concentration of dissolved Na, K, and Al from granite dissolution in water at 220°C

The dissolved major elements from granite dissolution at 160^{o}C, 170^{o}C, 200^{o}C, and 220^{o}C are presented in Figure 5.10, Figure 5.11, Figure 5.12, and Figure 5.13, respectively. The presence of Na, K, and Al suggest that the albite and K-feldspars from the granite dissolved to the liquid phase. It is seen that the concentration of Na, K and Al increased with time. No attempt was made to generate dissolution rate constant of albite and K-feldspar from the concentrations of Na, K or Al, since it was assumed that the granite is one mineral as a whole, and the dissolution rate was measured from the release of silica to the solution. The complete data is provided in Appendix B.2.

5.1.3 Influence of particle size on granite dissolution kinetics

This experiment was conducted to observe the effect of particle size on granite dissolution kinetics. The different particle size distributions would have different surface area, thus affecting the dissolution kinetics. Three different particle size distributions were chosen: 40 – 60 µm, 100 – 200 µm, and 200 – 400 µm.

5.1.3.1 Materials and experimental

The materials used in this granite dissolution experiment were the rock samples (with particle size distributions: 40 – 60 µm, 100 – 200 µm, and 200 – 400 µm), Milli-Q water, and 4% vol. nitric acid solution for liquid sample preservation. The rock samples were prepared following the procedures detailed in Chapter 4.2 and the start-up procedures as specified in Section 5.1.1.2. Fluid-rock interaction experiments were performed at 200^{o}C for 1, 3, 7, 14, 21 and 56 days in an oven at saturated vapour pressure. At the conclusion of every experimental period, the procedures outlined in Section 5.1.2.1 were followed.

5.1.3.2 Results and discussion

Results shows that the reactive silica concentration increases with time, and the equilibrium reactive silica concentration is the same for three different particle sizes. The time to achieve equilibrium is fastest for the smallest particle size, due to having a larger surface area. SigmaPlot was used to fit the experimental results according to the model from Equation (2.55)

to obtain the equilibrium silica concentration and dissolution rate constant. The result is shown in Figure 5.14.

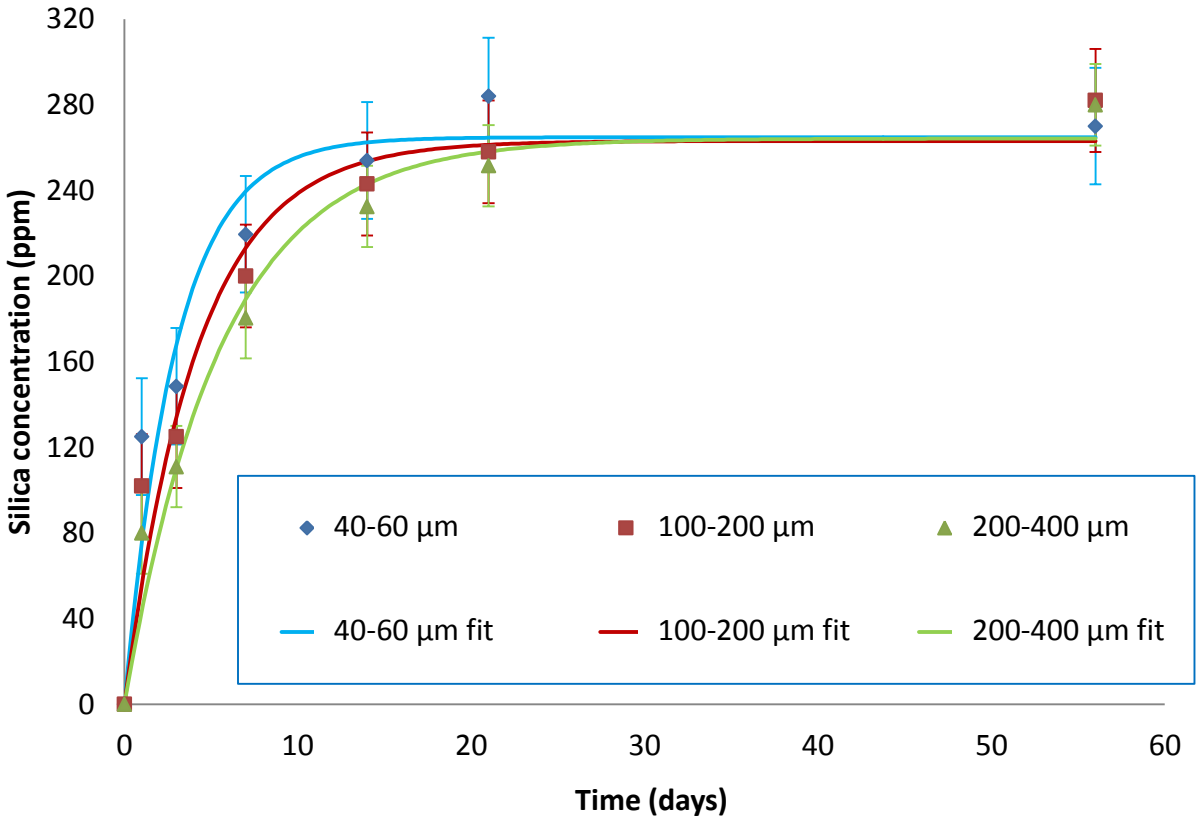

Figure 5.14 Reactive silica concentration profile for three different particle size (40 – 60 µm, 100 – 200 µm, and 200 – 400 µm) at 200°C in water

The constants obtained from Sigmaplot are shown in Table 5.5. However, the units of these constants must be converted to be applicable. The results of the conversions are given in Table 5.6. Using these constants, the dissolution rate constants were then calculated according to Section 5.1.2.2 using Equations (5.4) and (5.5). The calculated results of the dissolution rate constants based on geometric surface area and BET are given in Table 5.7 and Table 5.8, respectively.

Table 5.5 Constants from SigmaPlot for various particle sizes at 200°C

Particle size (µm)	a_0 *(ppm)*	a_1 *(d^{-1})*	*Standard error of estimate (ppm)*
40 – 60	264.81	0.3353	27.236
100 – 200	263.07	0.2375	24.037
200 – 400	264.19	0.1798	19.034

Table 5.6 Constants from SigmaPlot in terms of (molal) and $k^{\#}$ (s^{-1}) in water for various particle sizes at 200°C

Particle size (µm)	$m^{sat}_{H_4SiO_4}$*(molal)*	$k^{\#}$ *(s^{-1})*
40 – 60	0.0044	3.88×10^{-7}
100 – 200	0.0044	2.75×10^{-6}
200 – 400	0.0044	2.08×10^{-6}

Table 5.7 Dissolution rate constant for various particle size distribution based on geometric surface area

Particle size (µm)	Geometric k_f $(mol/m^2 \cdot s)$	$ln(k_f)$	$log(k_f)$
40 – 60	3.71×10^{-8}	-17.111	-7.4312
100 – 200	2.60×10^{-8}	-17.465	-7.5849
200 – 400	1.98×10^{-8}	-17.737	-7.7029

Table 5.8 Dissolution rate constant for various particle size distribution based on BET surface area

Particle size (µm)	BET k_f $(mol/m^2 \cdot s)$	$ln(k_f)$	$log(k_f)$
40 – 60	1.21×10^{-9}	-20.530	-8.9159
100 – 200	8.52×10^{-10}	-20.884	-9.0697
200 – 400	6.49×10^{-10}	-21.155	-9.1876

These calculated dissolution rate constants were also plotted against a compilation of literature values on quartz dissolution rates (Robinson, 1982; Worley, 1994) to allow comparison based on geometric surface area (Figure 5.15) and BET surface area (Figure 5.16).

It can be seen from the results that the dissolution rate constants based on geometric surface area are faster than those based on BET. According to Gautier et al. (2001), geometric based surface area may provide a more accurate parameter for dissolution rate determination. Their study revealed that as the BET surface increases as the dissolution progresses, little change was observed in the normalised dissolution rates. They explained that the increase in BET surface area consisted of mainly un-reactive etch pit walls, which does not affect the dissolution rate.

The dissolved major elements from granite dissolution at 200^{o}C using 40 – 60 µm, 100 – 200 µm, and 200 – 400 µm are presented in Figure 5.17, Figure 5.12 and Figure 5.18, respectively. The presence of Na, K, and Al verifies feldspar dissolution. It is also seen that the concentration of Na, K and Al increased with time. As mentioned in the previous section, no attempt was made to generate dissolution rate constant of albite and K-feldspar from the concentrations of Na, K or Al, since it was assumed that the granite is one mineral as a whole, and the dissolution rate was measured from the release of silica to the solution. The complete data set is provided in Appendix B.3.

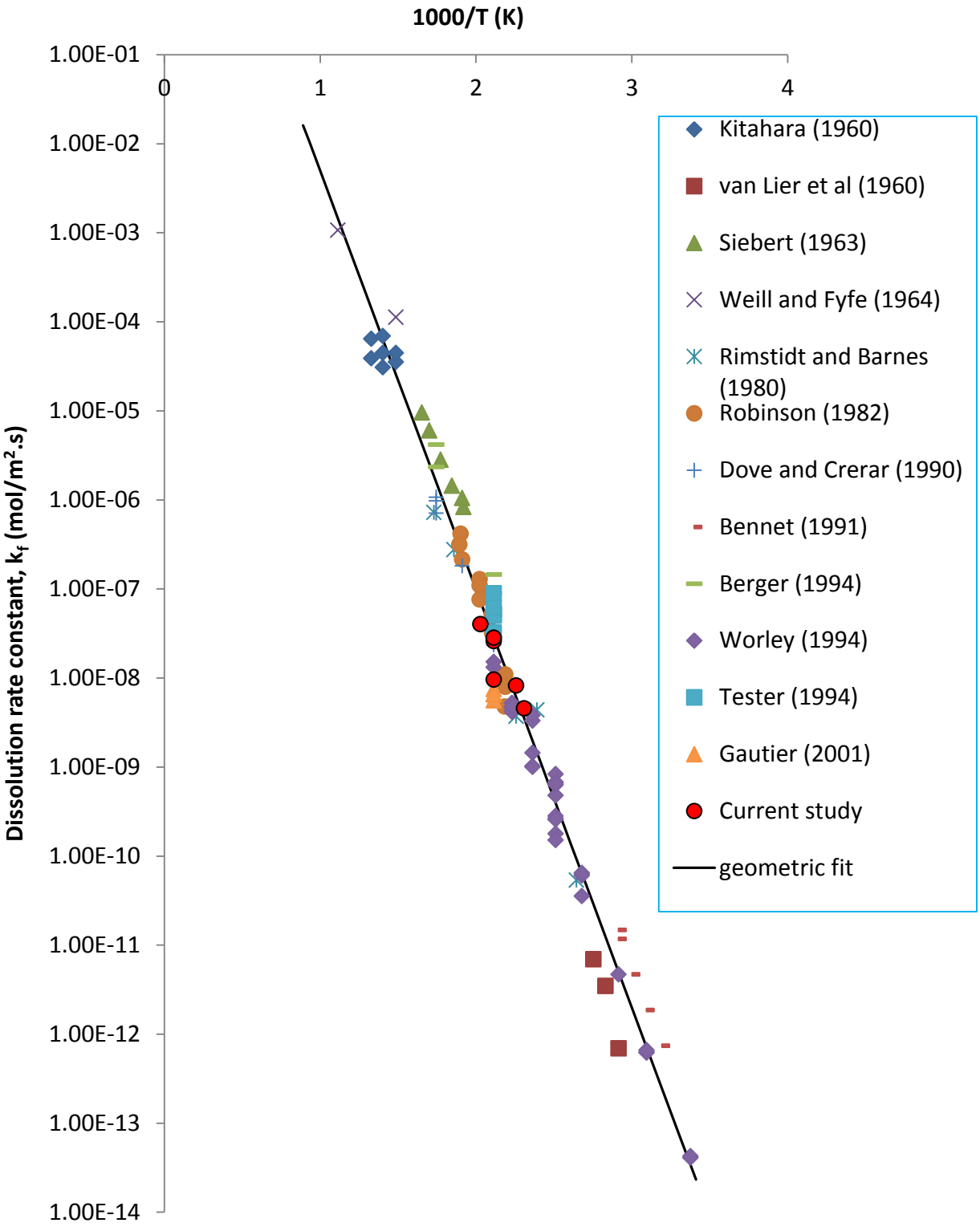

Figure 5.15 Comparison of silica dissolution rate constants (k_f) in pure water at various temperatures using geometric surface area basis

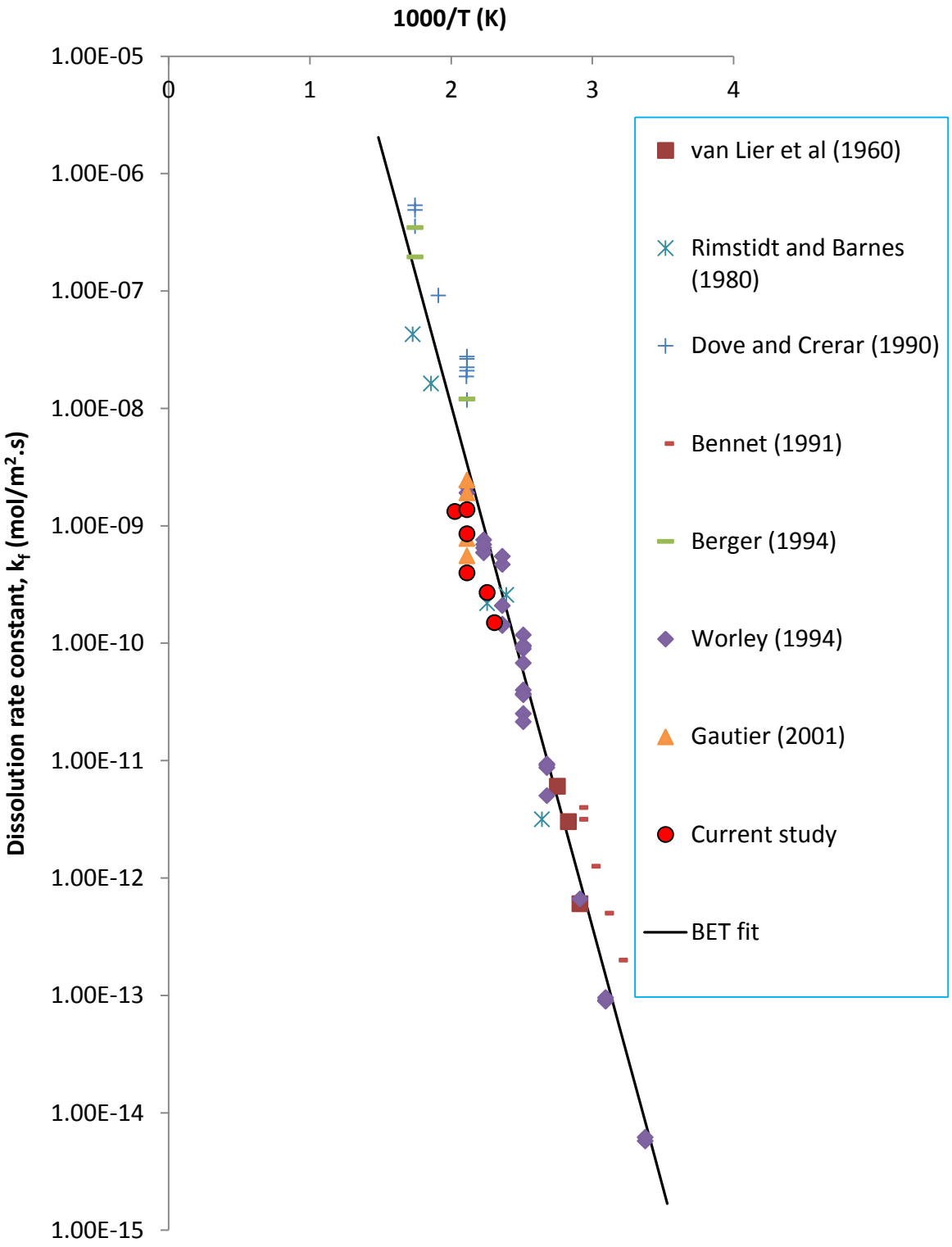

Figure 5.16 Comparison of silica dissolution rate constants (k_f) in pure water at various temperatures using BET surface area basis

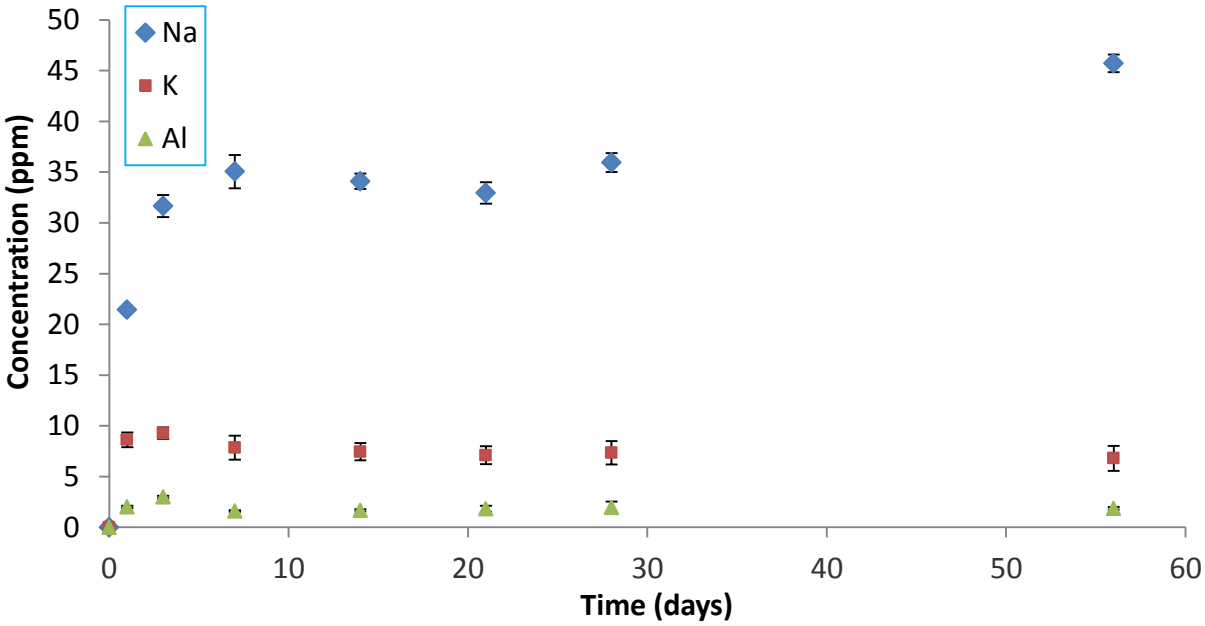

Figure 5.17 Concentration of dissolved Na, K, and Al from granite dissolution in water at 200°C using 40 – 60 µm particle size

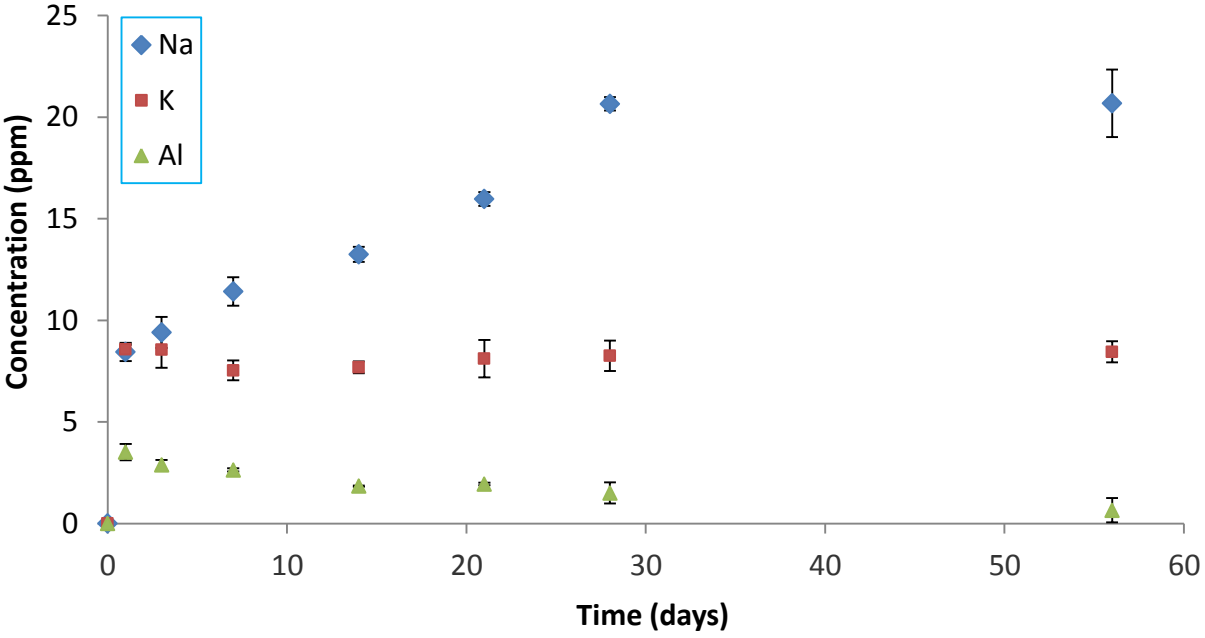

Figure 5.18 Concentration of dissolved Na, K, and Al from granite dissolution in water at 200°C using 200 – 400 µm particle size

5.1.4 Granite dissolution kinetics in NaCl solution

This experiment was conducted to generate the silica dissolution profile from the dissolution of the Habanero 3 granite and to observe any changes in the dissolution rate when salt is present in the solution. NaCl solution with a concentration of 250 ppm was chosen. This concentration was chosen based on Geodynamics' decision to maintain the calcium concentration of the inlet water not exceeding 40 ppm. The inlet water is a mixture of surface water from Darby's bore and Coopers Creek. The water analysis for Darby's bore is provided in Appendix G.

The average initial Ca concentration of Darby's bore water is 88.3 mg/L (ppm). Therefore the Darby's water needed to be diluted by a factor of 2.2 with Coopers Creek to achieve a concentration of 40 ppm. The average chloride concentration of Darby's bore water is 380 mg/L (ppm). Therefore the chloride concentration for the mixed water would be 380/2.2 = 173 ppm. From this information, the concentration for the NaCl solution is 285 ppm. However, a concentration of 250 ppm NaCl solution was chosen (containing 151 ppm chloride).

5.1.4.1 Materials and experimental

The materials used in the granite dissolution experiment are rock sample with particle size distribution 100 – 200 µm, 250 ppm NaCl, and 4% HNO_3. The rock samples were prepared following the procedures detailed in Chapter 4.2 and the start-up procedures as specified in Section 5.1.1.2 using the NaCl solution. Fluid-rock interaction experiments were performed at 200^{o}C for 1, 3, 7, 14, 21 and 56 days in an oven at saturated vapour pressure. At the conclusion of every experimental period, the procedures outlined in Section 5.1.2.1 were followed.

5.1.4.2 Results and discussion

Results show that the reactive silica concentration increases with time, and the equilibrium reactive silica concentrations at 200°C are approximately similar for water and 250 ppm NaCl solution.

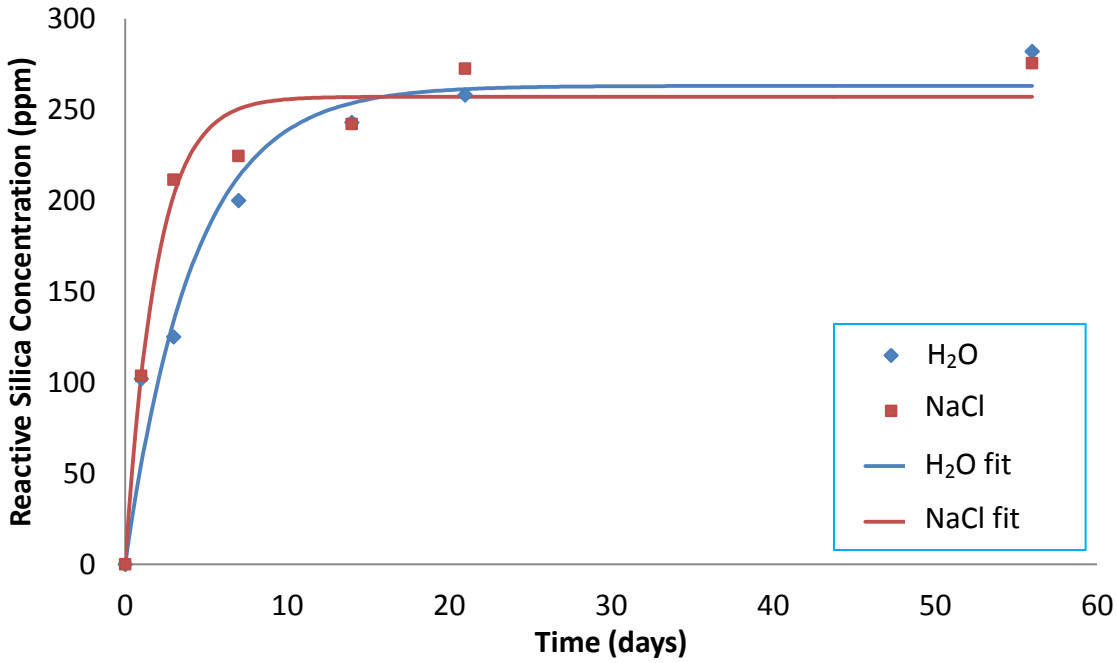

Figure 5.19 Comparison of granite dissolution profile in water and 250 ppm NaCl solution at 200°C in autoclave

The results showed that the system achieved equilibrium in the 250 ppm NaCl solution at a faster rate. The result is presented in Figure 5.19. SigmaPlot software was used to fit the experimental results according to the model from Equation (2.55) to obtain the equilibrium silica concentration and dissolution rate constant. The result is shown in Figure 5.19. The constants obtained from Sigmaplot are shown in Table 5.9. After converting to the appropriate units, the dissolution rate constants were then calculated according to Section 5.1.2.2 using Equations (5.4) and (5.5). The results of the conversions are given in Table 5.10. The calculated results of the dissolution rate constants based on geometric surface area and BET are given in Table 5.11 and Table 5.12, respectively.

Table 5.9 Constants from SigmaPlot for granite dissolution in water and NaCl solution at 200°C

Medium	a_0 *(ppm)*	a_1 *(d^{-1})*	*Standard error of estimate (ppm)*
Water	263.07	0.2375	24.04
NaCl	257.13	0.5197	17.54

Table 5.10 Calculated equilibrium silica concentration (molal) and $k^{\#}$ (s^{-1}) in water and NaCl solution at 200°C

Medium	$m^{sat}_{H_4SiO_4}$*(molal)*	$k^{\#}$ *(s^{-1})*
Water	0.0044	2.75×10^{-6}
NaCl	0.0043	6.02×10^{-6}

Table 5.11 Granite dissolution rate constant in water and NaCl solution based on geometric surface area

Medium	Geometric k_f $(mol/m^2 \cdot s)$	$ln(k_f)$	$log(k_f)$
Water	2.60×10^{-8}	-17.465	-7.5849
NaCl	5.58×10^{-8}	-16.702	-7.2537

Table 5.12 Granite dissolution rate constant in water and NaCl solution based on BET surface area

Particle size (μm)	BET k_f $(mol/m^2 \cdot s)$	$ln(k_f)$	$log(k_f)$
Water	8.52×10^{-10}	-20.884	-9.0697
NaCl	8.52×10^{-10}	-20.884	-9.0697

It is seen that the dissolution rate with the presence of NaCl is roughly double compared to that of pure water (based on both geometric and BET surface area). According to Dove and Crerar (1990), the presence of electrolytes increases the reaction rate. In their study, they observed

that the reaction rates increase with increasing electrolyte concentration up to 0.05 molal, and no further increase at higher concentrations.

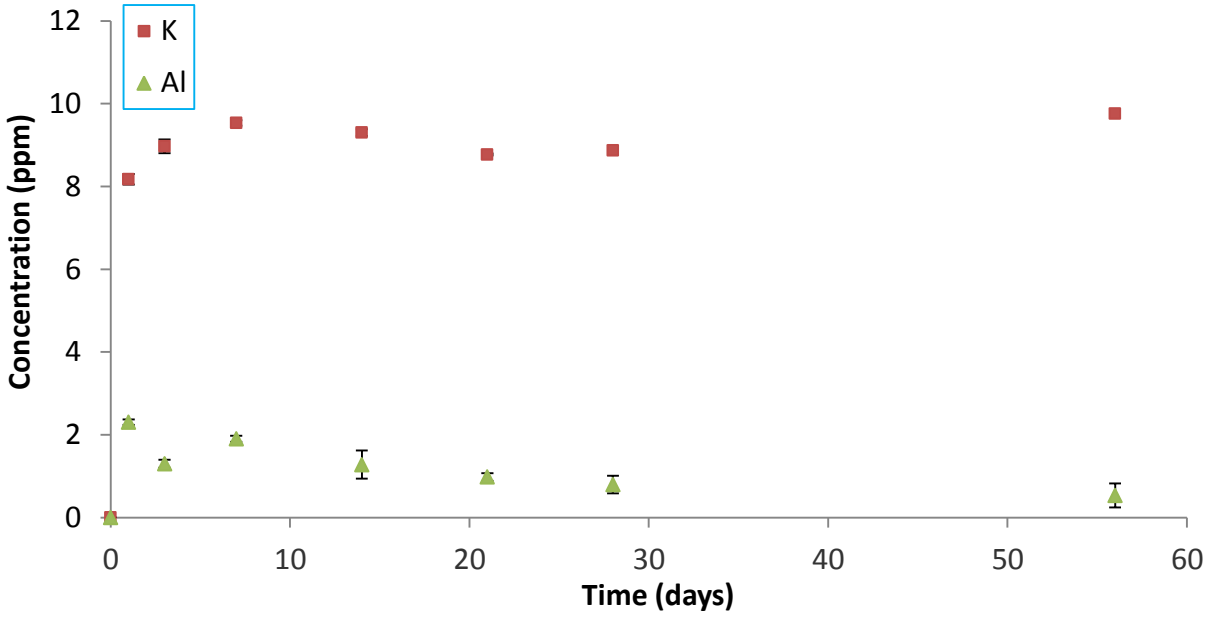

Figure 5.20 Concentration of dissolved K and Al from granite dissolution in 250 ppm NaCl at 200°C using 100 – 200 µm particle size

The dissolved K and Al concentration from granite dissolution in 250 ppm NaCl solution at 200°C is presented in Figure 5.20. The presence of K and Al verifies that the feldspars dissolved to the liquid phase. It is seen that the concentration of K increased initially, but then decreased to day 30, and followed by a slight increase at the end of the experiment. The concentration of Al increased precipitously on day 1 and decreased over the subsequent 56 days. This may be caused by mineral re-precipitation. Further investigation of mineral re-precipitation may be suggested for future studies. Another possibility is the starting sample for 1, 3, 7, 14, 21 and 56 days may not have the exact same mineral composition. The concentrations of Na were not included in the plot, since the concentration of sodium ions from the NaCl solution were relatively much higher compared to K and Al concentrations, and thus resulted in difficulties to distinguish the Na release from albite dissolution. As mentioned in previous sections, no attempt was made to generate dissolution rate constant of albite and K-feldspar from the

concentrations of K or Al, since it was assumed that the granite is one mineral as a whole, and the dissolution rate was measured from the release of silica to the solution. The complete data is provided in Appendix B.4.

5.1.5 Influence of pH on granite dissolution kinetics

This experiment was conducted to observe the effect of pH on the release of silica to solution. Four different pH buffer solutions were chosen.

5.1.5.1 Materials and experimental

The materials used to determine the equilibrium silica concentration are the rock sample with particle size distribution 100 – 200 µm, and pH 4, 7, 10 and 13 buffer solutions. The measured values of the pH buffer solutions are: 3.94, 6.85, 10.50, and 13.66. A summary of the composition of the buffer solution is given in Table 5.13 Composition of pH buffers. The volume of each buffers prepared were 250 mL.

Table 5.13 Composition of pH buffers and calculated pH at 200°C

Buffer	Measured at 25°C	Calculated for 25°C	Calculated for 200°C	Composition (molal)
pH 4	3.86	3.996	4.682	0.1656m CH_3COOH + 0.0343m CH_3COONa[a]
pH 7	6.85	7.010	6.517	0.2m H_3BO_3 + 0.0006m $Na_2B_4O_7.10H_2O$[b]
pH 10	9.85	10.03	9.052	0.05m H_3BO_3 + 0.044m NaOH[a]
pH 13	13.23	12.97	10.16	0.05m KCl + 0.1320m NaOH[a]

[a]) Qian et al (2010)

[b]) The University of Oklahoma (2013)

The rock samples were prepared following the procedures detailed in Chapter 4.2 and the start-up procedures as specified in Section 5.1.1.2 using the buffer solutions. Fluid-rock interaction experiments were performed at 200°C for seven different experimental periods in an oven at saturated vapour pressure. At the conclusion of every experimental period, the procedures outlined in Section 5.1.2.1 were followed.

5.1.5.2 Results and discussion

This section presents reactive silica concentrations from granite dissolution experiments in buffer solutions that have been compared with dissolution experiments in water. The complete data set is provided in Appendix B.5. Granite dissolution experiment in pH 4 buffer solution (pH 4.862 at 200°C) is provided in Figure 5.21. Results show that the reactive silica concentration increases with time in for both in buffer solution and pure water. It is seen that different equilibrium silica concentrations were achieved. A study by Knauss and Wolery (1988) concluded that the dissolution rate for quartz is independent of pH over the range pH 1 to pH 6 and suggested that only water was involved in the breaking of the Si – O bond. A study by Huang and Kiang (1972) confirmed that silica concentration from albite dissolution in organic acid was higher compared to that in pure water. In addition, a study by Bevan and Savage (1989) demonstrated that silica concentration from K-feldspar dissolution was higher in organic acid (pH ≈ 4) compared to that in pure water. Thus, the higher equilibrium silica concentration observed in the pH 4 buffer would have been caused by the presence of organic acid, as the pH 4 buffer used contains acetic acid.

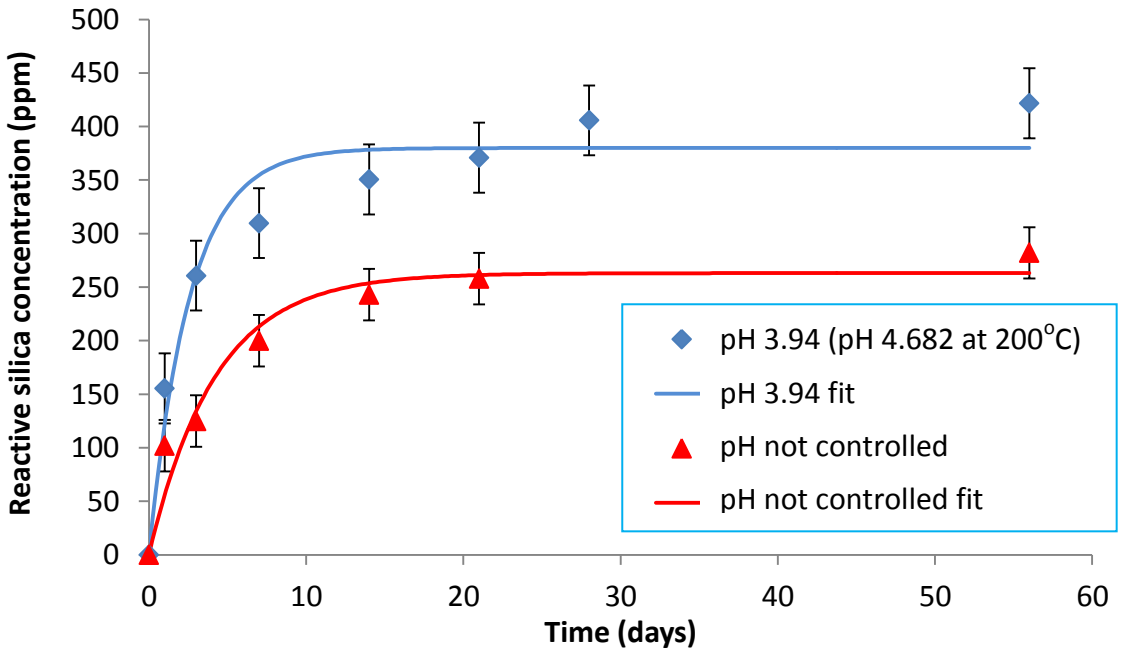

Figure 5.21 Comparison of granite dissolution profile in water and pH 4 buffer solution at 200°C in autoclave

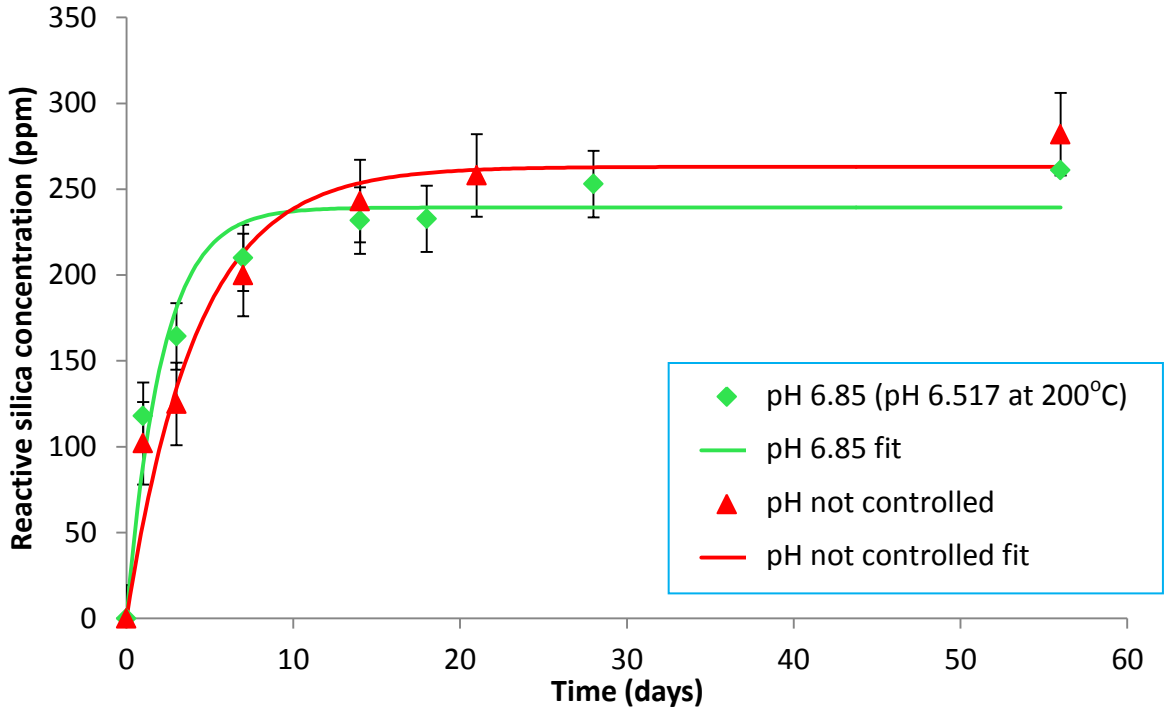

Figure 5.22 Comparison of granite dissolution profile in water and pH 7 buffer solution at 200°C in autoclave

According to Bevan and Savage (1989), the dissolution rate in organic acid was higher when compared to pure water and the increase in dissolution rate was due to the change of the pH-dependent mechanism of feldspar dissolution, and not affected by the preferential complexation of aluminium and/or silica. The result for granite dissolution experiment in pH 7 buffer solution (pH 6.517 at 200°C) is provided in Figure 5.22. Results show that the reactive silica concentration increases with time in both buffer solution and pure water. It is seen that similar equilibrium silica concentrations and similar dissolution rate were achieved. A slightly higher silica concentration in the uncontrolled pH experiment may be caused by the increase in pH after the dissolution reaction commenced and progressed. As the pH is greater than 8, the dissolved silica species that is significant is not solely $SiO_{2(aq)}$ or H_4SiO_4. The hydrogen atoms from H_4SiO_4 can dissociate as (Brown, 2011b):

$$H_4SiO_4 \rightleftharpoons H^+ + H_3SiO_4^- \quad \textbf{(5.11)}$$

The charged $H_3SiO_4^-$ ion is very soluble in water, so there is a large increase in silica solubility at higher pH as the silicic acid becomes dissociated (Brown, 2011b).

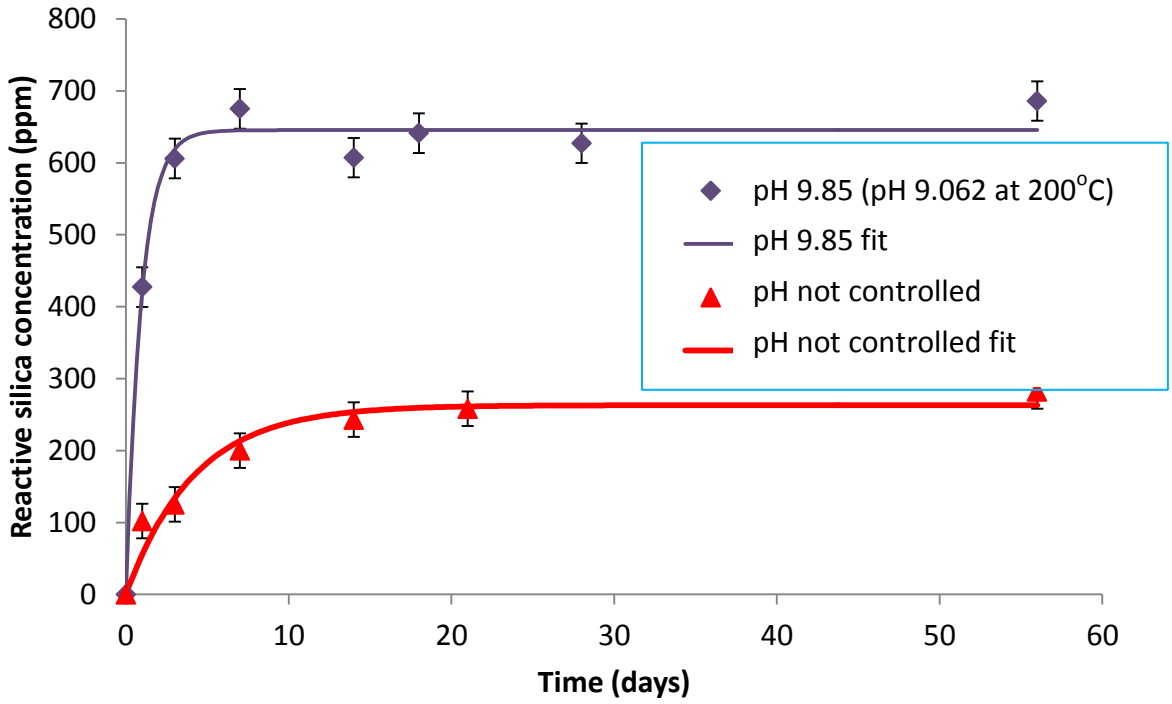

Figure 5.23 Comparison of granite dissolution profile in water and pH 10 buffer solution at 200°C in autoclave

Since pH was controlled at 6.85, the concentration of monomeric silica specie $H_3SiO_4^-$ is low and not significant. This condition may also explain the higher silica concentration from granite dissolution in pH buffer 10 (pH 9.052 at 200°C) and pH buffer 13 (pH 10.16 at 200°C). The experimental results for granite dissolution experiment in pH 10 buffer solution and pH 13 buffer solution are provided in Figure 5.22 and Figure 5.23, respectively. It is seen that the difference of the silica concentrations in higher pH buffers are more pronounce compared to the results from dissolutions in pure water. According to Brown (2011b), it seems that at very high pH further hydrogen dissociation is possible to form $H_2SiO_4^{2-}$ which is also soluble in water and may further increase the silica concentration.

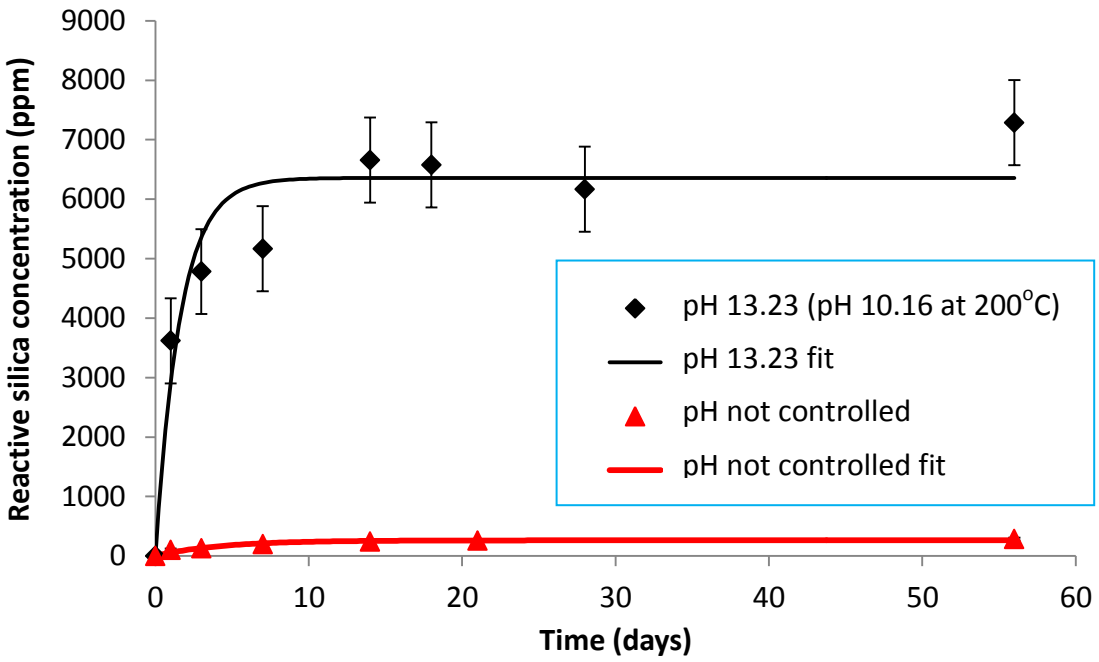

Figure 5.24 Comparison of granite dissolution profile in water and pH 13 buffer solution at 200°C in autoclave

SigmaPlot was used to fit the experimental results according to the model from Equation (2.55) to obtain the equilibrium silica concentration and dissolution rate constant. The constants obtained from Sigmaplot are shown in Table 5.14. After converting to the appropriate units, the dissolution rate constants were then calculated according to Section 5.1.2.2 using Equations (5.4) and (5.5). The results of the conversions are given in Table 5.15. The calculated results of the dissolution rate constants based on geometric surface area and BET are given in Table 5.16 and Table 5.17, respectively.

Table 5.14 Constants from SigmaPlot for various pH

Buffer Solution (at 200°C)	a_0 *(ppm)*	a_1 *(d^{-1})*	*Standard error of estimate (ppm)*
pH 4.682	379.94	0.3868	32.67
pH 6.517	239.32	0.4699	19.34
pH 9.052	645.44	1.0651	27.43
pH 10.16	6357.2	0.6164	628.4

Table 5.15 Calculated equilibrium silica concentration (molal) and $k^{\#}$ (s^{-1}) in water for various pH

Buffer solution (at 200°C)	$m^{sat}_{H_4SiO_4}$(molal)	$k^{\#}$ (s^{-1})
pH 4.682	0.0063	4.48×10^{-6}
pH 6.517	0.0040	5.44×10^{-6}
pH 9.052	0.0107	1.23×10^{-5}
pH 10.16	0.1058	7.13×10^{-6}

Table 5.16 Dissolution rate constant for various pH buffer solutions based on geometric surface area

Buffer solution (at 200°C)	Geometric k_f $(mol/m^2 \cdot s)$	$ln(k_f)$	$log(k_f)$
pH 4.682	6.10×10^{-8}	-16.612	-7.2145
pH 6.517	4.65×10^{-8}	-16.883	-7.3321
pH 9.052	2.85×10^{-7}	-15.072	-6.5459
pH 10.16	1.62×10^{-6}	-13.330	-5.7893

Table 5.17 Dissolution rate constant for various pH buffer solutions based on BET surface area

Buffer solution (at 200°C)	BET k_f $(mol/m^2 \cdot s)$	$ln(k_f)$	$log(k_f)$
pH 4.682	2.00×10^{-9}	-20.031	-8.6993
pH 6.517	1.52×10^{-9}	-20.302	-8.8169
pH 9.052	9.32×10^{-9}	-18.491	-8.0306
pH 10.16	5.32×10^{-8}	-16.749	-7.2741

Changes of the dissolution rate constant at different pH were presented in Figure 5.25 for geometric based surface area and Figure 5.26 for BET based surface area. The results were compared to the study by Brantley (2008) and shows a similar curve. The results from this study agrees that the dissolution rate increase at alkaline conditions (pH>8), and acidic conditions (pH<5).

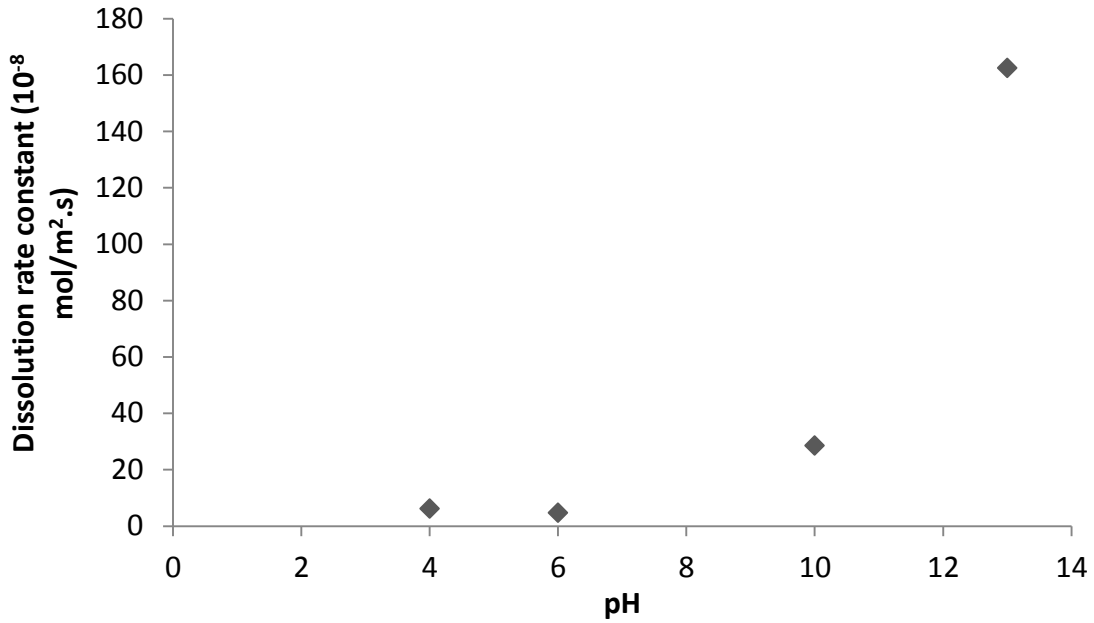

Figure 5.25 Comparison of dissolution rate constants in pH buffer solutions at 200°C in autoclave using geometric surface area basis

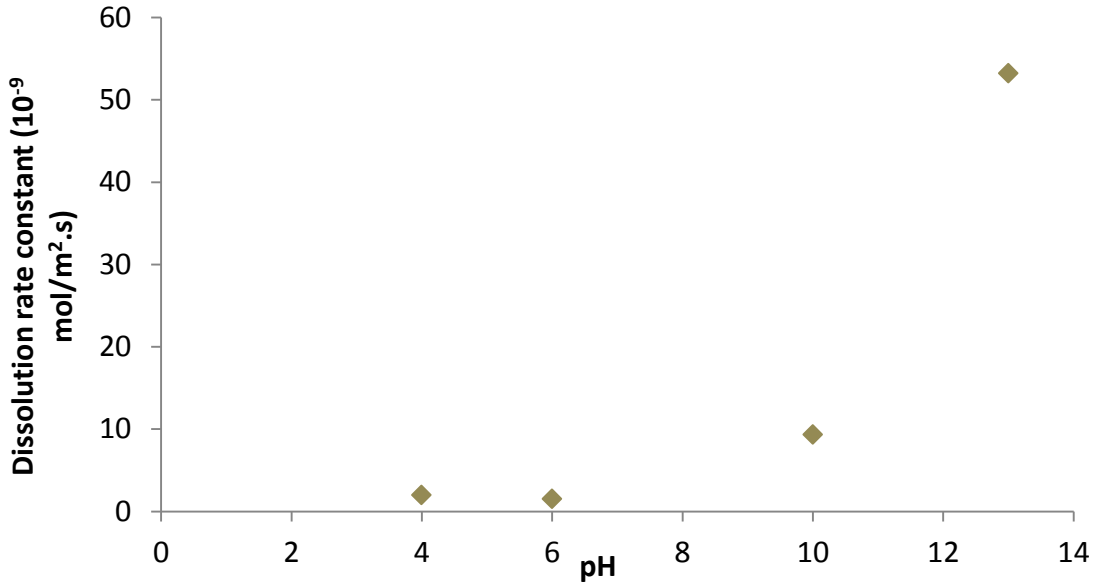

Figure 5.26 Comparison of dissolution rate constants in pH buffer solutions at 200°C in autoclave using BET surface area basis

5.2 Flow-through System

The second experimental system used to explore fluid-rock interaction is a closed loop flow-through set up. This flow-through system was designed to mimic the actual geothermal site, where water flows through a porous medium. Two different cell arrangements were used, recycled and non-recycled fluid, or open and closed loop systems. The geothermal cell operates by exploiting the thermosiphon principle, where the flow inside the cell is driven by the temperature difference along the cell. The detailed arrangements and parts of this geothermal cell are given in Section 5.2.1.

5.2.1 Initial design of the hydrothermal cell

The design of the hydrothermal cell was initially developed for the *in situ* neutron diffraction of crystallization and phase transitions (O'Neill et al., 2006). The preliminary design was based on a loop which consists of a reservoir with electrical heater, sample cell, double pipe heat exchanger and tubing connecting these three major items. A schematic diagram of the loop is

given in Figure 5.27. In this preliminary design, air is used as the cooling medium. A liquid coolant (e.g. water) would also be possible to be used as the cooling medium; however a cooling bath would be required to prevent vaporization and generation of low pressure steam.

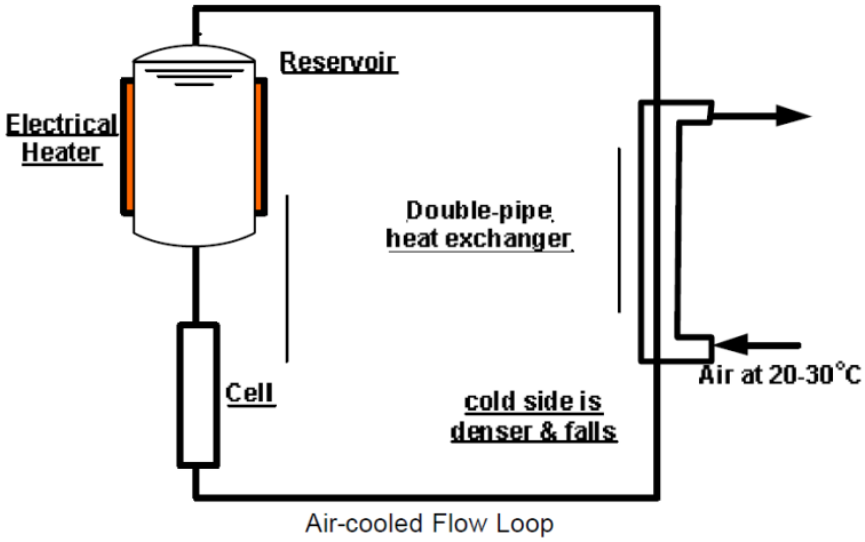

Figure 5.27 Air-cooled flow loop

This is a highly simplified model of the actual situation. The major difficulty with the thermosyphon (assuming that energy input occurs only in the reservoir) is that flow is in the wrong direction. It is crucial to ensure that the fluid flows in the correct direction. The reservoir needs to be hotter than the cell. It is possible to estimate the likely flow rate in the loop as this will determine necessary energy inputs for both heating and cooling. For this loop, an assumption that length L ~ W (width) was made. This assumption may be revised later.

$$\Delta P_{density\ difference} = (\rho(T_o) - \rho(T))g\Delta L \qquad \textbf{(5.12)}$$

where: $\rho(T_o)$ = the density at the cold leg (kg/m^3)

$\rho(T)$ = the density at the cold leg (kg/m^3)

g = gravitational acceleration $\left({}^{m}/_{s^2}\right)$

ΔL = length (m)

The assumption $\Delta L \sim \frac{L}{3}$ is based on the temperature profile. For a smooth pipe, the $\Delta P_{friction}$ is:

$$\Delta P_{friction} = f\left(\frac{\rho_{average} v^2}{2}\right) \times \left(\frac{2L + 2W}{D}\right) \cong 2fL\left(\frac{\rho_{average} v^2}{D}\right) \; for \; L \cong W \qquad \textbf{(5.13)}$$

where: f = the friction factor

ρ = density (kg/m^3)

v = flow velocity $(^m/_s)$

D = tube diameter (m)

To estimate the flow velocity inside the hydrothermal cell, it was assumed that $L \sim W$:

$$\Delta P_{friction} = 2fL\left(\frac{\rho_{average} v^2}{D}\right) \qquad \textbf{(5.14)}$$

Combining Equations (5.12) and (5.13):

$$(\rho(T_o) - \rho(T))g\frac{L}{3} = 2fL\left(\frac{\rho_{average} v^2}{D}\right) \; where \; \rho_{average} = \frac{(\rho(T_o) - \rho(T))}{2}$$

Rearranging:

$$v = \sqrt{\frac{(\rho(T_o) - \rho(T))gD}{3(\rho(T_o) - \rho(T))f}} \qquad \textbf{(5.15)}$$

At the design conditions for geothermal application, typical average leg temperature T = 320^{o}C (593K) and T_0 = 300^{o}C (573K). The properties of water at these conditions:

- Density $\rho = 666.8 \; kg/m^3$

  $\rho_0 = 712 \; kg/m^3$

- Viscosity $\mu = 0.90 \times 10^{-4} \; Pa.s$

  $\mu_0 = 0.89 \times 10^{-4} \; Pa.s$

Average conditions can be calculated:

$$\rho_{average} = \left(\frac{666.8 + 712.1}{2}\right) = 689.4\ kg/m^3$$

$$\mu_{average} = \left(\frac{0.89 + 0.9}{2}\right) \times 10^{-4} = 0.895 \times 10^{-4}\ Pa.s$$

Knowing that:

- Inside diameter: 6 mm
- Stainless steel absolute roughness: 0.0457 mm
- Relative roughness: $\frac{\varepsilon}{D} = \frac{0.0457}{6} = 0.0076$

Assuming that Blasius hold for a smooth pipe (Perry and Green, 1997):

$$f = \frac{0.079}{Re^{0.25}},\ \ where\ 4{,}000 < Re < 100{,}000 \qquad \textbf{(5.16)}$$

The equation to calculate the Reynolds number:

$$Re = \frac{D \times v \times \rho}{\mu} \qquad \textbf{(5.17)}$$

Equation (5.16) was used to calculate f after obtaining the Reynolds number, and compare the flow velocity guess to the calculated velocity using Equation (5.15). A trial and error approach was carried out to solve the flow velocity using the Solver add-in from Excel. The obtained flow velocity, $v = 0.129\ {}^{m}/_{s}$. The mass velocity can be calculated using Equation (5.18):

$$\dot{m} = \frac{\pi d^2}{4} \times \rho v \qquad \textbf{(5.18)}$$

$$\dot{m} = \frac{\pi(0.006)^2}{4} \times 689.4 \times 0.129 = 0.0025\ {}^{kg}/_{s}$$

5.2.2 Description of the updated geothermal cell

The set-up of this geothermal cell consist of three reservoirs, sample holder, tubing, valves and temperature measurement devices. A photo of the geothermal cell is given in Figure 5.32. The height and width of the cell is approximately 100 mm and 16 mm, respectively. The total cell volume is approximately 355 mL. The working volume of the cell is approximately 255 mL. The main reservoir is the heating reservoir. This vessel is wrapped with two heating elements that are connected in parallel to obtain similar heat output. The volume of the heating vessel is approximately 150 mL. Placed above the heating reservoir is the sample holder. Attached above the sample holder is a thermocouple which is connected to the heater relay controller to set the temperature. An expansion reservoir is employed to allow fluid expansion and to allow pressure reduction for continuous flow. The volume of the expansion reservoir is approximately 150 mL. A safety relief valve and a pressure relief vessel are employed for safety. The volume of the pressure relief vessel is approximately 300 mL. A pressure regulator is also installed to monitor the pressure. The reservoirs and the sample holder are connected with ¼ inch tubing made from titanium with standard Swagelok titanium fittings. Four thermocouples are installed to monitor the temperature changes throughout the cell and connected to a data logger.

To estimate the velocity inside the hydrothermal cell, it was assumed that $L \sim 6\,W$. Equation (5.15) becomes:

$$v = \sqrt{\frac{(\rho(T_o) - \rho(T))gD}{(\rho(T_o) - \rho(T))f} \times \frac{4}{7}} \qquad \textbf{(5.19)}$$

There were 4 thermocouples installed at different locations to obtain temperature readings of the hydrothermal cell. Water and NaCl 250 ppm solution were used as the circulating fluid. The temperature profile is provided in Figure 5.28. The average temperatures and properties are provided in Table 5.18.

Table 5.18 Data to calculate flow velocity in the hydrothermal cell (water)

Thermocouple	T_{ave} (℃)	$T_{ave}(K)$	$\rho\ (kg/m^3)$	$\mu\ (Pa.S)$
Set point	250.00	523.15	798.89	1.06×10^{-4}
T_1	245.43	518.58	805.57	1.08×10^{-4}
T_2	224.08	497.23	834.92	1.19×10^{-4}
T_3	212.76	485.91	849.15	1.26×10^{-4}
T_4	184.72	457.87	881.71	1.46×10^{-4}

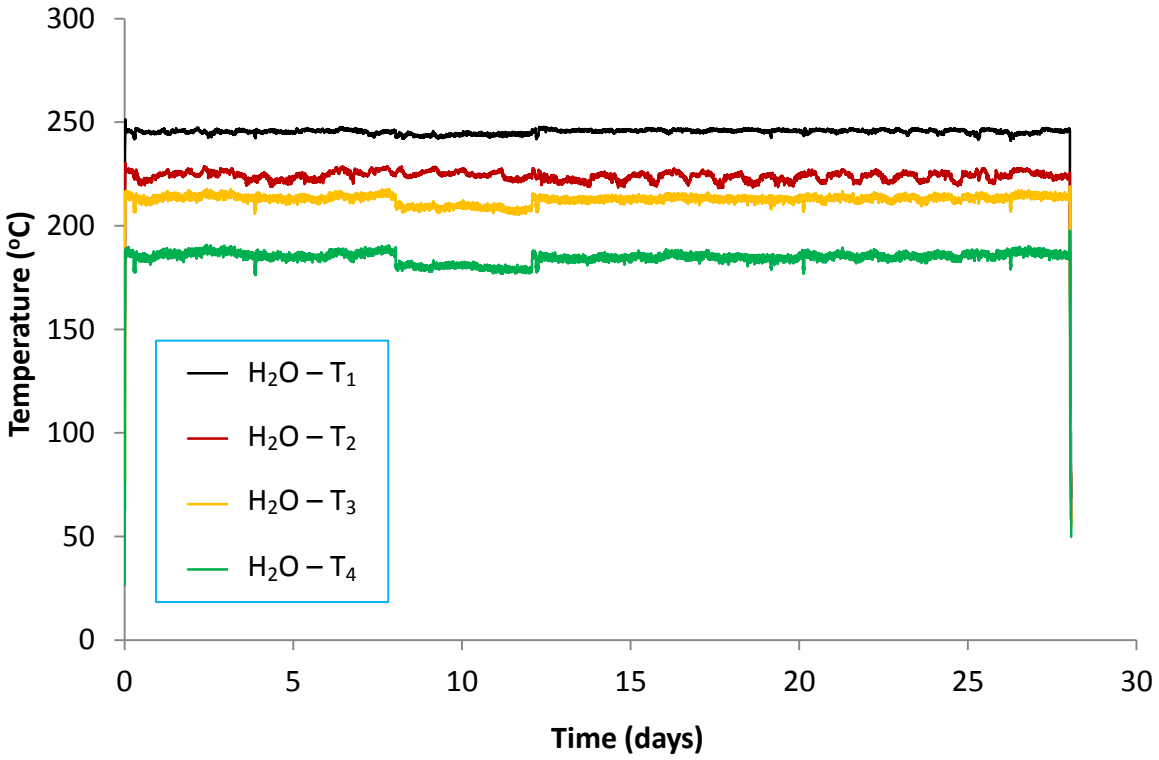

Figure 5.28 Temperature profile of the hydrothermal cell (water)

The approach to estimate the flow velocity in the hydrothermal cell is to calculate the flow between the thermocouples. The flow velocities between thermocouples are presented in Table 5.19.

Table 5.19 Average values between thermocouples (water)

	$\rho_{ave}\ (kg/m^3)$	$\mu_{ave}\ (Pa.S)$	Re	f	$v_{calc}\ (m/s)$
Set point – T_1	802.23	1.07 x 10^{-4}	5556.2	0.0092	0.1237
$T_1 - T_2$	820.25	1.14 x 10^{-4}	12253	0.0075	0.2831
$T_2 - T_3$	842.04	1.22 x 10^{-4}	7554.3	0.0085	0.1831
$T_3 - T_4$	865.43	1.36 x 10^{-4}	5839.1	0.0090	0.1528

The flow velocity in the hydrothermal cell is the average values of the flow velocities between thermocouples, $v_{calc} = 0.1857\ m/s = 18.57\ cm/s$. The mass velocity can be calculated using Equation (5.18), average density is $834.05\ kg/m^3$:

$$\dot{m} = \frac{\pi(0.006)^2}{4} \times 834.05 \times 0.1857 = 0.0044\ kg/s$$

Table 5.20 Data to calculate flow velocity in the hydrothermal cell (NaCl)

Thermocouple	T_{ave} (℃)	$T_{ave}(K)$	$\rho\ (kg/m^3)$	$\mu\ (Pa.S)$
Set point	250.00	523.15	798.89	1.06 x 10^{-4}
T_1	238.71	511.858	815.05	1.11 x 10^{-4}
T_2	224.61	497.7579	834.47	1.19 x 10^{-4}
T_3	214.81	487.9591	846.98	1.25 x 10^{-4}
T_4	189.08	462.2271	877.08	1.42 x 10^{-4}

Table 5.21 Average values between thermocouples (NaCl solution)

	$\rho_{ave}\ (kg/m^3)$	$\mu_{ave}\ (Pa.S)$	Re	f	$v_{calc}\ (m/s)$
Set point – T_1	806.97	1.09 x 10^{-4}	9080.21	0.0081	0.2040
$T_1 - T_2$	824.76	1.15 x 10^{-4}	9562.79	0.0080	0.2226
$T_2 - T_3$	840.73	1.22 x 10^{-4}	7054.00	0.0086	0.1704
$T_3 - T_4$	862.03	1.34 x 10^{-4}	5677.79	0.0091	0.1467

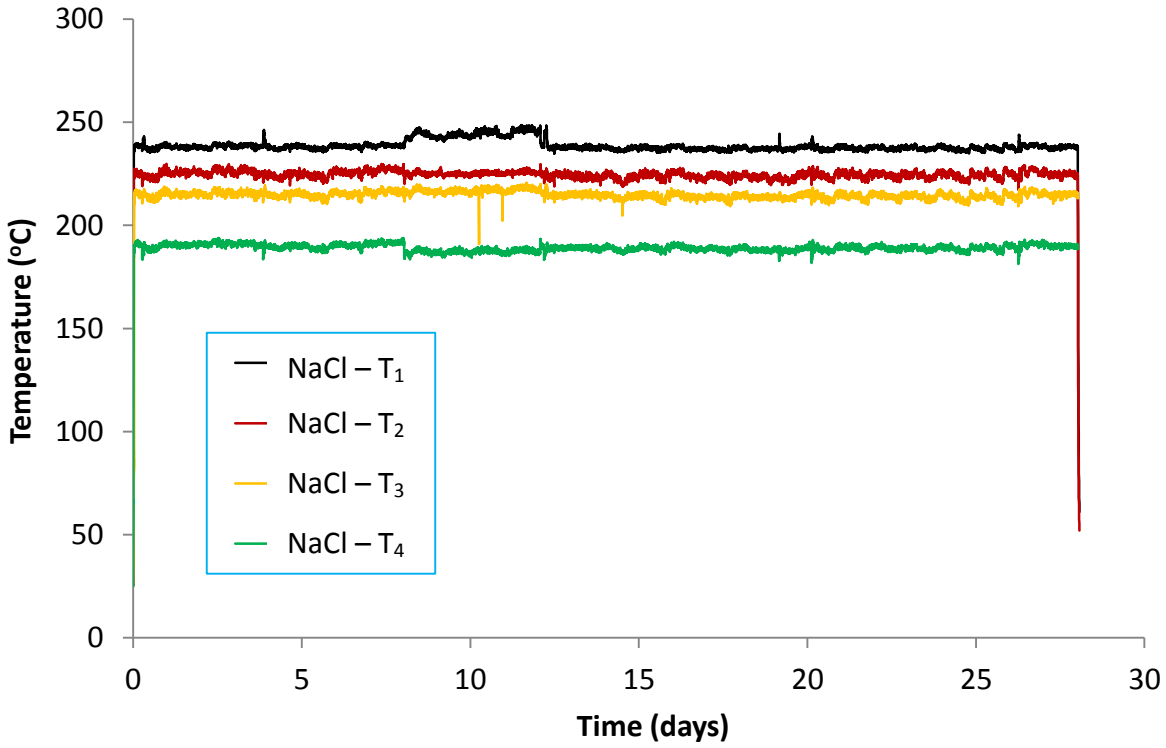

Figure 5.29 Temperature profile of the hydrothermal cell (NaCl solution)

The method above was again followed to estimate the flow velocity in the hydrothermal cell used for the experiment using NaCl solution 250 ppm. Since the concentration is very low, it was assumed that the properties are similar with pure water. The temperature profile is provided in Figure 5.29. The average temperatures and properties are provided in Table 5.20. The flow velocities between thermocouples are provided in Table 5.21. The flow velocity in the hydrothermal cell is $v_{calc} = 0.1859\ {}^{m}/_{s} = 18.59\ {}^{cm}/_{s}$. The mass velocity can be calculated using Equation (5.18), average density is $834.05\ kg/m^3$:

$$\dot{m} = \frac{\pi(0.006)^2}{4} \times 834.05 \times 0.1859 = 0.0044\ \ kg/s$$

5.2.3 Materials and preparation of the geothermal cell

The materials used to determine the equilibrium silica concentration are purified water (Milli-Q) and the rock sample with particle size distribution 100 – 200 µm. Two concentration of nitric acid were prepared, 0.1M and (4%), respectively.

5.2.4 Sample basket preparation

The sample basket is used to enclose the sample and maintain the sample to be in the sample holder and not circulating with the fluid. The sample basket is made from a 316 stainless steel woven mesh. Stainless steel was used to minimize the potential of corrosion. This stainless steel mesh was obtained from Locker Group Pty Ltd. The specifications of the woven wire mesh are woven 325 mesh x 49 SWG (standard wire gauge). This mesh size would be suitable to hold particle size greater than 35 µm. Approximately 10 cm x 10 cm of stainless steel mesh was cut. Then the wire mesh was rolled using a size 6 hex key to obtain the required diameter to fit the sample holder. One end of the wire basket was enveloped using pliers and further tightened with a vise. The other end was left open for latter sample loading. Size of sample basket may vary depending on sample size. This empty sample basket was weighed and weight recorded. The rock sample was then weighed and weight was recorded. This sample is loaded to the sample basket and the basket was closed using pliers and further tightened. The filled sample basket was weighed and total weight was recorded. The prepared sample was placed in a desiccator for moisture removal. After approximately 24 hours or no weight change was observed, the sample is ready for use. An image of the sample baskets are provided in Figure 5.30.

Figure 5.30 Photo of sample baskets (from left to right: 0.7 g sample, 3 g sample, 7 g sample)

Prior to first use, the geothermal cell apparatus was flushed with 0.1 M nitric acid to provide a passive oxide layer on the inside surface of the titanium tubing to minimize titanium dissolution. The cell was then rinsed with pure water to remove any contaminating acid. The pH of the rinsed water was measured to ensure acid has been removed thoroughly.

5.2.5 Experimental procedures

The cell is flushed with 0.1 M nitric acid to ensure that a passive oxide layer builds up on the surface of the titanium tubing in order to minimize titanium dissolution. The cell is then rinsed with deionised water to remove any contaminating acid. The pH of the rinsed water is then measured to ensure that the nitric acid has been rinsed out. Prior to introducing the circulating fluid, the pre-weighed basket was placed in the sample holder, just above the heated vessel (see Figure 5.31). Using approximately 0.7 g of rock sample wrapped in stainless steel mesh basket, fluid-rock interactions were performed for 1, 3, 7, 14, 21, and 28 days.

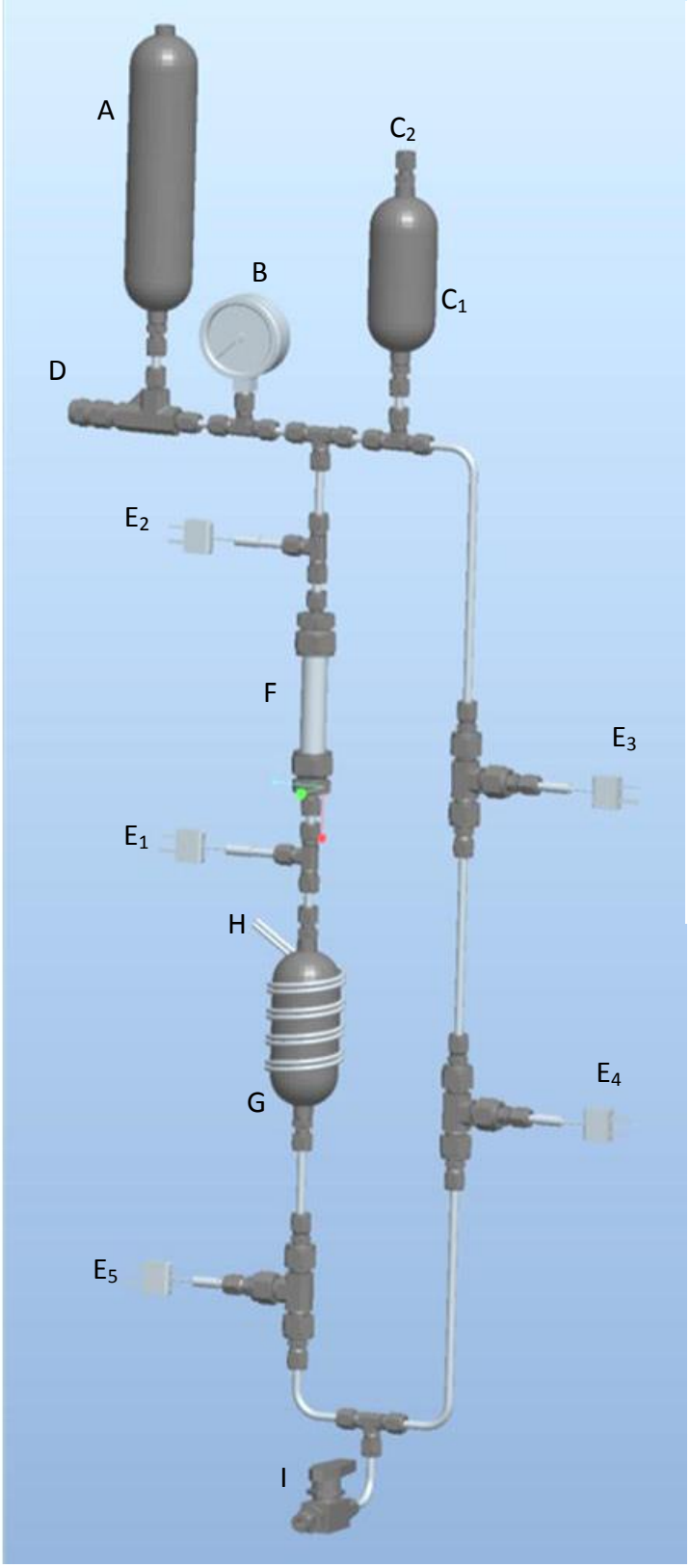

A : Pressure relief vessel

B : Pressure gauge

C_1 : Expansion reservoir

C_2 : Expansion reservoir cap

D : Safety relief valve

E_1 : Thermocouple 1

E_2 : Thermocouple for set point

E_3 : Thermocouple 2

E_4 : Thermocouple 3

E_5 : Thermocouple 4

F : Sample holder

G : Heating vessel/reservoir

H : Heating element

I : Ball valve to charge and discharge the cell

Figure 5.31 Updated geothermal cell

Figure 5.32 Geothermal flow-through cell

It was ensured that the basket did not disrupt the connecting fittings, and that the sample holder has been refitted tightly to avoid leakage. Water was filled from the bottom of the cell through the ball valve to minimise air bubbles inside the cell. A clear hose was connected to the expansion reservoir. At the point where the circulating fluid (water or NaCl solution) overflows through the hose, indicates that the cell is full. Some amount of water is required to be removed to allow expansion caused by heating. Knowing that:

at T = 20^{o}C, the volume is 1.0018 mL/g

at T = 250^{o}C, the volume is 1.2517 mL/g (~ mL/mL)

The volume of water at 250^{o}C is:

$$355 \times 1.2517 = 444.35\ mL$$

The available cell volume is only 355 mL, thus the volume of water required to be removed:

$$444.3535 - 355 = 89.35\ mL$$

For additional safety measure, it was chosen that the working volume would be 255 mL. Thus, instead of $89.35\ ml$, 100 mL water was removed from the cell to allow expansion. After 100 mL of water has been removed, the ball valve was closed. The temperature controller was set to 100^{o}C and slowly increased to 250^{o}C. This is done in order to detect any premature water or steam leakage. The working pressure will rise to the vapour pressure of 35 – 40 bar (at 250^{o}C). The temperature readings were recorded using a data logger and the pressure was manually monitored regularly. The experiment was run for the specified period. At conclusion of the interaction, the temperature controller was set to room temperature to allow the cell to cool and depressurize to atmospheric pressure (approximately 2 hours). The liquid was then sampled via the ball valve and collected for pH measurements. The liquid sample was then diluted to 1:10 ratio and preserved in 4% nitric acid. The samples were then stored for liquid analysis. The sample holder was then taken apart to collect the wire basket containing the sample. The sample was then dried in an oven at 120^{o}C for 48 hours. The basket was weighed after it is cooled in a desiccator for 24 hours (no weight change). The weight was recorded and

kept in a dessicator for rock analyses. The liquid sample and rock sample were analysed following the procedures outlined in Section 5.1.2.1. After each run, the cell was filled with 255 mL pure water and heated to 250^{o}C for 24 hours to wash the cell and to recover any lost dissolved silica. The non-recycled method (replacing water every 24 hours) is identical to the method described in Section 5.2.5, however, only the liquid was sampled and the rock sample remains in the sample holder. The procedure was repeated until the specified experimental period has been reached.

5.2.6 Results and discussion

This section presents the results for the recycled system and the replacing fluid system. The results consist of plots of dissolved silica concentration versus the interaction time period. Plots of major elements versus time were also provided.

5.2.6.1 Recycled system

In mineral dissolution kinetics, researchers have calculate silicate dissolution rates solely based on the release of silica to solution (Rimstidt and Barnes, 1980; Lasaga, 1984; Huang et al., 1986; Knauss and Wolery, 1986; Hellmann, 1994). This study measured the release of silica to solution to obtain the granite dissolution rate. Instead of identifying separately the dissolution rate for albite, quartz, and K-feldspar, the dissolution of granite was seen as one unit, as the scope of this study is to identify the silica dissolution rate from granite. The concentration of silica from granite dissolution in pure water with varying sample weight is provided in Figure 5.33. The complete data is provided in Appendix C. As expected, the concentration of silica increases with time and with increasing sample size. An increase in sample size would indicate an increase in surface area. With a larger amount of rock sample introduced to the system, more fine particles may exist for initial dissolution, therefore, more samples dissolved. As well, a decrease in solid/liquid ratio (increase in fluid/solid ratio) would indicate an increase in reaction rate. The results are provided in Table 5.22 to Table 5.26. These experimental results agree with the finding from a study by Huang et al. (1986), where the release rate of silica into solution increases with increasing fluid/rock ratio.

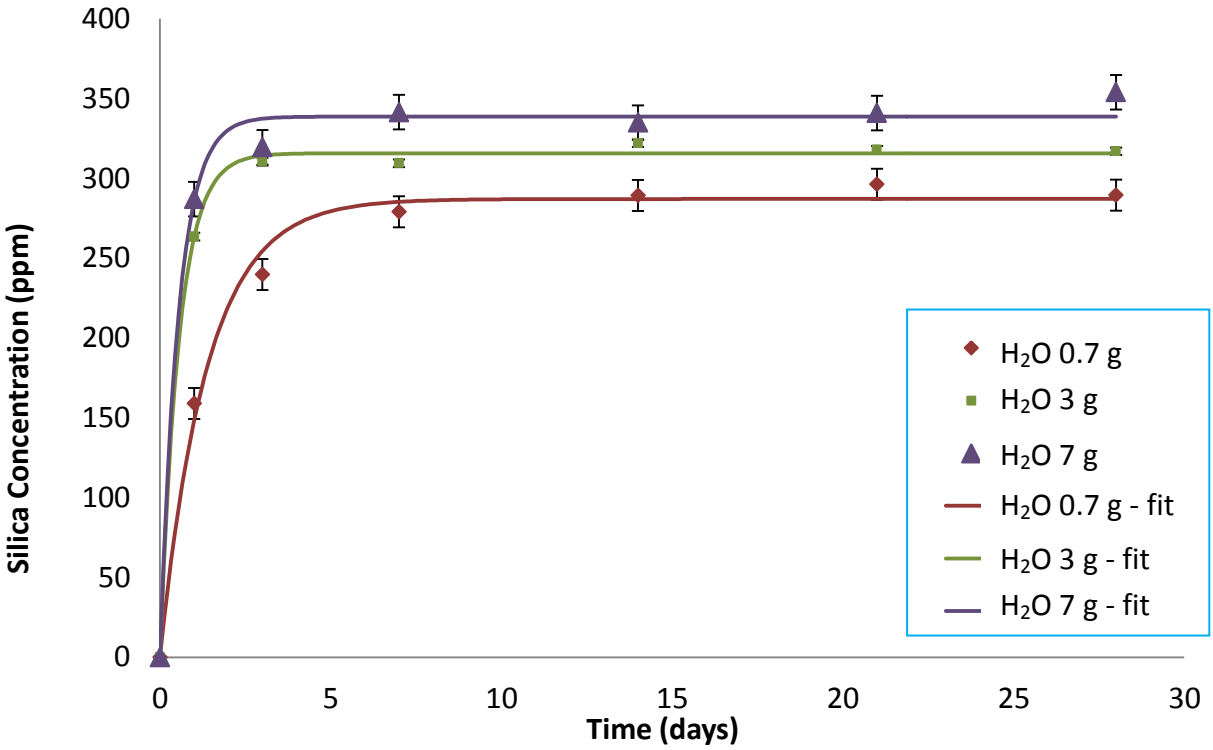

Figure 5.33 Dissolution in water with varying sample weight

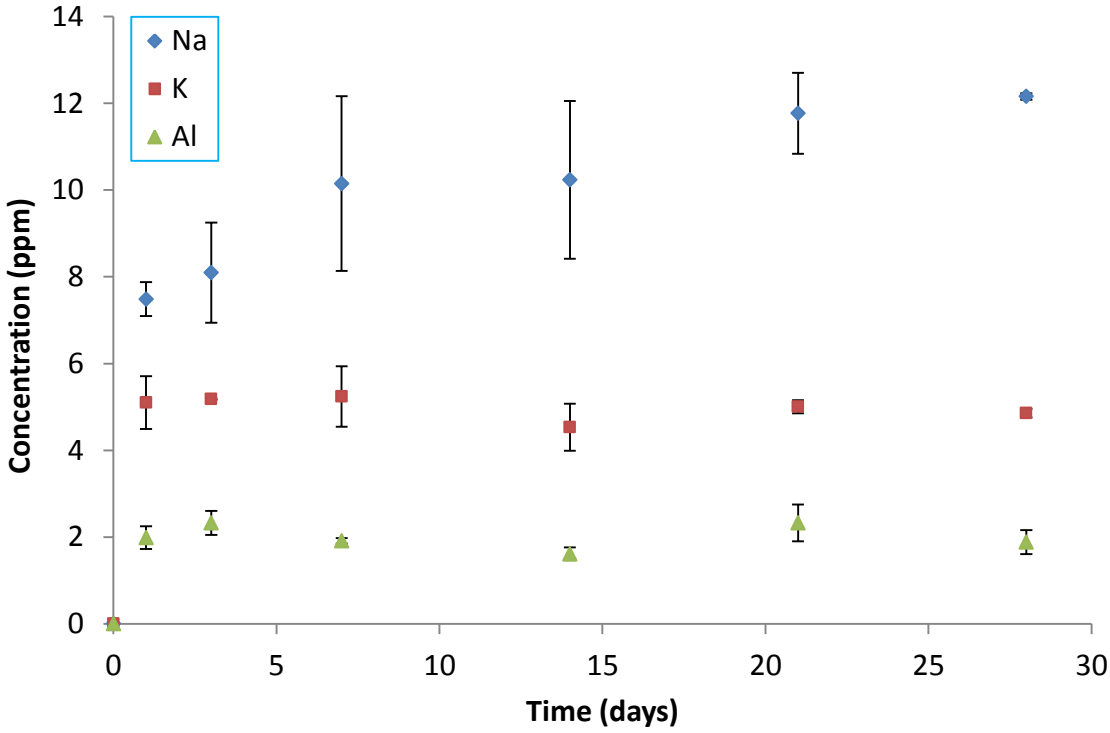

Figure 5.34 Concentration of dissolved Na, K, and Al in water with 0.7 g granite sample

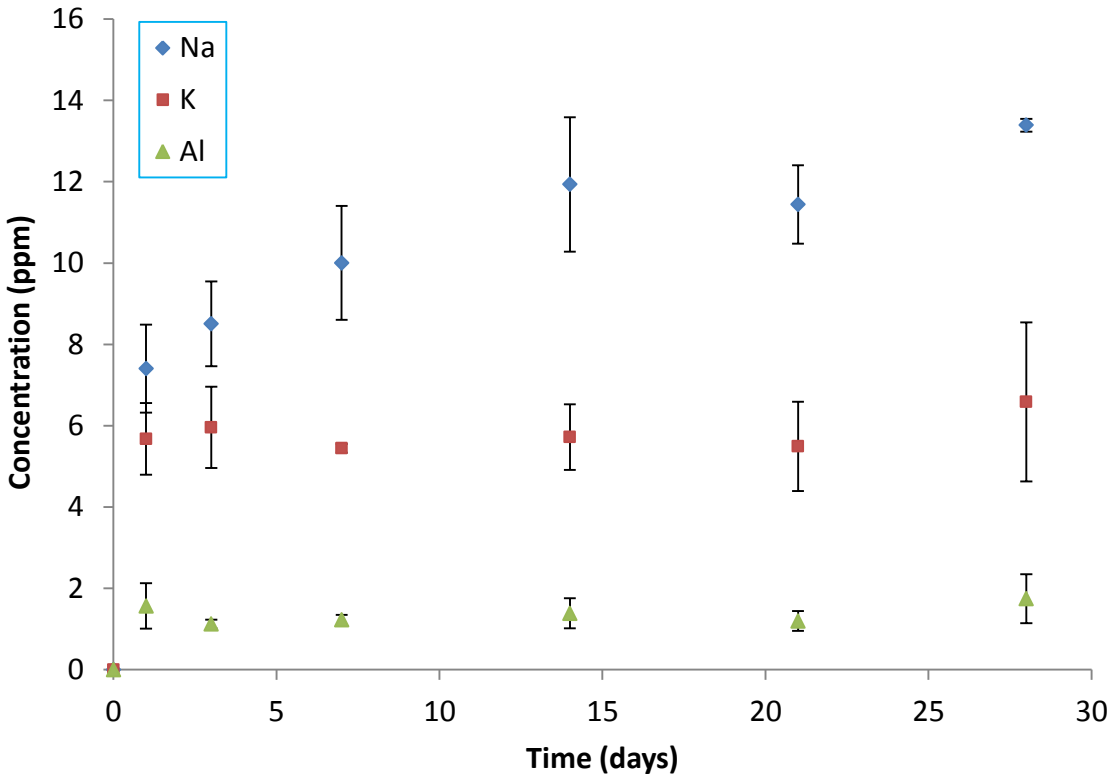

Figure 5.35 Concentration of dissolved Na, K, and Al in water with 3 g granite sample

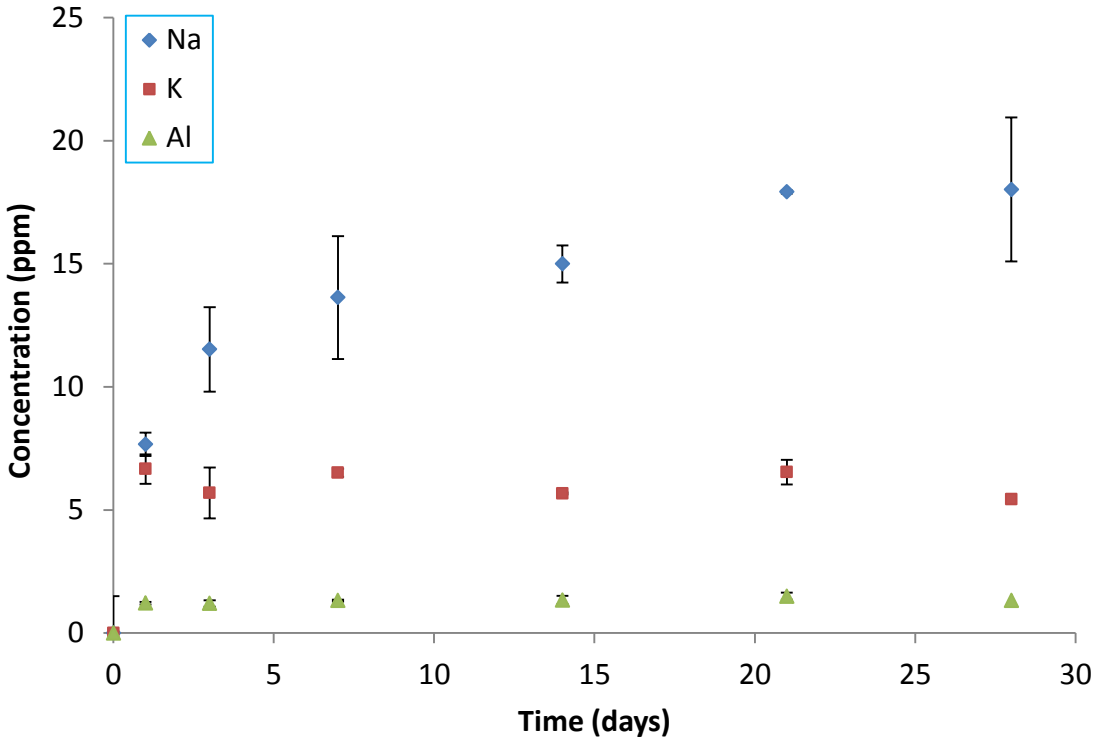

Figure 5.36 Concentration of dissolved Na, K, and Al in water with 7 g granite sample

The dissolved major elements from 0.7 g sample, 3 g sample and 7 g sample are provided in Figure 5.34, Figure 5.35, and Figure 5.36, respectively. The presence of Na, K and Al verifies the dissolution of feldspars from the granite to the liquid phase. As mentioned in the previous section, no attempt was made to generate dissolution rate constant of albite and K-feldspar from the concentrations of Na, K or Al, since it was assumed that the granite is one phase as a whole, and the dissolution rate was measured from the release of silica to the solution.

Although, dissolution of the stainless steel parts of the hydrothermal flow-through cell and/or the stainless steel basket may increase the concentration of aluminium. The concentration of Al seems to be depleted in the liquid phase. This was also observed in the study of albite dissolution by Huang et al. (1986). They suggest that precipitation of significant amounts of Al from the solution occurred from cooling to room temperature. In addition, it can be seen that the concentration of Na increases with increasing sample weight, indicating that the dissolution of albite was also influenced by fluid/rock ratio. The concentration of K on the other hand seems relatively constant with increasing sample weight.

The concentration of silica from granite dissolution in 250 ppm NaCl solution with varying the sample weight is provided in Figure 5.37. As expected, the concentration of silica increased with time and with increasing sample size. The dissolved major elements from 0.7 g sample, 3 g sample and 7 g sample in 250 ppm NaCl solution are provided in Figure 5.34, Figure 5.35, and Figure 5.36, respectively. The presence of K and Al verifies that the albite and K-feldspars from the granite dissolved to the liquid phase. The concentrations of Na were not included in the plot, since the concentration of Na^+ from the NaCl solution were significantly higher compared to K and Al concentrations, and thus resulted in difficulties to distinguish the sodium release from albite dissolution.

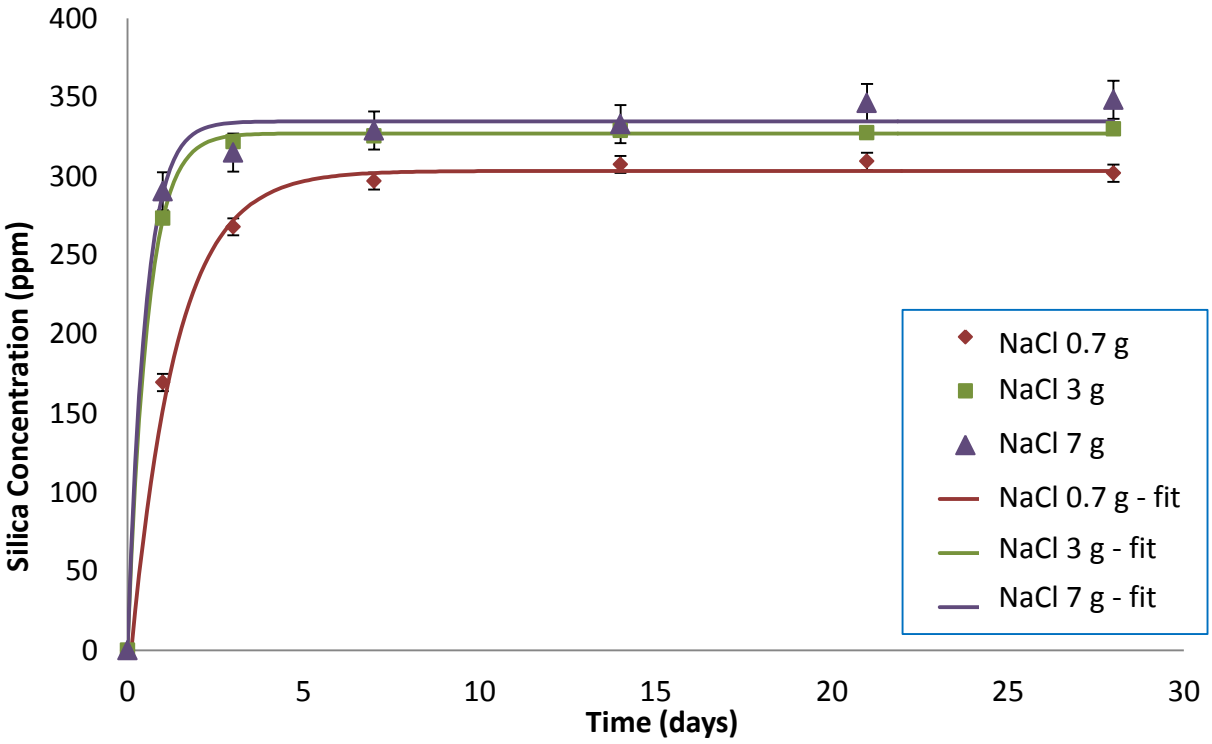

Figure 5.37 Dissolution in 250 ppm NaCl with varying sample weight

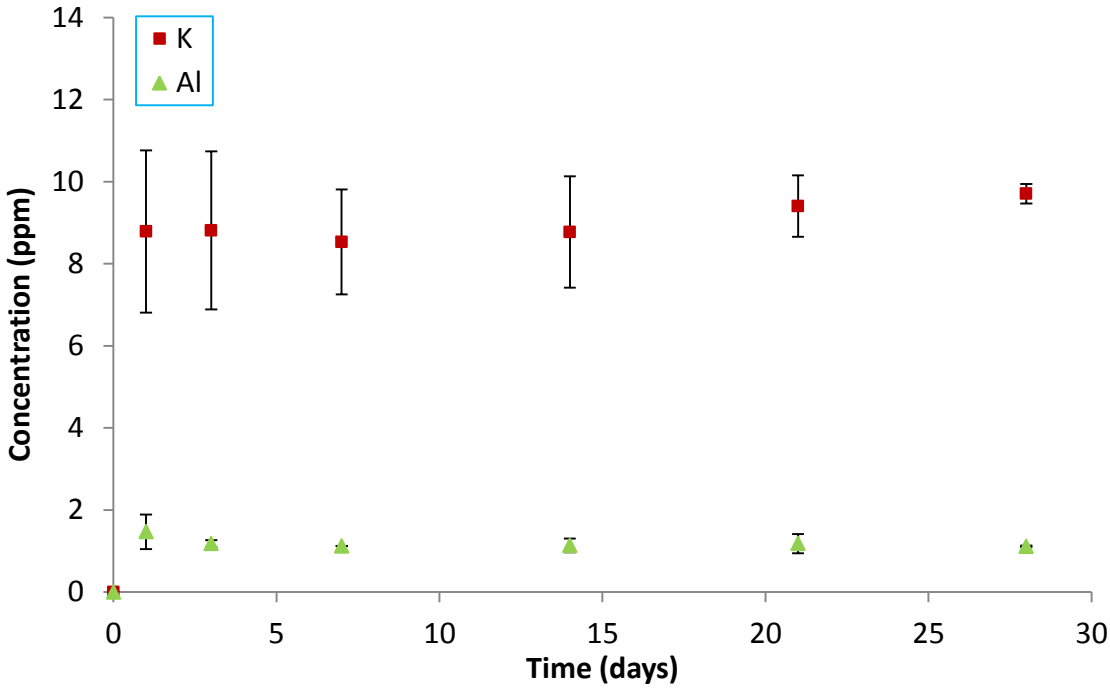

Figure 5.38 Concentration of dissolved K and Al in 250 ppm NaCl solution with 0.7 g granite sample

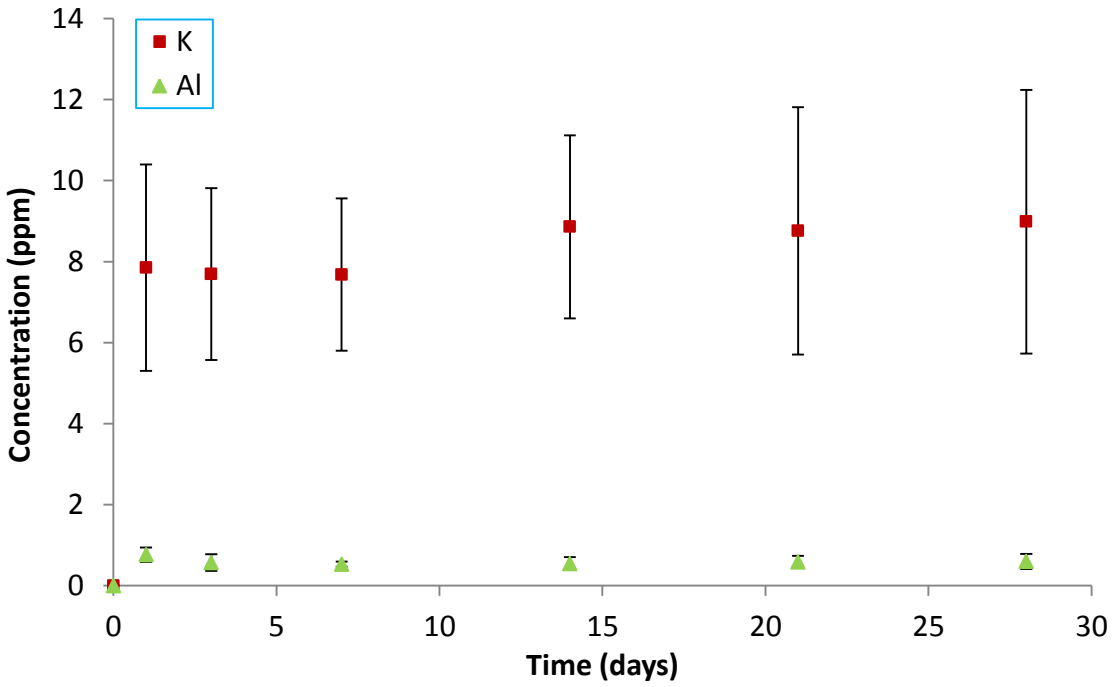

Figure 5.39 Concentration of dissolved K and Al in 250 ppm NaCl solution with 3 g granite sample

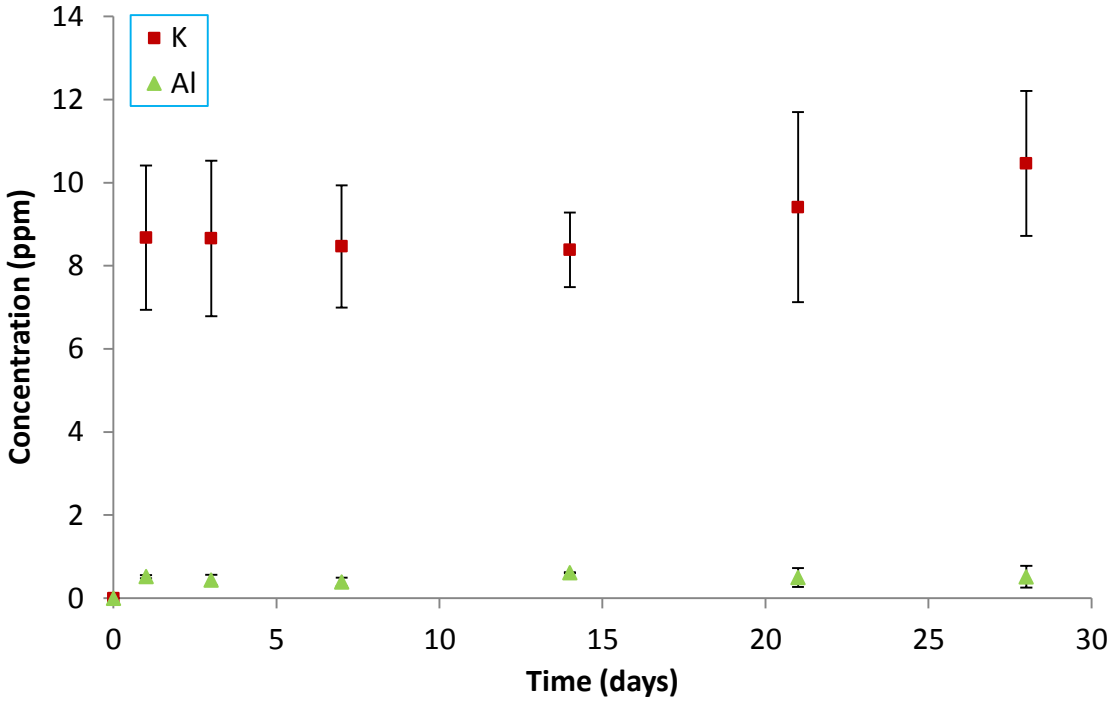

Figure 5.40 Concentration of dissolved K and Al in 250 ppm NaCl solution with 7 g granite sample

The results for granite dissolution in 250 ppm NaCl solution were found to have a similar trend to the results from granite dissolution in pure water. Plots comparing the silica release from dissolution in pure water and 250 ppm NaCl solution for the same sample weight are provided in Figure 5.41, Figure 5.42, and Figure 5.43 for 0.7 g, 3 g and 7 g samples, respectively. A possible explanation is that a dilute concentration of NaCl solution was used, thus only resulting in a small influence to the silica concentration. According to the study of Dove and Crerar (1990), the presence of electrolyte increased the dissolution rate compared to dissolution in pure water. The increase of dissolution rate was more pronounced in the presence of NaCl and KCl, depending on the concentration of the electrolytes (ionic strength). They also found that the reaction rate increased with increasing NaCl concentration up to 0.05 molal, and no further increase at higher concentration. The increase in reaction rate may be explained by three possibilities: The presence of electrolytes alters the equilibrium constant (K), thus increasing the reaction affinity $(1 - Q/K)$.

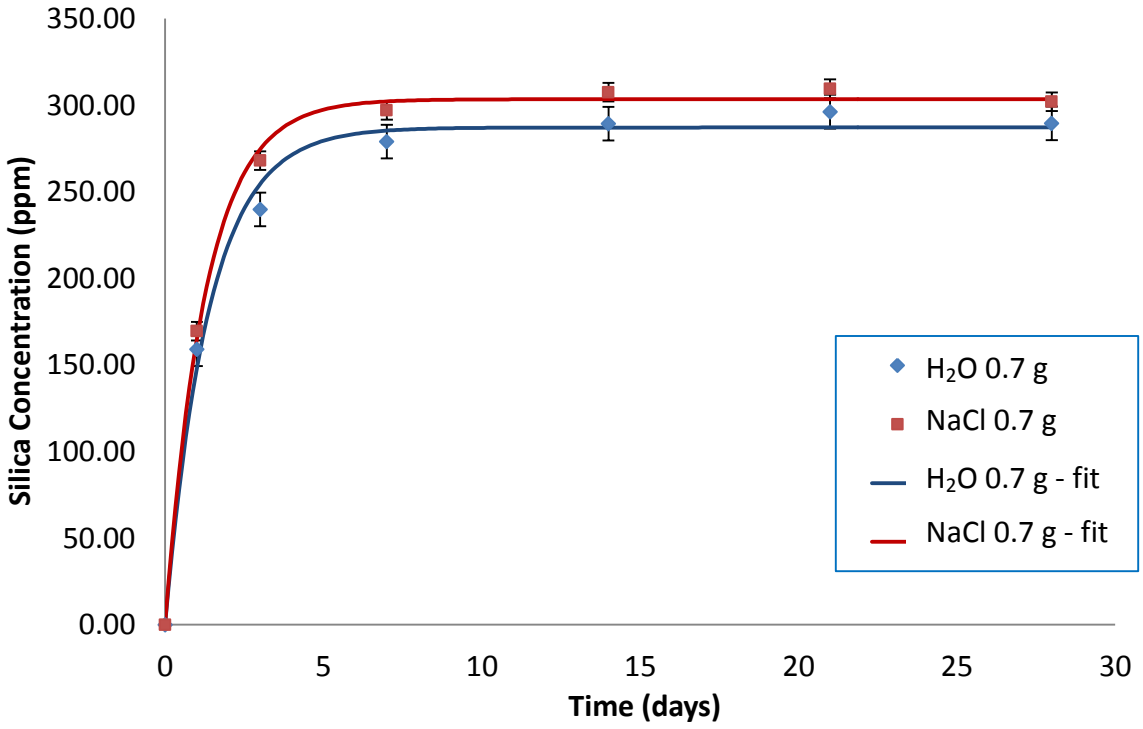

Figure 5.41 Comparison between dissolution in water and NaCl with 0.7 g granite sample

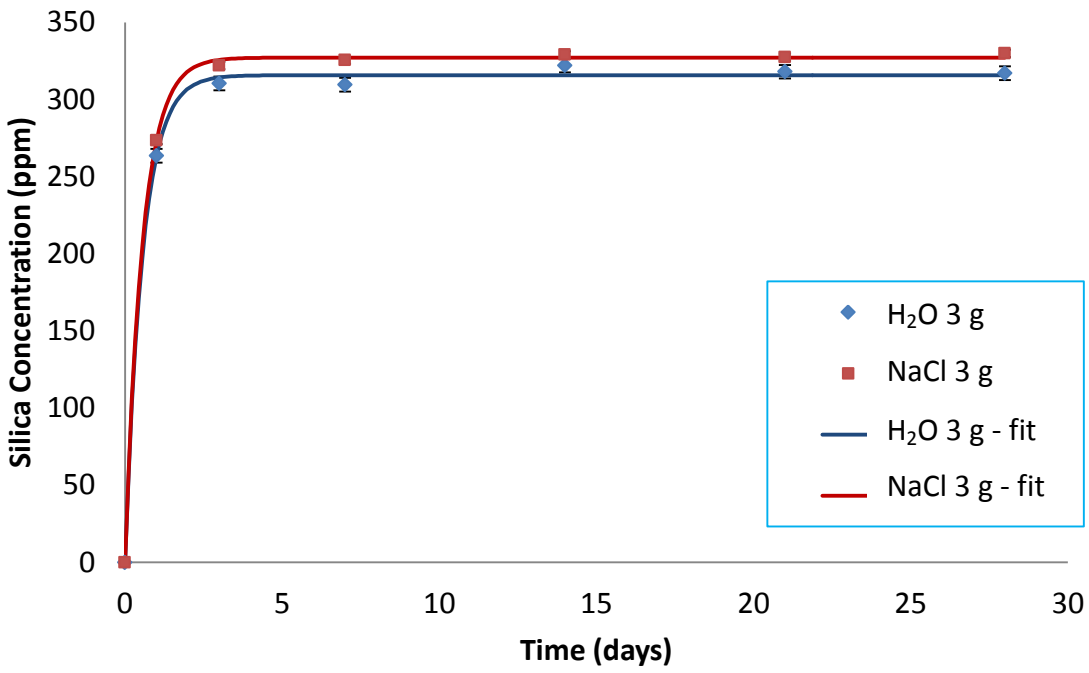

Figure 5.42 Comparison between dissolution in water and NaCl with 3 g granite sample

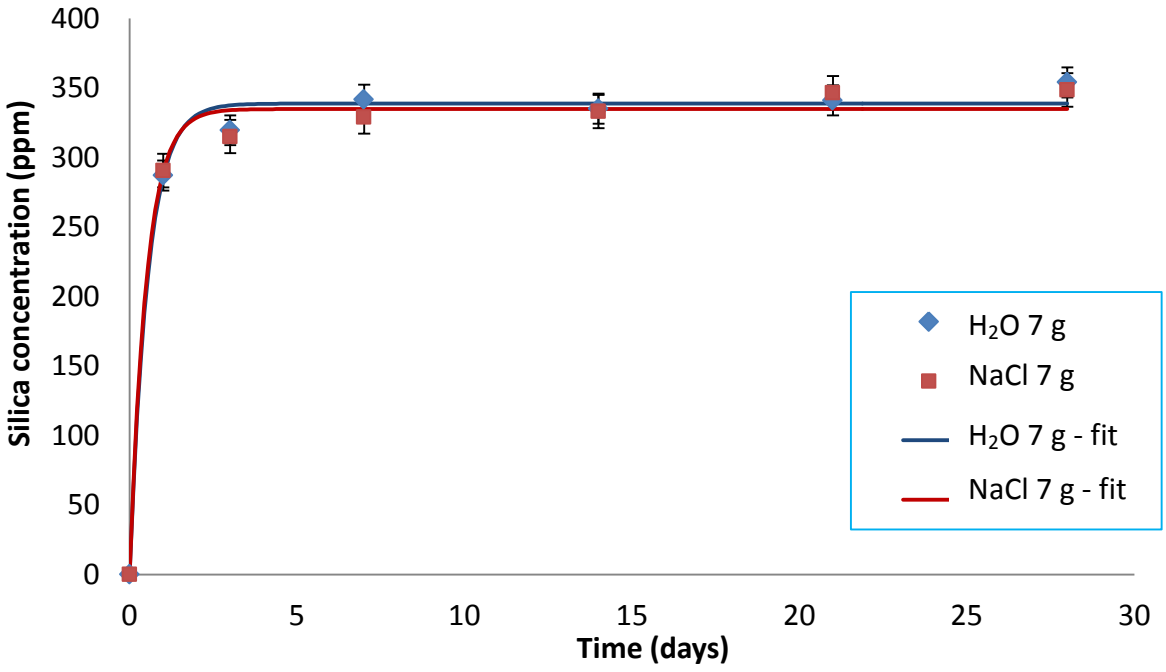

Figure 5.43 Comparison between dissolution in water and NaCl with 7 g granite sample

Table 5.22 Various liquid/rock ratios

Sample size (g)	Solid/liquid ratio (g/mL)
0.7232	352.6
3.0427	83.81
7.0718	36.06

Table 5.23 Constants from SigmaPlot for various liquid/rock ratios (water)

Liquid/solid ratio (mL/g)	a_0 *(ppm)*	a_1 *(d^{-1})*	*Standard error of estimate (ppm)*
36.06	338.70	1.8846	10.80
83.81	315.75	1.7929	4.455
352.6	287.10	0.7250	15.48

Table 5.24 Calculated equilibrium silica concentration (molal) and $k^{\#}$ (s^{-1}) in water for various liquid/rock ratios

Liquid/solid ratio (mL/g)	$m^{sat}_{H_4SiO_4}$*(molal)*	$k^{\#}$ *(s^{-1})*
36.06	0.0056	2.18×10^{-5}
83.81	0.0053	2.08×10^{-5}
352.6	0.0048	8.39×10^{-6}

Table 5.25 Dissolution rate in water for various liquid/rock ratios based on geometric surface area

Liquid/solid ratio (mL/g)	Geometric k_f $(mol/m^2 \cdot s)$	$ln(k_f)$	$log(k_f)$	Dissolution rate $(mol/kg \cdot s)$
36.06	3.43×10^{-7}	-14.885	-6.4647	1.23×10^{-7}
83.81	7.07×10^{-7}	-14.162	-6.1506	1.09×10^{-7}
352.6	1.09×10^{-6}	-13.726	-5.9611	4.01×10^{-8}

Table 5.26 Dissolution rate in water for various liquid/rock ratios based on BET surface area

Liquid/solid ratio (mL/g)	BET k_f $(mol/m^2 \cdot s)$	$ln(k_f)$	$log(k_f)$	Dissolution rate $(mol/kg \cdot s)$
36.06	1.12×10^{-8}	-18.304	-7.9494	1.23×10^{-7}
83.81	2.32×10^{-8}	-17.581	-7.6353	1.09×10^{-7}
352.6	3.58×10^{-8}	-17.145	-7.4458	4.01×10^{-8}

Table 5.27 Constants from SigmaPlot for various liquid/rock ratios (250 ppm NaCl)

Liquid/solid ratio (mL/g)	a_0 *(ppm)*	a_1 (d^{-1})	*Standard error of estimate (ppm)*
36.06	334.76	2.0002	12.02
83.81	327.15	1.8024	2.368
352.6	303.42	0.7851	5.411

Table 5.28 Calculated equilibrium silica concentration (molal) and $k^{\#}$ (s^{-1}) in 250 ppm NaCl for various liquid/rock ratios

Liquid/solid ratio (mL/g)	$m^{sat}_{H_4SiO_4}$*(molal)*	$k^{\#}$ (s^{-1})
36.06	0.0051	2.32×10^{-5}
83.81	0.0054	2.09×10^{-5}
352.6	0.0051	9.09×10^{-6}

Table 5.29 Dissolution rate in 250 ppm NaCl for various liquid/rock ratios based on geometric surface area

Liquid/solid ratio (mL/g)	Geometric k_f $(mol/m^2 \cdot s)$	$ln(k_f)$	$log(k_f)$	Dissolution rate $(mol/kg \cdot s)$
36.06	3.60×10^{-7}	-14.837	-6.4436	1.29×10^{-7}
83.81	7.38×10^{-7}	-14.1200	-6.1322	1.14×10^{-7}
352.6	1.26×10^{-6}	-13.594	-5.9037	4.59×10^{-8}

Table 5.30 Dissolution rate in 250 ppm NaCl for various liquid/rock ratio based on BET surface area

Liquid/solid ratio (mL/g)	BET k_f $(mol/m^2 \cdot s)$	$ln(k_f)$	$log(k_f)$	Dissolution rate $(mol/kg \cdot s)$
36.06	1.17×10^{-8}	-18.2556	-7.9283	1.29×10^{-7}
83.81	2.41×10^{-8}	-17.5385	-7.6169	1.14×10^{-7}
352.6	4.09×10^{-8}	-17.0125	-7.3884	4.59×10^{-8}

According to the Debye – Huckel theory, homogenous reaction rates are dependent on the activity and charge of the reactive intermediate species. This explains that the increase of rate constant is affected by an altered electrostatic environment which increases the product of the activity coefficients involved. In addition, the electrolytes increased the dissolution rate by increasing the access of water molecules to the siloxane bonds.

In all flow-through experiments, it was found that the equilibrium silica concentrations were lower compared to the equilibrium silica concentration extrapolated to 250^{o}C from the results using static autoclave experiments Section 5.1.1. A possible explanation is that temperature gradient exists in the flow-through cell. The temperature gradient enables flow in the cell. A rough estimation of the average temperature in the cell is approximately 223.4^{o}C or lower (Table 5.18 and Table 5.20) and the silica concentration was found to exhibit a better agreement at this temperature. In addition, quenching was avoided to preserve the flow though apparatus. The concentration of dissolved silica was measured by silicomolybdate determination. A difference in the concentration between quenched and non-quenched experiments may exist. When no quenching was performed, the silica may polymerize at long cooling time (2 hours), giving less measurable reactive silica in the solution (Brown, 2011a). After each experimental run, the cell was washed by circulating 255 mL pure water at 250^{o}C (24 hours wash cycle) to recover any lost dissolved silica. Approximately 50 ppm silica was recovered (no quenching performed). The granite sample after interaction were observed under a scanning electron microscope SEM) as well as analysed with X-ray diffraction.

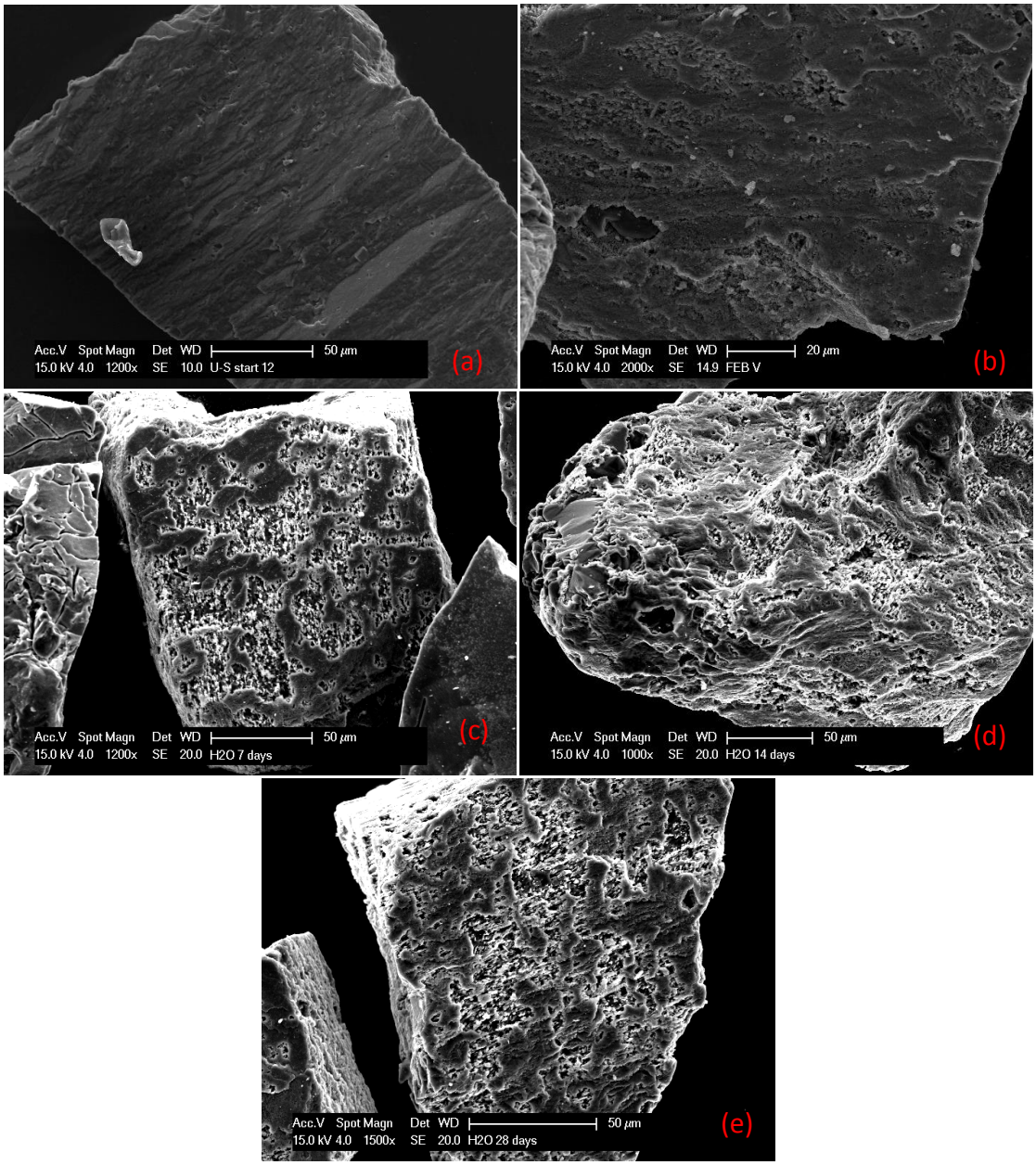

Figure 5.44 SEM images (0.7 g sample) of the rock sample surface: (a) starting rock (b) after 4 days experiment (c) after 7 days experiment (d) after 14 days experiment (e) after 28 days. Experiments performed in pure water

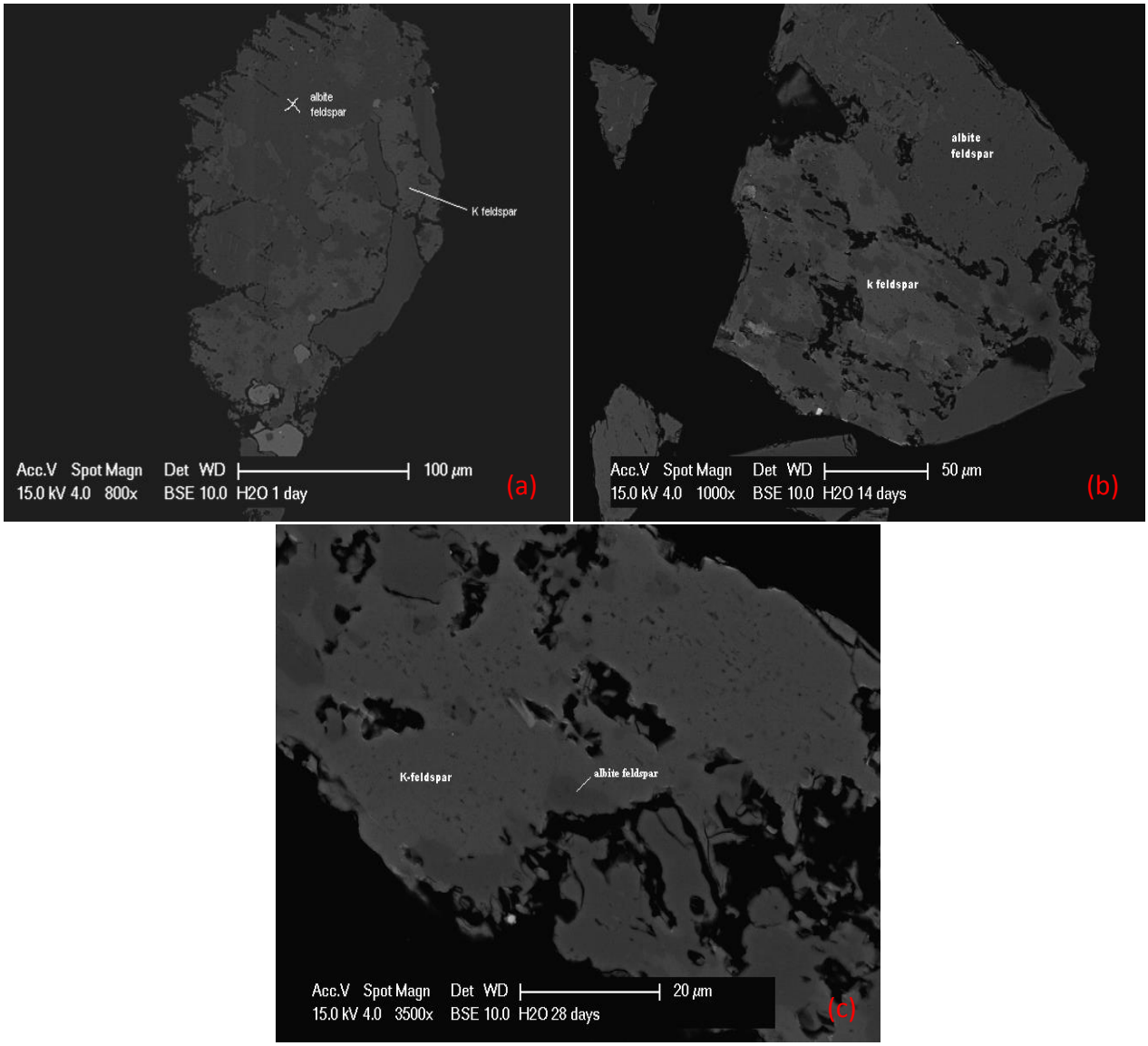

Figure 5.45 Backscatter SEM images of the granite (0.7 g sample) showing comparison of etch pits on albite and k-feldspar phase: (a) after 1 day experiment (b) after 14 days experiment (c) after 28 days. Experiments performed in pure water

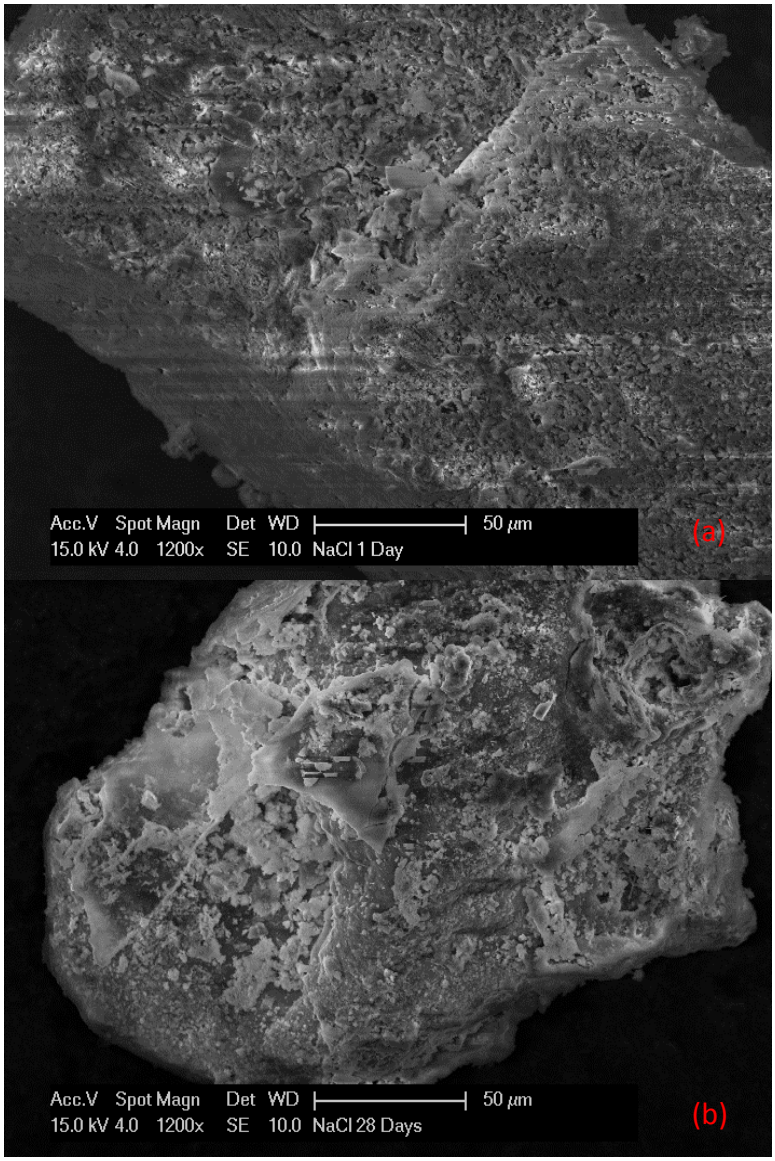

Figure 5.46 SEM images (0.7 g sample) of the rock sample surface: (a) after 1 day experiment (b) after 28 days. Experiments performed in 250 ppm NaCl

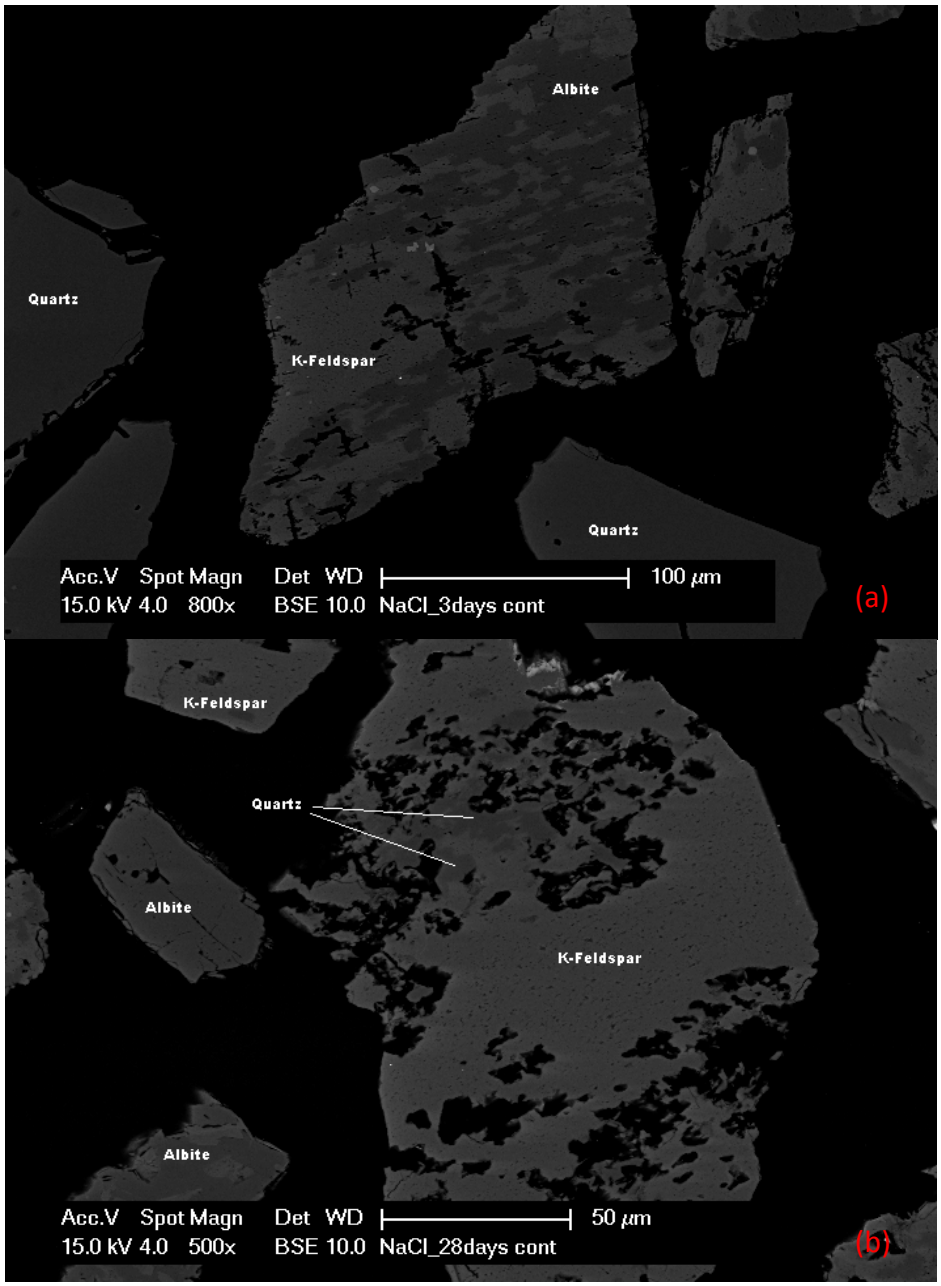

Figure 5.47 Backscatter SEM images of the granite (0.7 g sample) showing comparison of etch pits on albite and K-feldspar phase: (a) after 3 days experiment (b) after 30 days. Experiments performed in 250 ppm NaCl solution

SEM images were taken to observe the surface of the granite and to verify the components of the granite. SEM images using secondary electron (SE) detector enables the observation of surface particles, while the backscatter electron detector (BSE) enables the observation of different mineral phases. SEM images are provided in Figure 5.44 to Figure 5.47 for dissolution in water (0.7 g sample) and in 250 ppm NaCl solution (0.7 g sample), respectively. From the SEM surface images of the granite, etch pits were evident on quartz, albite and K-feldspar phases as the reaction progresses. It was also observed that precipitation occurred after 28 days of interaction in 250 ppm NaCl solution. Unfortunately, since the precipitation layer is quite thin, the microscope was unable to detect and identify species, and interference may occur from the mineral that it was attached to. From the backscatter SEM images, the minerals can be differentiated based on the dark and light shades and identified with the aid of EDAX, which produces an energy dispersive (ED) spectrum, showing elemental peaks at different energy (keV). An example of an ED spectrum for quartz containing elements Si and O is provided in Figure 5.58.

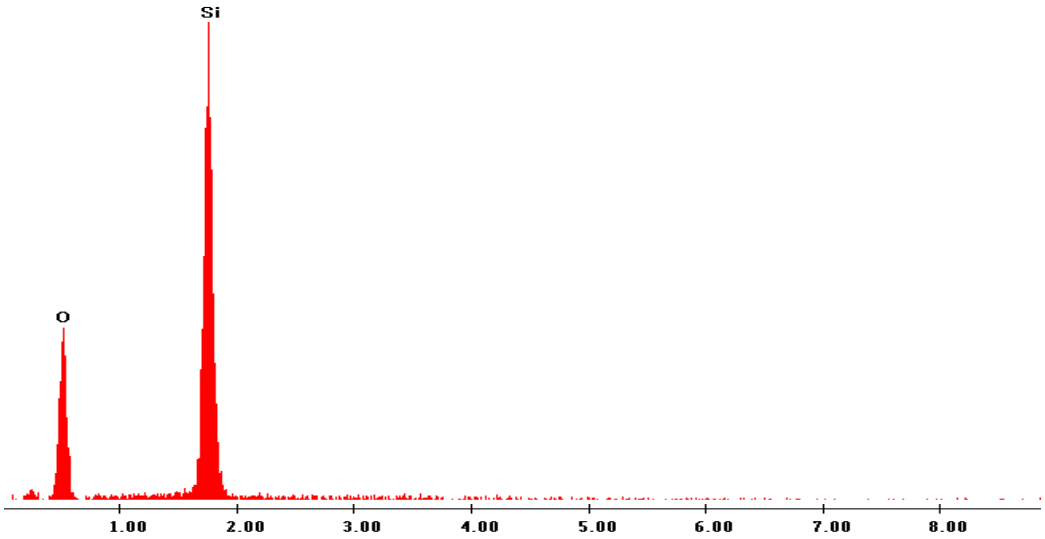

Figure 5.48 ED spectrum for quartz

X-ray diffraction (XRD) analyses were also undertaken to observe any changes of granite composition. XRD analyses for flow-through dissolution experiments using 0.7 g 3 g and 7 g in water are presented in Figure 5.49, Figure 5.50, and Figure 5.51, respectively.

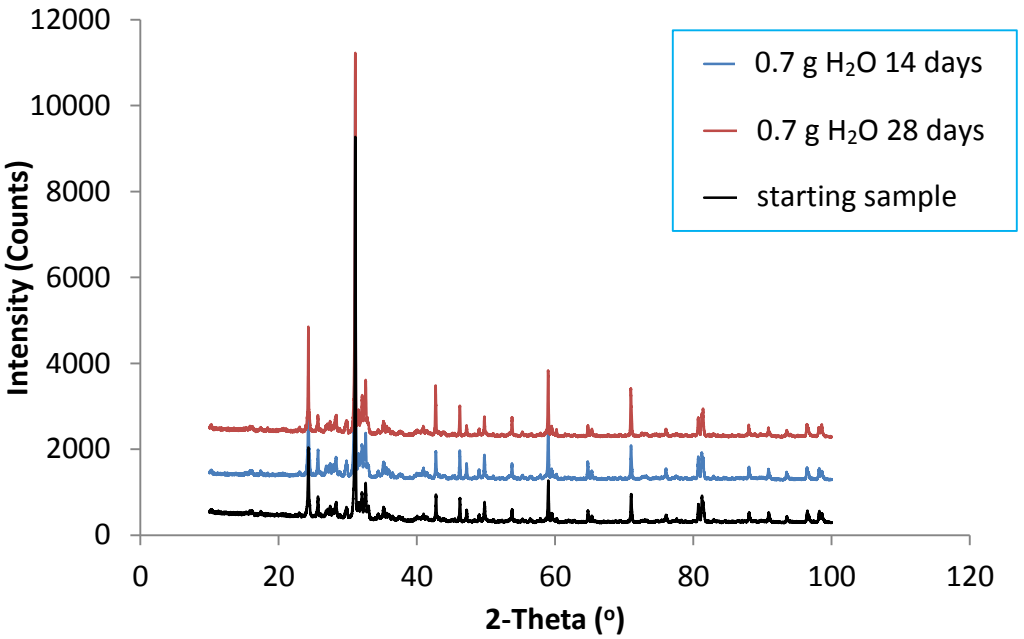

Figure 5.49 X-ray diffraction results for 14 and 28 days rock-fluid interaction periods for 0.7 g granite sample

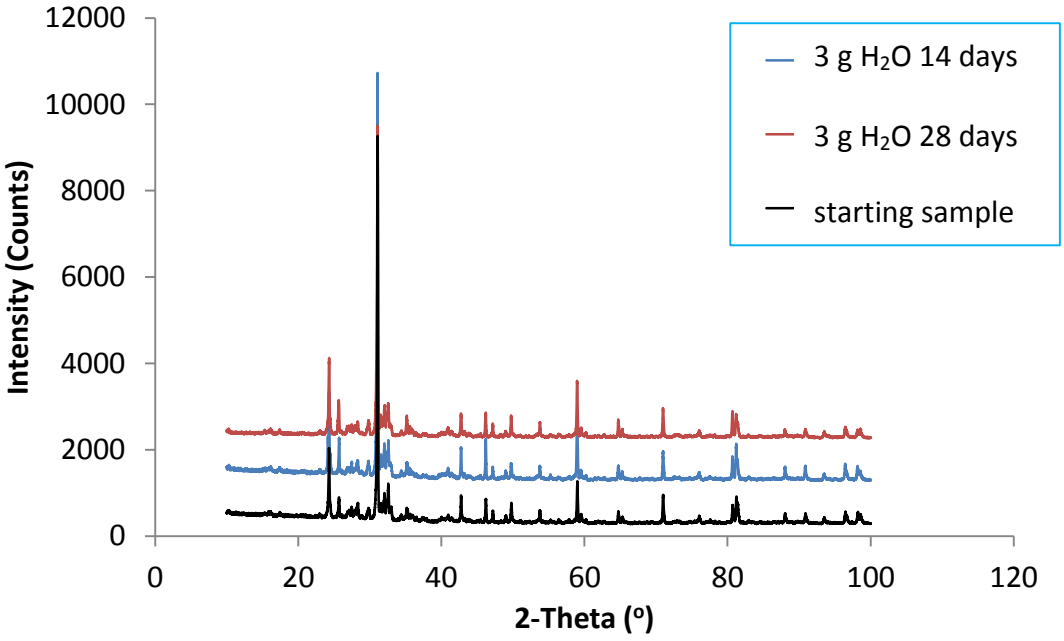

Figure 5.50 X-ray diffraction results for 14 and 28 days rock-fluid interaction periods for 3 g granite sample

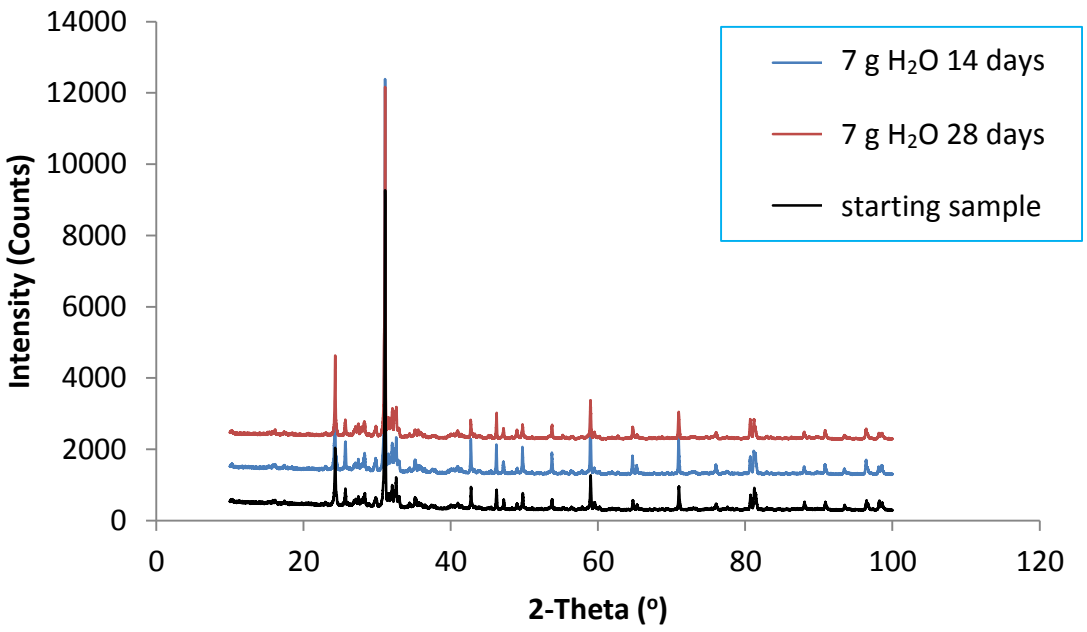

Figure 5.51 X-ray diffraction results for 14 and 28 days rock-fluid interaction periods for 7 g granite sample

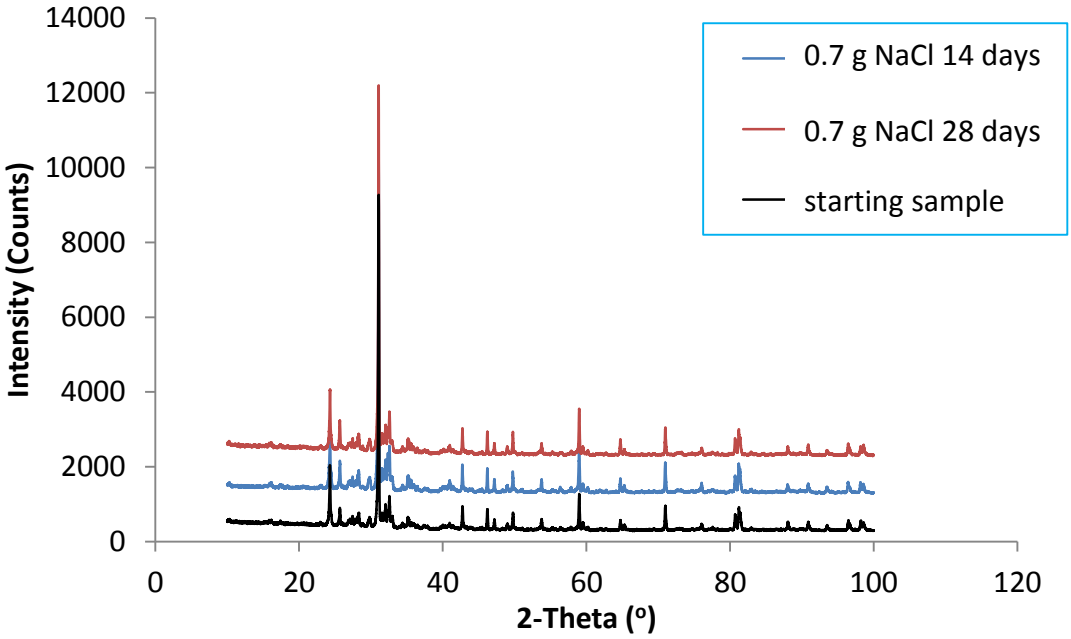

Figure 5.52 X-ray diffraction results for 14 and 28 days rock-fluid interaction periods in 250 ppm NaCl solution using 0.7 g granite sample

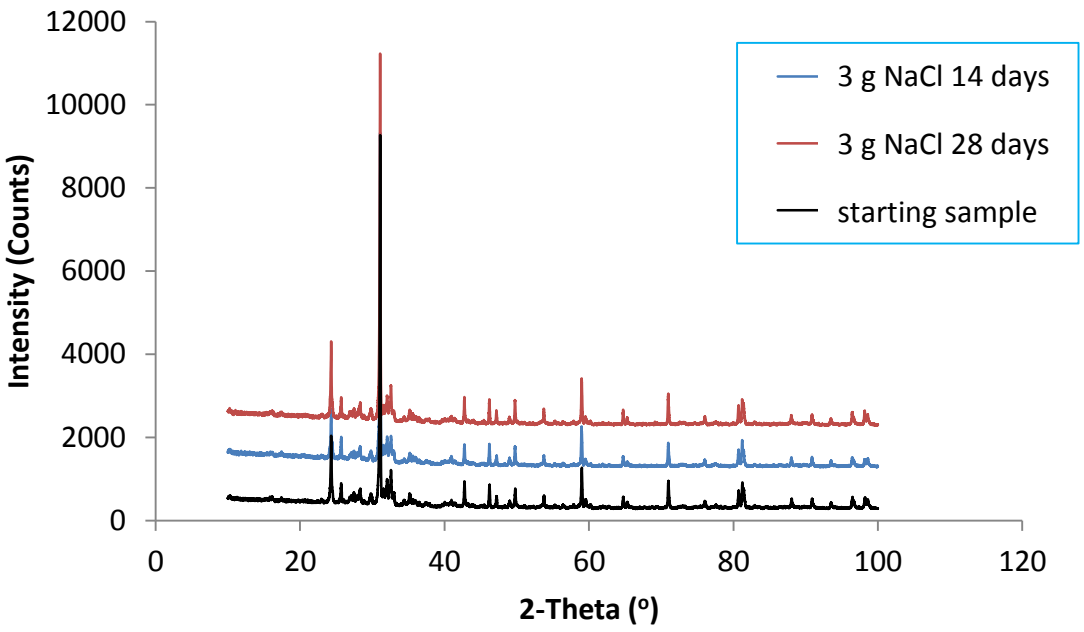

Figure 5.53 X-ray diffraction results for 14 and 28 days rock-fluid interaction periods in 250 ppm NaCl solution using 3 g granite sample

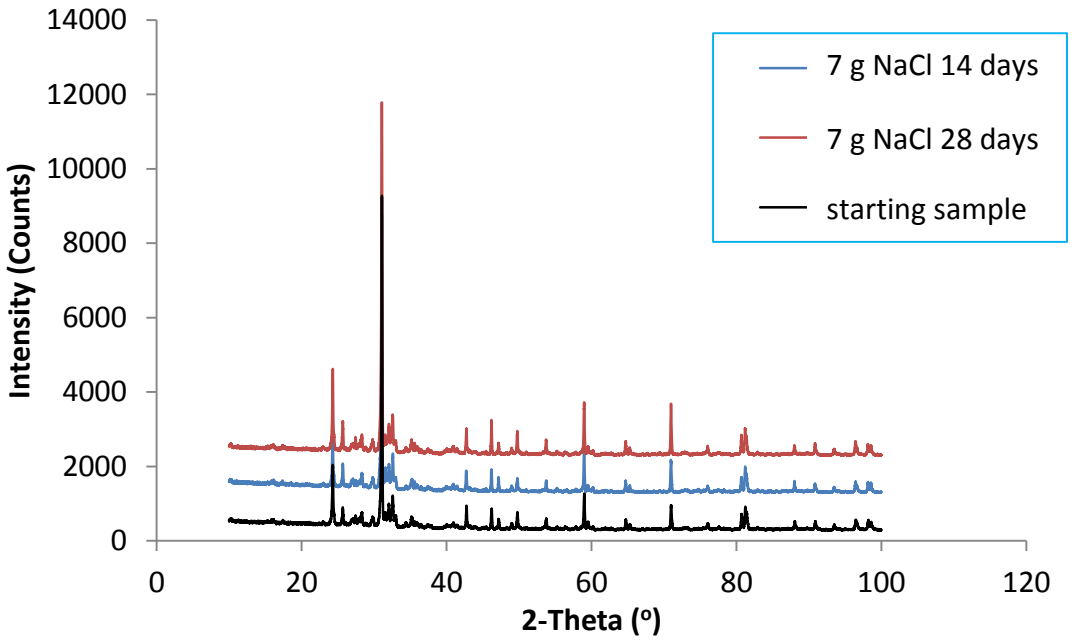

Figure 5.54 X-ray diffraction results for 14 and 28 days rock-fluid interaction periods in 250 ppm NaCl solution using 7 g granite sample

XRD analyses results showing comparison between interactions after 14 days and 28 days for experiments using 0.7 g, 3 g and 7 g in 250 ppm NaCl solution are presented in Figure 5.52, Figure 5.53, and Figure 5.54, respectively. The XRD plots showed that the phases in the samples remain fairly constant, indicating that no precipitation of new mineral occurs on the samples, although the XRD may unable detect quantities below 3% weight and cannot detect amorphous materials (e.g. amorphous SiO_2). Thus, perhaps an undetectable amount of precipitation may exist on the surface of the granite particles.

5.2.6.2 Non-recycled flow-through system

This study was undertaken to observe mineral dissolution by replacing the circulating fluid (fresh water) every 24 hours. This was an attempt to accelerate the dissolution rate and to mimic the condition of a geothermal site when fresh water or treated water from a precipitation tank (if any) is re-injected to the fracture. The rapid acceleration the fluid-rock interaction caused by frequent replacement of pure water may enable the identification of the more soluble mineral phases. The granite sample used was 0.7 g with particle size 100-200 µm. The interaction time chosen was 7 and 28 days, coupled with constant replacement of the recycling fluid with fresh fluid. The process of replacing this fluid requires terminating the interaction, completely draining the recycled fluid and replacing with fresh fluid. Results showed that more than 90 percent of the granite has dissolved to the solution after 28 days interaction. Table 5.31 and Table 5.32 present the amount of granite dissolved in water and 250 ppm NaCl solution, respectively. The results showing the comparison of silica concentration in water and 250 ppm NaCl solution is provided in Figure 5.55. Results showing concentrations of dissolved species in water and in NaCl are presented in Figure 5.56 and Figure 5.57, respectively. The complete data set is provided in Appendix D. It is seen from the concentration of species in solution that the quartz, albite and K-feldspar were dissolved as a consequence of fluid-rock interaction. The concentration of Na may be assumed to represent albite dissolution, and K to represent K-feldspar dissolution. Albite was observed to dissolve faster than K-feldspar and the dissolution rate reduced after 10 days. One explanation is that most of the albite was dissolving for up to 10 days and thus decreasing the surface area of the

albite. The decrease in surface area would reduce the dissolution rate. This was also observed for K-feldspar, where the dissolution rate reduced after approximately 12 days.

Table 5.31 Dissolved granite (% wt.) in pure water after 7 and 28 days

Interaction time (days)	Initial sample (g)	Remaining sample (g)	% wt. dissolved
7	0.7347	0.4467	39.20
28	0.7393	0.0738	90.02

Table 5.32 Dissolved granite (% wt.) in 250 ppm NaCl after 7 and 28 days

Interaction time (days)	Initial sample (g)	Remaining sample (g)	% wt. dissolved
7	0.7344	0.3857	47.48
28	0.7377	0.0194	97.37

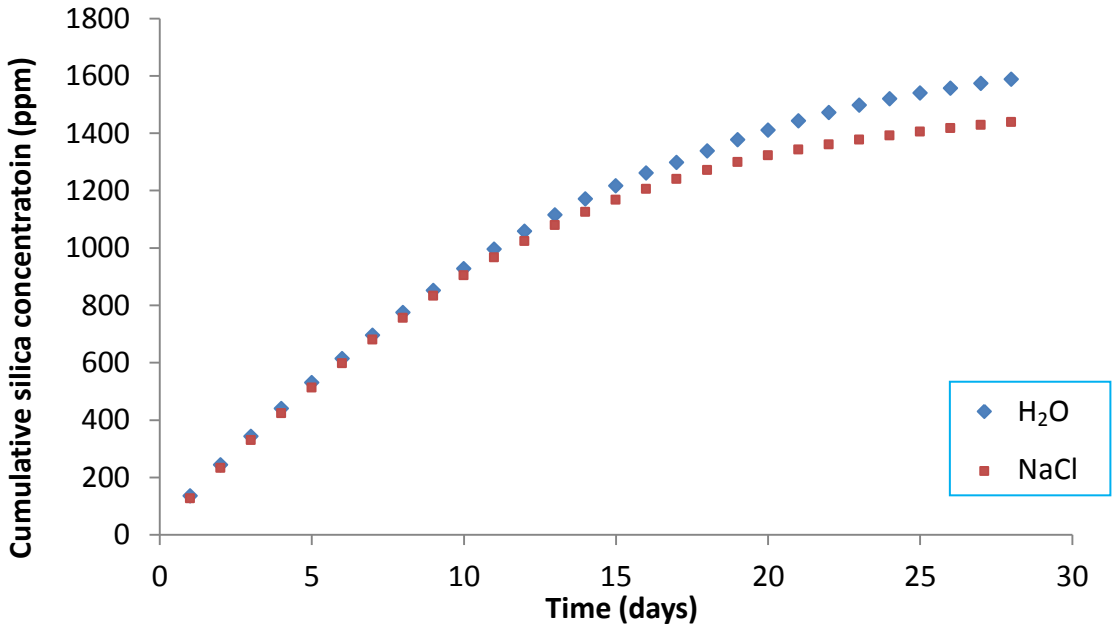

Figure 5.55 Comparison of cumulative silica concentration after 28 days replacing fluid

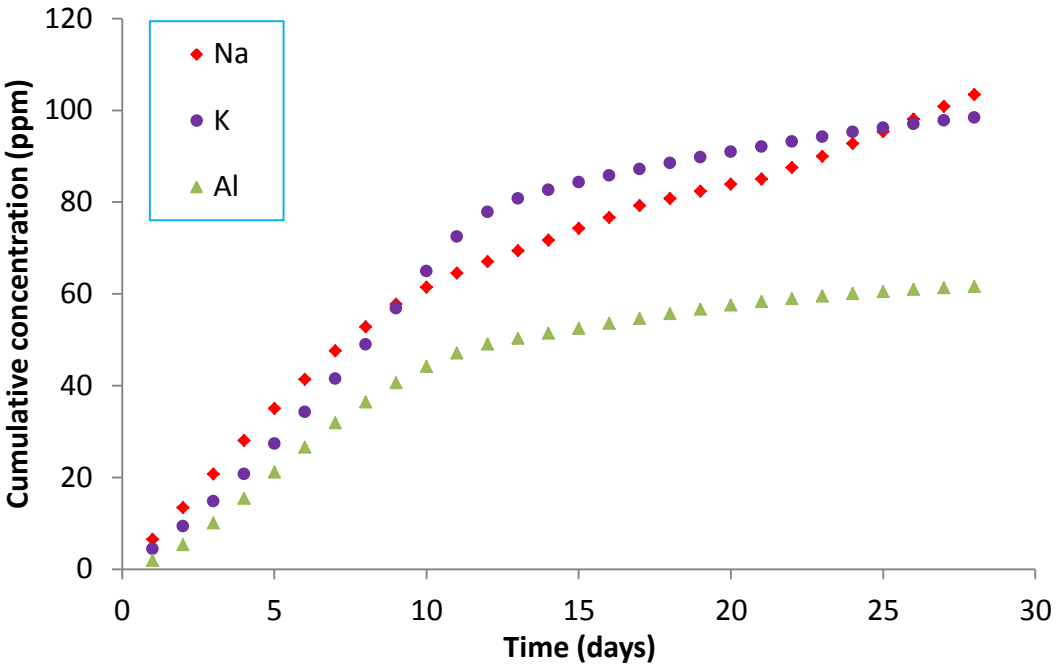

Figure 5.56 Comparison of cumulative Na, K and Al concentration after 28 days replacing water

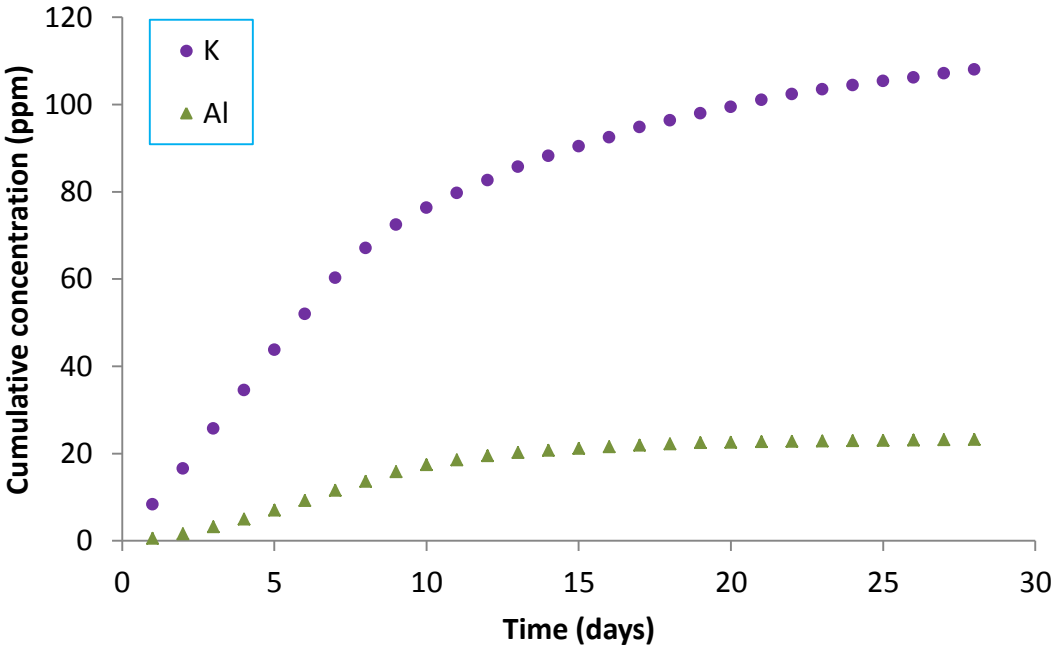

Figure 5.57 Comparison of cumulative K and Al concentration after 28 days replacing 250 NaCl solution

The dissolution rate of K-feldspar in 250 ppm NaCl solution was observed to be faster compared to that in pure water. It is seen from the concentration of K, that it achieved the same concentration with less time, approximately after 10 days. The production of Al in 250 ppm NaCl solution was observed to be slower compared to that in pure water. In addition, it was observed that the dissolution of Al in 250 ppm NaCl solution levelled off after approximately 10 days. Unfortunately, the sodium concentrations were not plotted since the sodium concentrations from the NaCl solutions were significantly higher and this resulted in difficulties in distinguishing the sodium release from albite dissolution.

SEM analyses on the granite surface in both secondary electron and back-scattered electron methods were undertaken for the starting granite sample as well for samples after 7 days and 28 days interaction with replacing water every 24 hours. The results are presented in Figure 5.58 and Figure 5.59. Figure 5.60 and Figure 5.61 show the results from experiments using the 250 ppm NaCl solution. For both sets of experiments, it is seen from the results that severe pitting exists on the surface of the granite, as a consequence of rapid dissolution due to the use of introducing fresh fluid every 24 hours. Since fresh fluid was replaced, it has more capacity to dissolve the granite, and would eventually dissolve the granite completely. From the surface SEM image, it was observed that fine particles existed between an on the surface of the granite. As rapid dissolution proceeds, the breakage of particles may occur thus increasing the surface area of the particles, enhancing the dissolution rate. Although, after a certain period, the amount of fine particles have been exhausted thus reducing the dissolution rate.

The dissolution of particles may be observed more clearly from the back-scattered electron images. Three major phases that are dominant are albite (darker shade), K-feldspar (lighter shade) and quartz (uniform grey shade). Images show that albite seems to be the more soluble phase, as more cavities were observed through the albite phases compared to the K-feldspar phases in the samples. It was also observed that the quartz phases were dissolving at a much slower rate. After 28 days interaction, the remaining phases were mostly quartz.

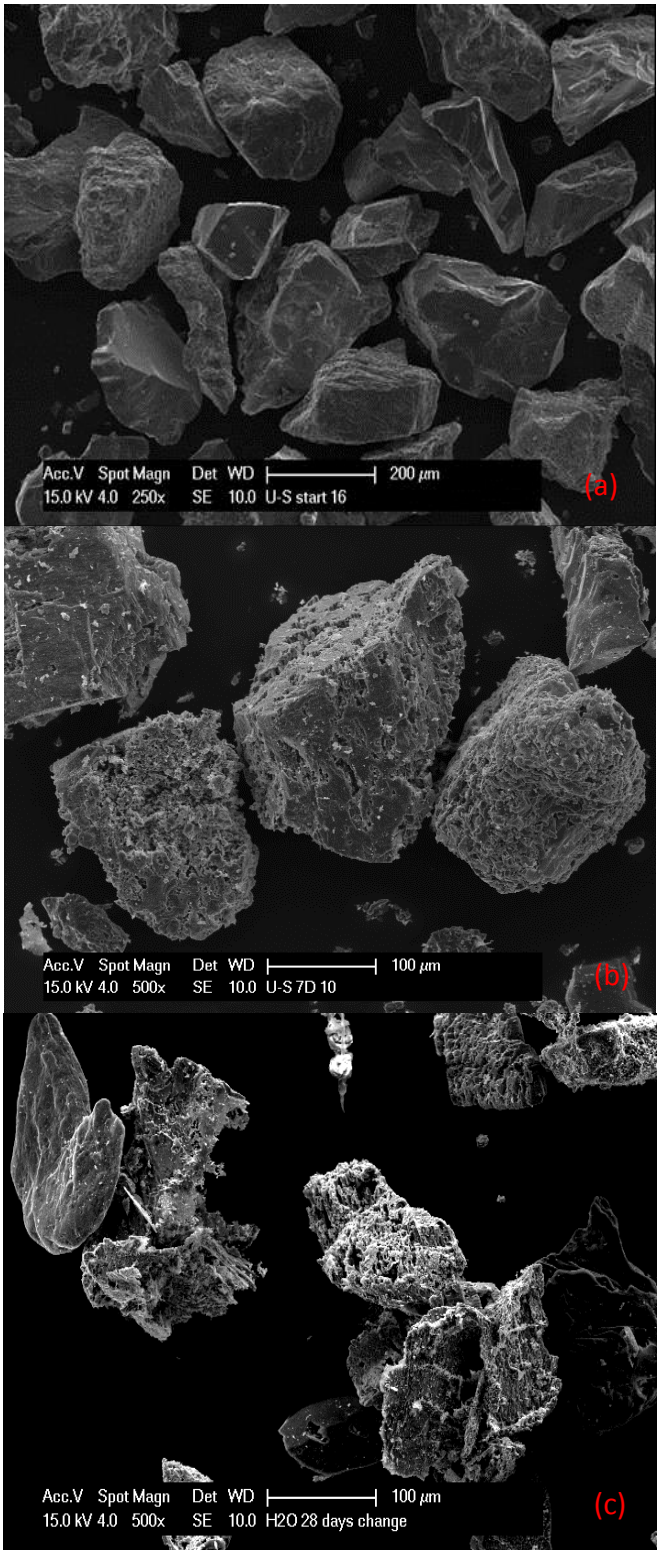

Figure 5.58 SEM images of the granite surface (a) starting sample, (b) after 7 days, and (c) after 28 days replacing water

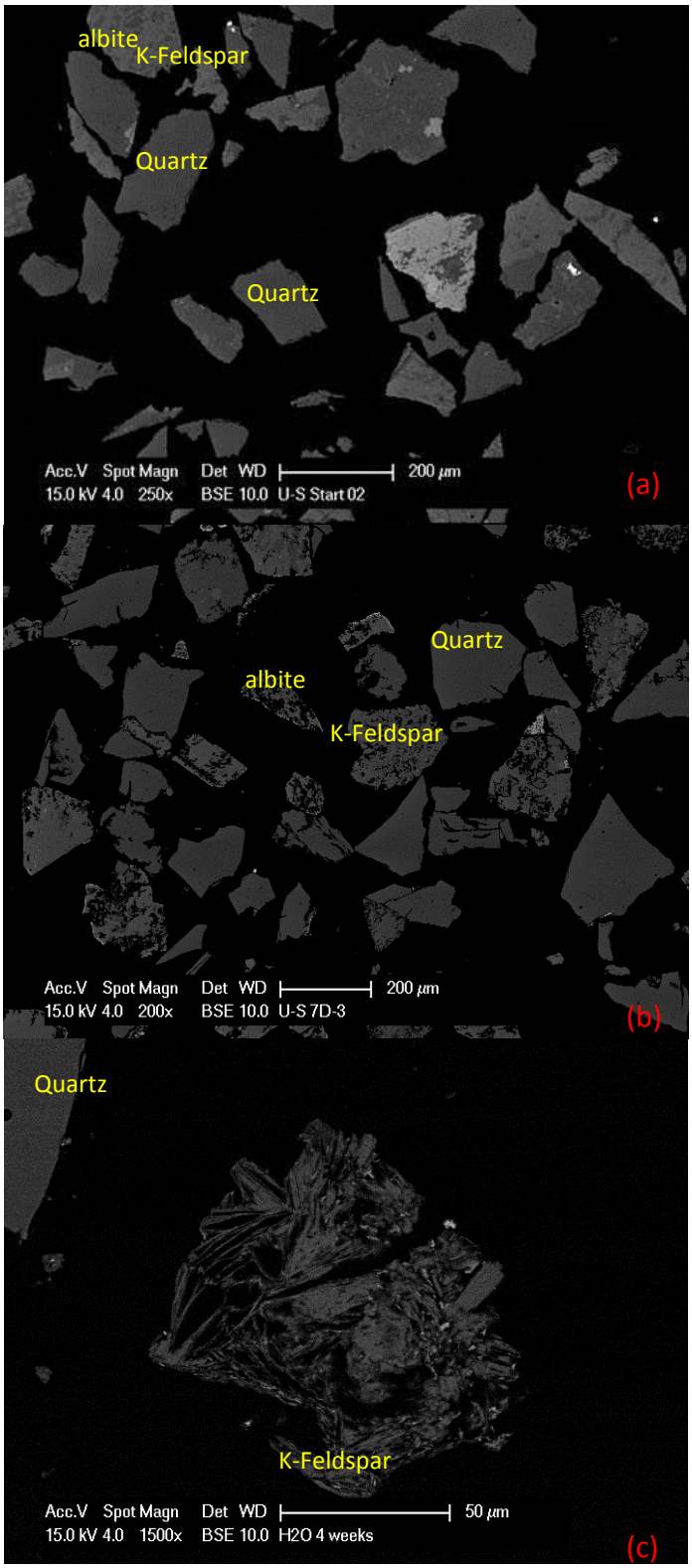

Figure 5.59 Backscatter SEM images of the granite showing (a) starting sample, (b) after 7 days interaction, and (c) 28 days replacing water

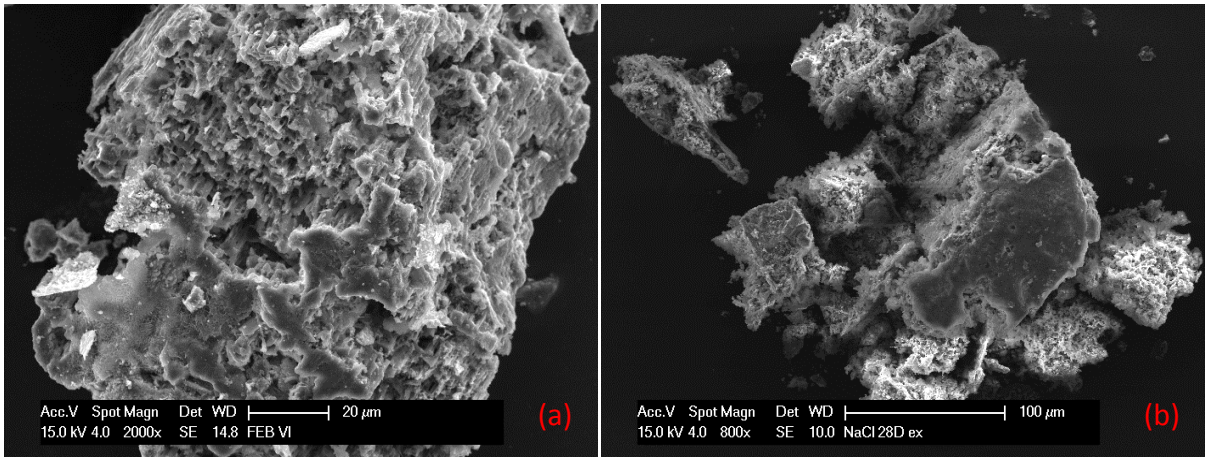

Figure 5.60 SEM images of the granite surface (a) after 7 days and (b) after 28 days replacing 250 ppm NaCl solution

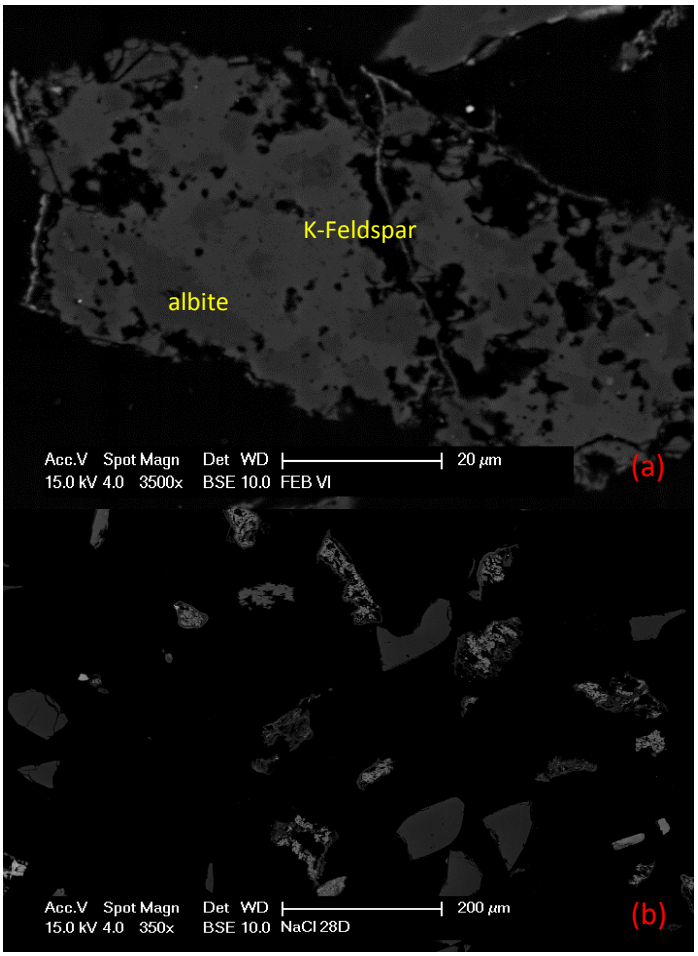

Figure 5.61 Backscatter SEM images of the granite showing (a) after 7 days interaction and (b) 28 days replacing 250 ppm NaCl solution

5.3 High Pressure Flow-through System

The high pressure flow-through system is a closed loop flow-through set up designed to mimic the actual geothermal site, where water flows through a porous medium. A photograph of the high pressure flow-through system is provided in Figure 5.62.

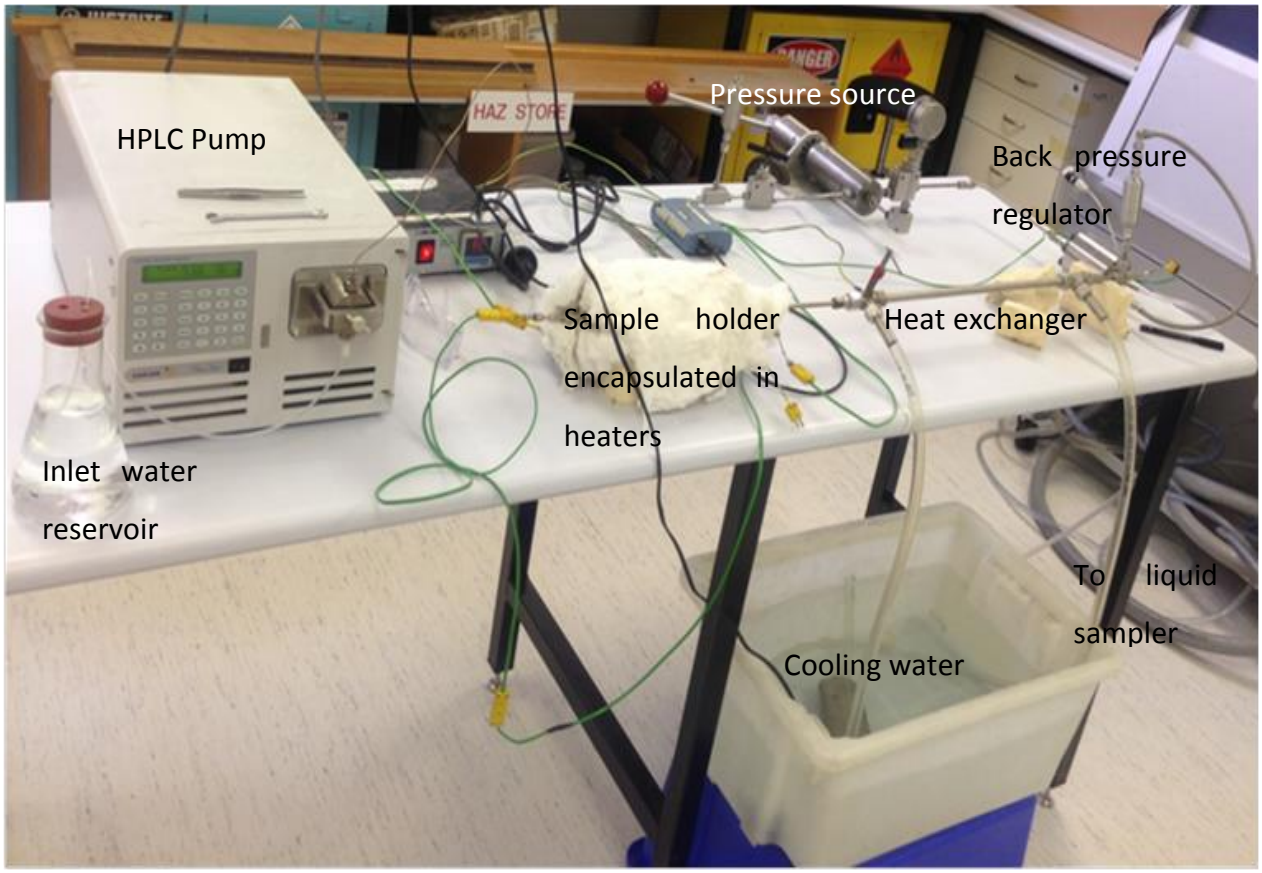

Figure 5.62 High pressure flow though cell

5.3.1 Description of the high pressure flow-through cell

This high pressure cell consist of a high performance liquid chromatography (HPLC) pump, a back pressure regulator, a water compression device to set the pressure of the system, a sample holder, inlet water reservoir, liquid sampler, a heat exchanger for cooling, tubing, valves and temperature measurement devices. The tubing was made from ¼ inch stainless steel (SS316) and connected with standard Swagelok stainless steel fittings. Thermocouples were

installed to monitor the temperature changes throughout the cell and connected to a temperature data logger. The temperature was controlled by a simple relay controller connected to two heaters that are arranged in parallel. The sample holder was encapsulated by the heaters and insulated. The working volume of the high pressure flow-through cell is approximately 75 mL. The pressure was applied by a water pump, where water is compressed to the desired pressure and maintained using a back-pressure regulator. The advantage of using the HPLC pump is the facility to set and control the flow rate. The heat exchanger has a length of approximately 30 cm, to allow cooling of the fluid, as the fluid temperature can affect the back pressure regulator. A pump was used to circulate the cooling water with a flow rate of 550 L/hr.

5.3.2 Materials and methods

The materials used to determine the equilibrium silica concentration are purified water (Milli-Q) and the rock sample with particle size distribution 100 – 200 µm. Two concentration of nitric acid were prepared, 0.1M and (4%), respectively.

5.3.3 Experimental procedures

The rock samples were prepared following the procedure in Chapter 5.1.1.1. Approximately 3 g of rock samples were prepared in a sample basket. Approximately 120 mL of pure water was added into the reservoir. The HPLC pump was then turned on and the flow rate was set to 2 mL/minute. When water flow has been achieved and confirmed at the outlet reservoir (liquid sampler), the pressure was then introduced to the system by pressurizing the back pressure regulator to the pressure set point. After the pressure set point has been reached, the heater controller was turned on. The reservoir must not be allowed to be empty to avoid the HPLC pump running dry. The temperature of the system was increased by 100^{o}C interval until the 250^{o}C set point was achieved. It was ensured that pure water was available in the reservoir when the temperature set point has been reached and sampling of the outlet water was commenced. The liquid sampler should store approximately 120 mL sample (1 hour interaction

period) and replaced every hour until 6 hours of interaction period has lapsed. The liquid phase was decanted to a polypropylene container and pH was measure. A volume of 5 mL was taken and diluted to a 1:10 ratio then preserved with 4% nitric acid to maintain the dissolved elements in solution and minimize polymerization that may occur (Brown, 2011a). The reactive silica (SiO_2 or H_4SiO_4) concentration was measured following the HACH silicomolybdate method using a HACH portable spectrophotometer DR2000. The solid phase (rock sample) was left in the sample basket and dried in an oven at 120^{o}C for 48 hours. The rock samples were then weighed and recorded. The complete data set is provided in Appendix E.

5.3.4 Results and discussion

This experiment was designed to determine the effect of pressure on silica dissolution. The experimental results confirm that the reactive silica concentration increases with temperature and pressure as illustrated in Figure 5.63.

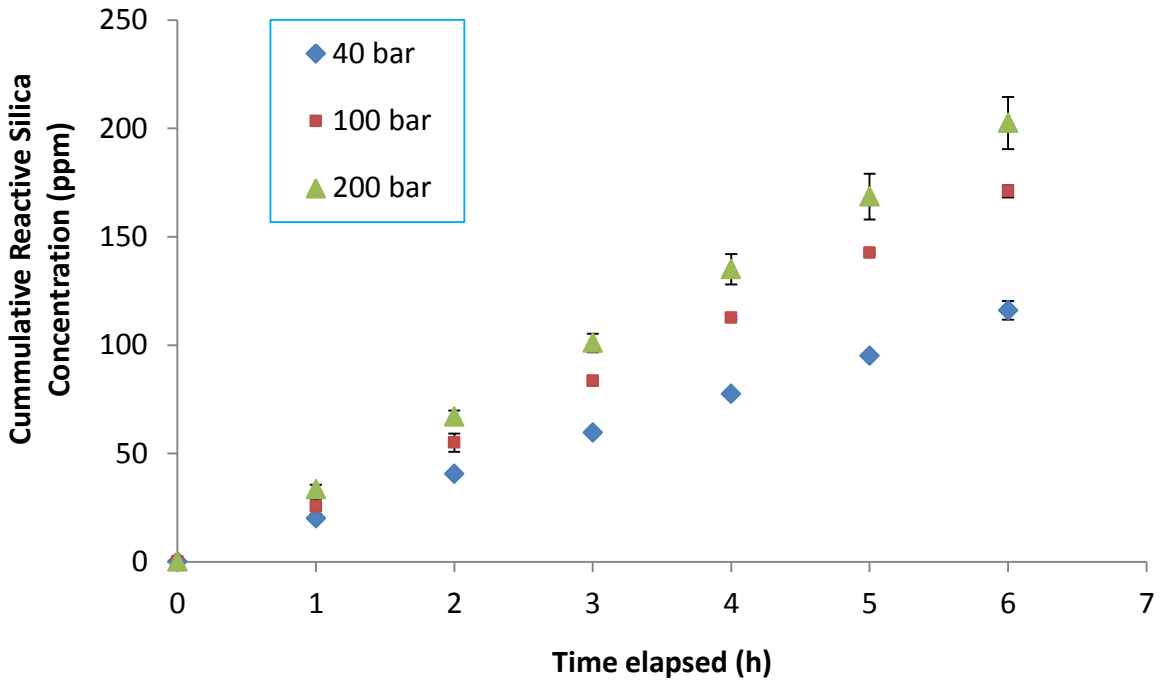

Figure 5.63 Effect of pressure on silica dissolution

The initial pH of the water was near neutral (approximately pH 5.5) and the solution pH increased over the 6 hours of interaction. The dissolution silica profile at various pressures after 6 hours interaction is presented in Figure 5.63. The results are in broad agreement with those from the studies by Fournier and Potter II (1982a) and Vala Ragnarsdóttir and Walther (1983) that the concentration of silica increases with pressure. Theoretical calculations showed that the reaction rate should be controlled by surface reaction, rather than transport effects.

The initial design of the high pressure flow-through cell was to allow fluid circulation in the system. Many experimental trials were undertaken and lead to the silica precipitation in the pump head of the HPLC pump, and on the diaphragm of the back-pressure regulator. This appears to be consistent with the experience in the geothermal industry where silica precipitates are often observed at the re-injection pump. Since this problem was not able to be resolved, the design was changed to a non-circulating system.

Figure 5.64 Silica precipitation on the diaphragm of a back-pressure regulator

5.4 Mass Transfer Coefficient Calculations

For the dissolution of quartz in water, the rate of reaction is governed by a two-step process as follows: the chemical/physical reaction between the quartz and water at the solid-liquid interface is coupled to the bulk mass transfer of the H_4SiO_4 molecules from the surface to the fluid (Robinson, 1982). Thus, for the rate law to be valid the reaction must be controlled by surface reaction and mass transfer limitation should not exist. In order to verify if this state applies, the mass transfer coefficient and the rate constant must not be in the same order of magnitude (Robinson, 1982). The Sherwood number can be used to calculate the mass transfer coefficient (Sherwood et al., 1975):

$$Sh = \frac{k_m d_p}{D_{AB}} = 2 + 0.6\, Re^{1/2}\, Sc^{1/3} \qquad \textbf{(5.20)}$$

where: Sh = Sherwood number

k_m = mass transfer coefficient ($^m/_s$)

d_p = average diameter of particle (m)

D_{AB} = diffusivity of H_4SiO_4 in water (m^2/s)

Sc = Schmidt number = υ/D_{AB}

υ = kinematic viscosity of water (m^2/s)

Re = Reynolds number

According to Worley (1994), the mass transfer from a spherical particle in a stagnant medium has a Sherwood number of 2, and this applies for the experiments using static autoclave where no mixing is introduced to the system. For the case of the flow through system, the liquid velocity must be known to calculate the Reynolds number according to Equation (5.21):

$$Re = \frac{d v \rho_l}{\mu_l} \qquad \textbf{(5.21)}$$

where: d = pipe diameter (m)

v = liquid velocity (m/s)

ρ_l = density of liquid (kg/m^3)

μ_l = liquid viscosity $(Pa \cdot s)$

Since the data of diffusivity of H_4SiO_4 in water is not readily available, the Wilke-Chang correlation was used to allow the estimation of liquid diffusivities at different temperatures, where D_{AB} is proportional to temperature to the first power and liquid velocity to the -1 power:

$$\frac{D_{AB\,(2)}}{D_{AB\,(1)}} = \frac{T_{(2)}}{T_{(1)}} \frac{\mu_{(1)}}{\mu_{(2)}} \qquad \textbf{(5.22)}$$

The subscripts (1) and (2) indicate the known data at a specific temperature and unknown data at a target temperature, respectively. Jander and Jahr (1934) cited in Robinson (1982) reported the diffusivity of H_4SiO_4 is 6.15 x 10^{-10} m/s at 20°C, and this value will be used as a reference to calculate D_{AB} at other temperatures. Therefore, with the known particle diameter, and the obtained values for Reynolds number, D_{AB}, and the Schmidt number, the mass transfer coefficient can be calculated and compared to the reaction rate constant.

An approach to calculate the average mass transfer calculation for suspended particles (Sherwood et al., 1975; Robinson, 1982) was also used to compare results: It is assumed that the particles are suspended in the flow through cell, the velocity following the Stokes' law terminal velocity:

$$U_{TS} = \frac{d_p^2 |\rho_s - \rho_l| g}{18 \mu_l} \qquad \textbf{(5.23)}$$

where: U_{TS} = Stokes' law terminal velocity $(^m/_S)$

d_p = average diameter of particle (m)

ρ_s = density of solid particles (kg/m^3)

ρ_l = density of liquid (kg/m^3)

g = gravitational acceleration = 9.81 (m/s^2)

μ_l = liquid viscosity $(Pa \cdot s)$

The velocity calculated using Equation (5.23) is then used to calculate the Reynolds number based on Stokes' law:

$$Re_{TS} = \frac{d_p^3 \rho_l |\rho_s - \rho_l| g}{18\mu_l^2} \quad \textbf{(5.24)}$$

After obtaining the Reynolds number based on Stokes' law, Table 5.33 is used to obtain the value of U_T/U_{TS}. Knowing the value of U_{TS} calculated using Equation (5.23), the value of U_T can be obtained.

Table 5.33 U_T/U_{TS} values for a range of Reynolds numbers

Re_{TS}	U_T/U_{TS}
1	0.9
10	0.65
100	0.37
1000	0.17
10000	0.007
100000	0.0023

A new Reynolds number is calculated using the U_T obtained from the method above by replacing the velocity in Equation (5.21). Therefore, with the known particle diameter and the obtained Sherwood number and diffusivity of H_4SiO_4, the mass transfer coefficient can be calculated and compared to the reaction rate constant. The results of mass transfer coefficients and comparison for the static system and the flow-through system are provided in Table 5.34 - Table 5.36, respectively. Since the mass transfer coefficients for static and flow-through system are several orders of magnitude larger than the reaction rate constant, the mass transfer limitations does not exist in the systems.

Table 5.34 Comparison of mass transfer rate and reaction rate constant for static system at different temperatures

T (°C)	$k_m\ (m/s)$	k_f geometry (m/s)	k_f BET (m/s)
160	6.05×10^{-5}	1.04×10^{-11}	3.41×10^{-13}
170	6.61×10^{-5}	2.46×10^{-11}	8.04×10^{-13}
200	8.38×10^{-5}	1.14×10^{-10}	3.73×10^{-12}
220	9.66×10^{-5}	2.15×10^{-10}	7.06×10^{-12}

Table 5.35 Comparison of mass transfer rate and reaction rate constant for static system with different particle size

$d_p\ (\mu m)$	$k_m\ (^m/_s)$	k_f geometry (m/s)	k_f BET (m/s)
40 - 60	3.23×10^{-4}	4.23×10^{-11}	1.75×10^{-12}
200 - 400	4.77×10^{-5}	1.24×10^{-10}	5.98×10^{-12}

Table 5.36 Comparison of mass transfer rate and reaction rate constant for flow-through system

T (°C)	Reynolds number	$k_m\ (m/s)$	k_f geometry (m/s)	k_f BET (m/s)
250	3283.7	4.92×10^{-3}	1.09×10^{-6}	3.58×10^{-8}
250 (using terminal velocity)	4046.0	5.44×10^{-3}		

Chapter 6 Granite – Fluid Interaction Modelling

The granite-fluid interaction modelling has been carried out with the aid of the Geochemist Workbench Standard 7.0 software with the LLNL database (thermo_MMS.dat). The modelling was undertaken to obtain the equilibrium silica concentration at various temperatures, dissolution rate constants, the amount of silica precipitation and the fracture sealing rate.

6.1 The Software

The Geochemist Workbench is a package of software tools capable of manipulating chemical reactions, calculating relevant stability diagrams and the equilibrium states of natural waters, tracing reaction processes, modelling reactive transport, and delivers the results in a graphical plot and report. The software was originally written by Craig Bethke with the assistance of Ming-Kuo Lee and Jeffrey Biesiadecki. The software package used in this study consists of a number of programs (Bethke and Yeakel, 2007a): *Rxn, Act2, Tact, SpecE8, React, and Gtplot*. The complete description and the guide to operate the software are provided in the documents which are included in the software package (Bethke, 1996; Bethke and Yeakel, 2007a; Bethke and Yeakel, 2007b; Bethke and Yeakel, 2007c; Bethke and Yeakel, 2007d).

6.2 The Kinetic Rate Law

In dissolution and precipitation reactions, geochemists normally consider that a reaction follows the five generalised steps mentioned in 2.4. A reaction is surface controlled when the speed of the surface reaction (a chemical reaction involving the breaking and creation of bonds) controls the reaction rate (Bethke, 1996). Many published rate laws for surface controlled reactions have been presented in a derived form of the transition state theory (Bethke, 1996). It is known

that at equilibrium the dissolution rate equals to the precipitation rate, thus the resulting net rate of reaction equals zero. In other words, the forward reaction rate equals the reverse reaction rate.

According to Bethke (1996), to formulate a reaction path, the rate of dissolution and precipitation of one or more minerals, $A_{\vec{k}}$, need to be controlled by kinetic rate laws. The reaction for $A_{\vec{k}}$:

$$A_{\vec{k}} \rightleftarrows V_{w\vec{k}}\, A_w + \sum_{\vec{i}} V_{i\vec{k}}\, A_i + \sum_{\vec{k}} V_{k\vec{k}}\, A_k + \sum_{\vec{k}} V_{m\vec{k}}\, A_m \qquad \textbf{(6.1)}$$

where: A_w : water

A_i : aqueous species

A_k : minerals

A_m : gases

$V_{w\vec{k}}$: is the number of moles of water in the reaction

$V_{i\vec{k}}$: is the number of moles of the basis species A_i

$V_{k\vec{k}}$: is the number of moles of the basis species A_k

$V_{m\vec{k}}$: is the number of moles of the basis species A_m

The rate law for Equation (6.1) follows the transition state model:

$$r_{\vec{k}} = \frac{dn_{\vec{k}}}{dt} = (A_s k_+)_{\vec{k}} \prod^{i} (a_i)^{P_{i\vec{k}}} \prod^{j} (a_i)^{P_{j\vec{k}}} \left(\frac{Q_{\vec{k}}}{K_{\vec{k}}} - 1 \right) \qquad \textbf{(6.2)}$$

where: $r_{\vec{k}}$: time rate of change

$n_{\vec{k}}$: mol number of mineral $A_{\vec{k}}$

A_s : surface area of the mineral (cm^2)

k_+ : intrinsic rate constant ($mol/cm^2.s$)

a_i : activity of the basis species A_i and

a_j : activity of the secondary species A_j

$K_{\vec{k}}$: equilibrium constant of the reaction

$Q_{\vec{k}}$: activity product for reaction

$P_{i\vec{k}}$ and $P_{j\vec{k}}$: exponents for each species; in practice, only a few species appear in the Π terms, and the values of $P_{i\vec{k}}$ and $P_{j\vec{k}}$ for most species are zero

The general rate law equation for quartz is:

$$r = A_s k_+ \left(\frac{Q}{K} - 1\right) \quad \textbf{(6.3)}$$

This equation is also valid for albite and K-feldspar in the pH range from 1.5 to 8. In the pH range above 8, the general rate law for albite and K-feldspar can be written as:

$$r = A_s k_+ a_{H^+}^{-\frac{1}{2}} \left(\frac{Q}{K} - 1\right) \quad \textbf{(6.4)}$$

The rate constant in Equations (6.2) and (6.3) can be related to temperature by the Arrhenius equation (refer to Equation (2.62).

Lasaga (1984) has compiled the literature values for the rate (rate constant) of silica release for mineral water reactions at 25^{o}C and pH 5. Hellmann (1994) reported the dissolution rate constant for albite at various temperatures and pH. The dissolution rate constant literature values for quartz, K-feldspar and albite used as a basis to expand to other temperatures are provided in Table 6.1. Using these rate constants and the published activation energy for the minerals, the pre-exponential factor can be calculated. The values of the activation energy and pre-exponential factor to calculate the rate constants for various temperatures are provided in Table 6.2. The calculated rate constants for quartz, albite, and K-feldspar are presented in Table 6.3 – Table 6.5, respectively.

Table 6.1 Rate of silica release from mineral used as basis

Mineral	Rate $(mol/m^2 \cdot s)$	Conditions
Quartz*	4.10 x 10^{-14}	T = 25°C, pH = 5
Albite**	1.19 x 10^{-11}	T = 200°C, pH neutral
K-feldspar*	1.67 x 10^{-12}	T = 25°C, pH = 5

*) (Lasaga, 1984)
**) (Hellmann, 1994)

Table 6.2 Activation energy and pre-exponential factor values used for modelling

Mineral	E_a (kJ/mol)	A
Quartz	72.0 (Rimstidt and Barnes, 1980)*	0.1688
Albite	68.8 (Hellmann, 1994)	0.7864
K-feldspar	51.88 (Brantley, 2008)**	0.0021

*this value is the average of the reported values
**value was converted from 12.4 kcal/mol

Table 6.3 Quartz dissolution rate constants calculated for various temperatures

T (°C)	T (K)	1/T	log k	k $(mol/m^2 \cdot s)$	ln k
25	298.15	0.0034	-13.387	4.10 x 10^{-14}	-30.825
160	433.15	0.0023	-9.4556	3.50 x 10^{-10}	-21.772
170	443.15	0.0023	-9.2597	5.50 x 10^{-10}	-21.321
200	473.15	0.0021	-8.7216	1.90 x 10^{-9}	-20.082
220	493.15	0.0020	-8.3992	3.99 x 10^{-9}	-19.340
223.4	496.55	0.0020	-8.3470	4.50 x 10^{-9}	-19.220
250	523.15	0.0019	-7.9619	1.09 x 10^{-8}	-18.333

Table 6.4 Albite dissolution rate constants calculated for various temperatures

T (^{o}C)	T (K)	1/T	log k	$k\ (mol/m^2 \cdot s)$	ln k
160	433.15	0.0023	-8.4014	3.97 x 10^{-9}	-19.345
170	443.15	0.0023	-8.2142	6.11 x 10^{-9}	-18.914
200	473.15	0.0021	-7.7000	2.00 x 10^{-8}	-17.730
220	493.15	0.0020	-7.3920	4.06 x 10^{-8}	-17.021
223.4	496.55	0.0020	-7.3421	4.55 x 10^{-8}	-16.906
250	523.15	0.0019	-6.9740	1.06 x 10^{-7}	-16.058

Table 6.5 K-feldspar dissolution rate constants calculated for various temperatures

T (^{o}C)	T (K)	1/T	log k	$k\ (mol/m^2 \cdot s)$	ln k
25	298.15	0.0034	-11.777	1.67 x 10^{-12}	-27.118
160	433.15	0.0023	-8.9443	1.14 x 10^{-9}	-20.595
170	443.15	0.0023	-8.8031	1.57 x 10^{-9}	-20.270
200	473.15	0.0021	-8.4153	3.84 x 10^{-9}	-19.377
220	493.15	0.0020	-8.1830	6.56 x 10^{-9}	-18.842
223.4	496.55	0.0020	-8.1454	7.15 x 10^{-9}	-18.755
250	523.15	0.0019	-7.8679	1.36 x 10^{-8}	-18.116

6.3 Modelling

The granite dissolution modelling was undertaken in four stages. In the first stage, the Rxn program was used to calculate the equilibrium constant of the mineral dissolution reaction for pure minerals (quartz, albite and K-Feldspar). In the second stage, simulation of the equilibrium concentration of silica at various temperatures using the React program was performed. In the third stage, the dissolution of granite was simulated using the React program. In the final stage,

the precipitation rate of silica was simulated and calculated. The output of the simulation was displayed by the GtPlot program and Microsoft Excel.

6.3.1 Basic reactions in the model

Rxn is used to calculate the equilibrium constant K of the mineral dissolution reaction. The Habanero 3 granite sample has a composition as provided in Table 3.9. In order to simplify the modelling and calculations, it was assumed that only the three major components exist in the granite, and the normalised granite composition is provided in Table 6.6.

Table 6.6 The composition of granite used in the model

Element	(wt. %)
Quartz	54.35
Albite	25.00
K-Feldspar	20.65

The reaction in the model involves quartz, albite and K-feldspars. Using the program Rxn, the reaction for quartz in water:

$$SiO_2 \rightleftharpoons SiO_{2(aq)} \quad \textbf{(6.5)}$$

for albite in water:

$$NaAlSi_3O_8 + 4H^+ \rightleftharpoons Na^+ + Al^{3+} + 3SiO_{2(aq)} + 2H_2O \quad \textbf{(6.6)}$$

and K-feldspar in water:

$$KAlSi_3O_8 + 4H^+ \rightleftharpoons K^+ + Al^{3+} + 3SiO_{2(aq)} + 2H_2O \quad \textbf{(6.7)}$$

Table 6.7 Log K calculated by Rxn for quartz, albite and K-feldspar

T (^{o}C)	Log K		
	Quartz	Albite	K-feldspar
0	-4.5021	3.916	0.4534
25	-3.9993	3.0973	0.0832
60	-3.5026	1.9915	-0.5137
100	-3.0951	0.9454	-1.1108
150	-2.7176	-0.0499	-1.6916
200	-2.4272	-0.8183	-2.1608
250	-2.1943	-1.5319	-2.6527
300	-2.0106	-2.5197	-3.4599

6.3.2 Simulation of the equilibrium silica concentration from granite dissolution using React

The program React was utilised to obtain the equilibrium silica concentration from granite dissolution at various temperatures. The program React requires the amount of each reactant to be specified, and the amount specified will be totally reacted according to the specified length of reaction and/or specified temperature (constant or dynamic). The equilibrium silica concentration in this study was determined by the silica release from the granite. The amount of quartz, albite, and K-feldspar reacted from the granite dissolution would have been very difficult to determine individually. Thus, the approach taken firstly is to obtain the amount of quartz, albite, and K-feldspar reacted in water individually at 250^{o}C. Knowing that the main composition of the granite is quartz, albite, and K-feldspar, by using the dissolution rate constant at 250^{o}C for the corresponding minerals provided in Table 6.3, Table 6.4 and Table 6.5, the program React can calculate the amount of minerals reacted for the specified reaction time, which is 56 days. The input for the system is provided in Figure 6.1 and Figure 6.2. The result is presented in Table 6.8.

Figure 6.1 Constraints on the initial system in React for granite dissolution at 250°C to obtain the reacted minerals individually

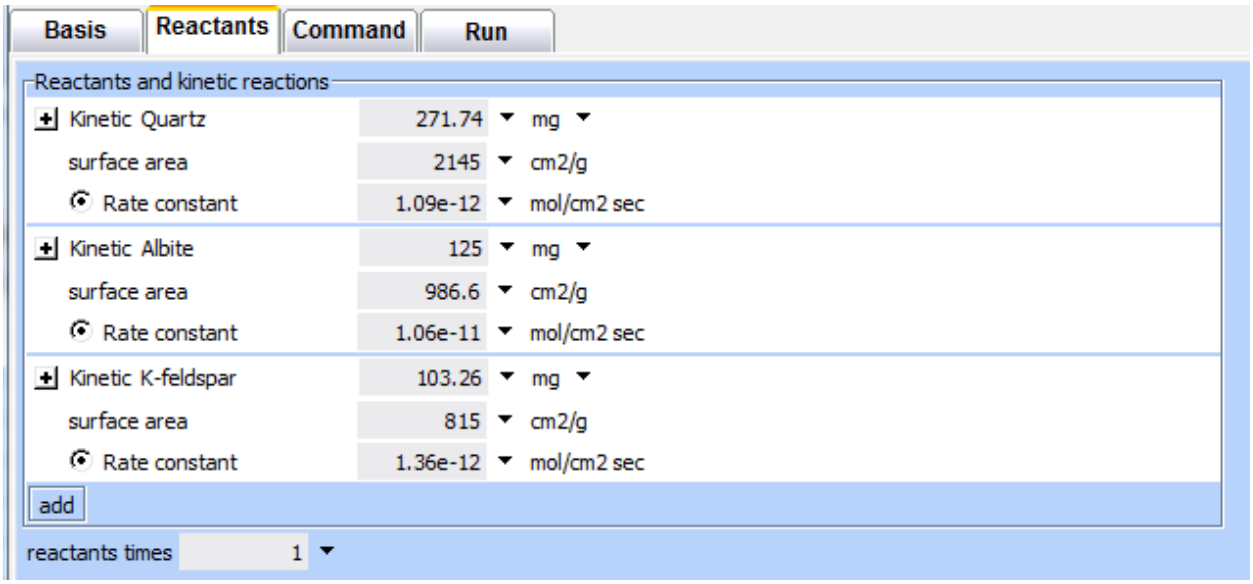

Figure 6.2 Specified reactants and kinetic reactions at 250°C to obtain the reacted minerals individually

Table 6.8 Reacted minerals calculated by React

Mineral	Reacted (mg)
Quartz	2.24
Albite	5.62
K-feldspar	7.752

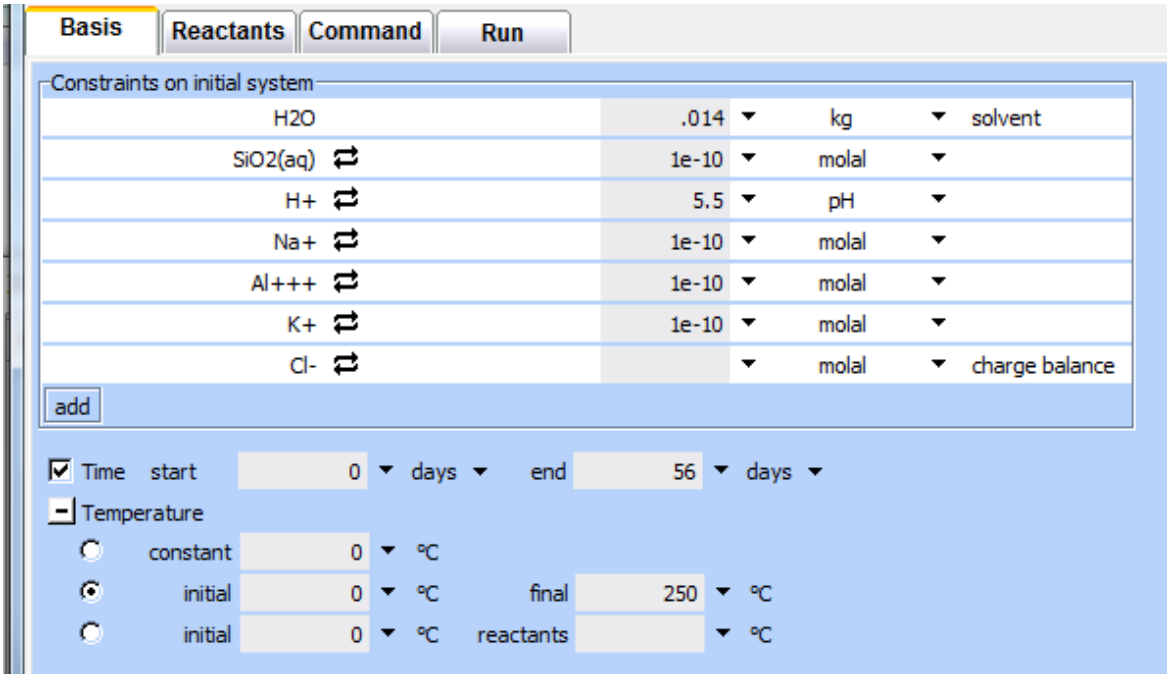

Figure 6.3 Constraints on the initial system in React to obtain the equilibrium silica concentration at various temperatures

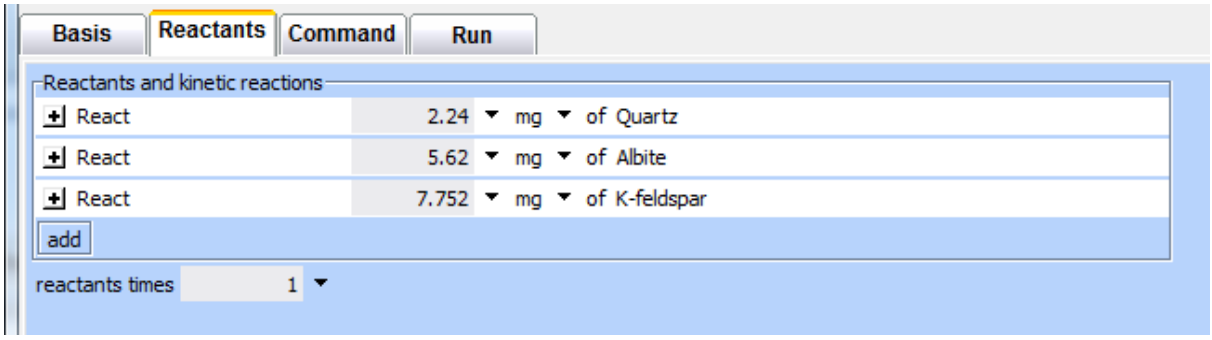

Figure 6.4 Specified reactants in React to obtain the equilibrium silica concentration at various temperatures

Using the calculated results of the amount of minerals dissolved the program React was used to simulate the silica equilibrium concentration from granite dissolution. As pure water was used, thus, the concentrations of dissolved ions were assumed to be very small. The input and the constraints are presented in Figure 6.3 and Figure 6.4. The result is plotted in Figure 6.5.

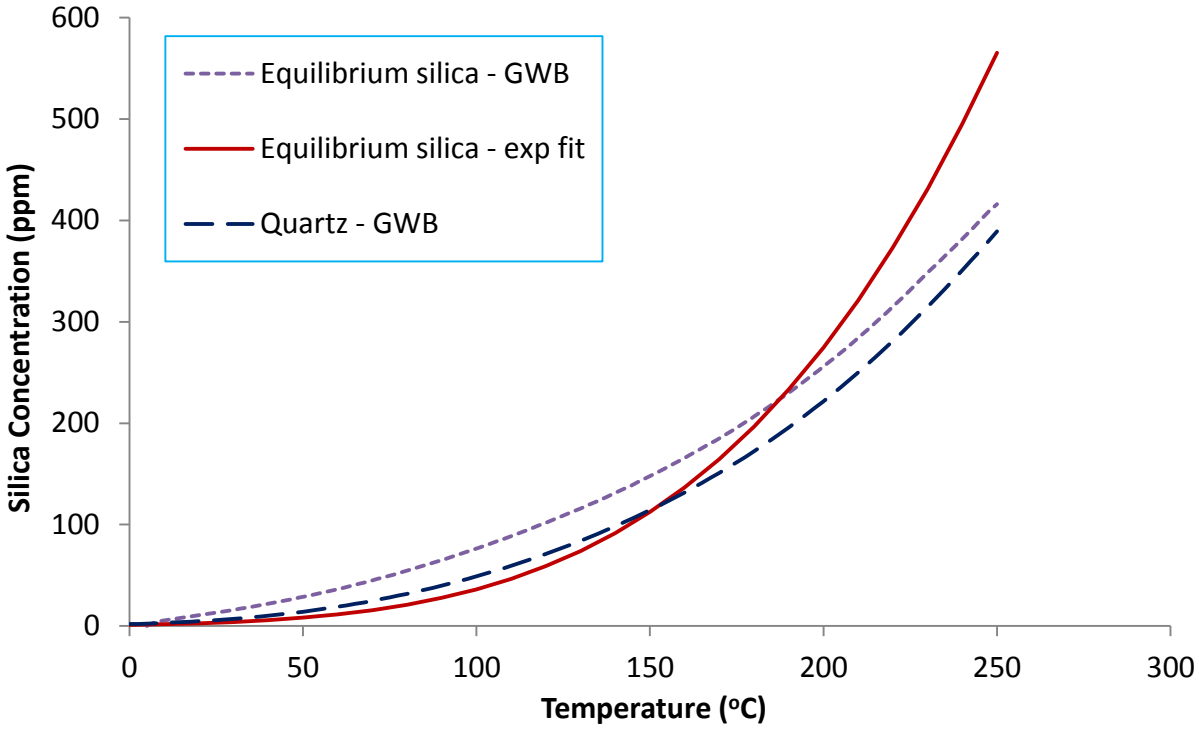

Figure 6.5 Equilibrium silica concentration from quartz dissolution at different temperature generated by GWB

It is seen that the difference of equilibrium silica concentration between the experimental fit and React output is quite significant. Since only the major components of the granite were included, this may have influenced the reaction path calculated by the program, hence affecting the silica concentration output. The assumption of the surface area used may be another contributing factor that caused the deviation of the model output with the experimental results. A further contributing factor may be the reaction rate constant chosen from literature. The published reaction rate constant may have different experimental conditions, such as different composition of minerals, particle size, duration of experiments, different reactors.

6.3.3 React simulations for granite dissolution experiments

The granite dissolution simulations were performed to fit the experimental data (concentrations of SiO_2, Na and K) using the model in the program React by altering the dissolution rate constant of the minerals. The three major components in the granite used in the simulations were quartz, albite and K-feldspar. The composition of the granite is presented in Table 6.6. The kinetic rate constant from the literature for the minerals at the corresponding temperatures are provided in Table 6.3, Table 6.4, and Table 6.5. This simulation enabled the determination of the reaction rate constant for the minerals quartz, albite and K-feldspar used in this study. In addition, this simulation was also carried out to observe the effect of solid/liquid ratio to the dissolved silica concentration. The experimental data from the flow through system using pure water was chosen for this simulation. The experimental data from using NaCl solution were not simulated as the sodium data would not reflect the dissolution of albite.

The variables that need to be specified in the basis of the React program for this particular simulation were: the amount of water, the initial concentration of the dissolved species in water, the initial pH, the operating temperature and the interaction period. As pure water was used, it was assumed that the concentrations of dissolved elements were very low. The pH of pure water used was approximately 5.5. The volume of pure water used in the hydrothermal flow-through cell was 255 mL (approximately 0.255 kg). An example of the constraints on the initial system is provided in Figure 6.6. Reactants are also required to be specified, including the mass of each reactants, the surface area of the reactants, and the kinetic reactions, as shown in Figure 6.7. In order to specify the mass of each the reactants, assuming all experiments had the same granite composition, the mass percentage of each reactant was multiplied with the mass of the sample. It was difficult to obtain the active surface area of the reactants. The approach used to approximate the surface area of the reactants was to multiply the total surface area of the sample based on BET surface area (the kinetic reaction rate from literature was based on BET surface area) with the weight percent of each reactant. This assumption may cause a deviation in the comparison between the model output and the experimental results.

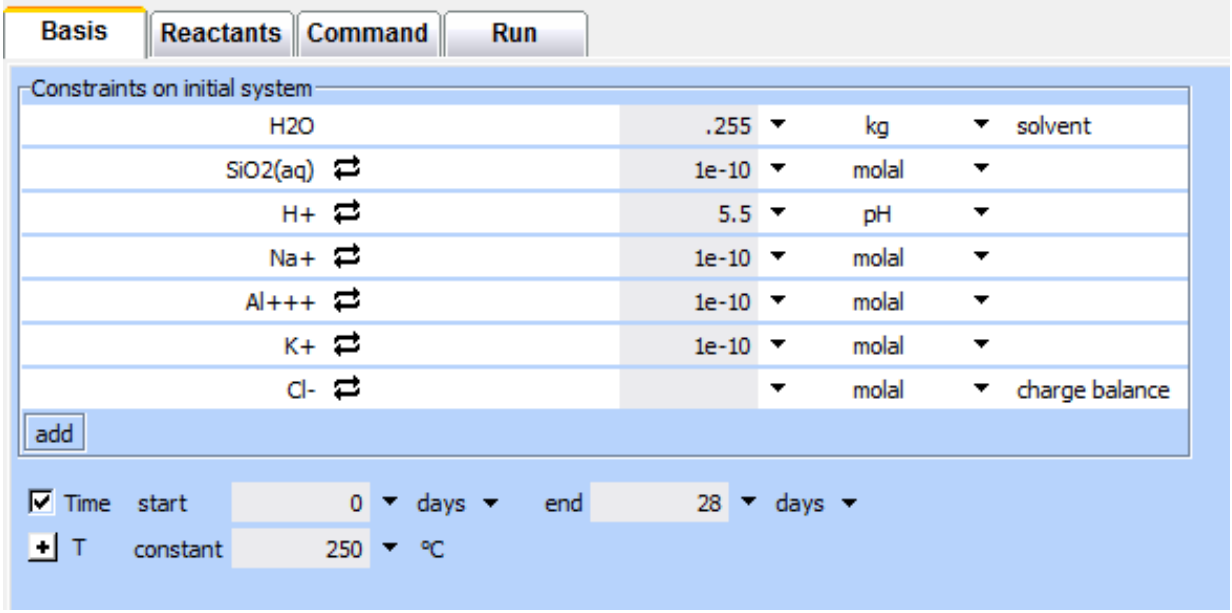

Figure 6.6 Constraints on the initial system in React for granite dissolution at 250°C

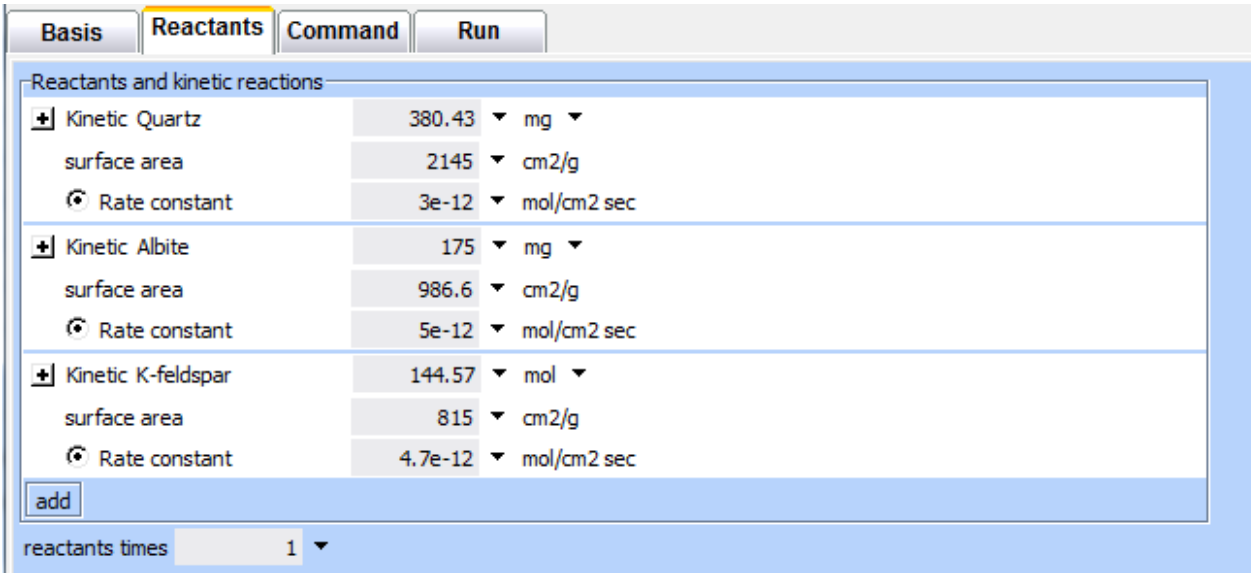

Figure 6.7 Specified reactants and kinetic reactions at 250°C for 0.7 g sample size

The constraints on the reactants, mass of reactants, and surface area of reactants that were specified 3g and 7g sample sizes are provided in Figure 6.8 and Figure 6.9, respectively.

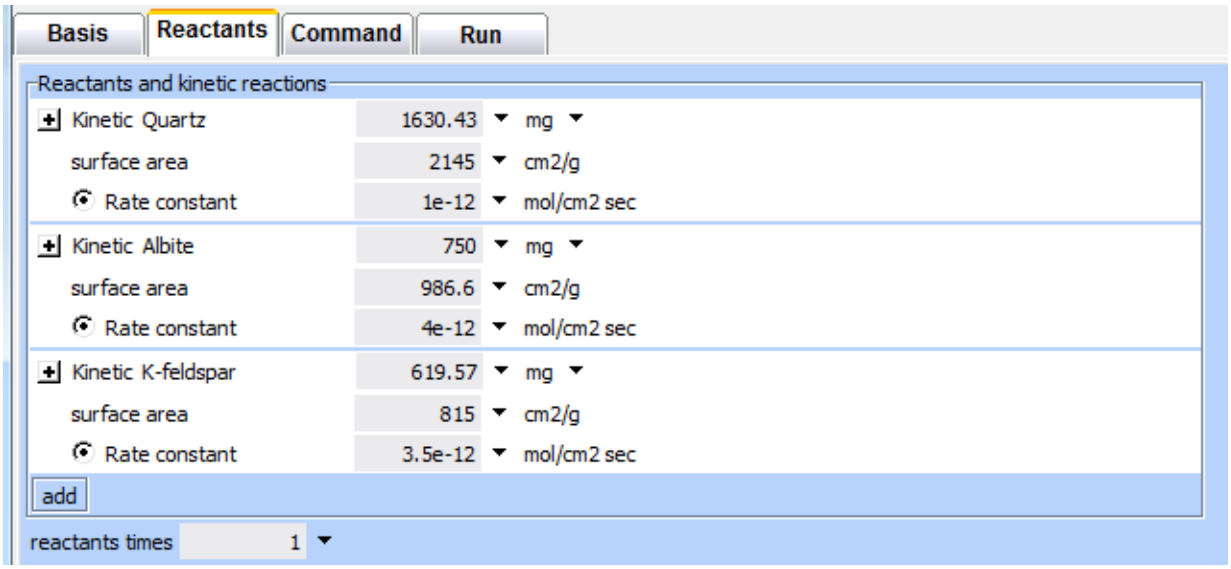

Figure 6.8 Specified reactants and kinetic reactions at 250°C for 3 g sample size

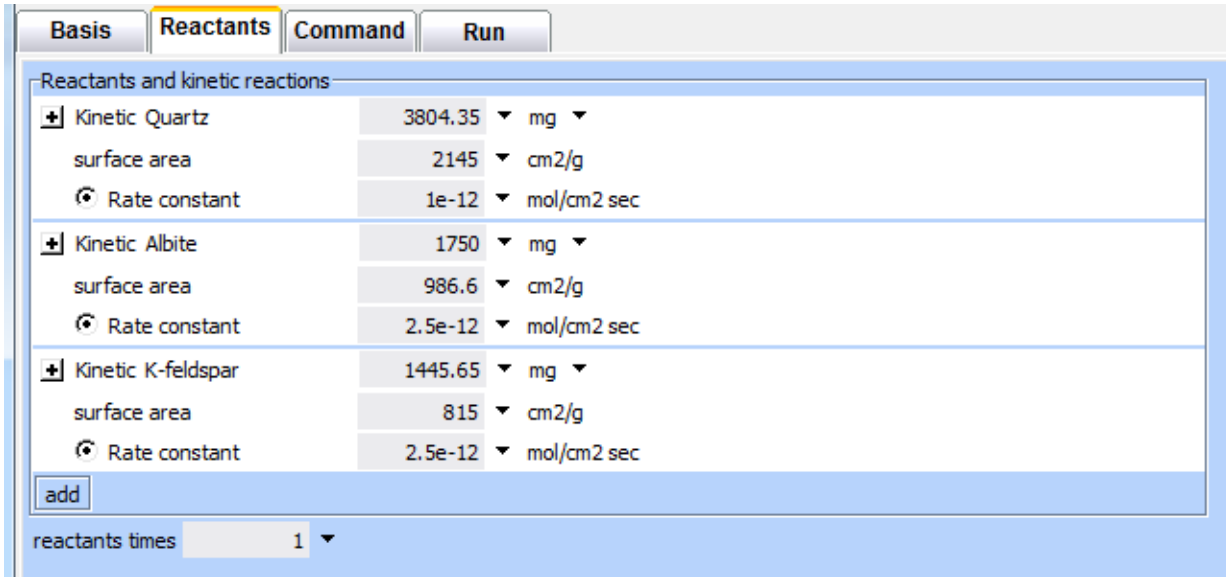

Figure 6.9 Specified reactants and kinetic reactions at 250°C for 7 g sample size

After the specification of reaction rate constant of the minerals, i.e. quartz, albite, and K-feldspar, the model would generate a dissolution profile for the chosen dissolved components. The concentrations of these dissolved components would reflect the amount of minerals dissolved. The concentration of dissolved SiO_2 in the fluid would reflect the combined dissolved quartz, albite and K-feldspar. The concentration of dissolved Na and K in the fluid would reflect

the dissolved Albite and K-feldspar respectively. The dissolution profiles showing the best fit to the SiO_2, Na and K experimental data are provided in Figure 6.10 to Figure 6.12 for sample size 0.7g, 3g and 7g respectively. The reaction rates constants that provided the best fit for different minerals and sample sizes are provided in Table 6.9.

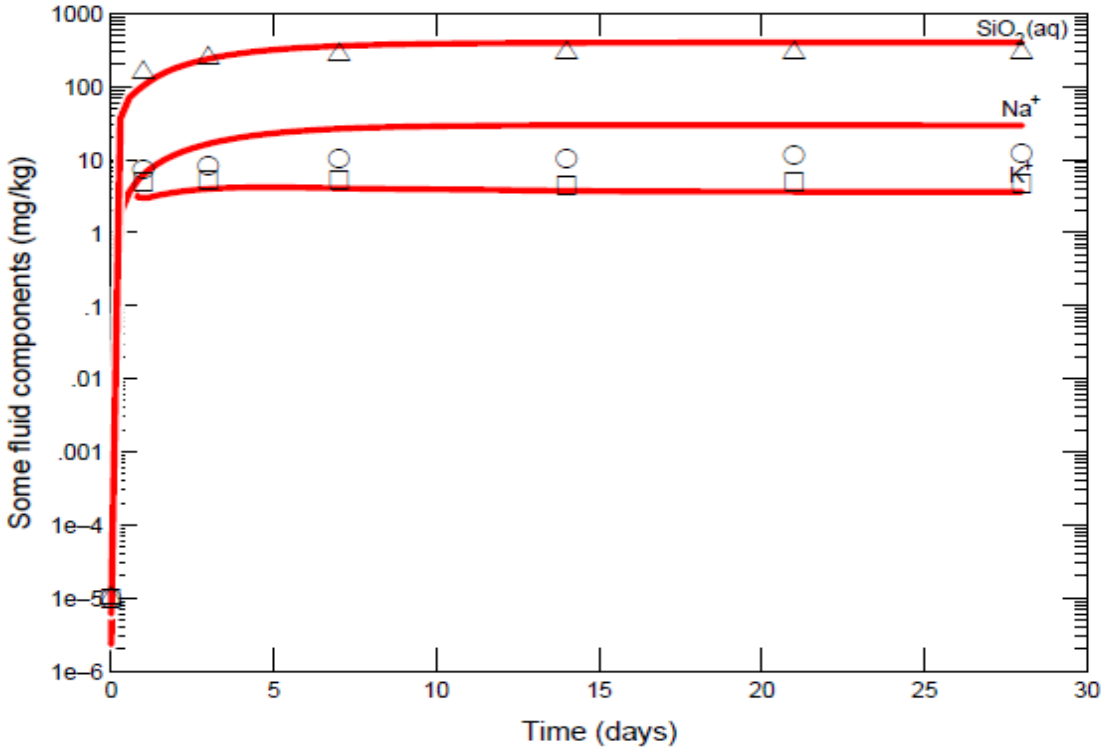

Figure 6.10 Concentrations of fluid components over time fitted using GWB to determine the reaction rate constant for 0.7 g sample size

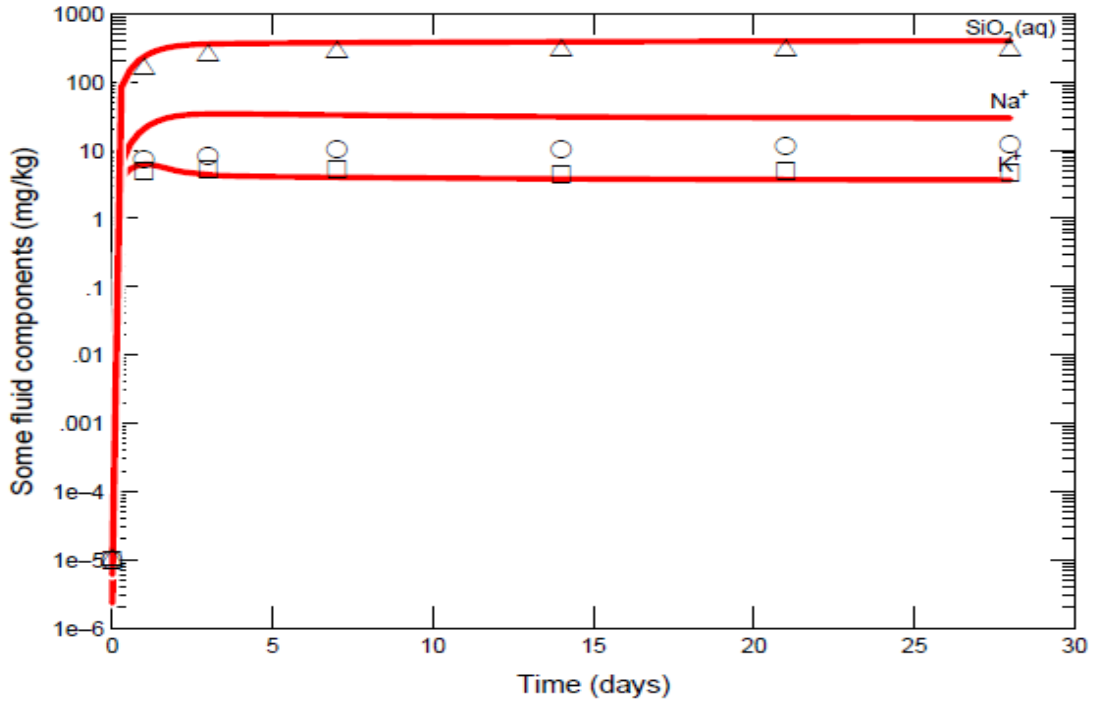

Figure 6.11 Concentrations of fluid components over time fitted using GWB to determine the reaction rate constant for 3 g sample size

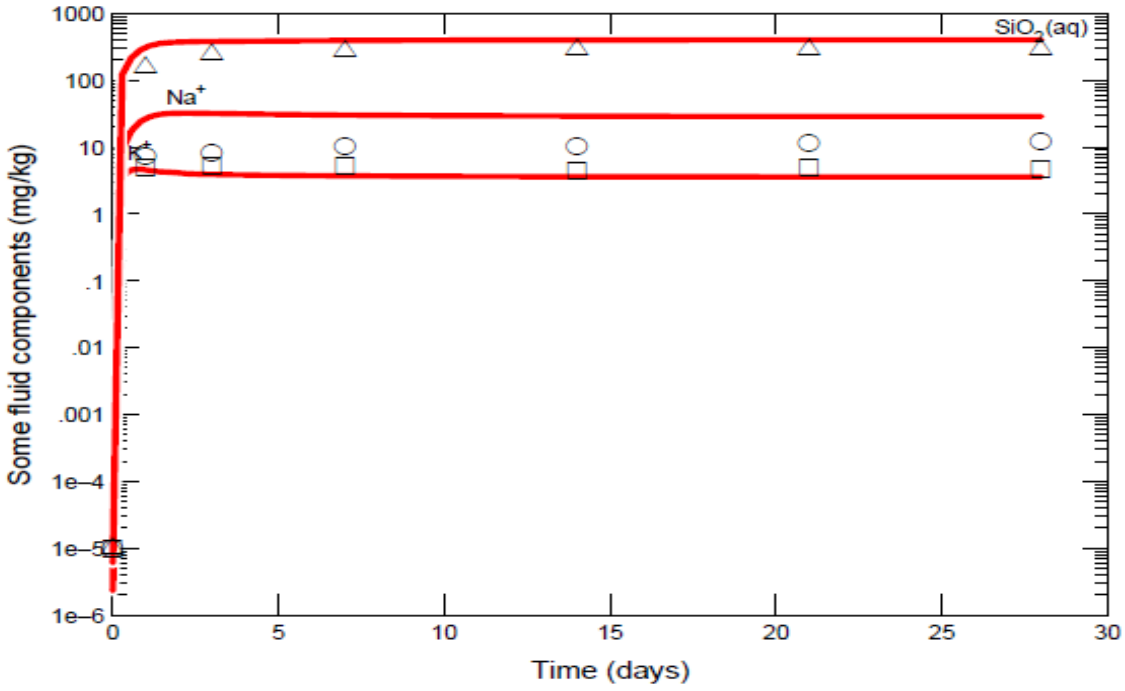

Figure 6.12 Concentrations of fluid components over time fitted using GWB to determine the reaction rate constant for 7 g sample size

Table 6.9 Reaction rate constant values from literature and GWB modelling

Minerals	Literature values ($mol/cm^2.s$)	Experimental reaction rate constant fitted using GWB ($mol/cm^2.s$)		
		0.7 g	3 g	7 g
Quartz	1.09×10^{-12}	3.0×10^{-12}	1.0×10^{-12}	1.0×10^{-12}
Albite	1.06×10^{-11}	5.0×10^{-12}	4.0×10^{-12}	2.5×10^{-12}
K-Feldspar	1.36×10^{-12}	4.7×10^{-12}	3.5×10^{-12}	2.5×10^{-12}

The combined React output showing the silica concentration (log scale) for different sample size is provided Figure 6.13. The results showed that the silica concentration increases with time, and a faster dissolution rate was observed with increasing sample size. This can be explained by the increase of surface area with the addition of larger sample mass. It was also necessary to observe which mineral dissolved most in the simulation. Figure 6.14 to Figure 6.16 show the amount of various dissolved minerals in water using 0.7g, 3g and 7g sample size, respectively. Note that the initial amount of the mineral is shown at day 0 and decreasing to day 28.

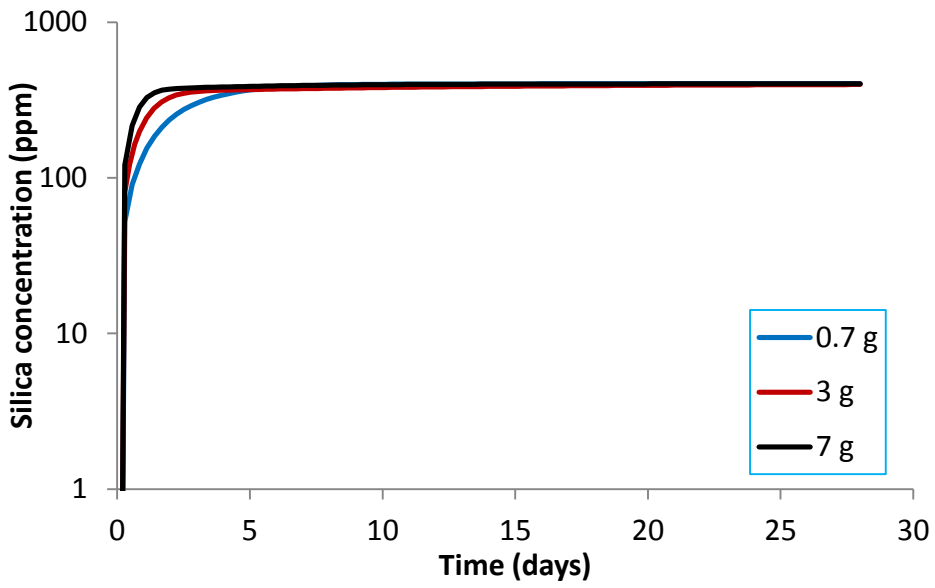

Figure 6.13 Silica concentrations from different sample sizes after data fitting using GWB

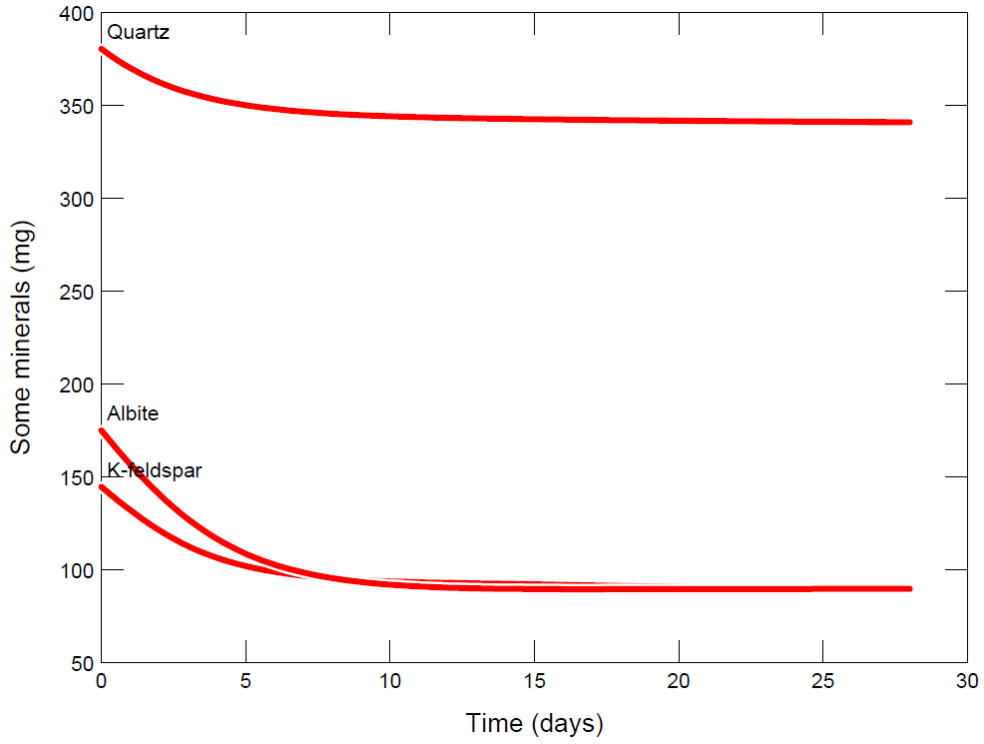

Figure 6.14 Amount of various minerals dissolved in water using 0.7 g sample size

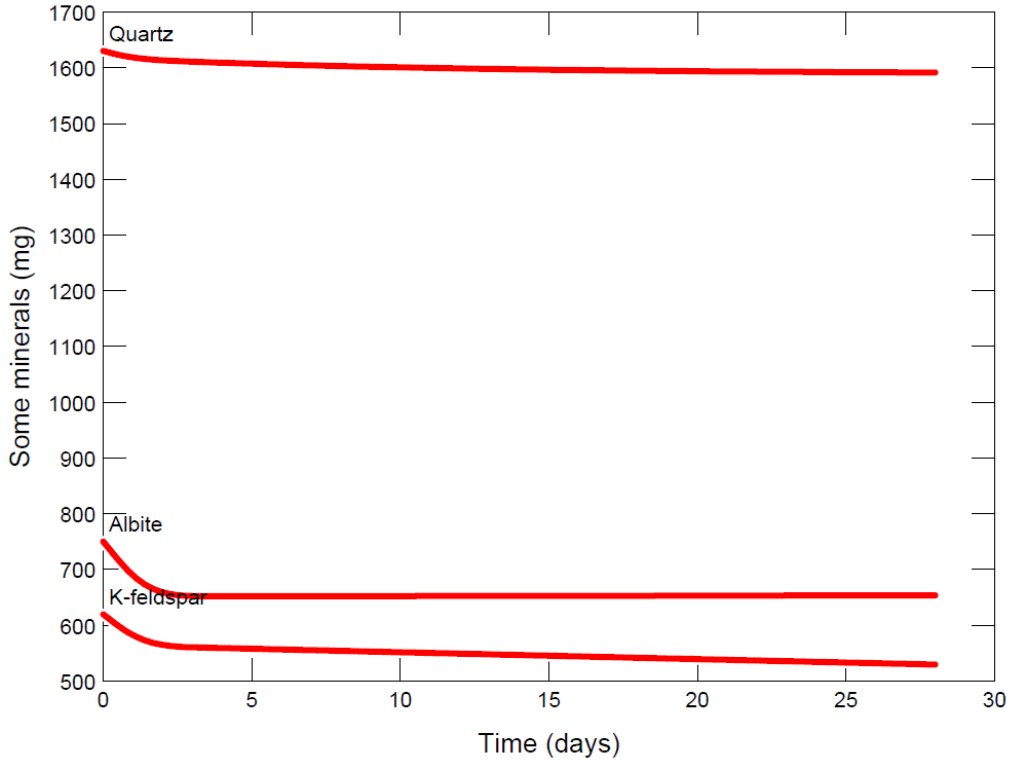

Figure 6.15 Amount of various minerals dissolved in water using 3 g sample size

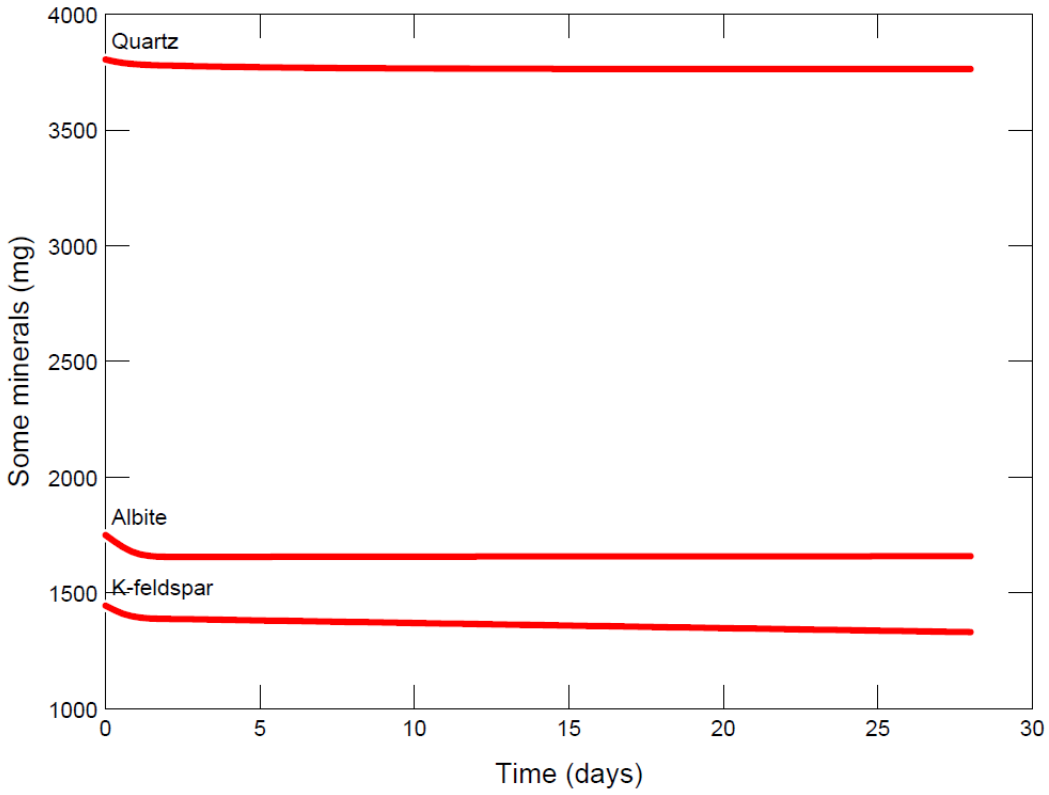

Figure 6.16 Amount of various minerals dissolved in water using 7 g sample size

It can be seen that in all simulations, albite showed the most drop from day 0 to day 28, which indicate that albite is the more soluble component in the granite and may be expected that most of the dissolved SiO_2 was the result of albite dissolution. The pH from the model output rose from 5.5 to approximately 8 at the end of the reaction period for all sample sizes. The program showed that the increase of pH was due to the increased amount of the dissolved albite and K-feldspar and the presence of quartz alone did not increase the pH.

6.3.4 Simulation of mineral precipitation from granite dissolution using React

In this section, a simulation of cooling in the React program will be used to predict the amount of silica that comes out of solution. The simulation was based on the quartz deposition in a fracture model by Bethke (1996). To model the precipitation, it was assumed that a packet of

fluid was in contact with the fracture walls over a polythermal reaction path. It was also assumed that the surface area of the fracture in contact with the packet of fluid was constant. With 1 kg of fluid, the surface area of the fracture lining is:

$$A_s = \frac{2000\Psi}{\rho\delta} \quad \textbf{(6.8)}$$

where: A_s : surface area of fracture lining (cm^2)

Ψ : surface roughness (surface area per unit area in cross section)

ρ : fluid density (assuming 1 g/cm^3)

δ : fracture aperture (assuming 10 cm)

In this simulation, it was assumed that the surface roughness is 2, and the fracture aperture is 10 cm. This results each kg of fluid is exposed to 400 cm^2 of granite surface, calculated from:

$$A_s = \frac{2000 \times 2}{1 \times 10} = 400\ cm^2$$

To simplify the model, the dimension and the fluid velocity is neglected. However, the length of time (Δt) for the fluid to travel from the high temperature condition to the cooler condition must be known. It was assumed that the residence time of the fluid inside the fracture or geothermal reservoir (250^{o}C) was Δt = 28 days and then flowed to the surface, and goes through a heat exchanger resulting in an outlet fluid temperature 90^{o}C. The variables that need to be specified in the basis of the React program for this particular simulation: the initial concentration of the dissolved species in water, the initial pH, the temperature range, and the interaction period. The constraints on the initial system in the basis pane and the kinetic constraints are provided in Figure 6.17 and Figure 6.18, respectively.

Since the active granite surface area is known, the individual active surface area for each mineral may be calculated. To assign the amount of quartz, albite and K-feldspar, the weight

composition is required (see Table 3.9). The calculated amount of quartz, albite and K-feldspar based on 400 cm^2 total active granite surface area is provided in Table 6.10. The specific surface areas of the components were set to unity, as the mass of the components has been set to the desired active surface area. The individual rate constant of the components was obtained from the previous simulation (see Section 6.3.3) and entered in the Reactants tab.

Table 6.10 Component mass based on the calculated active surface area

Component	Mass of component based on 400 cm^2 active surface area (g)
SiO_2	217.39
Na^+	100.00
K^+	82.609

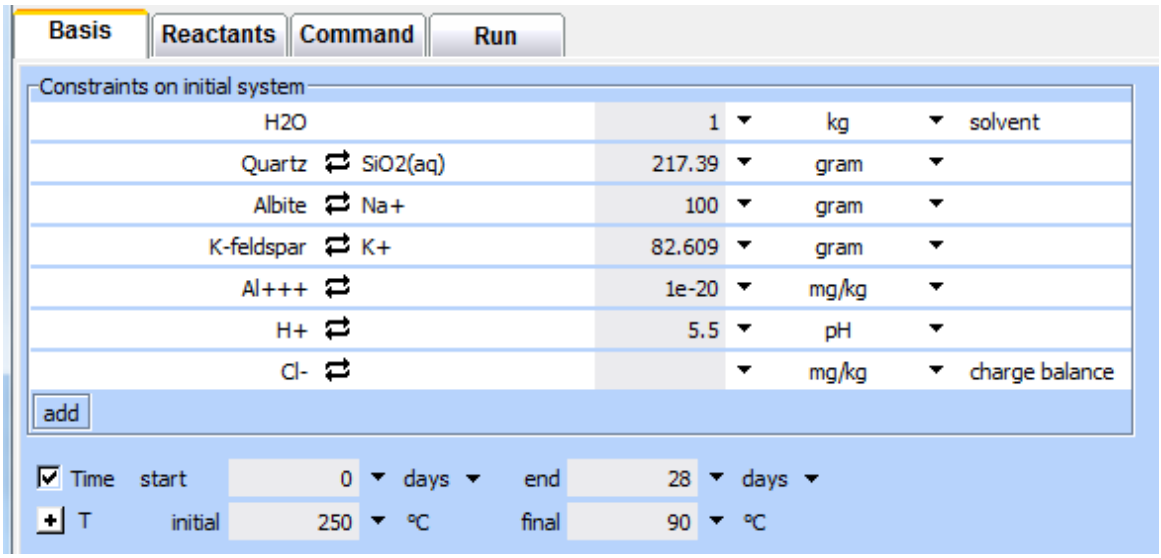

Figure 6.17 Constraints on the initial system for silica precipitation from water

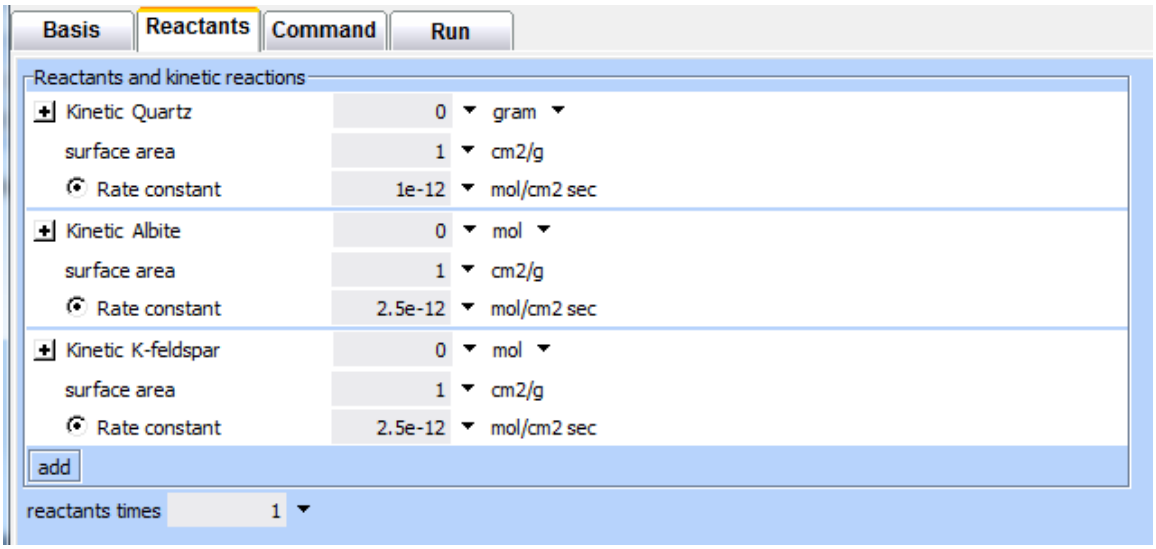

Figure 6.18 Specified surface area and kinetic reactions for silica precipitation from water

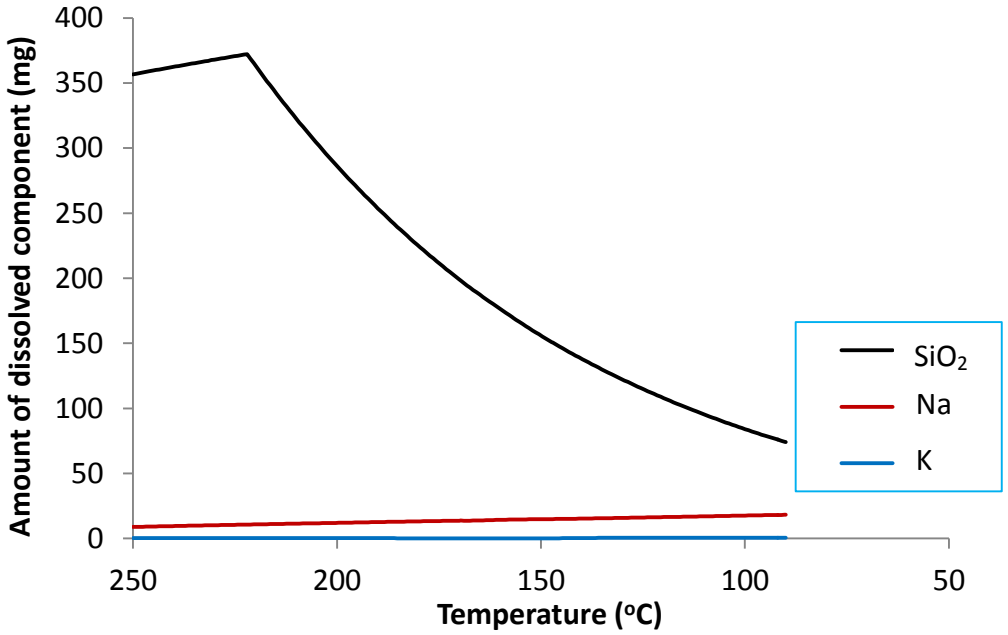

Figure 6.19 Changes in the amount of silica in water as the fluid cools

From the specified constraints, the React program produced an output showing the change in the amount of dissolved component through the cooling process. The result is presented in Figure 6.19. From this output, the amount of silica dissolved was approximately 372.2 mg, and the remaining silica in solution was 74.13 mg. This suggests that the amount of silica that may

precipitate was 298.1 mg over the period of 28 days. It is seen that the concentration of Na and K did not change much as the cooling occurs. This illustration confirms that only the silica comes out of solution.

Simulation of silica precipitation using 250 ppm NaCl solution was also performed. It was mentioned previously that the dissolution simulation of granite in NaCl solution was not preformed. It was mainly due to the difficulty to determine the amount of dissolved Na from the dissolution of albite due to the presence of NaCl in the system. Therefore, no individual mineral reaction rate constant for the dissolution of granite in NaCl solution was generated. To circumvent the lack of the reaction rate constants, it was decided that the available literature values of pre-exponential factors and activation energy for different minerals (see Table 6.2) were used. Since the sample has the same composition, the constraints on the initial system in the basis pane are identical for both water and NaCl system, and the same active surface area was used. The kinetic constraints are provided in Figure 6.20.

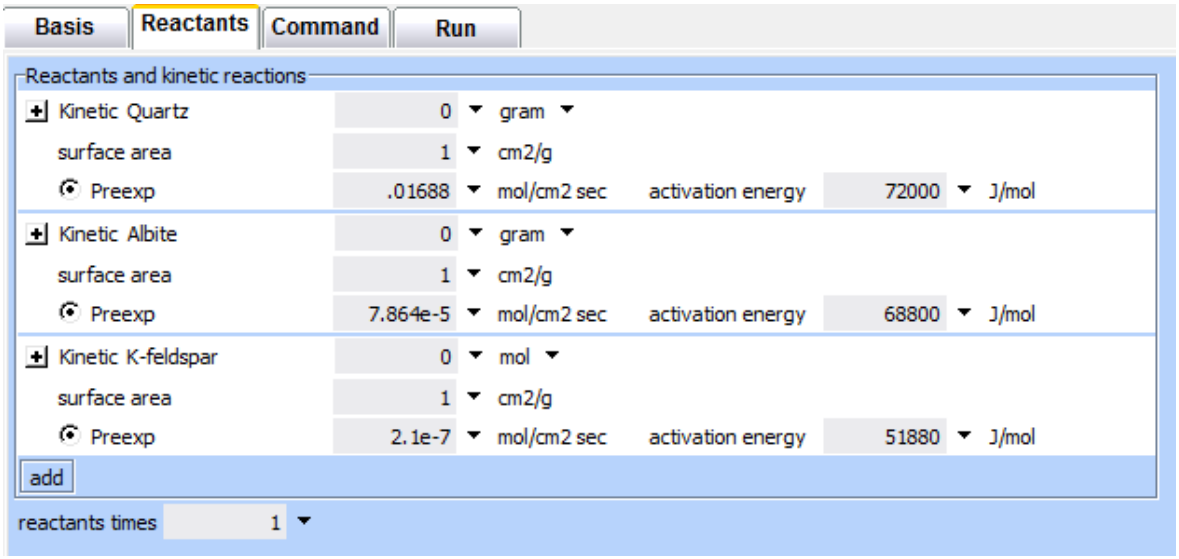

Figure 6.20 Constraints on the initial system in React for silica precipitation from 250 ppm NaCl solution

The amount of SiO_2, Na, and K during the cooling process is presented in Figure 6.21. From this output, the amount of silica dissolved was approximately 380.7 mg, and the remaining silica in

solution was 71.29 mg. This suggests that the amount of silica that may precipitate was 309.4 mg over the period of 28 days.

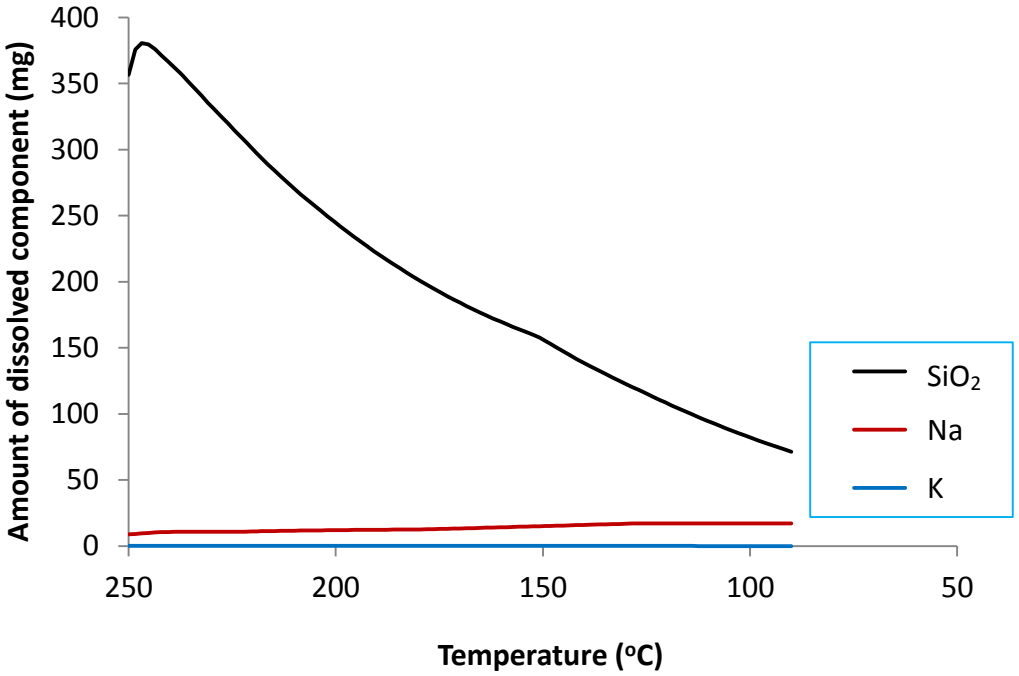

Figure 6.21 Changes in the amount of silica in 250 ppm NaCl as the fluid cools

According to Bethke (1996), the sealing rate, which is the negative rate at which fracture aperture changes, can be calculated using:

$$-\frac{d\delta}{dt} = \frac{r_{mineral} M_V \rho \delta}{1000} \qquad \textbf{(6.9)}$$

where: $-\frac{d\delta}{dt}$: sealing rate

$r_{mineral}$: mineral precipitation rate (mol/s from a kg of water)

ρ : fluid density (assuming 1 g/cm^3)

δ : fracture aperture (assuming 10 cm)

M_V : mineral's molar volume (cm^3/mol)

It was assumed that the dissolution rate is equal to the precipitation rate. The granite dissolution rate in water and NaCl are provided in Table 5.26 and Table 5.30, respectively. Using the granite composition data provided in Table 6.6 and the molecular weight of quartz, albite and K-feldspar, the mix molecular weight of the granite is 155.89 g/mol. From previous calculations, the mix density of the granite is 2.63 x 10^3 kg/m^3 (2.63 g/cm^3). Thus, the calculated mineral's molar volume is 59.32 cm^3/mol. From the available information, the sealing rate from granite dissolution in water is 2.30 cm/year, and the sealing rate from granite dissolution in NaCl solution is 2.41 cm/year.

Chapter 7 Conclusions and Recommendations

This section provides the results of preliminary analyses on the rock and fluid samples obtained from the hot dry rock geothermal site in Cooper Basin. The findings of the fluid-rock interaction experiments are summarised here, including the analyses of rock samples and water samples. This study measured the release of silica to solution to obtain the granite dissolution rate. Instead of identifying separately the dissolution rate for albite, quartz, and K-feldspar, the dissolution of granite was seen as one unit, as the scope of this study is to identify the silica dissolution rate from granite.

There were two experimental system used in this study, static and flow-through system. The purpose of the static system study was to obtain granite dissolution profiles at various conditions, mainly from the release of silica to the solution. The static autoclave reactors allow simple dissolution rate determination and proved to provide conclusive results. The equilibrium silica concentrations were obtained from dissolution at 120^{o}C, 140^{o}C, 160^{o}C, 170^{o}C, 200^{o}C and 220^{o}C for 56 days. The dissolution rate of granite in water was studied at 160^{o}C, 170^{o}C, 200^{o}C and 220^{o}C based on geometric and BET surface area. The dissolution rate law used is the global rate law which is provided in Equation (2.17) and has the same form as the dissolution rate law based on Transition State Theory (TST). The dissolution rate constants obtained from static autoclave reactors were compared with literature values for quartz, and a good agreement was observed. A possible explanation for this is that the components of the granite: quartz, albite and K-feldspar follow the same rate law (Bethke, 1996), and as quartz possess the slowest rate constant, this is rate limiting for granite dissolution. The obtained dissolution rate constants were then regressed using the Arrhenius equation describing a kinetic rate constant with an activation energy of 64.53 kJ/mol. This obtained activation energy was lower compared to the activation energy of quartz. This is because granite is a multiphase rock rather than a

homogenous phase. With the lower activation energy, as experimental suggest, the granite is more reactive compared to pure quartz. Granite dissolution studies were also performed using different particle size. As expected, the dissolution rate increases with increasing surface area and agree with the finding from a study by Huang et al. (1986). Another granite dissolution studies were performed to observe the dissolution rate in 250 ppm NaCl solution. Results also agreed with literature (Dove and Crerar, 1990) that the presence of electrolytes (in this case Na^+) increases the reaction rate. A study to observe the effect of pH on granite dissolution was also performed. The experimental results showed agreement with the literature (Huang and Kiang, 1972) where at acid conditions (low pH) and the presence of organic acid (acetic acid in this study) increased the dissolution rate. At higher pH, the silica concentration of silica increased significantly compared to dissolution in pure water. As the pH is greater than 8, the dissolved silica species that is significant is not solely $SiO_{2(aq)}$ or H_4SiO_4. The hydrogen atoms from H_4SiO_4 can dissociate and release $H_3SiO_4^-$ ion which is very soluble in water. At higher pH, further hydrogen dissociation is possible to form $H_2SiO_4^{2-}$ which is also soluble in water and may further increase the silica concentration (Brown, 2011b).

A suggestion for further studies are to perform granite dissolution experiments at other temperatures, therefore, by having more data points, the determination of activation energy for granite may be more accurate. In addition, separate dissolution studies on the individual components (quartz, albite and K-feldspar extracted from the granite), if possible, would result in valuable information to gain a more in depth understanding on granite dissolution.

Further granite dissolution studies were performed using a flow-through hydrothermal cell at 250^oC in water and in 250 ppm NaCl solution. This set up allows fluid flow through the samples inside the cell. The effect of rock/fluid ratios on granite dissolution rates was observed. The experimental results agree with the finding from a study by Huang et al. (1986), where the release rate of silica into solution increases with increasing fluid/rock ratio. The results from dissolution in water and 250 ppm NaCl solution were compared, and it was found to have a similar trend. A possible explanation is that a dilute concentration of NaCl was used, thus only

resulting in a small influence to the silica concentration, although results still showed slightly faster dissolution rate. The presence of Na^+ as expected increased the dissolution rate, as previously observed in the static autoclave experiment. A second set up using the hydrothermal flow-through cell was replacing the fluid every 24 hours (non-recycled system). This was performed to identify the more soluble phase of the granite composition. The SEM images of the granite surfaces showed severe pitting, and SEM back-scatter images with the aid of EDAX enables to identify that albite was more soluble compared to K-feldspar, and both were more soluble compared to quartz. These findings were supported by the published literature values of dissolution rate constant based on silica release, where the dissolution rate constant of albite was larger than K-feldspar, and both were larger compared to quartz. In addition to the above experiments, the effect of pressure on silica dissolution was also observed using a non-recycled high pressure flow-through cell. The results showed that more silica dissolved with increasing pressure, and this agrees with studies performed by Fournier and Potter II (1982a), and Vala Ragnarsdóttir and Walther (1983).

As mentioned above, the rate law used in the global rate law. In order for the rate law to be valid the reaction must be controlled by surface reaction and mass transfer limitation should not exist. In order to verify, the mass transfer coefficient and the rate constant must not be in the same order of magnitude (Robinson, 1982). Results showed that the mass transfer coefficients for static and flow-through system are several orders of magnitude larger than the reaction rate constant, thus mass transfer limitations do not exist in the systems.

Granite dissolution modelling was performed with the aid of the Geochemist Workbench Standard 7.0 software with the LLNL database (thermo_MMS.dat). The modelling was undertaken to obtain the equilibrium silica concentration at various temperatures, dissolution rate constant, the amount of silica precipitation and the fracture sealing rate. The modelling results showed that the difference between the equilibrium silica concentration from the experimental fit and React output is quite significant. Since only the major components of the granite were included, this may have influenced the reaction path calculated by the program,

hence affecting the silica concentration output. The next simulation performed was to obtain the dissolution rate constant of the individual mineral components from the granite dissolution experiment data in water and in 250 ppm NaCl solution using the flow-through system. By altering the rate constant of the minerals, the program would generate a dissolution profile for the chosen dissolved components. The dissolution profile generated by the program closest to the experimental results was assumed to be the dissolution rate constant.

In addition to the above simulations, the program React was used to calculate the amount or rate of silica precipitation with the assumption that the aperture of the fracture was 10 cm and the surface roughness was 2. From the granite dissolution in pure water simulation, it was found that the amount of silica that may precipitate was approximately 298.1 mg over the period of 28 days. From the granite dissolution in 250 ppm NaCl solution simulation, it was found that the amount of silica that may precipitate was approximately 309.4 mg over the period of 28 days. From the dissolution rate obtained from the experimental results, the fracture sealing rate from granite dissolution in water was: 2.30 cm/year and that in NaCl solution was 2.41 cm/year.

It has been pointed out that this is a simplified model and only the major components of the granite were included and this may have influenced the reaction path calculated by the program, hence affecting the silica concentration output and reaction rate. The assumption of the surface area used may be another contributing factor that caused the deviation of the model output with the experimental results. Another contributing factor may be the reaction rate constant chosen from literature. The published reaction rate constant may have different experimental conditions, such as different composition of minerals, particle size, duration of experiments, and different reactor designs. As well, input of the reaction rate constant was allowed for single minerals, and the model may not simulate the exact laboratory experimental conditions. In addition, this study measured the dissolution of granite solely from the release of silica to solution. Since the literature published reaction rate constant from pure minerals (for example albite), this reaction rate constant may not be the appropriate value to specify the

albite component in the granite. In other words, the reaction path of dissolving three pure minerals in water may not be identical to the dissolution mechanism in granites with the same mineral composition. Since the model output resulted in some differences compared to the experimental results, this means that modelling and experiments should work together to predict more accurate outputs.

In addition, it was found that transferring laboratory results to field situations were very challenging (Bethke, 1996). He mentioned that many minerals have been found to have dramatically different dissolution and precipitation rate in nature than in laboratory experiments. Furthermore, the determination of representing the surface area of minerals in natural samples have been extremely difficult (Aagaard and Helgeson, 1982) cited in Bethke (1996). Moreover, the state of the mineral samples in laboratory conditions are fresh and surface coatings have been likely to be removed, however, samples in the field may be shielded with oxide, hydroxide or organic coatings, which may limit the contact between the surface of the samples and the fluid. Besides the factors mentioned above, measurements error in laboratory may lead to discrepancy between laboratory studies and field studies. According to Brantley (1992) cited in Bethke (1996), the rate constant determined in different laboratories generally agree to a factor of about 30, and to obtain an agreement better than 5 may not be possible. Nonetheless, laboratory studies and simulations have been proven to be a valuable tool in the area of mineral dissolution and precipitation and providing a database of information.

Chapter 8 Nomenclature

A	interfacial area (m^2)
A	frequency factor or pre-exponential factor in Arrhenius equation ($mol/m^2.s$)
A	chemical affinity of the overall reaction
A_s	active surface area (m^2)
A_s	surface area of fracture lining (cm^2)
a^*	ratio of quartz surface area to fluid volume (m^{-1})
a_i	activity of the basis species
a_j	activity of the secondary species
C^∞	equilibrium silica concentration (ppm)
d	pipe diameter (m)
d_p	average diameter of particle (m)
dS	change of entropy of a system
d_eS	Sum of the entropy supplied to the system
d_iS	Entropy produced in the system
D_{AB}	diffusivity of H_4SiO_4 in water (m^2/s)
E_a	activation energy (J/mol)
g	gravitational acceleration = 9.81 m/s^2
K	equilibrium constant for dissolution reaction
k	kinetic rate constant for dissolution (m/s)
$k^\#$	pseudo kinetic rate constant for dissolution (s^{-1})
k_+	dissolution rate constant ($mol/cm^2.s$)
k_-	precipitation rate constant ($mol/cm^2.s$)
k_f	forward rate constant
k_m	mass transfer coefficient (m/s)
k_r	reverse rate constant
M_V	mineral's molar volume (cm^3/mol)

M_w	mass of water (kg)
$m_{H_4SiO_4}^{sat}$	equilibrium oncentration of dissolved silica (molal)
$m_{H_4SiO_4}$	concentration of silicic acid (molal)
P	pressure
$P_{i\vec{k}}$,$P_{j\vec{k}}$	exponents for each species; in practice, only a few species appear in the Π terms
Q	Activity product
R	gas constant (8.3143 J/K.mol)
Re	Reynolds number
r_f	forward reaction rate
r_r	reverse reaction rate
Sc	Schmidt number = $^{\upsilon}/_{D_{AB}}$
Sh	Sherwood number
t	time (s)
T_K	absolute temperature (Kelvin)
V	specific volume of pure water
ν	liquid velocity ($^{m}/_{s}$)
$-\Delta G_F^{T,P}$	the Gibbs' free energy of formation for the reaction

Greek symbols

δ	fracture aperture (assuming 10 cm)
μ_l	liquid viscosity $\left(^{kg}/_{m.s}\right)$
ρ_l	density of liquid $\left(^{kg}/_{m^3}\right)$
σ	rate of decomposition of the activated complex relative to that of the overall reaction

υ	kinematic viscosity of water $\left(m^2/_s\right)$
Ψ	surface roughness (surface area per unit area in cross section)
ξ	overall progress variable for the process
$-\frac{d\delta}{dt}$	sealing rate

Chapter 9 Bibliography

AAGAARD, P. & HELGESON, H. C. 1982. Thermodynamic and kinetic constraints on reaction rates among minerals and aqueous solutions. I. Theoretical considerations. *American Journal of Science,* 282**,** 237 - 285.

ANBEEK, C. 1992. The dependence of dissolution rates on grain size for some fresh and weathered feldspars. *Geochimica et Cosmochimica Acta,* 56**,** 3957-3970.

ARNÓRSSON, S. & STEFÁNSSON, A. 1999. Assessment of feldspar solubility constants in water in the range 0^{o} to 350^{o}C at vapor saturation pressures. *American Journal of Science,* 299**,** 173 - 209.

AYE, L. 2005. Alternative Energy Paper One. *Australian Rationalist,* 70**,** 23-28.

AZAROUAL, M. & FOUILLAC, C. 1997. Experimental study and modelling of granite-distilled water interactions at 180°C and 14 bars. *Applied Geochemistry,* 12**,** 55-73.

BENNETT, P. C. 1991. Quartz dissolution in organic-rich aqueous systems. *Geochimica et Cosmochimica Acta,* 55**,** 1781 - 1797.

BERGER, G., CADORE, E., SCHOTT, J. & DOVE, P. M. 1994. Dissolution rate of quartz in lead and sodium electrolyte solutions between 25 and 300^{o}C: Effect of the nature of surface complexes and reaction affinity. *Geochimica et Cosmochimica Acta,* 58**,** 541 - 551.

BETHKE, C. M. 1996. *Geochemical Reaction Modellng. Concepts and Applications,* New York, Oxford University Press.

BETHKE, C. M. & YEAKEL, S. 2007a. *The Geochemist's Workbench. Release 7.0. GWB Essentials Guide*.

BETHKE, C. M. & YEAKEL, S. 2007b. The Geochemist's Workbench. Release 7.0. Reaction Modeling Guide.

BETHKE, C. M. & YEAKEL, S. 2007c. The Geochemist's Workbench. Release 7.0. Reactive Transport Modeling Guide.

BETHKE, C. M. & YEAKEL, S. 2007d. The Geochemist's Workbench. Release 7.0. Reference Manual.

BEVAN, J. & SAVAGE, D. 1989. The effect of organic acids on the dissolution of K-feldspar under conditions relevant to burial diagenesis. *Mineralogical Magazine,* 53**,** 415 - 425.

BICKMORE, B. R., NAGY, K. L., GRAY, A. K. & BRINKERHOFF, A. R. 2006. The effect of $Al(OH)_4^-$ on the dissolution rate of quartz. *Geochimica et Cosmochimica Acta,* 70**,** 290 - 305.

BLUM, A. E. & STILLINGS, L. L. 1995. Feldspar dissolution kinetics. *Reviews in Mineralogy and Geochemistry,* 31**,** 291 - 351.

BRADY, P. V. & WALTHER, J. V. 1992. Surface chemistry and silicate dissolution at elevated temperatures. *American Journal of Science,* 292**,** 639 - 658.

BRANTLEY, S. L. 1992. Kinetics of Dissolution and Precipitation - Experimental and Field Results. *Water-Rock Interaction.* Rotterdam: Balkema.

BRANTLEY, S. L. 2008. Kinetics of Mineral Dissolution. *In:* BRANTLEY, S. L., KUBICKI, J. D. & WHITE, A. F. (eds.) *Kinetics of Water-Rock Interaction.* New York: Springer Science+Business Media, LLC.

BRANTLEY, S. L. & CONRAD, C. F. 2008. Analysis of Rates of Geochemical Reactions. *In:* BRANTLEY, S. L., KUBICKI, J. D. & WHITE, A. F. (eds.) *Kinetics of Water-Rock Interaction.* New York: Springer Science+Business Media, LLC.

BRANTLEY, S. L., KUBICKI, J. D. & WHITE, A. F. (eds.) 2008. *Kinetics of Water-Rock Interaction,* New York: Springer Science+Business Media, LLC.

BROWN, K. 2011a. *RE: Quartz dissolution and silica polymerization,* Personal communication via email.

BROWN, K. Thermodynamics and kinetics of silica scaling. International Workshop on Mineral Scaling, 25 - 27 May 2011b Manilla, Phillipines.

BROWN, K. & DUNSTALL, M. Silica scaling under controlled hydrodynamic conditions. Proceedings World Geothermal Congress 2000, 2000 Kyushu - Tohoku, Japan. 3039 - 3044.

BROWNE, P. R. L. 1978. Hydrothermal alteration in active geothermal fields. *Annual Review of Earth and Planetary Sciences,* 6**,** 229 - 250.

BURNS, K. L., WEBER, C., PERRY, J. & HARRINGTON, H. J. Status of the geothermal industry in Australia. Proceeding World Geothermal Congress 2000, 2000 Kyushu - Tohoku, Japan. 99 - 108.

BURTON, E. A., BOURCIER, W. L., BRUTON, C. J., ROBERTS, J. J. & CARLSON, S. R. 2004. Evidence for the impact of water-rock interaction on permeability in enhanced geothermal systems. *Geothermal Resources Council Transactions,* 28**,** 253-257.

CASTRO, M. R., LOPEZ, D. L., REYES, J. A., MATUS, A., MONTALVO, F. E. & GUERRA, C. E. 2006. Expected silica scaling from reinjection waters after installation of a binary cycle power station at Berlin geothermal field, El Salvador, Central America. *Geothermal Resources Council Transactions,* 30**,** 487-492.

CHAPRA, S. C. & CANALE, R. P. 2002. *Numerical Methods for Engineers: With software and programming applications. Fourth Edition,* Boston, McGraw Hill.

CHEN, Y. & BRANTLEY, S. L. 1997. Temperature- and pH-dependence of albite dissolution rate at acid pH. *Chemical Geology,* 135**,** 275 - 290.

CHEN, Y. B., S. L. 2000. Dissolution of forsteritic olivine at 65^{o}C and 2 < pH < 5. *Chemical Geology,* 165**,** 267 - 281.

CHOPRA, P. & HOLGATE, F. A GIS Analysis of Temperature in the Australian Crust. World Geothermal Congres, 24 -29 April 2005 2005 Antalya, Turkey.

CHOPRA, P. N. Status of the geothermal industry in Australia, 2000 - 2005. Proceedings World Geothermal Congress 2005, 2005 Antalya, Turkey. 1 - 8.

CHOU, L. & WOLLAST, R. 1984. Study of the weathering of albite at room temperature and pressure with a fluidized bed reactor. *Geochimica et Cosmochimica Acta,* 48**,** 2205 - 2217.

CO2CRC. 2012. *Capture images. Coal fired power plant* [Online]. Available: http://www.co2crc.com.au/imagelibrary3/capture.php [Accessed 22 June 2012.

DAVIS, M. C., WESOLOWSKI, D. J., ROSENQVIST, J., BRANTLEY, S. L. & MUELLER, K. T. 2011. Solubility and near-equilibrium dissolution rates of quartz in dilute NaCl solutions at 398–473K under alkaline conditions. *Geochimica et Cosmochimica Acta,* 75**,** 401-415.

DIPIPPO, R. 1985. A simplified method for estimating the silica scaling potential in geothermal power plants. *Geothermal Resources Council Bulletin***,** 3 - 9

DOVE, P. M. 1995. Kinetic and thermodynamic controls on silica reactivity in weathering environments. *Reviews in Mineralogy and Geochemistry,* 31**,** 235 - 290.

DOVE, P. M. 1999. The dissolution kinetics of quartz in aqueous mixed cation solutions. *Geochimica et Cosmochimica Acta,* 63**,** 3715 - 3727.

DOVE, P. M. & CRERAR, D. A. 1990. Kinetics of quartz dissolution in electrolyte solutions using a hydrothermal mixed flow reactor. *Geochimica et Cosmochimica Acta,* 54**,** 955-969.

DOVE, P. M., HAN, N. & J., D. Y. J. 2005. Mechanism of clasiccal crystal growth theory explain quartz and silicate dissolution behavior. *Proceedings of National Academy of Sciences,* 102**,** 15357 - 15362.

DUBOIS, I. E., HOLGERSSON, A., ALLARD, S. & MALMSTROM, M. E. Correlation between particle size and surface area for chlorite and K-feldspar. *In:* BIRKLE, P. & TORRES-ALVARADO, I. S., eds. 13th International Conference on Water-Rock Interaction, 2010 Guanajuato, Mexico. 717 - 720.

DURST, P. & VUATAZ, F. D. Fluid-rock interactions in hot dry rock reservoirs - A review of the HDR sites and detailed investigations of the Soultz-sous-Forets system. Proceeding World Geothermal Congress 2000, 2000 Kyushu - Tohoku, Japan. 3677 - 3682.

ELLIS, A. J. 1968. Natural hydrothermal systems and experimental hot-water/rock interaction: Reactions with NaCl solutions and trace metal extraction. *Geochimica et Cosmochimica Acta,* 32**,** 1356-1363.

EPA. 2005. *Fact sheet. Birdsville geothermal power station* [Online]. Available: http://www.ehp.qld.gov.au/register/p00834aa.pdf [Accessed 22 August 2012].

EVAN, M. G. & POLANYI, M. 1935. Some applications of the transition state method to calculation of reaction velocities, especially in solution. *Transaction of the Faraday Society,* 31**,** 875 - 894.

EYRING, H. 1935. The activated complex in chemical reactions. *Journal of Chemical Physics,* 3**,** 107 - 115.

FELIPE, M. A., KUBICKI, J. D. & FREEMAN, K. H. 2005. A mechanism for carbon isotope exchange between aqueous acetic acid and CO2/HCO3-: An ab initio study. *Organic Geochemistry,* 36**,** 835 - 850.

FOGLER, S. F. 2006. *Elements of Chemical Reaction Engineering. Fourth Edition*, Prentice Hall.

FORDHAM, M. 2008. *RE: Gas analysis procedure,* Personal communication via email.

FOURNIER, R. O. 1977. Chemical geothermometers and mixing models for geothermal systems. *Geothermics,* 5**,** 41 - 50.

FOURNIER, R. O. & POTTER II, R. W. 1982a. An equation correlating the solubility of quartz in water from 25° to 900°C at pressures up to 10,000 bars. *Geochimica et Cosmochimica Acta,* 46**,** 1969-1973.

FOURNIER, R. O. & POTTER II, R. W. 1982b. Revised and expanded silica (quartz) geothermometer. *Geothermal Resources Council Bulletin,* 11**,** 3 - 12.

FOURNIER, R. O. & ROWE, J. J. 1977. The solubility of amorphous silica in water at high temperatures and high pressures. *American Mineralogist,* 62**,** 1052-1056.

GANOR, J., ROUEFF, E., EREL, Y. & BLUM, J. D. 2005. The dissolution kinetics of a granite and its minerals - Implications for comparison between laboratory and field dissolution rates. *Geochimica et Cosmochimica Acta,* 69**,** 607 - 621.

GAUTIER, J.-M., OELKERS, E. H. & SCHOTT, J. 2001. Are quartz dissolution rates proportional to B.E.T. surface areas? *Geochimica et Cosmochimica Acta,* 65**,** 1059-1070.

GEO. 2012a. *Geothermal education office. Introduction to geothermal energy slide show. Slide 6 - Plate boundaries* [Online]. [Accessed 15 February 2012].

GEO. 2012b. *Geothermal education office. Introduction to geothermal energy slide show. Slide 69 - World elec. generation map* [Online]. Available: http://geothermal.marin.org/geopresentation/sld069.htm [Accessed 15 February 2012].

GEODYNAMICS. 2009a. *The Geodynamics Story* [Online]. Available: http://www.geodynamics.com.au/IRM/Company/ShowPage.aspx?CPID=1864 [Accessed 12 January 2009].

GEODYNAMICS. 2009b. *Power from the earth. Habanero 3. Australia's first commercial hot rock geothermal well* [Online]. Available: http://www.geodynamics.com.au/IRM/Company/ShowPage.aspx?CPID=1403 [Accessed 10 January 2009].

GIANELLI, G. & GRASSI, S. 2001. Water–rock interaction in the active geothermal system of Pantelleria, Italy. *Chemical Geology,* 181**,** 113-130.

GIGGENBACH, W. F. 1981. Geothermal mineral equilibria. *Geochimica et Cosmochimica Acta,* 45**,** 393 - 410.

GOTO, K. 1956. Effect of pH on polymerization of silicic acid. *Journal of Physical Chemistry,* 60**,** 1007 - 1008.

GRIGSBY, C. O. 1989. *Kinetics of Rock-Water Reactions.* Doctor of Philosophy, Massachusetts Institute of Technology.

GRIGSBY, C. O., TESTER, J. W., TRUJILLO JR, P. E. & COUNCE, D. A. 1989. Rock-water interactions in the Fenton Hill, new Mexico, hot dry rock geothermal systems I. fluid mixing and chemical geothermometry. *Geothermics,* 18**,** 629-656.

GUDMUNDSSON, J. S. & BOTT, T. R. 1979. Deposition of silica from geothermal waters on heat transfer surfaces. *Desalination,* 28**,** 125 - 145.

GURGENCY, H. 2010. Renewed Geodynamics Confidence. *e4hgurge's blog* [Online]. Available from: http://www.geothermal.uq.edu.au/13-April-2010 [Accessed 16 September 2010].

HACH 2000. *DR2010 Portable Spectrophotometer Procedures Manual*.

HELGESON, H. C., MURPHY, W. M. & AAGAARD, P. 1984. Thermodynamics and kinetic constraints on reaction rates among minerals and aqueous solutions. II. Rate constants, effective surface area. and the hydrolysis of feldspar. *Geochimica et Cosmochimica Acta,* 48**,** 2405 - 2432.

HELLMANN, R. 1994. The albite-water system: Part I. The kinetics of dissolution as a function of pH at 100, 200 and 300°C. *Geochimica et Cosmochimica Acta,* 58**,** 595-611.

HELLMANN, R., DAVAL, D. & TISSERAND, D. 2010. The dependence of albite feldspar dissolution kinetics on fluid saturation state at acid and basic pH: Progress towards a universal relation. *Comptes Rendus Geoscience,* 342**,** 676-684.

HELLMANN, R. & TISSERAND, D. 2006. Dissolution kinetics as a function of the Gibbs free energy of reaction: An experimental study based on albite feldspar. *Geochimica et Cosmochimica Acta,* 70**,** 364-383.

HODSON, M. E. 2006. Searching for the perfect surface area normalizing term--a comparison of BET surfacve area-, geometric surface area- and mass-normalized dissolution rates of anorthite and biotite. *Journal of Geochemical Exploration,* 88**,** 288 - 291.

HOLDREN, G. R. J. & BERNER, R. A. 1979. Mechanism of feldspar weathering--I. Experimental studies. *Geochimica et Cosmochimica Acta,* 43**,** 1161 - 1171.

HUANG, W. H. & KIANG, W. C. 1972. Laboratory dissolution of plagioclase feldspars in water and organic acids at room temperature. *American Mineralogist,* 57**,** 1849 - 1859.

HUANG, W. L., BISHOP, A. M. & BROWN, R. W. 1986. The effect of fluid/rock ratio on feldspar dissolution and illite formation under reservoir conditions. *Clay Minerals,* 21**,** 585 - 601.

ICENHOWER, J. P. & DOVE, P. M. 2000. The dissolution kinetics of amorphous silica into sodium chloride solutions: effects of temperature and ionic strength. *Geochimica et Cosmochimica Acta,* 64**,** 4193-4203.

ICOPINI, G. A., BRANTLEY, S. L. & HEANEY, P. J. 2005. Kinetics of silica oligomerization and nanocolloid formation as a function of pH and ionic strength at 25^{o}C. *Geochimica et Cosmochimica Acta,* 69**,** 293 - 303.

IHT. 2007. Howard: Carbon trading system for Australia by 2011. *International Herald Tribune - The Global Edition of The New York Times* [Online]. Available: http://www.iht.com/articles/ap/2007/07/17/asia/AS-GEN-Australia-Global-Warming.php [Accessed 26 January 2009].

ILER, R. K. 1955. *The Colloid Chemistry of Silica and Silicates,* New York, Cornell University Press.

ILIESCU, E. 2004. Environmental impact report and statement of environmental objectives. Cooper Basin, South Australia.

JANDER, G. & JAHR, K. F. 1934. Neuere Anschauungen uber die Hydrolyse anorganischer Salze und die Chemie der hochmolekularen Hydrolyseprodukte (einschlie lich der Iso- und Heteropolyverbindungen). *Kolliod-Beihefte,* 41.

KAMIYA, H., OZAKI, A. & IMAHASHI, M. 1974. Dissolution rate of powdered quartz in acid solution. *Geochemical Journal,* 8**,** 21 - 26.

KARINGITHI, C. W. Chemical geothermometers for geothermal exploration. Short Course IV on Exploration for Geothermal Resources, November 1 - 22, 2009 2009 Lake Naivasha, Kenya.

KITAHARA, S. 1960a. The polymerization of silicic acid obtained by the hydrothermal treatment of quartz and the solubility of amorphous silica. *The Review of Physical Chemistry of Japan,* 30**,** 131 - 137.

KITAHARA, S. 1960b. The solubility equilibrium and the rate of solution of quartz in water at high temperatures and high pressures. *The Review of Physical Chemistry of Japan,* 30**,** 122 - 130.

KNAUSS, K. G. & WOLERY, T. J. 1986. Dependence of albite dissolution kinetics as a function of pH and time at 25^{o}C and 70^{o}C. *Geochimica et Cosmochimica Acta,* 50**,** 2481 - 2497.

KNAUSS, K. G. & WOLERY, T. J. 1988. The dissolution kinetics of quartz as a function of pH and time at 70^{o}C. *Geochimica et Cosmochimica Acta,* 52**,** 43 - 53.

KUBICKI, J. D. 2008. Transition State Theory and Molecular Orbital Calculations Applied to Rates and Reaction Mechanisms in Geochemical Kinetics. *Kinetics of Water-Rock Interaction.* New York: Springer Science+Business Media, LLC.

LAGACHE, M. 1976. New data on the kinetics of the dissolution of alkali feldspars at 200°C in CO2 charged water. *Geochimica et Cosmochimica Acta,* 40**,** 157-161.

LAIDLER, K. J. 1965. *Chemical Kinetics,* New York, McGraw-Hill.

LANE, D. M. 2013. Online Statistic Education: A Multimedia Course of Study.

LASAGA, A. C. 1984. Chemical kinetics of water-rock interaction. *Journal of Geophysical Research,* 89**,** 4009 - 4025.

LAUGHLIN, A. W. & EDDY, A. 1977. Petrography and Geochemistry of Precanbrian Rocks from GT-2 and EE-1. Los Alamos Scientific Laboratory Report LA-6930-MS.

LI, K. 2012. *RE: Stainless steel autoclave,* Personal communication via email.

LIN, F. C. & CLEMENCY, C. V. 1981. Dissolution Kinetics of Phlogopite. I. Closed System. *Clays and Clay Minerals,* 29**,** 101 - 106.

MACHESKY, M. L. 1990. Influence of temperature on ion adsorption by hydrous metal oxides. In: D.C. Melchior and R. L. Bassett (Editors). *In:* MELCHIOR, D. C. & BASSETT, R. L. (eds.) *Chemical Modeling of Aqueous Systems II. ACS Symposium Series.*

MACKENZIE, F. T. & GEES, R. 1971. Quartz: Synthesis at earth-surface conditions. *Science, New Series,* 173**,** 533 - 535.

MARKS, N., SCHIFFMAN, P., ZIERENBERG, R. A., FRANZSON, H. & FRIDLEIFSSON, G. Ó. 2010. Hydrothermal alteration in the Reykjanes geothermal system: Insights from Iceland deep drilling program well RN-17. *Journal of Volcanology and Geothermal Research,* 189**,** 172-190.

MINDAT.ORG. 2010a. *Albite* [Online]. Available: http://www.mindat.org/min-96.html 2010].

MINDAT.ORG. 2010b. *Microcline* [Online]. Available: http://www.mindat.org/min-2704.html 2010].

MINDAT.ORG. 2010c. *Quartz* [Online]. Available: http://www.mindat.org/min-3337.html.

MINK, R. 2004. Geothermal energy. *Kirk-Othmer Encyclopaedia of Chemical Technology.*

MOREY, G. W., FOURNIER, R. O. & ROWE, J. J. 1962. The solubility of quartz in water in the temperature interval from 25° to 300°C. *Geochimica et Cosmochimica Acta,* 26**,** 1029-1043.

NAMI, P., SCHELLSCHMIDT, R., SCHINDLER, M. & TISCHNER, T. Chemical stimulation operations for reservoir development of the deep crystalline HDR/EGS system at Soultz-Sous-Forets (France). Proc. Thirty-Second Workshop in Geothermal Reservoir Engineering, 2008 California, USA.

NISHIMOTO, S. & YOSHIDA, H. 2010. Hydrothermal alteration of deep fractured granite: Effects of dissolution and precipitation. *Lithos,* 115**,** 153-162.

O'NEILL, B., TENAILLEAU, C., NGOTHAI, Y., STRUDER, A., BRUGGER, J. & PRING, A. 2006. A flow-through hydrothermal cell for in situ neutron diffraction studies of phase transformations. *Physica B,* 2**,** 942 - 945.

OWEN, L. B. 1975. Precipitation of amorphous silica from high-temperature hypersaline geothermal brine. Livermore: Lawrence Livermore Laboratory.

PALANDRI, J. L. & KHARAKA, Y. K. 2004. A Compilation of Rate Parameters of Water-Mineral Interaction Kinetics for Application to Geochemical Modeling. Menlo Park, California: U.S. Geological Survey and U.S Department of the Interior.

PERRY, R. H. & GREEN, D. W. 1997. *Perry's Chemical Engineer's Handbook,* New York, McGraw-Hill.

PFINGSTEN, W., PARIS, B., SOLER, J. M. & MADER, U. K. 2006. Tracer and reactive transport modeling of the interaction between high-pH fluid and fractured rock: Field and laboratory experiments. *Journal of Geochemical Exploration,* 90**,** 95-113.

PIRSA. 2011. *Status of Geothermal Licence Activity. DMITRE Geothermal Energy* [Online]. Available: http://www.pir.sa.gov.au/geothermal/ageg/status_of_geothermal_licence_activity [Accessed 19 July 2013].

PIRSA. 2012. *DMITRE Geothermal Energy. Annual Reports. Geothermal Exploration and Retention Licences* [Online]. Available: http://www.pir.sa.gov.au/geothermal/legislation__and__compliance/company_annual_reports [Accessed 22 June 2012].

POSEY-DOWTY, J., CRERAR, D. A., HELLERMAN, R. & CLARENCE, D. C. 1986. Kinetics of mineral-water reactions: Theory, design and application of circulating hydrothermal equipments. *American Mineralogist,* 71**,** 85-94.

PRIGOGINE, I. 1961. *Introduction to Thermodynamics of Irreversible Processes. Second, Revised Edition* New York, Inderscience Publishers.

PRIGOGINE, I. 1967. *Introduction to Thermodynamics of Irreversible Processes* New York, John Wiley & Sons, Inc.

QIAN, G., BRUGGER, J., SKINNER, W. M., CHEN, G. & PRING, A. 2010. An experimental study of the mechanism of the replacement of magnetite by pyrite up to 300°C. *Geochimica et Cosmochimica Acta,* 74**,** 5610-5630.

RICHARDS, H. G., SAVAGE, D. & ANDREWS, J. N. 1992. Granite-water reactions in an experimental Hot Dry Rock geothermal reservoir, Rosemanowes test site, Cornwall, U.K. *Applied Geochemistry,* 7**,** 193-222.

RIMSTIDT, J. D. 1979. *Kinetics of Silica-Water Reactions,* Thesis. The Pennsylvania State University.

RIMSTIDT, J. D. 1997. Quartz solubility at low temperatures. *Geochimica et Cosmochimica Acta,* 61**,** 2553-2558.

RIMSTIDT, J. D. & BARNES, H. L. 1980. The kinetics of silica-water reactions. *Geochimica et Cosmochimica Acta,* 44**,** 1683-1699.

ROBINSON, B. A. 1982. *Quartz dissolution and silica deposition in hot dry rock geothermal systems,* Thesis. Massachusetts Institute of Technology.

SAVAGE, D. 1986. Granite-water interactions at 100°C, 50 MPa: An experimental study. *Chemical Geology,* 54**,** 81-95.

SAVAGE, D., BATEMAN, K. & RICHARDS, H. G. 1992. Granite-water interactions in a flow-through experimental system with application to the hot dry rock geothermal system at Rosemanowes, Cornwall, UK. *Applied Geochemistry,* 7**,** 223-241.

SAVAGE, D., CAVE, M. R., MILLODOWSKI, A. E. & GEORGE, I. 1987. Hydrothermal alteration of granite by meteoric fluid: An example from the Carnmenellis granite, United Kingdom. *Contributions to Mineralogy and Petrology,* 96**,** 391-405.

SHERWOOD, T. K., PIGFORD, R. L. & WILKE, C. R. 1975. *Mass Transfer,* New York.

SIEBERT, H., YOUDELIS, W. V., LEJA, J. & LILGE, E. O. 1963. The kinetics of the dissolution of crystalline quartz in water at high temperatures and pressures. *Unit Processes in Hydrometallurgy,* 24**,** 284 - 299.

SOMERVILLE, M., WYBORN, D., CHOPRA, P. N., RAHMANN, S. S., ESTRELLA, D. & VAN DER MUELLEN, T. 1994. *Hot Dry Rocks Feasibility Study*, Energy Research and Development Corporation. Australia. Report 94/243.

ST. CLAIR, J. 2008. *RE: High pressure water sampling,* Personal communication via email.

STEFÁNSSON, A. & ARNÓRSSON, S. 2000. Feldspar saturation state in natural waters. *Geochimica et Cosmochimica Acta,* 64**,** 2567 - 2584.

SWITKOWSKI, Z., DRACOULIS, G., JOHNSTON, A., JOHNSTON, P., MCKIBBIN, W. & THOMAS, M. 2006. *Uranium Mining, Processing and Nuclear Energy - Opportunities for Australia, Report to the Prime Minister by the Uranium Mining, Processing and Nuclear Energy Review Taskforce,* Barton, Commonwelath of Australia.

TARCAN, G. 2005. Mineral saturation and scaling tendencies of waters discharged from wells (>150^{o}C) in geothermal areas of Turkey. *Journal of Volcanology and Geothermal Research,* 142**,** 263-283.

TENMA, N., YAMAGUCHI, T. & ZYVOLOSKI, G. 2008. The Hijiori hor dry rock test site, Japan. Evaluation and optimization of heat extraction from a two-layered reservoir. *Geothermics,* 37.

TESTER, J. W., WORLEY, W. G., ROBINSON, B. A., GRIGSBY, C. O. & FEERER, J. L. 1994. Correlating quartz dissolution kinetics in pure water from 25 to 625°C. *Geochimica et Cosmochimica Acta,* 58**,** 2407-2420.

THE UNIVERSITY OF OKLAHOMA. 2013. Buffers. Available: http://www.ou.edu/research/electron/bmz5364/buffers.html [Accessed 10 April].

TILL, R. & SPEARS, D. A. 1969. The determination of quartz in sedimentary rocks using an x-ray diffraction method. *Clays and Clay Minerals,* 17**,** 323 - 327.

UNSD. 2009. *Energy Statistic Database. United Nations Statistics Division* [Online]. Available: http://data.un.org/Data.aspx?q=geothermal&d=EDATA&f=cmID%3aEG [Accessed 5 February 2013].

VALA RAGNARSDÓTTIR, K. & WALTHER, J. V. 1983. Pressure sensitive "silica geothermometer" determined from quartz solubility experiments at 250 °C. *Geochimica et Cosmochimica Acta,* 47**,** 941-946.

VAN LIER, J. A., DE BRUYN, P. L. & OVERBEEK, J. T. G. 1960. The solubility of quartz. *The Journal of Physical Chemistry,* 64**,** 1675-1682.

VERMA, M. P. 2000a. Chemical thermodynamics of silica: A critique on its geothermometer. *Geothermics,* 29**,** 323 - 346.

VERMA, M. P. Revised quartz solubility temperature dependence equation along the water-vapor saturation curve. World Geothermal Congress, 2000b Kyushu - Tohoku, Japan. 1927 - 1932.

VOLOSOV, A. G., KHODAKOVSKIY, I. L. & N., R. B. 1972. Equilibria in the system SiO_2 - H_2O at elevated temperatures along the lower three-phase curve. *Geochemistry International,* 9**,** 362 - 377.

WEARE, N. M. & WEARE, J. H. 2002. Models of Geothermal Brine Chemistry. San Diego: University of California.

WEILL, D. F. & FYFE, W. S. 1964. The solubility of quartz in H_2O in the range 1000-4000 bars and 400-550°C. *Geochimica et Cosmochimica Acta,* 28**,** 1243 - 1255.

WESTENHAUS, B. 2011. The coming geothermal energy boom. Available: http://oilprice.com/Alternative-Energy/Geothermal-Energy/The-Coming-Geothermal-Energy-Boom.html.

WORLEY, W. G. 1994. *Dissolution kinetics and mechanism in quartz and granite-water systems,* Thesis. Massachusetts Institute of Technology.

WYBORN, D. 2008. *RE: Habanero 3 samples from drill cuttings,* Personal communication via email.

WYBORN, D. 2010. *RE: Darby's bore water and Cooper's Creek water mixture,* Personal communication via email.

WYBORN, D., DE GRAAF, L., DAVIDSON, S. & HANN, S. Development of Australia's first hot fractured rock (HFR) underground heat exchanger, Cooper Basin, South Australia. Proceeding World Geothermal Congress 2005, 2005 Antalya, Turkey. 423 - 430.

YANAGISAWA, N., MATSUNAGA, I., SUGITA, H., SATO, M. & OKABE, T. Scale precipitation during circulation test at the Hijiori HDR test field, Yamagata, Japan. Proc. World Geothermal Congress, 2005, 2005 Antalya, Turkey.

ZHANG, Y. 2008. *Geochemical Kinetics,* New Jersey, Princeton University Press.

Appendix A Summary of SigmaPlot Iteration Path

As previously mention in Section 2.4.2.2, the SigmaPlot non-linear model (exponential rise to maximum model) used to fit the experimental data is:

$$f(x) = a_0(1 - e^{-a_1 x}) + e \quad \textbf{(A.1)}$$

Correlating Equations (2.54) and (2.55):

where: $f(x)$ refers to $m_{H_4SiO_4}$

x refers to t

a_0 refers to $m^{sat}_{H_4SiO_4}$

a_1 refers to $k^{\#}$

By plotting the value of $m_{H_4SiO_4}$ versus time, the parameters a_0 and a_1 can be solved using the Gauss-Newton method (Chapra and Canale, 2002).

A.1 Gauss-Newton Method

The Gauss-Newton method provides solution based on determining the values of the parameters that minimize the sum of the residuals between the data and the non-linear equations (Chapra and Canale, 2002). This method requires iteration to obtain the solution. The summary of the iteration path is:

The relationship between the data and the non-linear equation is generally expressed in the form:

$$y_i = f(x_i, a_0, a_1, \dots, a_m) + e_i \quad \textbf{(A.2)}$$

With an abbreviated form to simplify:

$$y_i = f(x_i) + e_i \quad \textbf{(A.3)}$$

where: y_i is a measured value of the independent variable

x_i is the independent variable

$a_0, a_1, \dots, a_m$ are the parameters in the non-linear function

e_i is a random error

The non-linear model is then expanded in a Taylor series around the parameter values and truncated after the first derivative, such as:

$$f(x_i)_{j+1} = f(x_i)_j + \frac{\delta f(x_i)_j}{\delta a_0}\Delta a_0 + \frac{\delta f(x_i)_j}{\delta a_1}\Delta a_1 \quad \textbf{(A.4)}$$

where: j is the initial guess

j+1 is the prediction

$\Delta a_0 = a_{0,j+1} - a_{0,j}$

$\Delta a_1 = a_{1,j+1} - a_{1,j}$

Through the steps above, the model has been linearised with respect to the parameters. Substituting Equation (A.4) to (A.3):

$$y_i - f(x_i)_j = \frac{\delta f(x_i)_j}{\delta a_0}\Delta a_0 + \frac{\delta f(x_i)_j}{\delta a_1}\Delta a_1 + e_i \quad \textbf{(A.5)}$$

The above method in matrix form to obtain a solution:

$$\{D\} = \left[Z_j\right]\{\Delta A\} + \{E\} \quad \textbf{(A.6)}$$

where $\left[Z_j\right]$ is the matrix of partial derivatives of the function and n is the number of data points,

$$[Z_j] = \begin{bmatrix} \delta f_1/\delta a_0 & \delta f_1/\delta a_1 \\ \delta f_2/\delta a_0 & \delta f_2/\delta a_1 \\ \cdots & \cdots \\ \cdots & \cdots \\ \cdots & \cdots \\ \delta f_n/\delta a_0 & \delta f_n/\delta a_1 \end{bmatrix} \quad \textbf{(A.7)}$$

$\delta f_i/\delta a_k$ is the partial derivative of the function with respect to the k[th] parameter evaluated at the i[th] data point.

The function $f(x: a_0, a_1) = a_0(1 - e^{-a_1 x})$ has the partial derivatives with respect to the parameters:

$$\frac{\partial f}{\partial a_0} = 1 - e^{-a_1 x} \quad \textbf{(A.8)}$$

and

$$\frac{\delta f}{\partial a_1} = a_0 x e^{-a_1 x} \quad \textbf{(A.9)}$$

The vector $\{D\}$ contains the differences between the measurements and the values of the function:

$$\{D\} = \begin{Bmatrix} y_1 - f(x_1) \\ y_2 - f(x_2) \\ . \\ . \\ . \\ y_n - f(x_n) \end{Bmatrix} \quad \textbf{(A.10)}$$

The vector $\{\Delta A\}$ is the changes in the parameter values:

$$\{\Delta A\} = \begin{Bmatrix} \Delta a_0 \\ \Delta a_1 \\ . \\ . \\ . \\ \Delta a_m \end{Bmatrix} \quad \textbf{(A.11)}$$

The application of the least square theory to Equation (A.6) gives:

$$\left[[Z_j]^T [Z_j]\right] \{\Delta A\} = \left\{[Z_j]^T \{D\}\right\} \quad \textbf{(A.12)}$$

Rearranging Equation (A.12) to solve $\{\Delta A\}$:

$$\{\Delta A\} = \left[[Z_j]^T [Z_j]\right]^{-1} \left\{[Z_j]^T \{D\}\right\} \quad \textbf{(A.13)}$$

The value of $\{\Delta A\}$ is obtained from solving the above equation, and values for the parameters are iterated to obtain new improved values:

$$a_{0,j+1} = a_{0,j} + \Delta a_0$$
$$a_{1,j+1} = a_{1,j} + \Delta a_1$$

Convergence is obtained when $|\varepsilon_a|_k$ results in an acceptable stopping condition:

$$|\varepsilon_a|_k = \left|\frac{a_{k,j+1} - a_{0,j}}{a_{0,j+1}}\right| x100\% \quad \textbf{(A.14)}$$

A comparable stopping condition is to achieve the minimum value of the sum of the squares of the residual, S_r:

$$S_r = \sum_{i=1}^{n} (y_i - y^{new})^2 \quad \textbf{(A.15)}$$

Standard error of estimate (Lane, 2013) is given in the following equation:

$$S_{est} = \sqrt{\frac{S_r}{n}} \quad \textbf{(A.16)}$$

Substituting Equation (A.15) to (A.16) gives:

$$S_{est} = \sqrt{\frac{\sum_{i=1}^{n}(y_i - y^{new})^2}{n}} \quad \textbf{(A.17)}$$

Since the data are samples rather than population, the standard error of estimate becomes:

$$S_{est} = \sqrt{\frac{S_r}{n-2}} \quad \textbf{(A.18)}$$

Substituting Equation (A.15) to (A.18) gives:

$$S_{est} = \sqrt{\frac{\sum_{i=1}^{n}(y_i - y^{new})^2}{n-2}} \quad \textbf{(A.19)}$$

A.2 Sample calculations to obtain C^{∞} and $k^{\#}$

This section provides sample calculation using the Gauss-Newton method to solve the non-linear regression of the function $f(x) = C = C^{\infty}\left(1 - e^{-k^{\#}t}\right)$ and generate a curve-fit to the experimental data to obtain the equilibrium silica concentration (C^{∞}) and the pseudo rate constant $(k^{\#})$ for 160°C experiment. Since the concentration of silica is expressed both in units of ppm in the curve fitting, the equilibrium silica concentration will be represented in C^{∞} and the silica concentration in C, respectively. Table A.1 shows the raw and calculated data for the experiment at 160°C with initial guesses of C^{∞} = 100 ppm and $k^{\#}$= 0.001/d. The x data show time (days) and Y data show silica concentration (ppm) at time x.

Table A.1 160°C data with initial guesses of C^{∞} = 100 and $k^{\#}$ = 0.001

x	y_i	y^{new}	$(y_i-y^{new})^2$
0	0	0.00	0
1	20	0.10	396.012
3	41	0.30	1656.53
7	65	0.70	4134.80
14	87	1.39	7329.03
21	101	2.08	9785.54
56	142	5.45	18646.97
		Σ	41948.89

Following the steps shown in Section 2.4.2.2 is basically to obtain $\{\Delta A\}$. Using Equation (A.8), the partial derivatives with respect to a_0 is:

$$\frac{\partial f}{\partial a_0} = \frac{\partial f}{\partial C^{\infty}} = 1 - e^{-k^{\#}t}$$

Calculation result for x = 0 is:

$$\frac{\partial f}{\partial a_0} = \frac{\partial f}{\partial C^{\infty}} = 1 - e^{-0.001\times 0}$$

$$\frac{\partial f}{\partial C^{\infty}} = 1 - 1 = 0$$

Using Equation (A.9), the partial derivatives with respect to $a_1$is:

$$\frac{\delta f}{\partial a_1} = \frac{\delta f}{\partial k'} = C^{\infty} t e^{-k^{\#}t}$$

$$\frac{\delta f}{\partial k'} = 100 \times 0 \times e^{-0.001\times 0} = 0$$

By equating all data as above, the result is matrix [Z_0] according to Equation (A.7):

$$[Z_0] = \begin{bmatrix} 0.0 & 0.0 \\ 1.0 & 99.900 \\ 1.0 & 299.101 \\ 1.0 & 695.117 \\ 1.0 & 1380.54 \\ 1.0 & 2056.36 \\ 1.0 & 5295.02 \end{bmatrix}$$

The transpose of the matrix [Z_0] is:

$$[Z_0]^T = \begin{bmatrix} 0.0 & 1.0 & 1.0 & 1.0 & 1.0 & 1.0 & 1.0 \\ 0.0 & 99.900 & 299.101 & 695.117 & 1380.54 & 2056.36 & 5295.02 \end{bmatrix}$$

Multiplying matrix [Z_0] with its transpose:

$$[Z_0]^T[Z_0] = \begin{bmatrix} 6 & 9826.03 \\ 9826.03 & 34754354 \end{bmatrix}$$

Inverting the above matrix:

$$\left[[Z_0]^T[Z_0]\right]^{-1} = \begin{bmatrix} 0.3104 & -8.78 \times 10^{-5} \\ -8.78 \times 10^{-5} & 5.36 \times 10^{-8} \end{bmatrix}$$

The vector $\{D\}$ contains the differences between the measurements and the values of the function,

$$\{D\} = \begin{Bmatrix} 0.0 & - & 0.0 \\ 20.0 & - & 1.0 \\ 41.0 & - & 1.0 \\ 65.0 & - & 1.0 \\ 87.0 & - & 1.0 \\ 101.0 & - & 1.0 \\ 142.0 & - & 1.0 \end{Bmatrix} = \begin{Bmatrix} 0.0 \\ 19.0 \\ 40.0 \\ 64.0 \\ 86.0 \\ 100.0 \\ 141.0 \end{Bmatrix}$$

Vector $\{D\}$ is then multiplied by $[Z_0]^T$:

$$[Z_0]^T\{D\} = \begin{bmatrix} 450.00 \\ 1129309.48 \end{bmatrix}$$

The vector A, which is the changes in parameter values, is obtained by solving equation (A.13), where the least square theory has been applied:

$$\{\Delta A\} = \left[[Z_j]^T[Z_j]\right]^{-1}\left\{[Z_j]^T\{D\}\right\}$$

$$\{\Delta A\} = \begin{Bmatrix} 40.5699 \\ 0.0210 \end{Bmatrix} = \begin{Bmatrix} \Delta a_0 \\ \Delta a_1 \end{Bmatrix} = \begin{Bmatrix} \Delta C^{\infty} \\ \Delta k^{\#} \end{Bmatrix}$$

By adding the value of $\{\Delta A\}$ to the initial guesses of the parameters will result in new improved estimates for the subsequent guess,

$$a_{0,j+1} = a_{0,j} + \Delta a_0$$
$$a_{1,j+1} = a_{1,j} + \Delta a_1$$

$$\begin{Bmatrix} C^{\infty} \\ k^{\#} \end{Bmatrix} = \begin{Bmatrix} 100 \\ 0.001 \end{Bmatrix} + \begin{Bmatrix} 40.5699 \\ 0.0210 \end{Bmatrix} = \begin{Bmatrix} 140.5699 \\ 0.0220 \end{Bmatrix}$$

Using Microsoft Excel and the solver add-in to iterate the least squares of the residual S_r, the values of a_0 and a_1 were obtained. The summary of the Gauss-Newton result is provided in Table A.2.

Table A.2 Summary of the Gauss-Newton result with the least square of the residual

x	y_i	y^{new}	$(y_i-y^{new})^2$
0	0	0.00	0.00
1	20	10.52	89.91
3	41	29.20	139.28
7	65	58.71	39.60
14	87	92.31	28.21
21	101	111.56	111.24
56	142	135.71	39.51
		Σ	**447.75**

Using Equation (A.15) to calculate the least square of the residual, where $y^{new} = a_0(1 - e^{-a_1 x_i})$:

$$S_r = \sum_{i=1}^{n} [y_i - a_0(1 - e^{-a_1 x_i})]^2 \quad \textbf{(A.20)}$$

Least square of the residual, $\sum = 447.75$, with iteration results:

$$a_0 = C^{\infty} = 137.30\ ppm\ \left(m^{sat}_{H_4SiO_4} = 0.0023\ molal\right)$$
$$a_1 = k^{\#} = 0.0797/day = 9.22 \times 10^{-7}/s$$

Therefore, the sample calculation above clarifies the results from the SigmaPlot software.

Appendix B Static System

The static system was used for a variety of rock interaction experiments. This appendix provides the data for the experiments carried out to determine the equilibrium silica concentration, silica dissolution kinetics, influence of particle size on silica dissolution kinetics, effect of NaCl on silica dissolution kinetics, and influence of pH on silica dissolution kinetics.

B.1 Equilibrium Silica Concentration at Various Temperatures

This section provides the data from granite dissolution experiments in pure water to obtain the equilibrium silica concentration at various temperatures. The chosen particle size range was 100 – 200 µm and the duration of the experiment was 56 days. The data includes the initial sample weight, final pH after experiments, concentration of dissolved reactive silica, and concentration of the major cation dissolved (Na, K, Al). The weight of the granite samples after the experiments were not reported, as it was difficult to accurately measure the remaining granite samples.

Table B.1 Initial sample used and pH after experiment – Run I

T (^{o}C)	Initial weight of sample (g)	pH after experiment
120	0.5066	8.54
140	0.5079	8.41
160	0.5017	8.42
170	0.5020	8.10
200	0.5021	8.47
220	0.5043	8.57

Table B.2 Initial sample used and pH after experiment – Run II

T (^{o}C)	Initial weight of sample (g)	pH after experiment
120	0.5036	8.35
140	0.5039	8.73
160	0.5035	8.66
170	0.5039	8.39
200	0.5014	8.54
220	0.5030	8.35

Table B.3 Experimental results showing equilibrium reactive silica concentration at different temperatures

T (^{o}C)	Reactive silica concentration I (ppm)	Reactive silica concentration II (ppm)	Average reactive silica concentration (ppm)	Standard deviation (ppm)
120	58	54	56	2.83
140	90	98	94	5.66
160	133	141	137	5.66
170	170	180	175	7.07
200	274	290	282	11.31
220	330	370	350	28.28

Table B.4 Experimental results showing equilibrium silica concentration (ICP-OES) at different temperatures

T (^{o}C)	Silica concentration I (ppm)	Silica concentration II (ppm)	Average silica concentration (ppm)	Standard deviation (ppm)
120	55.2	57.8	56.5	1.82
140	94.8	105.9	100.3	7.87
160	151.5	140.3	145.9	7.87
170	186.1	190.4	188.3	3.03
200	312.3	282.4	297.4	21.18
220	337.2	394.5	365.8	40.54

The experimental results were then plotted in terms of log C versus 1/T(K) to obtain a linear fit, and an equation was developed to correlate the silica dissolution for the rock sample from Habanero 3 well at various temperatures.

Table B.5 Dissolved major cation data for various temperatures in pure water – Run I

T (^{o}C)	Dissolved Na Concentration (ppm)	Dissolved K Concentration (ppm)	Dissolved Al Concentration (ppm)	Dissolved Ca Concentration (ppm)
120	8.5995	4.2290	1.3191	6.7535
140	12.0935	5.0744	1.5648	4.9874
160	23.5401	5.9834	2.4276	5.6490
170	24.5788	10.0924	1.9313	5.9741
200	28.6638	14.9879	2.0311	6.9202
220	31.0929	16.5691	2.6891	8.8970

Table B.6 Dissolved major cation data for various temperatures in pure water – Run II

T (^{o}C)	Dissolved Na Concentration (ppm)	Dissolved K Concentration (ppm)	Dissolved Al Concentration (ppm)	Dissolved Ca Concentration (ppm)
120	8.6156	4.2391	1.3307	7.2755
140	12.1100	5.0828	1.5809	5.2317
160	24.1654	6.5414	2.5104	6.1528
170	25.8816	10.1810	2.7759	6.5527
200	28.9589	15.5310	2.3455	7.3099
220	32.5922	17.3143	2.7137	9.1497

Table B.7 Average Dissolved major cation data for various temperature in pure water

T (^{o}C)	Average Dissolved Na Concentration (ppm)	Average Dissolved K Concentration (ppm)	Average Dissolved Al Concentration (ppm)	Average Dissolved Ca Concentration (ppm)
120	7.4853	5.0996	1.9867	0.1475
140	8.0930	5.1791	2.3293	0.2080
160	10.1492	5.2395	1.9121	0.2652
170	10.2357	4.5333	1.6134	0.1640
200	11.7685	5.0054	2.3254	0.1248
220	12.1572	4.8573	1.8853	0.2018

Table B.8 Standard deviation cation data for various temperature in pure water

T (^{o}C)	Standard Deviation Dissolved Na Concentration (ppm)	Standard Deviation Dissolved K Concentration (ppm)	Standard Deviation Dissolved Al Concentration (ppm)	Standard Deviation Dissolved Ca Concentration (ppm)
120	0.01	0.01	0.01	0.37
140	0.01	0.01	0.01	0.17
160	0.44	0.39	0.06	0.36
170	0.92	0.06	0.60	0.41
200	0.21	0.38	0.22	0.28
220	1.06	0.53	0.02	0.18

B.2 Granite Dissolution Kinetics

This section provides the data from granite dissolution experiments in water to determine the granite dissolution kinetics at 160^{o}C, 170^{o}C, 200^{o}C and 220^{o}C. These experiments used approximately 0.5 g granite in approximately 14 mL of pure water. The pH of the starting pure water is approximately 5.50.

B.2.1 Static experiments at 160^{o}C

This section provides initial sample weight, final pH after experiments, concentration of dissolved reactive silica, and concentration of the major cation dissolved in pure water at 160^{o}C. The weight of the granite samples after the experiments were not reported, as it was difficult to accurately measure the remaining granite samples.

Table B.9 Initial sample used and pH after experiment (160^{o}C) – Run I

Duration of experiment (days)	Initial weight of sample (g)	pH after experiment
1	0.5009	5.68
3	0.5005	6.18
7	0.5010	6.39
14	0.5007	7.43
21	0.5011	8.21
56	0.5035	8.42

Table B.10 Initial sample used and pH after experiment (160^{o}C) – Run I

Duration of experiment (days)	Initial weight of sample (g)	pH after experiment
1	0.5010	5.65
3	0.5008	6.03
7	0.5014	6.42
14	0.5012	7.64
21	0.5018	8.11
56	0.5024	8.66

Table B.11 Reactive silica data in pure water at 160°C

Duration of experiment (days)	Reactive silica concentration I	Reactive silica concentration II	Reactive silica concentration average	Standard deviation	Standard error of estimate
1	23	17	20	4.24	9.46
3	39	43	41	2.83	9.46
7	62	68	65	4.24	9.46
14	82	92	87	7.07	9.46
21	99	103	101	2.83	9.46
56	136	148	142	8.49	9.46

Table B.12 Dissolved major cation data in pure water at 160°C – Run I

Duration of experiment (days)	Dissolved Na Concentration (ppm)	Dissolved K Concentration (ppm)	Dissolved Al Concentration (ppm)
1	7.6362	5.6137	2.6257
3	7.4587	5.9953	1.6578
7	9.7209	7.0460	1.8006
14	13.267	6.9241	2.8333
21	15.204	5.1848	2.1050
56	18.540	5.9834	2.4276

Table B.13 Dissolved major cation data in pure water at 160°C – Run II

Duration of experiment (days)	Dissolved Na Concentration (ppm)	Dissolved K Concentration (ppm)	Dissolved Al Concentration (ppm)
1	7.7785	6.6351	2.7322
3	9.1410	6.7852	1.7499
7	11.2427	7.9719	1.9993
14	15.9516	8.1068	2.9765
21	15.8656	5.6152	2.2586
56	19.1654	6.5414	2.5104

Table B.14 Average dissolved major cation data in pure water at 160°C

Duration of experiment (days)	Average Dissolved Na Concentration (ppm)	Average Dissolved K Concentration (ppm)	Average Dissolved Al Concentration (ppm)
1	7.7074	6.1244	2.6789
3	8.2999	6.3902	1.7038
7	10.482	7.5089	1.8999
14	14.609	7.5154	2.9049
21	15.535	5.4000	2.1818
56	18.853	6.2624	2.4690

Table B.15 Standard deviation dissolved major cation data in pure water at 160°C

Duration of experiment (days)	Standard Deviation Dissolved Na Concentration (ppm)	Standard Deviation Dissolved K Concentration (ppm)	Standard Deviation Dissolved Al Concentration (ppm)
1	0.10	0.72	0.08
3	1.19	0.56	0.07
7	1.08	0.65	0.14
14	1.90	0.84	0.10
21	0.47	0.30	0.11
56	0.44	0.39	0.06

B.2.2 Static experiments at 170°C

This section provides initial sample weight, final pH after experiments, concentration of dissolved reactive silica, and concentration of the major cation dissolved in pure water at 170°C.

Table B.16 Initial sample used and pH after experiment (170°C) – Run I

Duration of experiment (days)	Initial weight of sample (g)	pH after experiment
1	0.5007	5.68
3	0.5003	6.34
7	0.5009	6.60
14	0.5008	7.84
21	0.5009	8.47
56	0.5020	8.10

Table B.17 Initial sample used and pH after experiment (170^{o}C) – Run I

Duration of experiment (days)	Initial weight of sample (g)	pH after experiment
1	0.5012	5.72
3	0.5016	6.45
7	0.5005	6.89
14	0.5004	7.69
21	0.5017	8.35
56	0.5024	8.39

Table B.18 Reactive silica data in pure water at 170^{o}C

Duration of experiment (days)	Reactive silica concentration I	Reactive silica concentration II	Reactive silica concentration average	Standard deviation	Standard error of estimate
1	31	35	33	2.83	8.28
3	44	50	47	4.24	8.28
7	84	94	89	7.07	8.28
14	130	154	142	16.97	8.28
21	164	174	169	7.07	8.28
56	170	180	175	7.07	8.28

Table B.19 Dissolved major cation data in pure water at 170°C – Run I

Duration of experiment (days)	Dissolved Na Concentration (ppm)	Dissolved K Concentration (ppm)	Dissolved Al Concentration (ppm)
1	7.7980	7.3495	1.0079
3	8.9420	5.5254	1.5328
7	10.995	9.4877	1.9105
14	15.108	9.0428	1.9313
21	17.706	9.3491	1.9987
56	20.579	10.092	2.1407

Table B.20 Dissolved major cation data in pure water at 170°C – Run II

Duration of experiment (days)	Dissolved Na Concentration (ppm)	Dissolved K Concentration (ppm)	Dissolved Al Concentration (ppm)
1	8.9804	7.45	1.5602
3	10.799	5.71	1.7145
7	12.527	9.65	2.0689
14	15.424	9.17	2.1501
21	18.681	9.42	2.1778
56	21.882	10.18	2.7759

Table B.21 Average dissolved major cation data in pure water at 170°C

Duration of experiment (days)	Average Dissolved Na Concentration (ppm)	Average Dissolved K Concentration (ppm)	Average Dissolved Al Concentration (ppm)
1	8.3892	7.4013	1.2841
3	9.8706	5.6161	1.6236
7	11.7609	9.5697	1.9897
14	15.2657	9.1064	2.0407
21	18.1934	9.3828	2.0883
56	21.2302	10.1367	2.4583

Table B.22 Standard deviation dissolved major cation data in pure water at 170°C

Duration of experiment (days)	Standard Deviation Dissolved Na Concentration (ppm)	Standard Deviation Dissolved K Concentration (ppm)	Standard Deviation Dissolved Al Concentration (ppm)
1	0.84	0.07	0.39
3	1.31	0.13	0.13
7	1.08	0.12	0.05
14	0.22	0.09	0.19
21	0.69	0.05	0.08
56	0.92	0.06	0.60

B.2.3 Static experiments at 200°C

This section provides initial sample weight, final pH after experiments, concentration of dissolved reactive silica, and concentration of the major cation dissolved in pure water at 200°C.

Table B.23 Initial sample used and pH after experiment (200°C) – Run I

Duration of experiment (days)	Initial weight of sample (g)	pH after experiment
1	0.5005	5.47
3	0.5020	5.65
7	0.5014	6.35
14	0.5014	8.85
21	0.5022	8.19
56	0.5021	8.47

Table B.24 Initial sample used and pH after experiment (200°C) – Run II

Duration of experiment (days)	Initial weight of sample (g)	pH after experiment
1	0.5008	5.88
3	0.5004	6.02
7	0.5007	6.48
14	0.5007	7.94
21	0.5006	8.46
56	0.5014	8.54

Table B.25 Reactive silica data in pure water at 200°C

Duration of experiment	Reactive silica concentration I	Reactive silica concentration II	Reactive silica concentration average	Standard deviation	Standard error of estimate
1	102	102	102	0.00	24.04
3	130	120	125	7.07	24.04
7	212	188	200	16.97	24.04
14	246	240	243	4.24	24.04
21	262	254	258	5.66	24.04
56	288	276	282	8.49	24.04

Table B.26 Dissolved major cation data in pure water at 200°C – Run I

Duration of experiment (days)	Dissolved Na Concentration (ppm)	Dissolved K Concentration (ppm)	Dissolved Al Concentration (ppm)
1	8.6865	7.0871	2.8160
3	10.936	7.1501	1.8250
7	12.277	8.0754	1.6933
14	16.981	9.2308	1.6355
21	18.567	11.0809	2.0324
56	23.664	14.988	2.0311

Table B.27 Dissolved major cation data in pure water at 200°C – Run II

Duration of experiment (days)	Dissolved Na Concentration (ppm)	Dissolved K Concentration (ppm)	Dissolved Al Concentration (ppm)
1	9.4474	7.9025	2.9917
3	11.2555	7.7585	1.9527
7	13.4539	8.4802	1.7595
14	17.9238	9.9049	1.6958
21	20.6803	11.2513	2.2204
56	23.969	15.531	2.3455

Table B.28 Average dissolved major cation data in pure water at 200°C

Duration of experiment (days)	Average Dissolved Na Concentration (ppm)	Average Dissolved K Concentration (ppm)	Average Dissolved Al Concentration (ppm)
1	9.0670	7.4948	2.9038
3	11.0958	7.4543	1.8888
7	12.8656	8.2778	1.7264
14	17.4522	9.5678	1.6657
21	19.6235	11.1661	2.1264
56	23.8114	15.2595	2.1883

Table B.29 Standard deviation dissolved major cation data in pure water at 200°C

Duration of experiment (days)	Standard Deviation Dissolved Na Concentration (ppm)	Standard Deviation Dissolved K Concentration (ppm)	Standard Deviation Dissolved Al Concentration (ppm)
1	0.54	0.58	0.12
3	0.84	0.43	0.09
7	0.23	0.29	0.05
14	0.83	0.48	0.04
21	0.67	0.12	0.13
56	0.21	0.38	0.22

B.2.4 Static experiments at 220°C

This section provides initial sample weight, final pH after experiments, concentration of dissolved reactive silica, and concentration of the major cation dissolved in pure water at 220°C.

Table B.30 Initial sample used and pH after experiment (220°C) – Run I

Duration of experiment (days)	Initial weight of sample (g)	pH after experiment
1	0.5004	5.95
3	0.5005	6.35
7	0.5005	6.54
14	0.5049	8.15
21	0.5009	8.39
56	0.5043	8.27

Table B.31 Initial sample used and pH after experiment (220^{o}C) – Run I

Duration of experiment (days)	Initial weight of sample (g)	pH after experiment
1	0.5008	5.84
3	0.5014	6.61
7	0.5011	7.37
14	0.5007	8.28
21	0.5018	8.49
56	0.5030	8.35

Table B.32 Reactive silica data in pure water at 220^{o}C

Duration of experiment	Reactive silica concentration I	Reactive silica concentration II	Reactive silica concentration average	Standard deviation	Standard error of estimate
1	138	140	139	1.41	32.85
3	173	191	182	12.73	32.85
7	258	244	251	9.90	32.85
14	290	304	297	9.90	32.85
21	333	323	328	7.07	32.85
56	340	360	350	14.14	32.85

Table B.33 Dissolved major cation data in pure water at 220°C – Run I

Duration of experiment (days)	Dissolved Na Concentration (ppm)	Dissolved K Concentration (ppm)	Dissolved Al Concentration (ppm)
1	11.274	5.8116	2.4304
3	15.482	8.0407	1.9340
7	15.991	14.043	1.7529
14	16.929	9.9916	1.4588
21	19.856	13.852	2.5274
56	24.093	16.569	2.6891

Table B.34 Dissolved major cation data in pure water at 220°C – Run II

Duration of experiment (days)	Dissolved Na Concentration (ppm)	Dissolved K Concentration (ppm)	Dissolved Al Concentration (ppm)
1	11.995	6.7436	2.5178
3	16.908	8.5402	2.0585
7	17.983	15.239	1.9121
14	18.196	10.729	1.6063
21	20.485	14.807	2.6555
56	25.592	17.314	2.7137

Table B.35 Average dissolved major cation data in pure water at 220°C

Duration of experiment (days)	Average Dissolved Na Concentration (ppm)	Average Dissolved K Concentration (ppm)	Average Dissolved Al Concentration (ppm)
1	11.634	6.2776	2.4741
3	16.195	8.2904	1.9962
7	17.093	14.641	1.8325
14	17.456	10.360	1.5326
21	20.170	14.329	2.5914
56	24.843	16.942	2.7014

Table B.36 Standard deviation dissolved major cation data in pure water at 220°C

Duration of experiment (days)	Standard Deviation Dissolved Na Concentration (ppm)	Standard Deviation Dissolved K Concentration (ppm)	Standard Deviation Dissolved Al Concentration (ppm)
1	1.01	0.66	0.06
3	0.92	0.35	0.09
7	0.51	0.85	0.11
14	0.44	0.52	0.10
21	0.75	0.68	0.09
56	1.06	0.53	0.02

B.3 Particle Size

This section provides the data from granite dissolution experiments in pure water to observe the effects of particle size to granite dissolution kinetics at 200^{o}C. Particle size may be associated with surface area. Three particle size ranges were chosen, 40 – 60 µm, 100 – 200 µm, and 200 - 400 µm.

B.3.1 40 – 60 µm

This section provides initial sample weight, final pH, concentration of dissolved reactive silica, and concentration of the major dissolved cation from granite dissolution in pure water at 200^{o}C using 40 – 60 µm particle size.

Table B.37 Initial sample used and pH after experiment (40 – 60 µm) – Run I

Duration of experiment (days)	Initial weight of sample (g)	pH after experiment
1	0.5005	5.47
3	0.5020	5.65
7	0.5014	6.35
14	0.5014	8.85
21	0.5022	8.19
56	0.5021	8.96

Table B.38 Initial sample used and pH after experiment (40 – 60 µm) – Run II

Duration of experiment (days)	Initial weight of sample (g)	pH after experiment
1	0.5008	5.55
3	0.5007	5.73
7	0.5012	6.62
14	0.5006	8.28
21	0.5014	8.35
56	0.5020	8.67

Table B.39 Reactive silica data in pure water (40 – 60 µm) at 200^{o}C

Duration of experiment (days)	Reactive silica concentration I	Reactive silica concentration II	Reactive silica concentration average	Standard deviation	Standard error of estimate
1	122	128	125	4.24	32.22
3	149	148	148.5	0.71	32.22
7	218	221	219.5	2.12	32.22
14	253	255	254	1.41	32.22
21	281	287	284	4.24	32.22
56	268	272	270	2.83	32.22

Table B.40 Dissolved major cation data in pure water (40 – 60 µm) – Run I

Duration of experiment (days)	Dissolved Na Concentration (ppm)	Dissolved K Concentration (ppm)	Dissolved Al Concentration (ppm)
1	21.316	8.1077	1.9422
3	30.890	8.8710	2.8973
7	33.883	7.0229	1.5500
14	33.557	6.8460	1.5985
21	32.198	6.4936	1.6223
56	45.098	5.9329	1.7874

Table B.41 Dissolved major cation data in pure water (40 – 60 µm) – Run II

Duration of experiment (days)	Dissolved Na Concentration (ppm)	Dissolved K Concentration (ppm)	Dissolved Al Concentration (ppm)
1	21.552	9.1411	2.0940
3	32.430	9.6763	3.0694
7	36.210	8.6800	1.6618
14	34.620	8.0486	1.7458
21	33.682	7.7221	2.0353
56	46.323	7.6704	1.9555

Table B.42 Average dissolved major cation data in pure water (40 – 60 µm)

Duration of experiment (days)	Average Dissolved Na Concentration (ppm)	Average Dissolved K Concentration (ppm)	Average Dissolved Al Concentration (ppm)
1	21.434	8.6244	2.0181
3	31.660	9.2736	2.9833
7	35.047	7.8515	1.6059
14	34.088	7.4473	1.6721
21	32.940	7.1078	1.8288
56	45.711	6.8017	1.8715

Table B.43 Standard deviation dissolved major cation data in pure water (40 – 60 µm)

Duration of experiment (days)	Standard Deviation Dissolved Na Concentration (ppm)	Standard Deviation Dissolved K Concentration (ppm)	Standard Deviation Dissolved Al Concentration (ppm)
1	0.17	0.73	0.11
3	1.09	0.57	0.12
7	1.65	1.17	0.08
14	0.75	0.85	0.10
21	1.05	0.87	0.29
56	0.87	1.23	0.12

B.3.2 100 – 200 μm

The same experimental data was for static autoclave experiment at 200^{o}C presented in Appendix B.2.3.

B.3.3 200 – 400 μm

This section provides initial sample weight, final pH, concentration of dissolved reactive silica, and concentration of the major dissolved cation from granite dissolution in pure water at 200^{o}C using 200 – 400 μm particle size.

Table B.44 Initial sample used and pH after experiment (200 – 400 μm) – Run I

Duration of experiment (days)	Initial weight of sample (g)	pH after experiment
1	0.5020	5.33
3	0.5015	6.10
7	0.5032	6.58
14	0.5032	8.69
21	0.5015	8.29
56	0.5040	8.05

Table B.45 Initial sample used and pH after experiment (200 – 400 μm) – Run II

Duration of experiment (days)	Initial weight of sample (g)	pH after experiment
1	0.5020	5.83
3	0.5015	6.34
7	0.5032	6.68
14	0.5032	8.38
21	0.5015	8.42
56	0.5040	8.37

Table B.46 Reactive silica data in pure water (200 – 400 µm) at 200°C

Duration of experiment (days)	Reactive silica concentration I	Reactive silica concentration II	Reactive silica concentration average	Standard deviation	Standard error of estimate
1	82	78	80	2.83	19.03
3	160	159	159.5	0.71	19.03
7	182	179	180.5	2.12	19.03
14	235	230	232.5	3.54	19.03
21	253	250	251.5	2.12	19.03
56	250	245	247.5	3.54	19.03

Table B.47 Dissolved major cation data in pure water (200 – 400 µm) – Run I

Duration of experiment (days)	Dissolved Na Concentration (ppm)	Dissolved K Concentration (ppm)	Dissolved Al Concentration (ppm)
1	8.1233	8.4070	3.2366
3	8.8605	7.9204	2.7070
7	10.928	7.1883	2.5808
14	12.977	7.4796	1.8194
21	15.728	7.4641	1.9050
56	19.508	8.0857	0.2303

Table B.48 Dissolved major cation data in pure water (200 – 400 µm) – Run II

Duration of experiment (days)	Dissolved Na Concentration (ppm)	Dissolved K Concentration (ppm)	Dissolved Al Concentration (ppm)
1	8.7535	8.7327	3.8009
3	9.9380	9.1787	3.0562
7	11.920	7.8838	2.6916
14	13.501	7.8918	1.8658
21	16.212	8.7593	1.9880
56	21.856	8.8137	1.0825

Table B.49 Average dissolved major cation data in pure water (200 – 400 µm)

Duration of experiment (days)	Average Dissolved Na Concentration (ppm)	Average Dissolved K Concentration (ppm)	Average Dissolved Al Concentration (ppm)
1	8.4384	8.5698	3.5188
3	9.3993	8.5495	2.8816
7	11.424	7.5361	2.6362
14	13.239	7.6857	1.8426
21	15.970	8.1117	1.9465
56	20.682	8.4497	0.6564

Table B.50 Standard deviation dissolved major cation data in pure water (200 – 400 µm)

Duration of experiment (days)	Standard Deviation Dissolved Na Concentration (ppm)	Standard Deviation Dissolved K Concentration (ppm)	Standard Deviation Dissolved Al Concentration (ppm)
1	0.45	0.23	0.40
3	0.76	0.89	0.25
7	0.70	0.49	0.08
14	0.37	0.29	0.03
21	0.34	0.92	0.06
56	1.66	0.51	0.60

B.4 Influence of salt

This section provides the data from granite dissolution experiments in 250 ppm NaCl solution to determine the granite dissolution kinetics at 200^{o}C. The particle size range chosen was 100 – 200 µm.

Table B.51 Initial sample used and pH after experiment in 250 ppm NaCl at 200^{o}C – Run I

Duration of experiment (days)	Initial weight of sample (g)	pH after experiment
1	0.5023	5.6
3	0.5021	6.48
7	0.5027	8.06
14	0.5033	8.33
21	0.5033	8.42
56	0.5040	8.63

Table B.52 Initial sample used and pH after experiment in 250 ppm NaCl at 200°C – Run II

Duration of experiment (days)	Initial weight of sample (g)	pH after experiment
1	0.5022	5.64
3	0.5023	6.63
7	0.5045	7.86
14	0.5037	8.47
21	0.5022	8.52
56	0.5038	8.74

Table B.53 Reactive silica data in 250 ppm NaCl at 200°C

Duration of experiment (days)	Reactive silica concentration I	Reactive silica concentration II	Reactive silica concentration average	Standard deviation	Standard error of estimate
1	105	102	103.5	0.21	17.541
3	213	210	211.5	0.21	17.541
7	226	223	224.5	0.21	17.541
14	244	240	242	0.28	17.541
21	275	270	272.5	0.35	17.541
56	274	277	275.2	0.21	17.541

Table B.54 Dissolved major cation data in 250 ppm NaCl at 200°C – Run I

Duration of experiment (days)	Dissolved Na Concentration (ppm)	Dissolved K Concentration (ppm)	Dissolved Al Concentration (ppm)
1	98.690	5.6137	2.6257
3	108.38	5.9953	1.6578
7	105.72	7.0460	1.8006
14	108.26	6.9241	2.8333
21	115.25	5.1848	2.1050
56	124.90	5.9834	2.4276

Table B.55 Dissolved major cation data in 250 ppm NaCl at 200°C – Run II

Duration of experiment (days)	Dissolved Na Concentration (ppm)	Dissolved K Concentration (ppm)	Dissolved Al Concentration (ppm)
1	100.32	6.6351	2.7322
3	110.32	6.7852	1.7499
7	106.63	7.9719	1.9993
14	109.80	8.1068	2.9765
21	115.39	5.6152	2.2586
56	125.52	6.5414	2.5104

Table B.56 Average dissolved major cation data in 250 ppm NaCl at 200°C

Duration of experiment (days)	Average Dissolved Na Concentration (ppm)	Average Dissolved K Concentration (ppm)	Average Dissolved Al Concentration (ppm)
1	99.505	8.1737	2.3036
3	109.35	8.9709	1.2989
7	106.18	9.5377	1.9056
14	109.03	9.3034	1.2787
21	115.32	8.7710	0.9798
56	125.21	9.7609	0.5346

Table B.57 Standard deviation dissolved major cation data in 250 ppm NaCl at 200°C

Duration of experiment (days)	Standard Deviation Dissolved Na Concentration (ppm)	Standard Deviation Dissolved K Concentration (ppm)	Standard Deviation Dissolved Al Concentration (ppm)
1	1.15	0.13	0.07
3	1.36	0.17	0.09
7	0.65	0.06	0.07
14	1.09	0.08	0.34
21	0.10	0.02	0.10
56	0.43	0.04	0.29

B.5 Influence of pH

This section provides the data from granite dissolution experiments in pH buffer solution to observe the granite dissolution kinetics at 200^{o}C at constant pH. Four pH buffer solutions were chosen, pH 3.9, 6.8, 10 and 13. The particle size range chosen for this experiment was 100 – 200 µm.

B.5.1 pH 4 buffer solution

This section provides initial sample weight, final pH after experiments, concentration of dissolved reactive silica, and concentration of the major cation dissolved in pH 4 buffer solution at 200^{o}C. The weight of the granite samples after the experiments were not reported, as it was difficult to accurately measure the remaining granite samples.

Table B.58 Initial sample used and pH after experiment in pH 4 buffer – Run I

Duration of experiment (days)	Initial weight of sample (g)	pH after experiment
1	0.5014	3.63
3	0.5007	3.52
7	0.5024	3.38
14	0.5024	3.42
21	0.5028	3.41
28	0.5031	3.27
56	0.5033	3.47

Table B.59 Initial sample used and pH after experiment in pH 4 buffer – Run II

Duration of experiment (days)	Initial weight of sample (g)	pH after experiment
1	0.5021	3.65
3	0.5028	3.50
7	0.5021	3.44
14	0.5023	3.42
21	0.503	3.48
28	0.5018	3.44
56	0.5049	3.32

Table B.60 Reactive silica data in pH 4 buffer at 200^{o}C

Duration of experiment (days)	Reactive silica concentration Run I (ppm)	Reactive silica concentration Run II (ppm)	Average reactive silica concentration (ppm)	Standard deviation (ppm)
1	155	156	155.5	0.71
3	263	258.5	260.75	3.18
7	303.5	316	309.75	8.84
14	350	351	350.5	0.71
21	369.5	372.5	371.0	2.12
28	395.5	416	405.75	14.50
56	669	457	421.75	49.85

B.5.2 pH 7 buffer solution

This section provides the initial sample weight, final pH after experiments, concentrations of the reactive silica, and major cation dissolved in pH 7 buffer solution at 200^{o}C.

Table B.61 Initial sample used and pH after experiment in pH 7 buffer – Run I

Duration of experiment (days)	Initial weight of sample (g)	pH after experiment
1	0.5036	6.76
3	0.5070	6.81
7	0.5039	6.84
14	0.5036	6.92
18	0.5033	6.94
28	0.5050	6.96
56	0.5047	6.79

Table B.62 Initial sample used and pH after experiment in pH 7 buffer – Run II

Duration of experiment (days)	Initial weight of sample (g)	pH after experiment
1	0.5037	6.47
3	0.5023	6.04
7	0.5042	6.72
14	0.5041	6.87
18	0.503	6.47
28	0.5054	6.96
56	0.5053	6.61

Table B.63 Reactive silica data in pH 7 buffer at 200°C

Duration of experiment (days)	Reactive silica concentration Run I (ppm)	Reactive silica concentration Run II (ppm)	Average reactive silica concentration (ppm)	Standard deviation (ppm)
1	11.6	12	118	2.83
3	15.25	17.6	164.25	16.6
7	22	20	210	14.1
14	24.2	22.15	231.75	14.5
18	22.65	23.9	232.75	8.84
28	24.95	25.65	253	4.95
56	32.05	37.1	261	35.7

B.5.3 pH 10 buffer solution

This section provides the initial sample weight, final pH after experiments, concentrations of the reactive silica, and major cation dissolved in pH 10 buffer solution at 200°C.

Table B.64 Initial sample used and pH after experiment in pH 10 buffer – Run I

Duration of experiment (days)	Initial weight of sample (g)	pH after experiment
1	0.5023	10
3	0.505	10.06
7	0.5069	9.68
14	0.5039	10.03
21	0.5039	9.65
28	0.5046	9.83
56	0.5051	10.03

Table B.65 Initial sample used and pH after experiment in pH 10 buffer – Run II

Duration of experiment (days)	Initial weight of sample (g)	pH after experiment
1	0.5025	10.09
3	0.5043	10.12
7	0.507	9.67
14	0.5034	10
21	0.5043	9.61
28	0.502	9.81
56	0.5024	9.89

Table B.66 Reactive silica data in pH 10 buffer at 200^{o}C

Duration of experiment (days)	Reactive silica concentration Run I (ppm)	Reactive silica concentration Run II (ppm)	Average reactive silica concentration (ppm)	Standard deviation (ppm)
1	429	425.5	427.25	2.47
3	545	667	606	86.27
7	679.5	670.5	675	6.36
14	621.5	593	607.25	20.15
18	655	577.5	641.25	54.80
28	634	620.5	627.25	9.55
56	684.5	787	685.75	72.48

B.5.4 pH 13 buffer solution

This section provides the initial sample weight, final pH after experiments, concentrations of the reactive silica, and major cation dissolved in pH 13 buffer solution at 200^{o}C.

Table B.67 Initial sample used and pH after experiment in pH 13 buffer – Run I

Duration of experiment (days)	Initial weight of sample (g)	pH after experiment
1	0.5026	13.24
3	0.5028	13.2
7	0.5055	12.76
14	0.5024	13.36
18	0.5036	13.23
28	0.5019	12.85
56	0.5018	13.01

Table B.68 Initial sample used and pH after experiment in pH 13 buffer – Run I

Duration of experiment (days)	Initial weight of sample (g)	pH after experiment
1	0.5026	13.3
3	0.5023	13.16
7	0.5052	12.58
14	0.503	13.46
18	0.5048	13.24
28	0.5025	12.86
56	0.5056	13.05

Table B.69 Reactive silica data in pH 13 buffer at 200^{o}C

Duration of experiment (days)	Reactive silica concentration Run I (ppm)	Reactive silica concentration Run II (ppm)	Average reactive silica concentration (ppm)	Standard deviation (ppm)
1	3390	3845	3617.5	321.73
3	4900	4665	4782.5	166.17
7	5430	4900	5165	374.77
14	5585	7730	6657.5	1516.74
18	6345	6805	6575	325.27
28	5860	6475	6167.5	304.06
56	7240	7330	7285	63.64

Appendix C Recycled Flow-through System

The flow-through system was used for fluid-rock interaction experiments using two different fluids, water and 250 ppm NaCl solution. This section presents the experimental data for both fluids.

C.1 Fluid-Rock Interaction in Pure Water

The fluid-rock interaction in pure water is divided in to three experiments based on the weight of the sample. This experiment was undertaken to observe the effect of rock to water ratio. Three different sample weights were chosen, 0.7 g, 3 g and 7 g.

C.1.1 Sample weight 0.7 g

The fluid-rock interaction experiments were carried out in two runs to obtain reproducible results. The experimental data for Run I and Run II are presented in Table C.1 and Table C.2, respectively, while the average values of the weight of dissolved sample and the percentage of dissolved sample are presented in Table C.3. The average initial sample is 0.7218 g.

Table C.1 Experimental data using 0.7 g sample in pure water - Run I

Duration of experiment (days)	Initial weight of sample (g)	Weight of sample after experiment (g)	Weight of dissolved sample (g)	Amount dissolved (%)	pH after experiment
1	0.7408	0.6886	0.0522	7.05	7.44
3	0.7410	0.6611	0.0799	10.78	7.77
7	0.7442	0.6453	0.0989	13.29	7.35
14	0.7353	0.6195	0.1158	15.75	7.72
21	0.7136	0.5883	0.1253	17.56	7.98
28	0.7411	0.6047	0.1364	18.41	8.20

Table C.2 Experimental data using 0.7 g sample in pure water – Run II

Duration of experiment (days)	Initial weight of sample (g)	Weight of sample after experiment (g)	Weight of dissolved sample (g)	Amount dissolved (%)	pH after experiment
1	0.7067	0.6485	0.0582	8.24	7.56
3	0.7074	0.6344	0.073	10.32	7.81
7	0.7081	0.6111	0.097	13.70	7.45
14	0.7089	0.602	0.1069	15.08	7.59
21	0.7093	0.588	0.1213	17.10	7.46
28	0.7056	0.6083	0.0973	18.78	8.62

Table C.3 Average values from Run I and Run II for 0.7 g sample in pure water

Duration of experiment (days)	Average weight of dissolved sample (g)	Average amount dissolved (%)	Average pH after experiment
1	0.0552	7.64	7.50
3	0.0765	10.55	7.79
7	0.0980	13.49	7.40
14	0.1114	15.41	7.66
21	0.1233	17.33	7.72
28	0.1169	18.59	8.41

Table C.4 Reactive silica data for 0.7 g sample in pure water

Duration of experiment (days)	Reactive silica concentration Run I (ppm)	Reactive silica concentration Run II (ppm)	Average reactive silica concentration (ppm)	Standard deviation (ppm)
1	166	152	159.00	9.90
3	244	236	239.75	5.30
7	282	276	279.00	4.24
14	288	291	289.25	2.47
21	307	286	296.25	14.50
28	289	290	289.50	0.71

Table C.5 Dissolved major cation data for 0.7 g sample in pure water – Run I

Duration of experiment (days)	Dissolved Na Concentration (ppm)	Dissolved K Concentration (ppm)	Dissolved Al Concentration (ppm)
1	7.2073	5.5300	2.1697
3	7.2777	5.1908	2.1343
7	8.7237	4.7453	1.8680
14	8.9515	4.1515	1.7188
21	12.4300	5.1137	2.6241
28	12.2096	4.7855	1.6899

Table C.6 Dissolved major cation data for 0.7 g sample in pure water – Run II

Duration of experiment (days)	Dissolved Na Concentration (ppm)	Dissolved K Concentration (ppm)	Dissolved Al Concentration (ppm)
1	7.7632	4.6691	1.8037
3	8.9084	5.1675	2.5243
7	11.5746	5.7336	1.9561
14	11.5199	4.9150	1.5081
21	11.1069	4.8971	2.0268
28	12.1049	4.9291	2.0806

Table C.7 Average Dissolved major cation data for 0.7 g sample in pure water

Duration of experiment (days)	Average Dissolved Na Concentration (ppm)	Average Dissolved K Concentration (ppm)	Average Dissolved Al Concentration (ppm)
1	7.4853	5.0996	1.9867
3	8.0930	5.1791	2.3293
7	10.1492	5.2395	1.9121
14	10.2357	4.5333	1.6134
21	11.7685	5.0054	2.3254
28	12.1572	4.8573	1.8853

Table C.8 Standard deviation cation data for 0.7 g sample in pure water

Duration of experiment (days)	Standard Deviation Dissolved Na Concentration (ppm)	Standard Deviation Dissolved K Concentration (ppm)	Standard Deviation Dissolved Al Concentration (ppm)
1	0.39	0.61	0.26
3	1.15	0.02	0.28
7	2.02	0.70	0.06
14	1.82	0.54	0.15
21	0.94	0.15	0.42
28	0.07	0.10	0.28

C.1.2 Sample weight 3 g

The experimental data for Run I and Run II are presented in Table C.9 and Table C.10, respectively, while the average values of the weight of dissolved sample and the percentage of dissolved sample are presented in Table C.11. The average initial sample weight is 3.0427 g.

Table C.9 Experimental data using 3 g sample in pure water – Run I

Duration of experiment (days)	Initial weight of sample (g)	Weight of sample after experiment (g)	Weight of dissolved sample (g)	Amount dissolved (%)	pH after experiment
1	3.0273	2.9117	0.1156	3.82	7.68
3	3.0299	2.9001	0.1298	4.28	8.21
7	3.0324	2.9004	0.1320	4.35	7.48
14	3.0465	2.8960	0.1505	4.94	7.30
21	3.0290	2.8570	0.1720	5.68	7.73
28	3.0491	2.8653	0.1838	6.34	7.96

Table C.10 Experimental data using 3 g sample in pure water – Run II

Duration of experiment (days)	Initial weight of sample (g)	Weight of sample after experiment (g)	Weight of dissolved sample (g)	Amount dissolved (%)	pH after experiment
1	3.0511	2.9594	0.0917	3.01	7.57
3	3.0568	2.9407	0.1161	3.80	7.58
7	3.0512	2.9138	0.1374	4.50	7.30
14	3.0560	2.8995	0.1565	5.12	7.60
21	3.0336	2.8585	0.1751	5.77	7.34
28	3.0499	2.8722	0.1777	5.83	7.71

Table C.11 Average values from Run I and Run II for 3 g sample in pure water

Duration of experiment (days)	Average weight of dissolved sample (g)	Average amount dissolved (%)	Average pH after experiment
1	0.1037	3.41	7.63
3	0.1230	4.04	7.90
7	0.1347	4.43	7.39
14	0.1535	5.03	7.45
21	0.1736	5.73	7.54
28	0.1808	6.08	7.84

Table C.12 Reactive silica data for 3 g sample in pure water

Duration of experiment (days)	Reactive silica concentration I (ppm)	Reactive silica concentration II (ppm)	Average reactive silica concentration (ppm)	Standard deviation (ppm)
1	263	264	263.5	0.71
3	301	320	310.5	13.44
7	295	324	309.5	20.51
14	305	339	322	24.04
21	307	329	318	15.56
28	298	336	317	26.87

Table C.13 Dissolved major cation data for 3 g sample in pure water – Run I

Duration of experiment (days)	Dissolved Na Concentration (ppm)	Dissolved K Concentration (ppm)	Dissolved Al Concentration (ppm)
1	8.1684	6.2994	1.9641
3	9.2414	6.6660	1.1994
7	10.9932	5.5196	1.3149
14	13.1010	6.2923	1.6491
21	12.1243	6.2648	1.3692
28	13.2780	7.9686	2.1728

Table C.14 Dissolved major cation data for 3 g sample in pure water – Run II

Duration of experiment (days)	Dissolved Na Concentration (ppm)	Dissolved K Concentration (ppm)	Dissolved Al Concentration (ppm)
1	6.6402	5.0522	1.1720
3	7.7678	5.2529	1.0461
7	9.0129	5.3670	1.1362
14	10.7673	5.1504	1.1233
21	10.7591	4.7126	1.0262
28	13.5032	5.2009	1.3225

Table C.15 Average dissolved major cation data for 3 g sample in pure water

Duration of experiment (days)	Average Dissolved Na Concentration (ppm)	Average Dissolved K Concentration (ppm)	Average Dissolved Al Concentration (ppm)
1	7.4043	5.6758	1.5681
3	8.5046	5.9595	1.1228
7	10.0031	5.4433	1.2255
14	11.9342	5.7213	1.3862
21	11.4417	5.4887	1.1977
28	13.3906	6.5847	1.7476

Table C.16 Standard deviation major cation data for 3 g sample in pure water

Duration of experiment (days)	Standard Deviation Dissolved Na Concentration (ppm)	Standard Deviation Dissolved K Concentration (ppm)	Standard Deviation Dissolved Al Concentration (ppm)
1	1.08	0.88	0.56
3	1.04	1.00	0.11
7	1.40	0.11	0.13
14	1.65	0.81	0.37
21	0.97	1.10	0.24
28	0.16	1.96	0.60

C.1.3 Sample weight 7 g

The experimental data for Run I and Run II are presented in Table C.17 and Table C.18, respectively, while the average values of the weight of dissolved sample and the percentage of dissolved sample are presented in Table C.19. The average initial sample weight is 7.0718 g.

Table C.17 Experimental data using 7 g sample in pure water – Run I

Duration of experiment (days)	Initial weight of sample (g)	Weight of sample after experiment (g)	Weight of dissolved sample (g)	Amount dissolved (%)	pH after experiment
1	7.0695	6.9546	0.1149	1.63	7.70
3	7.0445	6.9164	0.1281	1.82	7.53
7	7.0701	6.9257	0.1444	2.04	7.10
14	7.0778	6.9063	0.1715	2.42	6.98
21	7.0759	6.8915	0.1844	2.61	7.25
28	7.0734	6.8909	0.1825	2.58	7.07

Table C.18 Experimental data using 7 g sample in pure water – Run II

Duration of experiment (days)	Initial weight of sample (g)	Weight of sample after experiment (g)	Weight of dissolved sample (g)	Amount dissolved (%)	pH after experiment
1	7.0726	6.9581	0.1145	1.62	8.01
3	7.0751	6.9468	0.1283	1.81	7.32
7	7.0755	6.9314	0.1441	2.04	6.81
14	7.0744	6.9214	0.153	2.16	6.75
21	7.0769	6.9162	0.1607	2.27	7.15
28	7.0753	6.9009	0.1744	2.46	6.98

Table C.19 Average values from Run I and Run II for 7 g sample in pure water

Duration of experiment (days)	Average weight of dissolved sample (g)	Average amount dissolved (%)	Average pH after experiment
1	0.1147	1.62	7.86
3	0.1282	1.82	7.43
7	0.1443	2.04	6.96
14	0.1623	2.29	6.87
21	0.1725	2.44	7.20
28	0.1785	2.52	7.03

Table C.20 Reactive silica data for 7 g sample in pure water

Duration of experiment (days)	Reactive silica concentration I (ppm)	Reactive silica concentration II (ppm)	Average reactive silica concentration (ppm)	Standard deviation (ppm)
1	289	285	287	2.83
3	324	315	319.5	6.36
7	344	339	341.5	3.54
14	332	338	335	4.24
21	343	339	341	2.83
28	357	351	354	4.24

Table C.21 Dissolved major cation data for 7 g sample in pure water – Run I

Duration of experiment (days)	Dissolved Na Concentration (ppm)	Dissolved K Concentration (ppm)	Dissolved Al Concentration (ppm)
1	8.0019	7.7196	1.1707
3	12.7323	6.1123	1.1614
7	15.3947	7.2369	1.4083
14	15.5278	5.7842	1.3094
21	17.8664	6.5080	1.6159
28	20.0838	5.7919	1.4173

Table C.22 Dissolved major cation data for 7 g sample in pure water – Run II

Duration of experiment (days)	Dissolved Na Concentration (ppm)	Dissolved K Concentration (ppm)	Dissolved Al Concentration (ppm)
1	7.3317	5.5998	1.2528
3	10.3087	5.2705	1.2372
7	11.8665	5.7723	1.2222
14	14.4538	5.5545	1.3703
21	17.9638	6.5578	1.3709
28	15.9468	5.0778	1.2159

Table C.23 Average dissolved major cation data for 7 g sample in pure water

Duration of experiment (days)	Average Dissolved Na Concentration (ppm)	Average Dissolved K Concentration (ppm)	Average Dissolved Al Concentration (ppm)
1	7.6668	6.6597	1.2118
3	11.5205	5.6914	1.1993
7	13.6306	6.5046	1.3152
14	14.9908	5.6694	1.3398
21	17.9151	6.5329	1.4934
28	18.0153	5.4348	1.3166

Table C.24 Standard deviation major cation data for 7 g sample in pure water

Duration of experiment (days)	Standard Deviation Dissolved Na Concentration (ppm)	Standard Deviation Dissolved K Concentration (ppm)	Standard Deviation Dissolved Al Concentration (ppm)
1	0.47	1.50	0.06
3	1.71	0.60	0.05
7	2.49	1.04	0.13
14	0.76	0.16	0.04
21	0.07	0.04	0.17
28	2.93	0.50	0.14

C.2 Fluid-Rock Interaction in 250 ppm NaCl Solution

The fluid-rock interaction in 250 ppm NaCl solution is divided in to three experiments based on the weight of the sample. This experiment was undertaken to observe the effect of salt in the fluid and the effect of rock/water ratio. For latter comparison, the initial weights of the sample chosen were identical to the fluid-rock interaction experiment in pure water, 0.7 g, 3 g and 7 g.

C.2.1 Sample weight 0.7 g

The experimental data for Run I and Run II are presented in Table C.25 and Table C.26, respectively, while the average values of the weight of dissolved sample and the percentage of dissolved sample are presented in Table C.27. The average initial sample weight for this experiment is 0.7252 g.

Table C.25 Experimental data using 0.7 g sample in 250 ppm NaCl solution – Run I

Duration of experiment (days)	Initial weight of sample (g)	Weight of sample after experiment (g)	Weight of dissolved sample (g)	Amount dissolved (%)	pH after experiment
1	0.7452	0.6815	0.0637	8.55	7.27
3	0.7538	0.6639	0.0899	11.93	7.58
7	0.7409	0.6286	0.1123	15.16	7.21
14	0.7225	0.5890	0.1335	18.48	7.59
21	0.7540	0.6007	0.1533	20.33	7.73
28	0.7387	0.5820	0.1567	21.21	8.74

Table C.26 Experimental data using 0.7 g sample in 250 ppm NaCl solution – Run II

Duration of experiment (days)	Initial weight of sample (g)	Weight of sample after experiment (g)	Weight of dissolved sample (g)	Amount dissolved (%)	pH after experiment
1	0.7091	0.6592	0.0499	7.04	7.65
3	0.7083	0.6276	0.0807	11.39	7.88
7	0.7054	0.6084	0.0970	13.75	7.61
14	0.7068	0.5971	0.1097	15.52	7.41
21	0.7106	0.5821	0.1285	18.08	7.40
28	0.7076	0.5821	0.1255	18.67	8.20

Table C.27 Average values from Run I and Run II for 0.7 g sample in 250 ppm NaCl

Duration of experiment (days)	Average weight of dissolved sample (g)	Average amount dissolved (%)	Average pH after experiment
1	0.0568	7.79	7.46
3	0.0853	11.66	7.73
7	0.1047	14.45	7.41
14	0.1216	17.00	7.50
21	0.1409	19.21	7.57
28	0.1411	19.94	8.47

Table C.28 Reactive silica data for 0.7 g sample in 250 ppm NaCl solution

Duration of experiment (days)	Reactive silica concentration I (ppm)	Reactive silica concentration II (ppm)	Average reactive silica concentration (ppm)	Standard deviation (ppm)
1	153	186	169.50	23.33
3	263	273	268.00	7.07
7	315	279	297.00	25.46
14	330	285	307.50	31.82
21	318	301	309.50	12.02
28	309	295	302.00	9.90

Table C.29 Dissolved major cation data for 0.7 g sample in 250 ppm NaCl solution – Run I

Duration of experiment (days)	Dissolved Na Concentration (ppm)	Dissolved K Concentration (ppm)	Dissolved Al Concentration (ppm)
1	108.7095	10.1825	1.7698
3	115.7294	10.1743	1.2432
7	118.6713	9.4370	1.1207
14	115.7463	9.7336	1.2561
21	118.3491	9.9316	1.3479
28	105.7597	9.5358	1.1277

Table C.30 Dissolved major cation data for 0.7 g sample in 250 ppm NaCl solution – Run II

Duration of experiment (days)	Dissolved Na Concentration (ppm)	Dissolved K Concentration (ppm)	Dissolved Al Concentration (ppm)
1	93.7074	7.3900	1.1714
3	93.0852	7.4489	1.1182
7	95.0319	7.6251	1.1275
14	92.5743	7.8121	1.0164
21	93.4135	8.8765	1.0183
28	95.0176	9.8750	1.1014

Table C.31 Average dissolved major cation data for 0.7 g sample in 250 ppm NaCl solution

Duration of experiment (days)	Average Dissolved Na Concentration (ppm)	Average Dissolved K Concentration (ppm)	Average Dissolved Al Concentration (ppm)
1	101.2084	8.7862	1.4706
3	104.4073	8.8116	1.1807
7	106.8516	8.5311	1.1241
14	104.1603	8.7728	1.1363
21	105.8813	9.4041	1.1831
28	100.3886	9.7054	1.1145

Table C.32 Standard deviation major cation data for 0.7 g sample in 250 ppm NaCl solution

Duration of experiment (days)	Standard Deviation Dissolved Na Concentration (ppm)	Standard Deviation Dissolved K Concentration (ppm)	Standard Deviation Dissolved Al Concentration (ppm)
1	10.61	1.97	0.42
3	16.01	1.93	0.09
7	16.72	1.28	0.00
14	16.39	1.36	0.17
21	17.63	0.75	0.23
28	7.60	0.24	0.02

C.2.2 Sample weight 3 g

The experimental data for Run I and Run II are presented in Table C.33 and Table C.34, respectively, while the average values of the weight of dissolved sample and the percentage of dissolved sample are presented in Table C.35. The average initial sample weight for this experiment is 3.0392 g.

Table C.33 Experimental data using 3 g sample in 250 ppm NaCl – Run I

Duration of experiment (days)	Initial weight of sample (g)	Weight of sample after experiment (g)	Weight of dissolved sample (g)	Amount dissolved (%)	pH after experiment
1	3.0069	2.8783	0.1286	4.28	7.88
3	3.0319	2.8860	0.1459	4.84	7.34
7	3.0450	2.8767	0.1683	5.53	7.88
14	3.0468	2.8717	0.1751	6.08	7.63
21	3.0142	2.8241	0.1901	6.31	7.46
28	3.0493	2.8350	0.2143	6.52	7.81

Table C.34 Experimental data using 3 g sample in 250 ppm NaCl – Run II

Duration of experiment (days)	Initial weight of sample (g)	Weight of sample after experiment (g)	Weight of dissolved sample (g)	Amount dissolved (%)	pH after experiment
1	3.0506	2.9584	0.0922	3.02	7.22
3	3.0522	2.9391	0.1131	3.71	7.52
7	3.0501	2.9299	0.1202	3.94	7.70
14	3.0328	2.8912	0.1416	4.67	7.61
21	3.0416	2.8524	0.1892	6.22	7.75
28	3.0493	2.8575	0.1918	6.29	7.69

Table C.35 Average values from Run I and Run II for 3 g sample in 250 ppm NaCl

Duration of experiment (days)	Average weight of dissolved sample (g)	Average amount dissolved (%)	Average pH after experiment
1	0.1104	3.65	7.55
3	0.1295	4.27	7.43
7	0.1443	4.73	7.79
14	0.1584	5.37	7.62
21	0.1896	6.26	7.61
28	0.2031	6.40	7.75

Table C.36 Reactive silica data for 3 g sample in 250 ppm NaCl solution

Duration of experiment (days)	Reactive silica concentration I (ppm)	Reactive silica concentration II (ppm)	Average reactive silica concentration (ppm)	Standard deviation (ppm)
1	275	272	273.5	2.12
3	313	331	322	12.73
7	313	338	325.5	17.68
14	317	341	329	16.97
21	319	336	327.5	12.02
28	320	340	330	14.14

Table C.37 Dissolved major cation data for 3 g sample in 250 ppm NaCl solution – Run I

Duration of experiment (days)	Dissolved Na Concentration (ppm)	Dissolved K Concentration (ppm)	Dissolved Al Concentration (ppm)
1	101.03	9.6540	0.8900
3	107.64	9.1916	0.7147
7	109.12	9.0076	0.5753
14	101.80	10.459	0.6550
21	117.08	10.917	0.6891
28	113.66	11.290	0.7270

Table C.38 Dissolved major cation data for 3 g sample in 250 ppm NaCl solution – Run II

Duration of experiment (days)	Dissolved Na Concentration (ppm)	Dissolved K Concentration (ppm)	Dissolved Al Concentration (ppm)
1	96.146	6.0500	0.6409
3	94.917	6.1894	0.4221
7	96.900	6.3539	0.4857
14	97.651	7.2626	0.4326
21	96.931	6.5984	0.4784
28	101.75	6.6850	0.4649

Table C.39 Average dissolved major cation data for 3 g sample in 250 ppm NaCl solution

Duration of experiment (days)	Average Dissolved Na Concentration (ppm)	Average Dissolved K Concentration (ppm)	Average Dissolved Al Concentration (ppm)
1	98.5896	7.8520	0.7655
3	101.2791	7.6905	0.5684
7	103.0096	7.6807	0.5305
14	99.7233	8.8607	0.5438
21	107.0059	8.7577	0.5837
28	107.7080	8.9873	0.5959

Table C.40 Standard deviation major cation data for 3 g sample in 250 ppm NaCl solution

Duration of experiment (days)	Standard Deviation Dissolved Na Concentration (ppm)	Standard Deviation Dissolved K Concentration (ppm)	Standard Deviation Dissolved Al Concentration (ppm)
1	3.46	2.55	0.18
3	9.00	2.12	0.21
7	8.64	1.88	0.06
14	2.93	2.26	0.16
21	14.25	3.05	0.15
28	8.42	3.26	0.19

C.2.3 Sample weight 7 g

The experimental data for Run I and Run II are presented in Table C.41 and Table C.42, respectively, while the average values of the weight of dissolved sample and the percentage of dissolved sample are presented in Table C.43. The average initial sample weight for this experiment is 7.0666 g.

Table C.41 Experimental data using 7 g sample in 250 ppm NaCl solution – Run I

Duration of experiment (days)	Initial weight of sample (g)	Weight of sample after experiment (g)	Weight of dissolved sample (g)	Amount dissolved (%)	pH after experiment
1	7.0518	6.9273	0.1245	1.77	7.48
3	7.0499	6.9172	0.1327	1.88	7.59
7	7.0528	6.9069	0.1459	2.07	7.33
14	7.0779	6.8964	0.1815	2.56	7.42
21	7.0476	6.8521	0.1955	2.77	7.29
28	7.0692	6.8702	0.1990	2.82	7.86

Table C.42 Experimental data using 7 g sample in 250 ppm NaCl solution – Run II

Duration of experiment (days)	Initial weight of sample (g)	Weight of sample after experiment (g)	Weight of dissolved sample (g)	Amount dissolved (%)	pH after experiment
1	7.0721	6.954	0.1181	1.67	7.76
3	7.0753	6.9442	0.1311	1.85	7.40
7	7.0764	6.9313	0.1451	2.05	7.10
14	7.0756	6.9086	0.167	2.36	7.36
21	7.0757	6.9057	0.17	2.40	6.90
28	7.0746	6.8981	0.1765	2.49	7.20

Table C.43 Average values from Run I and Run II for 7 g sample in 250 ppm NaCl

Duration of experiment (days)	Average weight of dissolved sample (g)	Average amount dissolved (%)	Average pH after experiment
1	0.1213	1.72	7.62
3	0.1319	1.87	7.50
7	0.1455	2.06	7.22
14	0.1743	2.46	7.39
21	0.1828	2.59	7.10
28	0.1877	2.65	7.53

Table C.44 Reactive silica data for 7 g sample in 250 ppm NaCl solution

Duration of experiment (days)	Reactive silica concentration I (ppm)	Reactive silica concentration II (ppm)	Average reactive silica concentration (ppm)	Standard deviation (ppm)
1	289	292	290.5	2.12
3	318	312	315.0	4.24
7	335	323	329.0	8.49
14	334	332	333.0	1.41
21	351	342	346.5	6.36
28	352	345	348.5	4.95

Table C.45 Dissolved major cation data for 7 g sample in 250 ppm NaCl solution – Run I

Duration of experiment (days)	Dissolved Na Concentration (ppm)	Dissolved K Concentration (ppm)	Dissolved Al Concentration (ppm)
1	112.3529	9.9069	0.4927
3	108.8290	9.9832	0.5263
7	106.7481	9.5064	0.4663
14	107.3335	9.0192	0.6057
21	120.6715	11.0288	0.6611
28	119.6557	11.6997	0.7003

Table C.46 Dissolved major cation data for 7 g sample in 250 ppm NaCl solution – Run II

Duration of experiment (days)	Dissolved Na Concentration (ppm)	Dissolved K Concentration (ppm)	Dissolved Al Concentration (ppm)
1	85.1985	7.4465	0.5462
3	94.0085	7.3324	0.3544
7	93.8479	7.4255	0.3148
14	95.6533	7.7485	0.6219
21	95.7429	7.7934	0.3373
28	103.4548	9.2335	0.3320

Table C.47 Average dissolved major cation data for 7 g sample in 250 ppm NaCl solution

Duration of experiment (days)	Average Dissolved Na Concentration (ppm)	Average Dissolved K Concentration (ppm)	Average Dissolved Al Concentration (ppm)
1	98.7757	8.6767	0.5195
3	101.4187	8.6578	0.4404
7	100.2980	8.4660	0.3906
14	101.4934	8.3838	0.6138
21	108.2072	9.4111	0.4992
28	111.5552	10.4666	0.5162

Table C.48 Standard deviation major cation data for 7 g sample in 250 ppm NaCl solution

Duration of experiment (days)	Standard Deviation Dissolved Na Concentration (ppm)	Standard Deviation Dissolved K Concentration (ppm)	Standard Deviation Dissolved Al Concentration (ppm)
1	19.20	1.74	0.04
3	10.48	1.87	0.12
7	9.12	1.47	0.11
14	8.26	0.90	0.01
21	17.63	2.29	0.23
28	11.46	1.74	0.26

Appendix D Non-recycled Flow-through System

This section presents the raw data of silica, sodium, potassium and aluminium concentrations after 7 days and 28 days replacing water and 250 ppm NaCl solution at 250^{o}C using 100-200 µm particle size.

Table D.1 Silica concentration in pure water and 250 ppm NaCl solution after 7 days

Time (days)	Silica concentration in water (ppm)	Silica concentration in 250 ppm NaCl (ppm)
1	98.1	99
2	85.8	86.5
3	77.7	86.7
4	69.8	76.3
5	67	73.6
6	66.8	74.8
7	67.4	74.4

Table D.2 Na, K and Al concentration in pure water after 7 days

Time (days)	Na concentration (ppm)	K concentration (ppm)	Al concentration (ppm)	pH
1	11.010	3.1252	1.2451	6.82
2	8.9439	3.0426	1.7180	6.65
3	7.8311	3.9490	2.9345	6.53
4	7.4551	4.6941	3.6937	6.44
5	7.4827	5.2362	4.0645	6.49
6	7.0554	5.4582	4.1409	6.38
7	6.7510	5.7525	4.2507	6.41

Table D.3 K and Al concentration in 250 ppm NaCl solution after 7 days

Time (days)	K concentration (ppm)	Al concentration (ppm)	pH
1	7.3899	0.6410	6.42
2	10.4169	1.0554	6.87
3	9.5212	1.3675	6.66
4	10.8761	1.6569	6.75
5	9.6718	1.8729	6.51
6	10.4520	2.2045	6.85
7	8.6026	2.2213	6.68

Table D.4 Silica concentration in pure water and 250 ppm NaCl solution after 28 days

Time (days)	Silica concentration in water (ppm)	Silica concentration in 250 ppm NaCl (ppm)
1	1.359	1.264
2	1.079	1.067
3	0.997	0.967
4	0.963	0.936
5	0.903	0.89
6	0.843	0.852
7	0.811	0.821
8	0.794	0.767
9	0.77	0.764
10	0.76	0.71
11	0.684	0.627
12	0.622	0.567
13	0.571	0.56

Table D.5 Silica concentration in pure water and 250 ppm NaCl solution after 28 days (cont.)

Time (days)	Silica concentration in water (ppm)	Silica concentration in 250 ppm NaCl (ppm)
14	0.55	0.456
15	0.466	0.426
16	0.442	0.387
17	0.37	0.346
18	0.395	0.312
19	0.392	0.272
20	0.341	0.234
21	0.32	0.201
22	0.294	0.182
23	0.251	0.163
24	0.224	0.145
25	0.197	0.132
26	0.177	0.124
27	0.165	0.118
28	0.141	0.101

Table D.6 Na, K and Al concentration in pure water after 28 days

Time (days)	Na concentration (ppm)	K concentration (ppm)	Al concentration (ppm)	pH
1	6.4539	4.3639	1.9142	6.77
2	6.9593	4.9875	3.4090	6.80
3	7.2797	5.4406	4.7355	6.83
4	7.3177	5.9414	5.3738	6.83

Table D.7 Na, K and Al concentration in pure water (cont.) after 28 days (cont.)

Time (days)	Na concentration (ppm)	K concentration (ppm)	Al concentration (ppm)	pH
5	6.9894	6.6137	5.6883	6.79
6	6.3444	6.8640	5.4574	6.87
7	6.2109	7.2945	5.3141	6.88
8	5.2594	7.4338	4.5310	6.77
9	4.9185	7.9129	4.1541	6.65
10	3.7339	8.0974	3.5861	6.68
11	3.0184	7.4748	2.8910	6.79
12	2.5363	5.3809	1.9639	6.80
13	2.3420	2.9181	1.2583	6.69
14	2.3594	1.8931	1.1225	6.74
15	2.5452	1.7028	1.0433	6.70
16	2.3874	1.4229	1.1085	6.65
17	2.5439	1.4113	1.0438	6.77
18	1.5261	1.3193	1.0755	6.62
19	1.6024	1.2781	0.9609	6.69
20	1.5545	1.2031	0.9296	6.86
21	1.1408	1.0649	0.7363	6.96
22	2.4996	1.1612	0.6358	6.52
23	2.4604	1.0392	0.5303	6.67
24	2.7458	1.0518	0.5845	7.10
25	2.5856	0.8781	0.4465	6.74
26	2.7321	0.8389	0.4232	6.99
27	2.7575	0.7499	0.3543	6.74
28	2.5993	0.6893	0.3044	6.78

Table D.8 K and Al concentration in 250 ppm NaCl solution after 28 days

Time (days)	K concentration (ppm)	Al concentration (ppm)	pH
1	8.3823	0.5927	6.78
2	8.2134	1.0158	6.82
3	9.1690	1.5951	6.76
4	8.7899	1.7670	6.81
5	9.2498	2.0737	6.87
6	8.2106	2.2180	6.79
7	8.2338	2.2808	6.76
8	6.8144	2.1164	6.74
9	5.3676	2.1683	6.76
10	3.9015	1.5820	6.85
11	3.3716	1.1613	6.83
12	2.9815	0.9359	6.79
13	3.0326	0.7484	6.69
14	2.5243	0.4946	6.78
15	2.1739	0.4013	6.80
16	2.0422	0.3817	6.82
17	2.3869	0.3573	6.71
18	1.5413	0.3074	6.76
19	1.5848	0.2908	6.78
20	1.4954	0.1128	6.85
21	1.5745	0.0969	6.88
22	1.3120	0.0842	6.65
23	1.1135	0.0922	6.67

Table D.9 K and Al concentration in 250 ppm NaCl solution (cont.) after 28 days

Time (days)	K concentration (ppm)	Al concentration (ppm)	pH
24	0.9741	0.0656	6.93
25	0.9534	0.0794	6.79
26	0.8015	0.0635	6.84
27	0.9546	0.0656	6.62
28	0.8819	0.0847	6.93

Appendix E High Pressure Flow-through System

The high pressure flow-through system was used for fluid-rock interaction experiments at three different pressures, 40, 100 and 200 bar. This section presents the experimental data including the sample information, and silica concentration.

Table E.1 Sample information after 6 hours interaction at different pressures (Run I)

Pressure (bar)	Initial sample (g)	remaining sample (g)	Sample dissolved (%wt.)
40	3.0325	2.9735	1.95
100	3.0303	2.9589	2.36
200	3.0308	2.9551	2.50

Table E.2 Sample information after 6 hours interaction at different pressures (Run II)

Pressure (bar)	Initial sample (g)	remaining sample (g)	Sample dissolved (%wt.)
40	3.0356	2.9826	1.75
100	3.0357	2.9661	2.29
200	3.0334	2.9419	3.02

Table E.3 Silica concentration after 6 hours interaction at 40 bar

Time (hours)	SiO2 I	SiO2 II	Average	Standard deviation	pH I	pH II
1	21	19	20	1.41	6.71	6.54
2	20	21	20.5	0.71	6.45	6.65
3	19	19	19	0.00	6.60	6.53
4	18	18	18	0.00	6.36	6.42
5	18	17	17.5	0.71	6.41	6.58
6	23	19	21	2.83	6.63	6.72

Table E.4 Silica concentration after 6 hours interaction at 100 bar

Time (hours)	SiO2 I	SiO2 II	Average	Standard deviation	pH I	pH II
1	23	28	25.5	3.54	6.20	6.47
2	29	30	29.5	0.71	6.31	6.54
3	30	27	28.5	2.12	6.46	6.42
4	31	27	29	2.83	6.69	6.44
5	30	30	30	0.00	6.58	6.58
6	30	27	28.5	2.12	6.85	6.49

Table E.5 Silica concentration after 6 hours interaction at 200 bar

Time (hours)	SiO2 I	SiO2 II	Average	Standard deviation	pH I	pH II
1	32	35	33.5	2.12	6.57	6.78
2	33	34	33.5	0.71	6.76	6.92
3	33	35	34.0	1.41	6.82	7.08
4	32	36	34.0	2.83	6.88	7.10
5	31	36	33.5	3.54	6.74	7.26
6	33	35	34.0	1.41	6.65	7.04

Appendix F Mass Transfer Coefficient

This section presents the data and sample calculations to obtain the mass transfer coefficient for both the static system and flow-through system

F.1 Static system

To calculate the mass transfer coefficient, Equation (5.20) is used. According to Worley (1994), the mass transfer from a spherical particle in a stagnant medium has a Sherwood number of 2. Sample calculation for 160°C with particle size 100 – 200 $\left(d_p = 1.76 \times 10^{-4}\ m\right)$:

$$Sh = \frac{k_m d_p}{D_{AB}} = 2 \qquad \textbf{(F.1)}$$

Calculating D_{AB} at 160°C (433.15K):

$$D_{AB\ (160℃)} = \frac{T_{(160℃)}}{T_{(20℃)}} \frac{\mu_{(20℃)}}{\mu_{(160℃)}} \times D_{AB\ (20℃)} \qquad \textbf{(F.2)}$$

$$D_{AB\ (160℃)} = \frac{433.15}{293.15} \frac{\times (1.00 \times 10^{-3})}{\times (1.70 \times 10^{-3})} \times 6.15 \times 10^{-10}$$

$$D_{AB\ (160℃)} = 5.35 \times 10^{-9}\ {}^{m^2}/_{s}$$

Knowing D_{AB} and d_p, the mass transfer coefficient can be calculated:

$$k_m = \frac{2 \times (5.35 \times 10^{-9})}{1.76 \times 10^{-4}} = 6.05 \times 10^{-5}\ {}^{m}/_{s}$$

Table F.1 Mass transfer coefficient data for static system

T (°C)	T (K)	ρ_l (kg/m^3)	μ_l (Pas)	d_p (m)	D_{AB} (m^2/s)	k_m (m/s)
160	433.15	907.45	1.70 x 10^{-4}	1.76 x 10^{-4}	5.35 x 10^{-9}	6.05 x 10^{-5}
170	443.15	897.45	1.60 x 10^{-4}	1.76 x 10^{-4}	5.84 x 10^{-9}	6.61 x 10^{-5}
200	473.15	864.66	1.34 x 10^{-4}	1.76 x 10^{-4}	7.40 x 10^{-9}	8.38 x 10^{-5}
220	493.15	840.22	1.22 x 10^{-4}	1.76 x 10^{-4}	8.53 x 10^{-9}	9.66 x 10^{-5}

F.2 Flow-through system

The liquid velocity has been calculated according to the design specification and must be known to calculate the Reynolds number according to Equation (5.21):

$$Re = \frac{d_p \nu \rho_l}{\mu_l} \quad \textbf{(F.3)}$$

where: d_p = average diameter of particle (m)

ν = liquid velocity $(^{m}/_{s})$

ρ_l = density of liquid $\left(^{kg}/_{m^3}\right)$

μ_l = liquid viscosity $\left(^{kg}/_{m.s}\right)$

The Sherwood number was used to calculate the mass transfer coefficient according to Equation (5.20):

$$Sh = \frac{k_m d_p}{D_{AB}} = 2 + 0.6\, Re^{\frac{1}{2}}\, Sc^{\frac{1}{3}} \quad \textbf{(F.4)}$$

Since the data of diffusivity of H_4SiO_4 in water is not readily available, The Wilke-Chang correlation was used to allow the estimation of liquid diffusivities at different temperatures, where D_{AB} is proportional to temperature to the first power and liquid velocity to the -1 power:

$$\frac{D_{AB\,(2)}}{D_{AB\,(1)}} = \frac{T_{(2)}}{T_{(1)}}\frac{\mu_{(1)}}{\mu_{(2)}} \qquad \textbf{(F.5)}$$

The subscript (1) and (2) indicates the known data at a specific temperature and unknown data at a target temperature, respectively. Jander and Jahr (1934) cited in Robinson (1982) reported the diffusivity of H_4SiO_4 is 6.15 x 10^{-10} m/s at 20°C, and this will be used as a reference to calculate D_{AB} at other temperatures. Therefore, with the known particle diameter, and the obtained values for Reynolds number, D_{AB}, and Schmidt number, the mass transfer coefficient can be calculated and compared to the reaction rate constant. An approach to calculate the average mass transfer calculation for suspended particles (Sherwood et al., 1975; Robinson, 1982) was also undertaken to compare results: It is assumed that the particles are suspended in the flow through cell, the velocity following the Stokes' law terminal velocity:

$$U_{TS} = \frac{d_p^2|\rho_s - \rho_l|g}{18\mu_l} \qquad \textbf{(F.6)}$$

where: U_{TS} = Stokes' law terminal velocity $\left({}^{m}/_{s}\right)$

d_p = average diameter of particle (m)

ρ_s = density of solid particles $\left({}^{kg}/_{m^3}\right)$

ρ_l = density of liquid $\left({}^{kg}/_{m^3}\right)$

g = gravitational acceleration = 9.81 $\left({}^{m}/_{s^2}\right)$

μ_l = liquid viscosity $\left({}^{kg}/_{m.s}\right)$

The velocity calculated using Equation (5.23) is then used to calculate the Reynolds number based on Stokes' law:

$$Re_{TS} = \frac{d_p^3 \rho_l |\rho_s - \rho_l| g}{18\mu_l^2} \quad \textbf{(F.7)}$$

After obtaining the Reynolds number based on Stokes' law, Table 5.33 is used to obtain the value of U_T/U_{TS}. Knowing the value of U_{TS} calculated using Equation (5.23), the value of U_T can be obtained. A new Reynolds number is calculated using the U_T obtained from the method above replacing the velocity in Equation (5.21). Therefore, with the known particle diameter and the obtained Sherwood number and diffusivity of H_4SiO_4, the mass transfer coefficient can be calculated and compared to the reaction rate constant.

Appendix G Darby's Bore Water Analyses

This section presents the water analyses for Darby's bore water.

Table G.1 Darby's bore water analysis March 2007

Darby's bore water analysis March 2007	concentration (mg/L)
Alkalinity as CaCO3	150
Bicarbonate as CaCO3	150
Carbonate as CaCO3	<10
Hydroxide as CaCO3	<10
Chloride	420
Sulfate	165
Calcium	87.3
Iron	<0.01
Potassium	10.2
Magnesium	15.9
Sodium	278
Phosphorus	<0.02
Sulphur	54.9
Silicon	7.8

Table G.2 Darby's bore water analysis August 2008

Darby's bore water analysis August 2008	Concentration
Dissolved Metals in water by ICP-AES	(mg/L)
Calcium	83.5
Iron	0.016
Magnesium	17
Potassium	8.9
Silicon	6.13
Sodium	280
Sulphur	67
Total metals in water by ICP-AES	(mg/L)
Aluminium	<0.01
Barium	0.15
Calcium	84.2
Iron	0.023
Magnesium	175
Manganese	<0.005
Silicon	6.26
Strontium	0.811
Total sulphate in water by ICP-AES	(mg/L)
Sulfate	201

Table G.3 Darby's bore water analysis August 2008 (cont.)

Darby's bore water analysis August 2008	Concentration
Alkalinity in water	(mg/L)
Total alkalinity as CaCO3	143
Bicarbonate as CaCO3	143.1
Carbonate as CaCO3	<10
Hydroxide as CaCO3	<10
Anions in water by titration	(mg/L)
Chloride	370
Fluoride	0.6
Chlorine in water	(mg/L)
Free chlorine	<0.1
Total chlorine	<0.1
Apparent colour in water	(CU)
Apparent colour	<2
True colour in water	(CU)
True colour	<2
Conductivity in water	(µS/cm)
Electrical conductivity	1890
Ammonia in water by FIA	mg/L
Ammonia as N	<0.02

Table G.4 Darby's bore water analysis August 2008 (cont.)

Darby's bore water analysis August 2008	Concentration
Nitrates in water by FIA	(mg/L)
Nitrate as N	3.7
Nitrite as N	<0.01
Nox as N	3.7
Oil and grease in water by gravimetry	(mg/L)
grease and oil	<5
Dissolved solids in water	(mg/L)
Total dissolved solids	1100
Total dissolved solids by EC in water	(mg/L)
Total dissolved solids	1100
Suspended solids in water	(mg/L)
Total suspended solids	<20
TOC in water by analyser	(mg/L)
Total organic carbon	2.4
Turbidity in water	(NTU)
Turbidity	0.8

Table G.5 Darby's bore water analysis November 2008

Darby's bore water analysis November 2008	value	units
Calcium	94	mg/L (ppm)
Magnesium	19	mg/L (ppm)
Sodium	290	mg/L (ppm)
Potassium	9.4	mg/L (ppm)
Iron (Total)	0.27	mg/L (ppm)
Iron (Soluble)	<0.01	mg/L (ppm)
Aluminium (Soluble)	<0.01	mg/L (ppm)
Manganese (Total)	<0.01	mg/L (ppm)
Suspended solids	<10	mg/L (ppm)
Boron	0.46	mg/L (ppm)
Strontium	0.8	mg/L (ppm)
Sulphate	210	mg/L (ppm)
Nitrate as N	<1.0	mg/L (ppm)
Chloride	350	mg/L (ppm)
Bi-Carbonate alkalinity as CaCO3	100	mg/L (ppm)
Carbonate alkalinity as CaCO3	<10	mg/L (ppm)
Hydroxide alkalinity as CaCO3	<10	mg/L (ppm)
Barium	0.12	mg/L (ppm)
Phosphate as P	<1.0	mg/L (ppm)
Silicon	7.1	mg/L (ppm)
Electrical conductivity	1960	µS/cm
Total dissolved solids (by EC)	1080	mg/L (ppm)
pH	7	pH units
Total alkalinity as CaCO3	<10	mg/L (ppm)
Total hardness as CaCO3	-	mg/L (ppm)

Table G.6 Darby's bore water analysis November 2008 (cont.)

Darby's bore water analysis November 2008	value	units
Fluoride	<1.0	mg/L (ppm)
Copper Zinc	<0.01	mg/L (ppm)
Arsenic	0.02	mg/L (ppm)
Aluminium (Total)	<0.01	mg/L (ppm)
	<0.01	mg/L (ppm)